



HAL
open science

Second Harmonic Generation as a Complementary Technique for Characterization of Powdered Organics

Lina Yuan

► **To cite this version:**

Lina Yuan. Second Harmonic Generation as a Complementary Technique for Characterization of Powdered Organics. Analytical chemistry. Normandie Université, 2017. English. NNT: 2017NORMR044. tel-01689719

HAL Id: tel-01689719

<https://theses.hal.science/tel-01689719>

Submitted on 22 Jan 2018

HAL is a multi-disciplinary open access archive for the deposit and dissemination of scientific research documents, whether they are published or not. The documents may come from teaching and research institutions in France or abroad, or from public or private research centers.

L'archive ouverte pluridisciplinaire **HAL**, est destinée au dépôt et à la diffusion de documents scientifiques de niveau recherche, publiés ou non, émanant des établissements d'enseignement et de recherche français ou étrangers, des laboratoires publics ou privés.



Normandie Université

THÈSE

Pour obtenir le diplôme de doctorat

Chimie des Matériaux

Préparée au sein de l'Université de Rouen Normandie

La Génération de Seconde Harmonique comme Technique Complémentaire pour la Caractérisation des Poudres Organiques

**Présentée et soutenue par
Lina YUAN**

**Thèse soutenue publiquement le 30 Juin 2017
devant le jury composé de**

Mme. Patricia SEGONDS	PR. Institut NEEL, Université Grenoble Alpes	Rapporteur
M. Michel FERRIOL	PR. Université de Lorraine	Rapporteur
Mme. Christine MARTIN	DR. CRISMAT, ENSICAEN	Examineur
M. Jean-Jacques COUNIOUX	PR. Université de Lyon	Examineur
M. Olivier MONNIER	Dr. Directeur Physical Quality & Process Safety Group, Sanofi-Aventis	Examineur
Mme. Valérie DUPRAY	MCF-HDR. SMS, Université de Rouen Normandie	Co-directrice de thèse
M. Gérard COQUEREL	PR. SMS, Université de Rouen Normandie	Directeur de thèse

Thèse dirigée par Gérard COQUEREL et Valérie DUPRAY, Laboratoire Sciences et Méthodes Séparatives (SMS)





Normandie Université

PhD THESIS

In view to obtain the degree of Doctor of Philosophy in Science

Materials Chemistry

Submitted to the Faculty of Science - University of Rouen Normandie in partial fulfillment of the requirements for the degree

Second Harmonic Generation as a Complementary Technique for Characterization of Powdered Organics

Presented and defended by
Lina YUAN

Defended the June, 30th 2017

in front of the dissertation committee composed of

Mme. Patricia SEGONDS	PR. Institut NEEL, Université Grenoble Alpes	Reviewer
M. Michel FERRIOL	PR. Université de Lorraine	Reviewer
Mme. Christine MARTIN	DR. CRISMAT, ENSICAEN	Examiner
M. Jean-Jacques COUNIOUX	PR. Université de Lyon	Examiner
M. Olivier MONNIER	Dr. Head of Physical Quality & Process Safety Group, Sanofi-Aventis	Examiner
Mme. Valérie DUPRAY	MCF-HDR, SMS, Université de Rouen Normandie	Co-supervisor
M. Gérard COQUEREL	PR. SMS, Université de Rouen Normandie	Supervisor

Supervised by Gérard COQUEREL and Valérie DUPRAY, Laboratory Sciences et Méthodes Séparatives (SMS)



Acknowledgements

Looking back my three years studied in SMS lab, I received enormous helps and supports from my professors, colleagues, family and friends. Here, I would like to express my gratitude to them.

First of all, my sincere thanks go to my thesis supervisor, Professor Gérard Coquerel, who gave me this precious opportunity to come to France and start my thesis. Under your guidance, I entered the field of solid-state chemistry and heterogeneous equilibria. You used your knowledgeable expertise and insightful views to inspire me how to conduct research and how to be a qualified researcher. You yourself set as an example to show me that research is to share and knowledge is borderless.

Special thanks to Dr. Valérie Dupray, my thesis co-supervisor. Thank you for bringing me the knowledge in physics and nonlinear optics, and always being patient and kind. Along my thesis, you devoted much efforts to follow every detail from experiments to writings. Numerous discussions we had regularly guided me on the right track. Your meticulousness and thoroughness deeply influenced me. During these three years, I worked with confidence and expects since I know you will always stand by my sides.

Then, I'd like to thank Dr. Simon Clevers, who is a non-official supervisor and a close friend to me. Thank you for teaching me the basic knowledge at the beginning of my thesis, for giving many constructive opinions and for the countless discussions we had along my thesis. Thank you also for accompanying to eat in ESPE and for sharing happiness and sorrow.

Thanks go to Dr. Morgane Sanselme for teaching me the knowledge on X-ray diffraction and for bringing the candy and chocolate, which encouraged me to write my manuscript. Thanks to Dr. Nicolas Couvrat for the knowledge of thermal analysis and discussions we had. To Dr. Gabin Gbabode, with whom I often had nice discussions and new things to discovery. Thanks to Dr. Samuel Petit, Dr. Yohann Cartigny and Dr. Clément Brandel and all the permanent staff in SMS lab.

I would like to thank Ghislaine, for settling me down when I arrived, for dealing with all the administrative procedures and for teaching me arts and French, without you I could not speak French as fluent as I could now.

Many thanks to my dear colleagues, who have been my friends now, Emilie, Grace, FX, Clément DSJ, Bienvenu, Manon, Benjamin, Antoine, Mélanie, Quentin, Lina H, Aliou and Ryusei. You helped me going through difficulties encountered in science and daily life, sharing knowledge and personal stories, making jokes and travelling together, which made my Ph.D life more interesting and colourful.

I also want to thank the reviewers of the present thesis and the members of the jury. Thank you for your time spent on this thesis and I expect your comments will lead to very interesting discussions during the defence.

Lastly, many thanks to my family and friends, who always support and encourage me even though you are 8000 km away.

Table of Contents

Introduction	1
Chapter I. Generalities	5
I-1. Crystals and Crystal Structures	7
I-1-1. Crystals	7
I-1-2. Crystal Structures	8
I-1-2-1. Crystal Lattices	8
I-1-2-2. Symmetry in Crystals	8
I-1-2-3. The Classification of Point Groups	10
I-1-3. Space Groups	10
I-1-3-1. The Basics of Space Groups	10
I-1-3-2. Space Group Frequencies	11
I-1-3-3. Non-centrosymmetric and Cubic Crystal Classes	11
I-1-3-4. Space Group Determination	12
I-2. Thermodynamics of Phase Equilibria	14
I-2-1. Basic Notions	14
I-2-2. Gibbs Phase Rule	14
I-2-3. Gibbs Free Energy	15
I-2-4. Stable Equilibrium and Metastable Equilibrium	16
I-2-5. Unary Systems	17
I-2-6. Binary Systems	17
I-2-6-1. Types of Binary Systems	17
I-2-6-2. Lever Rule	18
I-2-6-3. Eutectic Phase Diagrams	19
I-2-6-4. Peritectic Phase Diagrams	21
I-2-7. Ternary Systems	23
I-3. Solid-state Phase Transitions	24
I-3-1. Crystalline Solids	24
I-3-2. Paths of Forming Crystals	25
I-3-3. Phase Transitions	26
I-3-3-1. The Classification of Phase Transitions	26
I-3-3-2. Order-disorder Transitions	28
I-3-3-3. Landau's Phenomenological Approach	29
I-3-4. Kinetics of Solid-state Phase Transitions	29
I-3-4-1. The Relationship between Kinetics and Thermodynamics	29
I-3-4-2. Crystallization under Isothermal Conditions	30
I-3-4-3. Crystallization under Non-isothermal Conditions	32

I-4. Second Harmonic Generation	33
I-4-1. Linear Optics	33
I-4-2. Nonlinear Optics	34
I-4-2-1. Nonlinear Optics in Life	34
I-4-2-2. The Origin of Nonlinear Optics	35
I-4-2-3. Introduction of Second Harmonic Generation	36
I-5. Powder Second Harmonic Generation	45
I-5-1. Introduction of Power SHG	45
I-5-2. The Behaviors of Materials for Power SHG	45
I-5-3. Description of the Experimental Devices: Powder SHG and Powder TR-SHG	47
I-5-3-1. Powder SHG Set-up	47
I-5-3-2. Powder TR-SHG Set-up	48
I-5-4. The Applications of Powder SHG and Powder TR-SHG	49
I-5-4-1. Supplementary Tool to Assign Space Group	49
I-5-4-2. Spotting Conglomerates	50
I-5-4-3. Characterization of Sample Purity	54
I-5-4-4. Detection of Solid-solid Phase Transitions	54
Chapter II. Phase Diagram Investigations by TR-SHG	65
II-1. Stable Eutectic Phase Diagram Investigations — Urea/Water System	67
II-1-1. Introduction	67
II-1-2. Principle of Eutectic Phase Diagram Determinations by TR-SHG	69
II-1-3. Experimental Details	71
II-1-3-1. Preparation of the Samples	71
II-1-3-2. TR-SHG Experimental Procedures	72
II-1-4. Measurements of Hypoeutectic Compositions between Urea and Water by TR-SHG	72
II-1-5. Measurements of Hypereutectic Compositions between Urea and Water by TR-SHG	74
II-1-6. Plot of the Eutectic Phase Diagram between Urea and Water by TR-SHG	75
II-1-7. Precise Determination of the Eutectic Composition between Urea and Water by TR-SHG	76
II-1-8. Discussions	77
II-1-9. Conclusion and Perspectives	79
II-2. Metastable Eutectic Phase Diagram Investigations — 1,3-Dimethylurea (DMU)/Water System	81
II-2-1. Introduction	81
II-2-2. Preparation of the Samples	84
II-2-3. Establishment of an Experimental Protocol to Study the Metastable Equilibrium between SS II and Water	84
II-2-4. TR-SHG Analysis in the Metastable SS II/Water System	86
II-2-4-1. SHG Response in the SS II/Water System	86
II-2-4-2. Measurements of Hypoeutectic Compositions between SS II and Water by TR-SHG	86

II-2-4-3. Measurements of Hypereutectic Compositions between SS II and Water by TR-SHG	87
II-2-5. Plot of the Metastable Eutectic Phase Diagram between SS II and Water by TR-SHG	88
II-2-6. Precise Determination of the Metastable Eutectic Composition between SS II and Water by TR-SHG	89
II-2-6-1. Method 1: Differentiate the Liquidus and Solidus of compositions Close to the Eutectic Composition	89
II-2-6-2. Method 2: Enhanced SHG Signal due to the Eutectic Microstructure	90
II-2-7. Discussions	93
II-2-7-1. Discussions about the Methods to Precise the Metastable Eutectic Composition	93
II-2-7-2. Discussions about the TR-SHG Curve in the Hypoeutectic Compositions	94
II-2-7-3. Discussions about the Liquidus in the SS II/Water Metastable Eutectic Phase Diagram	96
II-2-8. Conclusion	97
II-3. Investigations of Hexamethylenetetramine (HMT)/Water System by TR-SHG	99
II-3-1. Introduction	99
II-3-2. Study of the Eutectic Phase Diagram in HMT/Water System by TR-SHG	100
II-3-2-1. Measurements of Hypoeutectic Compositions between HMT•6H ₂ O and Water by TR-SHG	101
II-3-2-2. Measurements of Hypereutectic Compositions between HMT•6H ₂ O and Water by TR-SHG	102
II-3-2-3. Plot of the Eutectic Phase Diagram between HMT•6H ₂ O and Water by TR-SHG	103
II-3-3. Study of the Peritectic Equilibrium in HMT/Water System by TR-SHG	104
II-3-4. Discussions	105
II-3-5. Conclusion and Perspectives	107
Chapter III. Kinetics Studies by TR-SHG	111
III-1. Investigations of the Crystallization of 1,3-Dimethylurea Monohydrate (DMU•H₂O) by TR-SHG	113
III-1-1. Introduction	113
III-1-2. Energy Calculations of DMU and DMU•H ₂ O (Thermodynamics)	115
III-1-3. Mechanism of the Crystallization of DMU•H ₂ O	117
III-1-3-1. Second Harmonic Response of the Crystallization of DMU•H ₂ O	117
III-1-3-2. Kinetics of the Crystallization of DMU•H ₂ O	118
III-1-4. Activation Energy Calculation Based on the TR-SHG Measurements	121
III-1-5. Discussions	122
III-1-6. Conclusion	123
III-2. Monotropic Phase Transition of 2-Adamantanone Studied by TR-SHG	124
III-2-1. Introduction	124
III-2-2. Phase Transitions of 2O-A Studied by TR-SHG	125
III-2-3. Path of the Monotropic Transition from HT Phase to the LT Phase	126
III-2-4. Kinetics of the Monotropic Transition from Metastable LT phase to the Stable LT Phase	127

III-2-5. Activation Energy Calculation Based on the TR-SHG Measurements	129
III-2-6. Conclusion	130
Chapter IV. Solid-solid Phase Transitions Investigated by TR-SHG	133
IV-1. A Newly Discovered Polymorph of 1-Fluoro-adamantane (1-F-A) Investigated by TR-SHG	135
IV-1-1. Introduction	135
IV-1-2. Purification Procedure for 1-F-A	137
IV-1-3. Characterization of 1-F-A Phase Transition by DSC and Cold-stage Microscope	137
IV-1-4. TR-SHG Measurements	137
IV-1-5. Crystals Structure of MT Phase Determined from XRPD	140
IV-1-6. Mechanism of MT \leftrightarrow LT Phase Transition	142
IV-1-7. Variation of the Order Parameter with Temperature	144
IV-1-8. Conclusion and Perspectives	147
IV-2. Phase Transitions of Adamantane Investigated by TR-SHG	148
IV-2-1. Introduction	148
IV-2-2. Preparation of the Sample	149
IV-2-3. Characterization of Adamantane Phase Transitions by DSC and XRPD	149
IV-2-4. TR-SHG Measurements of Adamantane Phase Transitions	151
IV-2-4-1. Existence of an Intermediate Phase?	151
IV-2-4-2. Transition Mechanism of Adamantane	152
IV-2-5. Conclusion and Perspectives	152
General Conclusion and Perspectives	159
Appendices	165
Appendix I. Table of 230 Space Groups	167
Appendix II. Form of the d-Matrix for Different Symmetry Classes in General Conditions and Kleinman Symmetry	168
Appendix III. Purging Methods and Evaluation of the Efficiency	170
Appendix IV. Reliability of TR-SHG Measurements	172
Appendix V. Identification and Quantification of the Impurities in 1-Fluoro-adamantane	174
Appendix VI. Experimental Details	177

Introduction

In the solid-state, materials containing a given chemical entity can exist in multiple phases, including polymorphs, salts, solvates and co-crystal. Various phases of a given compound commonly have different physical or chemical properties (such as solubility, dissolution rate, stability, and bioavailability). The full characterization of the phase transitions, in particular for organic products like pharmaceuticals and fine chemicals, can afford along its life time and is of great importance in many fields. Therefore, an accurate determination of the structural properties of the crystalline solid phases is necessary.

Phase transitions are controlled by thermodynamics and kinetics. Thermodynamic considerations decide the ultimate stability of the solid phases, whereas kinetics tell the possible pathway and how fast a change can occur. Both aspects must be taken into account to build a comprehensive picture of the phase transitions. Phase diagrams are useful graphical representations of the phase transitions and the most popular techniques used for their determinations are thermal analysis (TA), differential thermal analysis (DTA) and differential scanning calorimetry (DSC) accompanied by X-ray diffraction and microscopy observations. DSC has an advantage over DTA and TA, is to give precise value of enthalpy of thermal events in addition to temperature. Nevertheless, many thermal effects can occur in narrow temperature ranges that make the interpretations of the DSC curves (i.e., the separation of the different thermal events) difficult or even impossible. For example, in the case of a eutectic phase diagram, eutectic temperature and liquidus temperature are often too close to be distinguished when the compositions are close to the eutectic composition. It is thus impossible to determine eutectic temperature, liquidus temperature and the precise eutectic composition from direct experimental DSC curves. Tammann graph and deconvolution process could be applied, but regrettably, the estimation treatment would give a less accurate result.

A commonly used technique to determine the kinetics of phase transitions is DSC. The volume fraction of the transferred phase can be obtained from the corresponding enthalpy released. Unfortunately, this calculation is only a rough estimation. Moreover, in some cases, the transition is so slow that the thermal event would spread over a large time/temperature scale, which makes the calculation impossible.

As we previously mentioned, the precise characterization of the crystalline phase is an aspect that must not be neglected. Crystals, more precisely perfect crystals, in which the atoms arrange in an ordered array, provide an important starting point for understanding properties of solids. Many organic materials go through mesophases (partial ordered) in passing from the crystal to the isotropic liquid. One mesophase that retain a 3-dimensional crystal lattice with translational order but orientational disorder (i.e., disordered crystal mesophases) is known as "plastic crystal". As the temperature of such a material is raised, a point is reached at which the molecules become energetic enough to overcome the rotational energy barriers. Therefore, the crystal structure or even the symmetry could be slightly changed. However, the detection of this change could be too subtle to be captured by "usual techniques".

To solve the above issues, classical techniques, such as differential scanning calorimetry, X-ray diffraction, spectroscopy and microscopy might not sufficient. Therefore, the development of complementary analytical methods in addition to the classical techniques is beneficial.

In 1968, Kurtz and Perry developed a nonlinear optical method — second harmonic generation (SHG) on powder, to detect the crystalline non-centrosymmetry with a high sensitivity. Then, this method has raised certain interests since suitable single crystals are often easily not available. Besides, although some examples of the use of second harmonic generation for the characterization of the phases transitions can be found in literature, but mainly for inorganic compounds. This technique has not been widely applied for powdered organics and the use in laboratories is often limited to a simple measurement at ambient temperature by a newly synthesized compound to rapidly evaluate its potential for nonlinear optical applications.

The aim of the present Ph.D thesis is to extend the applications of powder SHG method and to combine this technique with other classical techniques to understand more deeply the phase behaviors and to solve problematic issues encountered in some solid-state materials.

The results of this research work are presented in this document organized as follows:

In chapter I, basic notions about crystals, crystal structures, thermodynamics of phase equilibria and solid-solid phase transitions will be introduced. Also, the second harmonic generation and

powder SHG will be detailed.

In chapter II, SHG signal variations versus temperature (TR-SHG) will be interpreted and used to study the binary eutectic phase diagram between urea and water. The possibility to accurately determine eutectic composition by TR-SHG will be discussed. In the following parts, metastable eutectic phase diagram between 1,3-dimethylurea and water, system between hexamethylenetetramine and water will also be studied. The effects of phase-matchable and non-phase-matchable materials on the SHG signal will be detailed.

In chapter III, the kinetics studies by TR-SHG will be presented. The first case deals with the kinetics of crystallization of 1,3-dimethylurea monohydrate. The second case study is devoted to the monotropic phase transition of 2-adamantanone.

Chapter IV focus on the investigations of solid-solid transitions by TR-SHG. Case study of adamantane and 1-fluoro-adamantane will be detailed.

Finally, the general conclusion will briefly summarize the main results of this thesis and future potential work will be proposed.

Chapter I

Generalities

This chapter gives an overview of the basic notions that help to understand the manuscript. Notions in crystals and crystal structures, thermodynamics of phase equilibria, solid-state phase transitions, second harmonic generation and powder second harmonic generation will be introduced.

I-1. Crystals and Crystal Structures

In this paragraph, the notion of “crystal” is introduced and the way atoms arranged in crystals will be illustrated by crystallography. Many chemical (including biochemical) and physical properties depend on crystal structure and knowledge of crystallography is essential if the properties of materials are to be understood and exploited¹.

I-1-1. Crystals

Gas, liquid and solid are the three general states of matter with different degrees of atomic or molecular mobility. The molecules move freely and randomly in a gas or liquid, while in the solid-state, this motion is confined to a fixed position. Solids can either be crystalline or amorphous. If the atoms arrange in a strict and periodic array (long-range order, LRO), this material is a **crystal**. By contrast, if only a short-range order (SRO) is present, the material is **amorphous**². Figure I-1 shows the arrangements of atoms in these two cases.

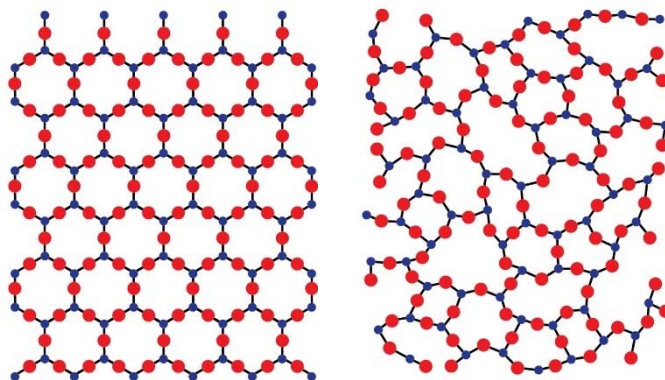


Figure I-1. 3D arrangement of atoms in a crystal (left) and a short-range order in an amorphous material (right).

Crystals are the most ordered manner to pack the materials and are almost always the most stable solid-state. They comprise a rigid lattice of molecules, atoms or ions, the locations of which can be used to characterize the crystals. Johannes Kepler³, is the first person to relate the external form or shape of a crystal to its underlying structure. In his paper “a new year’s gift or the six-cornered snowflake’, he asked why snowflakes always have six corners, never five or

seven? Thanks to the modern techniques of X-ray crystallography, the lattice dimensions and interfacial angles of crystals are revealed with high precision. This part will be introduced in the following.

I-1-2. Crystal Structures

I-1-2-1. Crystal Lattices

As illustrated above, crystals are three-dimensional, periodic arrays of atoms or molecules. They have distinct structures made up of a **lattice**. The group of atoms or molecules that repeats itself is called a **unit cell** and it contains the complete structural information. The smallest possible unit cell is called a **primitive unit cell**. The parameters a , b , c , α , β and γ that define a primitive unit cell are called **unit cell parameters** (see Figure I-2).

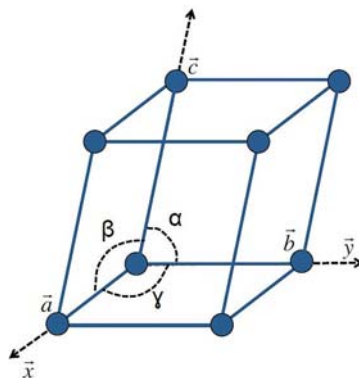


Figure I-2. Schematic representation of a unit cell defined by primitive translation vectors.

I-1-2-2. Symmetry in Crystals

Symmetry (Greek=harmony, regularity) means the repetition of a motif and thus the agreement of parts of an ensemble. An object is symmetric if it cannot be distinguished before and after transformation⁴. The three simple symmetry elements are:

- symmetry about a point (a center of symmetry)
- symmetry about a line (an axis of symmetry)
- symmetry about a plane (a plane of symmetry)

In the crystalline solids, many of the geometric shapes are recognized as being symmetrical. However, only a limited number of symmetry elements can be found. 1, 2, 3, 4, 6, $\bar{1}$, $\bar{2}=m$, $\bar{3}$, $\bar{4}$, $\bar{6}$ (in Hermann-Mauguin notation). 5-fold, 7-fold, 8-fold, or higher-fold rotation axes are not possible in crystals, since the external shape of a crystal is based on a geometric arrangement

of atoms. We cannot combine objects with 5-fold and 8-fold apparent symmetry to completely fill space⁵. As illustrated below (Figure I-3).

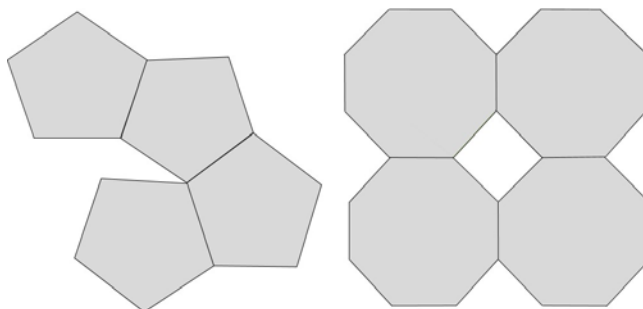


Figure I-3. Packing of objects displaying 5- and 8-fold symmetry. They do not fill completely space and therefore they are not compatible with crystals (but with quasi-crystals¹).

There are only 32 possible combinations of the above-mentioned symmetry elements, including the asymmetric state (no elements of symmetry), these are called the **32 point groups (PG)**. For convenience, these 32 PG are grouped into **7 crystal systems** (Table I-1)².

Table I-1. Overview over the 7 crystal systems: they are defined by the lengths and angles of the primitive translation vectors and exhibit different levels of symmetry.

Crystal System	Lengths	Angles
Triclinic	$a \neq b \neq c$	$\alpha \neq \beta \neq \gamma$
Monoclinic	$a \neq b \neq c$	$\alpha = \beta = 90^\circ \neq \gamma$
Orthorhombic	$a \neq b \neq c$	$\alpha = \beta = \gamma = 90^\circ$
Trigonal	$a = b = c$	$\alpha = \beta = \gamma \neq 90^\circ$
Tetragonal	$a \neq b \neq c$	$\alpha = \beta = \gamma = 90^\circ$
Hexagonal	$a = b \neq c$	$\alpha = \beta = 90^\circ, \gamma = 120^\circ$
Cubic	$a = b = c$	$\alpha = \beta = \gamma = 90^\circ$

However, the choice of a unit cell does not always lead to a simple lattice, the above crystal systems are not sufficient to describe all the possible lattices and thus it is not yet the best solution for a classification with respect to symmetry. Bravais⁶ introduced several “modes” noted as P (primitive), I (body centered), F (face centered), A, B or C (one face centered). The combination of these centering types with 7 crystal systems conducts to the classification of the **14 Bravais lattices**. The combination of 14 bravais lattices and 32 point groups constitutes **73 symmorphic space group**.

¹ A quasicrystal has an ordered structure, but lacks translational symmetry.

I-1-2-3. The Classification of Point Groups

Point groups containing inversion centers are **centrosymmetric**, otherwise they are **non-centrosymmetric**. Mathematically, if there is an atom at position (x, y, z) relative to the center of symmetry, there must also be an atom at (-x, -y, -z) (Appendix I)¹. Non-centrosymmetric is further divided into chiral and polar types. **Chiral point groups**, in which only rotation or screw axes are contained. For **polar point groups**, every operation leaves more than one common point unmoved (For example, the point group of 2, in which all points on the 2-fold axis are left unmoved by the operation of the 180° rotation⁷). The classification of point groups into centrosymmetric achiral (CA), non-centrosymmetric chiral (NC) and non-centrosymmetric achiral (NA) is shown below (Table I-2).

Table I-2. Point groups classified as CA: centrosymmetric achiral, NC: non-centrosymmetric chiral and NA: non-centrosymmetric achiral.

	CA	NC	NA
	$\bar{1}$ $\bar{3}$ $\bar{3}m$ $m\bar{3}$ $m\bar{3}m$	1 2 3 4 6	$\bar{4}$ $\bar{6}$
	2/m 4/m 6/m	32 23	$\bar{4}2m$ $\bar{4}3m$ $\bar{6}m2$
Point Group	$m\bar{m}\bar{m}$ 4/mmm 6/mmm	222 422 432 622	m mm2 3m 4mm 6mm

I-1-3. Space Groups

I-1-3-1. The Basics of Space Groups

In repeating lattices in 3 dimensions, two translational symmetry elements are introduced:

- **Screw axis** (rotation followed by translation: 2₁, 3₁, 3₂, 4₁, 4₂, 4₃, 6₁, 6₂, 6₃, 6₄, 6₅)
- **Glide plane** (reflection followed by translation: a, b, c, d and n).

Combination of the 14 Bravais lattices with the 32 point groups and these translational elements results in the **230 space groups (SG)** (see Figure I-4), i.e., 230 distinct ways of packing repeating object in 3D, which describes all possible crystal symmetries⁸. A summary of all the space groups are given in the International Tables for Crystallography.

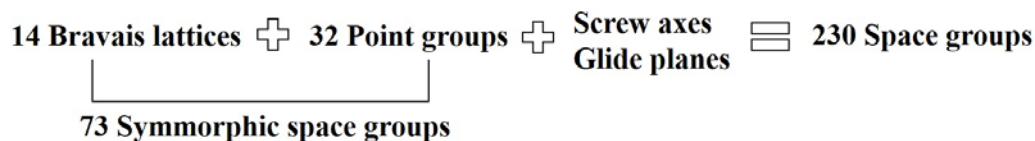


Figure I-4. All the necessary elements to form space groups.

I-1-3-2. Space Group Frequencies

Although there are 230 space groups, in practice the symmetry of the known crystal structures is not evenly distributed. It often depends on the type of materials (e.g., metallic, inorganic or organic). Metals, which are made of simple atoms, often crystallize in highly symmetrical crystalline systems (hexagonal, cubic)⁹. In the case of inorganic compounds, the most representative space groups are included in more various crystalline systems (frequently occurs in the SG of $Pnma$, $P2_1/c$, $Fm\bar{3}m$, $Fd\bar{3}m$, $I4/mmm$)^{10,11}. For “small” organic compounds (polymers and proteins are excluded), over 95% of the structures belong to either the triclinic, monoclinic or orthorhombic crystal systems, which have low symmetries.

Based on the *Cambridge Structural Database (CSD)* released in January 2017, 865,342 structures are included. 677,467 (78 %) structures crystallize in centrosymmetric space groups, 187,875 (22 %) in non-centrosymmetric space groups. 141,626 (16 %) structures crystallize in **Sohncke space groups** (Chiral SG). Table I-3 shows the 10 most frequently observed space groups in the CSD 2017. Among the 865,342 fully defined crystal structures, 87.8% crystallize in only 10 space groups, among which 15.8% crystallize in 5 non-centrosymmetric space groups (in bold).

Table I-3. The top 10 space group frequency ranking in CSD released in January 2017.

Space Group	$P2_1/c$	$P\bar{1}$	$C2/c$	$P2_12_12_1$	$P2_1$	$Pbca$	$Pna2_1$	$Pnma$	Cc	$P1$
Frequency (%)	34.5	24.7	8.4	7.2	5.2	3.3	1.4	1.1	1.0	1.0

I-1-3-3. Non-centrosymmetric and Cubic Crystal Classes

Is it possible that a crystal belongs to a cubic lattice while exhibits non-centrosymmetric properties? The answer is yes. Gallium arsenide (GaAs) provides one of the example. Gallium arsenide crystallizes in the zinc blende structure (named after the well-known mineral form of zinc sulfide), which has a cubic space group $F\bar{4}3m$ (non-centrosymmetric). Compared with the structure of diamond, which crystallizes in a centrosymmetric space group $Fd\bar{3}m$. Both materials crystallize in the cubic crystal lattice (Figure I-5), but the arrangement of atoms within the lattice allows carbon but not zinblende to possess a center of inversion symmetry¹².

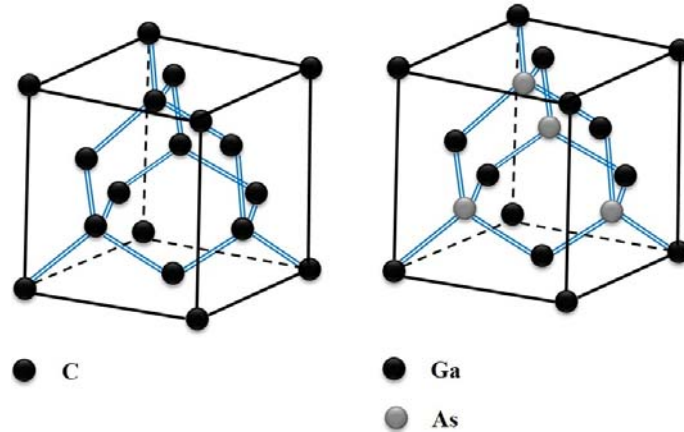


Figure I-5. The structure of (a) diamond, the structure is centrosymmetric and (b) zincblende, the structure is non-centrosymmetric. Both possess a cubic lattice.

I-1-3-4. Space Group Determination

Since the early 20th century, the physics of diffraction by crystals has been worked out in detail. When the wavelength of the radiation is similar to that of the atoms spacing in a crystal, the scattering occurs, which is called **diffraction**. And the electronic magnetic waves are diffracted by atoms in a characteristic way, called a **diffraction pattern**. Since the wavelength of X-rays (0.5-2 angstroms) is in the same range than the atoms in crystals and the X-rays are cheap and easy to obtain, the X-ray diffraction becomes the most widespread technique for structure determination (we should notice that the electron and neutron diffractions are also of great help, as these reveal features that are complementary to X-rays)⁶.

Bragg's law gives the required condition for the X-ray diffraction (Figure I-6): $2d_{hkl} \sin\theta = n\lambda$. d_{hkl} is the distance between the planes, θ is the angle of irradiation, n is a natural integer, and λ is the wavelength of the incident rays. For a given plane (hkl) with an interplanar distance of d_{hkl} , constructive interference only occurs when Bragg's law is satisfied.

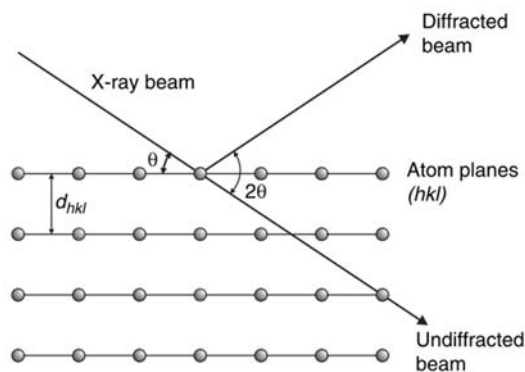


Figure I-6. Schematic illustration of Bragg's law for X-ray diffraction.

Usually, two methods: **single crystal X-ray diffraction (SCXRD)** and **X-ray powder diffraction (XRPD)** are used. The SCXRD is considered as the best method for structure determinations, but it requires a single and stable crystal (generally between 50-250 microns in size), which is difficult to obtain for some materials. XRPD is a simple technique in terms of sample preparation, but certain structural information can be lost. Here, we need to make two notions clear: single crystal and powder. The repetition of the unit cell by means of lattice translations gives rise to a particle in which the periodicity and the chemical nature of the crystal phase are homogeneous. The particle is limited by planar interfaces corresponding to specific reticular plans in the structure. Such a particle is called a **single crystal**. **Powder** can be regarded as dozens of randomly arranged small crystallites.

The positions and intensities of the diffraction peaks obtained from either SCXRD or XRPD are a function of the arrangements of the atoms in space and some other atomic properties, such as the atomic number of the atoms. It is possible to deduce the arrangement of the atoms in the crystal and their chemical nature by the indexing of diffraction peaks.

Three steps are required to determine the space groups^{1,13}:

- Determine the positions of the diffraction peaks to extract the information about the size of the unit cell and systematic existence of diffraction spots (68 direct determinations without ambiguity) among 230 SG.
- Calculate intensities of the diffraction patterns and relate these data to the crystal structure.
- It is necessary to recreate an image of the crystal, the crystal structure itself, using the information contained in the diffraction pattern.

Correct space group determination of a crystal structure is not always trivial. In a large number of publications¹⁴⁻¹⁷, the space groups turn out to have been incorrectly determined. The determination of “centrosymmetric or non-centrosymmetric” is probably the most irksome problem. For many of the most common pairs of space groups $P\bar{1}$ and $P1$, $P2_1$ and $P2_1/c$, Cc and $C2/c$, and $Pna2_1$ and $Pnam$, the choice between the two is ambiguous¹⁸.

I-2. Thermodynamics of Phase Equilibria

The following part will be dedicated to basic notions of thermodynamics of phase equilibria (heterogeneous equilibria) with special attention to organic systems. You may notice that the phase equilibria exist everywhere in our daily life. In a boiling pan of water, the bubbles of steam are formed by the water itself. The system reaches the equilibrium by changing phase from liquid to vapor. When you drink a beer, the rising bubbles signify gases dissolved in the beer and forming a separate phase. We make roads safer between the ice and snow by spreading salt to lower the melting point of water.

I-2-1. Basic Notions

A **phase** corresponds to a part of the system considered as homogeneous with uniform physical and chemical characteristics, in principle separable from the rest of the system. When several phases take place in a system (gas, solid(s) and liquid(s)), the equilibria between these different phases are called **heterogeneous equilibria**¹⁹. A graphical representation of the various phases present in equilibrium as a function of intensive variables (classically the pressure and the temperature) is a **phase diagram**. It is a convenient tool employed in material science and in pharmaceutical industry during the development of a new product and its production process²⁰. An exception to the rule that only true equilibrium states are recorded on phase diagrams is found in the representation of so-called **metastable equilibria (non-equilibria)**.

I-2-2. Gibbs Phase Rule

Degree of freedom (or variance) F is the number of variables (temperature, pressure and composition) that can be changed independently without changing the phases of the system. **Gibbs phase rule** describes the possible degrees of freedom (F) in a closed system at equilibrium in terms of the number of separate phases (P) and the number of independent components (C) in the system, which is derived from thermodynamic principles by Josiah W. Gibbs in the 1870s²¹:

$$F = C - P + 2 \quad (I-1)$$

The number 2 in the equation refers to the number of intensive variables considered (the pressure and the temperature). The phase rule determines the constraints that are placed upon a

phase diagram and is a guide to the interpretation of experimental observations²². For example, in the case of a **unary system** (only one independent component is considered, Figure I-7), the phase rule gives: $F=1-P+2=3-P$.

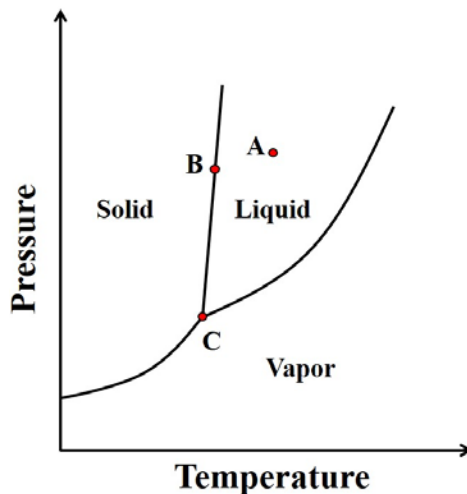


Figure I-7. A unary phase diagram.

- Point A: only liquid exist, $P=1$, the phase rule gives: $F=2$. This implies two degrees of freedom. Within limits, the pressure and temperature can be changed independently or together, and point A will still be in the liquid domain.
- Point B: the solid and liquid coexist, $P=2$, the phase rule gives: $F=1$. There is only one degree of freedom. If the temperature is changed, the pressure must also be adjusted to remain on the boundary.
- Point C: solid, liquid and vapor co-exist, $P=3$, the phase rule gives $F=0$. There are zero degree of freedom. All three phases coexist at one point with fixed temperature and pressure, which is called **triple point**²³.

I-2-3. Gibbs Free Energy

A system is at equilibrium when thermal equilibrium, mechanical equilibrium and chemical equilibrium are concomitantly reached in every of its open subsystems (i.e., phases). The state of equilibrium requires no further tendency for the system to change and corresponds to the lowest **Gibbs free energy**²⁴, labelled G . The thermodynamic relationship between G and the entropy is written as (suppose that the pressure is constant):

$$G = H - TS \quad (I-2)$$

- G: Gibbs free enthalpy ($\text{J}\cdot\text{mol}^{-1}$), H: enthalpy ($\text{J}\cdot\text{mol}^{-1}$),
- T: temperature (K), S: entropy ($\text{J}\cdot\text{mol}^{-1}\cdot\text{K}^{-1}$).

Attention should be paid that Gibbs free energy is not energy. Although G has the units of energy (joules, or in its intensive form, $\text{J}\cdot\text{mol}^{-1}$), it lacks one of the most important attributes of energy in that it is not conserved.

I-2-4. Stable Equilibrium and Metastable Equilibrium

As illustrated in Figure I-8, A is at stable equilibrium with the lowest free energy G. B lies at a local minimum of free energy but do not have the lowest possible value of G. It is at the metastable equilibrium state.

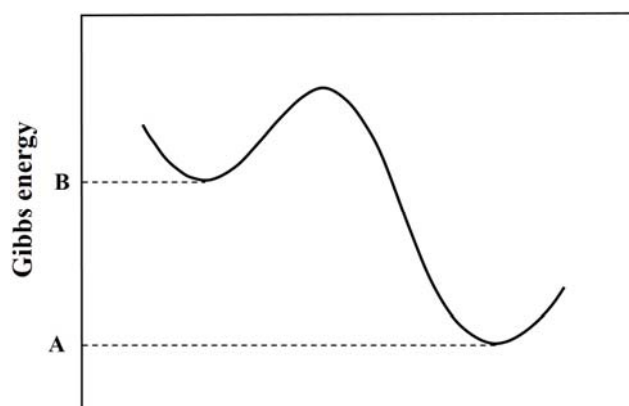


Figure I-8. Gibbs free energy for different states in a system. A has the lowest free energy and therefore is at the equilibrium state. B is at a state of metastable equilibrium.

A phase diagram tells us the phases in equilibrium, their compositions and proportions, also gives a starting point from which the non-equilibrium can be inferred¹⁹. Based on the Ostwald rule of stages, when the system is out of equilibrium, the intermediate metastable states will be involved before reaching the final stable state. Generally, the metastable state should irreversibly change to the equilibrium state. But the time spent in the metastable state can vary within a range of 10^{-12} to 10^9 s^{25,26}. In some particular cases, the metastable equilibrium is more favorable to reach than the equilibrium state²⁷. It is important to understand the metastable phases and to construct the metastable phase diagrams. However, due to the difficulty in the experimental determination, the metastable phase diagrams are often calculated and extrapolated from the equilibrium phase diagrams²⁸. Extrapolations to metastable conditions may give quite different and even wrong results²⁹.

I-2-5. Unary Systems

Figure I-7 refers to a one-component system (unary system). The thermodynamic stability of each phase in the equilibrium as a function of temperature is given by the minimization of the G-curves (Figure I-9). Below T_1 , the most stable phase is solid. At T_1 , the G values of both the solid phase and the liquid phase are equal (the two phases are in equilibrium), the phase changes from solid to liquid, T_1 is the melting point. Between T_1 and T_2 , liquid phase is the stable phase. At T_2 , liquid changes to vapor, represents the boiling point. Above T_2 , vapor is the stable phase.

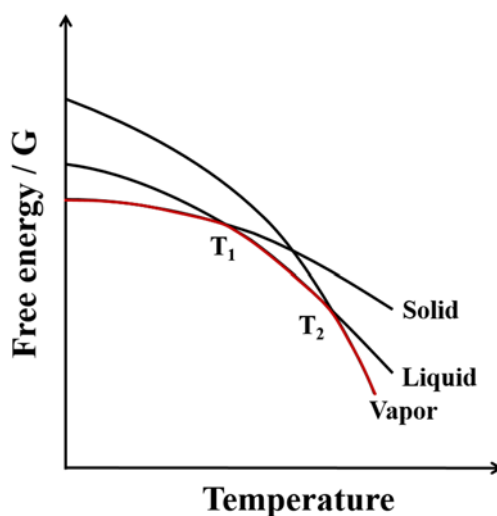


Figure I-9. Gibbs free energy curves for a unary system. The red line shows free energy curve of the system.

I-2-6. Binary Systems

I-2-6-1. Types of Binary Systems

A **binary phase diagram** consists of two independent components, showing the equilibrium constitution. When pressure is fixed, it is a diagram with temperature and composition as axes¹⁹. All types of reactions are illustrated in Table I-4 and Figure I-10 shows the various types of equilibrium that can be encountered in binary phase diagrams.

Table I-4. Types of invariant reactions in a binary equilibrium phase diagram at constant pressure³⁰.

Reaction	Eutectic	Monotectic	Metatectic	Peritectic
Phase equilibrium	$L \leftrightarrow S_1 + S_2$	$L_1 \leftrightarrow S_1 + L_2$	$S_1 \leftrightarrow S_2 + L$	$S_1 + L \leftrightarrow S_2$
Reaction	Syntectic	Eutectoid	Peritectoid	Monotectoid
Phase equilibrium	$L_1 + L_2 \leftrightarrow S$	$S_1 \leftrightarrow S_2 + S_3$	$S_1 + S_2 \leftrightarrow S_3$	$S_{1a} \leftrightarrow S_{1b} + S_2$

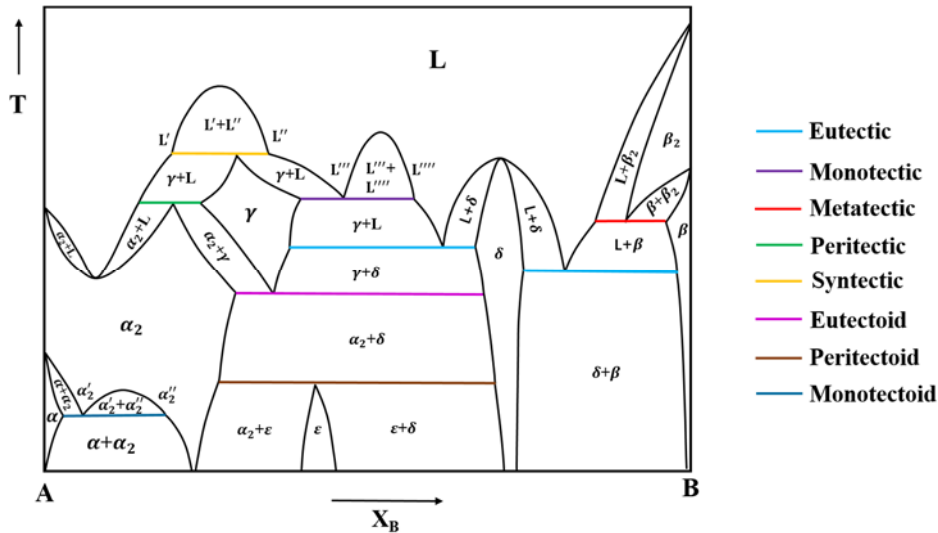


Figure I-10. Binary phase diagram showing different types of equilibria (colored segments). The suffix “-oid” corresponds to invariants with solid phases only.

I-2-6-2. Lever Rule

For a binary system of known composition and temperature that is at equilibrium, at least three kinds of information are available: (i) the phases that are present, (ii) the compositions of these phases, and (iii) the percentages or fractions of the phases³¹. To determine the percentages or fractions of the phases present in this phase diagram, the **tie line** (across the two-phase region) should be used in conjunction with a simple mathematical procedure that is called the **lever rule**, which is a tool to apportion the components (illustrated in Figure I-11).

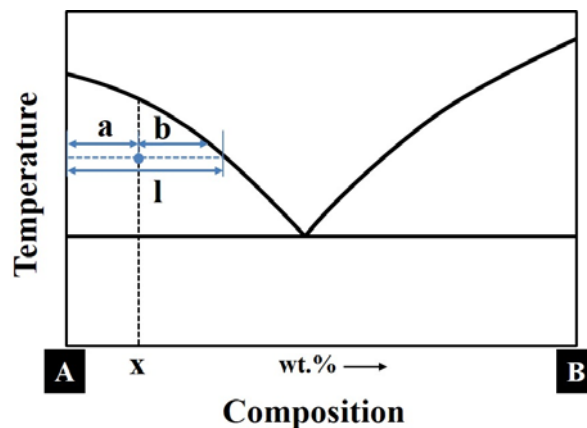


Figure I-11. Binary eutectic phase diagram to illustrate the lever rule.

For the composition of x , the tie-line is of length l while the lengths of the segments to either side of the constitution point are a and b respectively. The weight fractions of liquid and solid in the alloy are $w^{\text{liq}} = \frac{a}{l}$, $w^{\text{sol}} = \frac{b}{l}$. This illustrates why the name is the lever rule — it is

analogous to balance two weights on either side, with the shorter distance belonging to the greater weight. One should note that the lever rule can be applied only if the compositions of phases are expressed in terms of weight percent of the components.

Two types of phase diagrams were studied in detail in this thesis. One is eutectic phase diagrams and the other one is the peritectic phase diagrams.

I-2-6-3. Eutectic Phase Diagrams

Eutectic refers to a specific type of phase diagram, or part of a phase diagram, as illustrated in Figure I-12, where a homogeneous liquid solidifies into two different solid phases³². The three-phase reaction that takes place at the invariant point, E (**eutectic point**), is called a **eutectic reaction** (from the Greek word for “good fusion”). The temperature that corresponds to the eutectic point is called **eutectic temperature (T_E)**, which defines the lowest melting point of the system. The corresponding composition is **eutectic composition (X_E)**. The composition to the left of the eutectic point is called a **hypoeutectic composition** (the Greek word for “less than”); to the right is a **hypereutectic composition** (meaning “greater than”)²⁰.

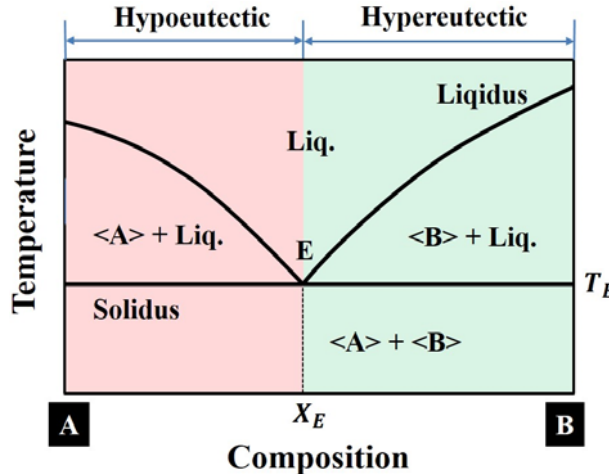


Figure I-12. A binary eutectic phase diagram.

I-2-6-3-1. Eutectic Solidification

In a binary eutectic phase diagram, the schematic representation of crystalline structures on cooling is shown in Figure I-13. For composition 1, upon cooling, it forms A crystals in liquid when it passes through the liquidus. When cools through the eutectic temperature, the remaining liquid freezes to form a eutectic mixture of A and B. Therefore, the final microstructure of 1 contains proeutectic A in a matrix of eutectic (A and B). For composition 2 (exactly the eutectic

composition), upon cooling from the liquid state, it converts from a liquid to a solid at the eutectic temperature. The resulting solid contains both A and B phases. The composition 3 is similar to composition 1, except the final microstructure has proeutectic B in a matrix of eutectic.

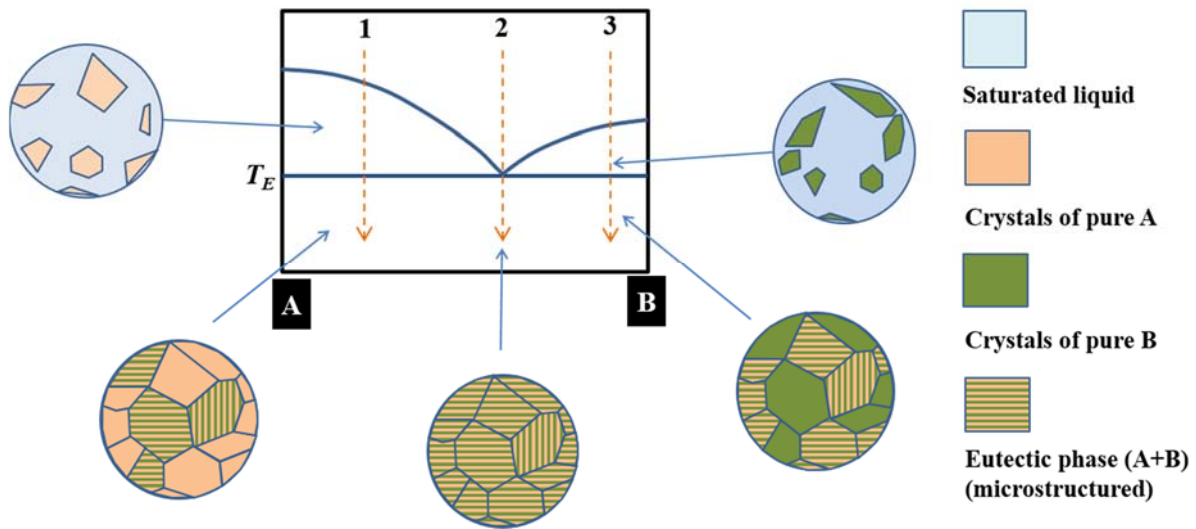


Figure I-13. Schematic of eutectic freezing.

I-2-6-3-2. Eutectic Mixtures

Eutectic Mixtures are characterized by the simultaneous growth of two phases from a single liquid, resulting in a microstructure with globally a fixed ratio of the two phases. The relative fractions of the eutectic microstructure can be found by treating the eutectic as a separate phase and applying lever rule. It can be classified according to two criteria:

- Lamellar or fibrous morphology of the phases. When there are approximately equal volume fractions of the phases (nearly symmetrical phase diagram), eutectic systems generally have a lamellar structure (Figure I-14-(a)). While if one phase is present in a small volume fraction, this phase will in most cases tend to form fibers (Figure I-14-(b)).
- Regular or irregular growth. If both phases are non-faceted (usually when both are metallic), the eutectic solid will exhibit a regular morphology. While if one phase is faceted, the eutectic morphology often becomes irregular (Figure I-14-(c)).

The eutectic growth is essentially solute diffusion controlled. However, during eutectic solidification, the A and B phases grow side by side in a cooperative manner. The B atoms rejected by the A phase are needed for the growth of the B phase, and vice versa. The solute

then needs only to diffuse along the solid-liquid interface from one phase to the other. This is the fundamental reason for the occurrence of eutectic growth²⁰.

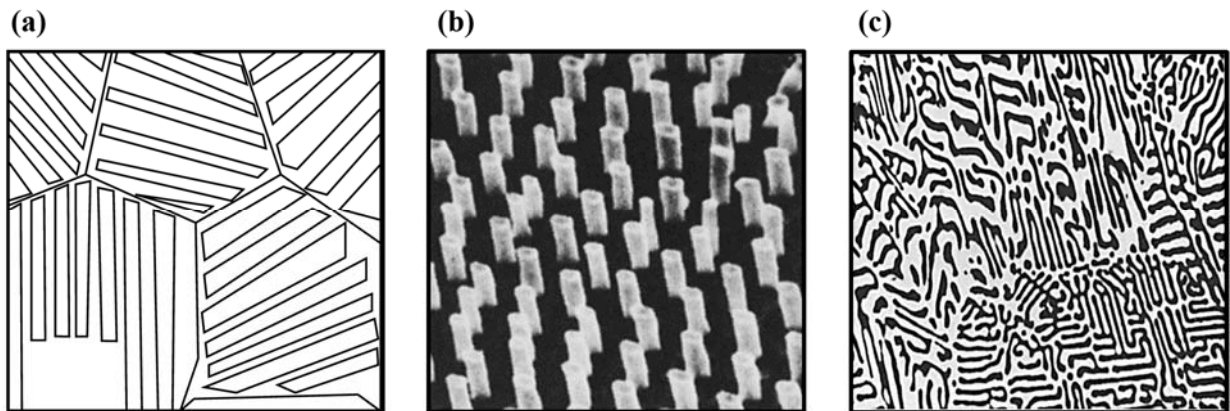


Figure I-14. Eutectic structures with (a) a lamellar structure, (b) a fibrous structure, and (c) irregular “Chinese script” eutectic consisting of faceted Mg_2Sn phase in a magnesium matrix.

I-2-6-4. Peritectic Phase Diagrams

The term **peritectic** refers to reactions in which a liquid phase reacts with at least one solid phase to form a new solid phase²⁰. The generalized form of this peritectic reaction is: $\alpha + L \leftrightarrow \beta$, as is shown in Figure I-15, the peritectic temperature is T_p .

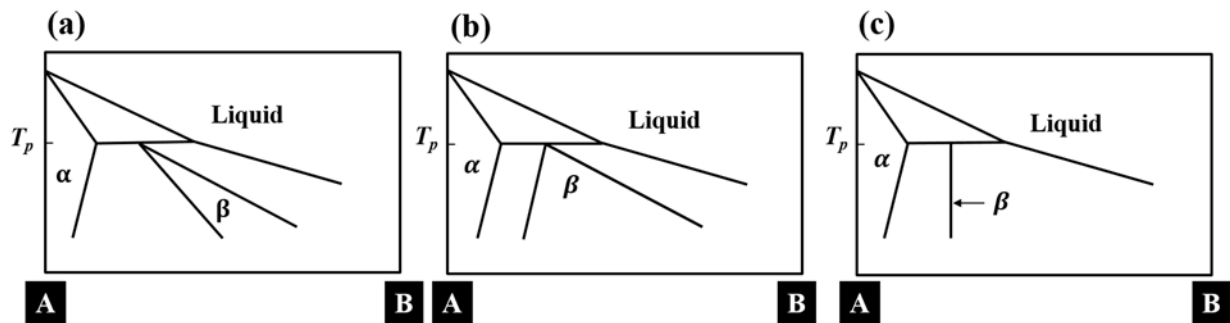


Figure I-15. Types of peritectic systems. (a) Type A system where the $\beta/\alpha + \beta$ solvus and the β solidus have slopes of the same sign. (b) Type B system where the slopes have opposite signs. (c) Type C system where the β phase has a limited composition.

I-2-6-4-1. Peritectic Solidification

Upon cooling from the melt (Figure I-16-(a)), the liquidus is reached at temperature T_1 , where crystals of α phase begin to form. The composition of this phase changes along the solidus and reaches the peritectic line. The peritectic reaction occurs: liquid and α react together to form β under equilibrium conditions. All the previously formed α as well as the liquid must be consumed and the freezing must be completed isothermally by this process.

The formed β phase surrounds the solid α particles, as shown in Figure I-16-(b), α atoms must diffuse through the β crust to reach the liquid for the reaction to continue. However, diffusion through the solid phase is much slower than diffusion through a liquid. As the peritectic reaction continues, the α layer gets thicker and the reaction slows down even more.

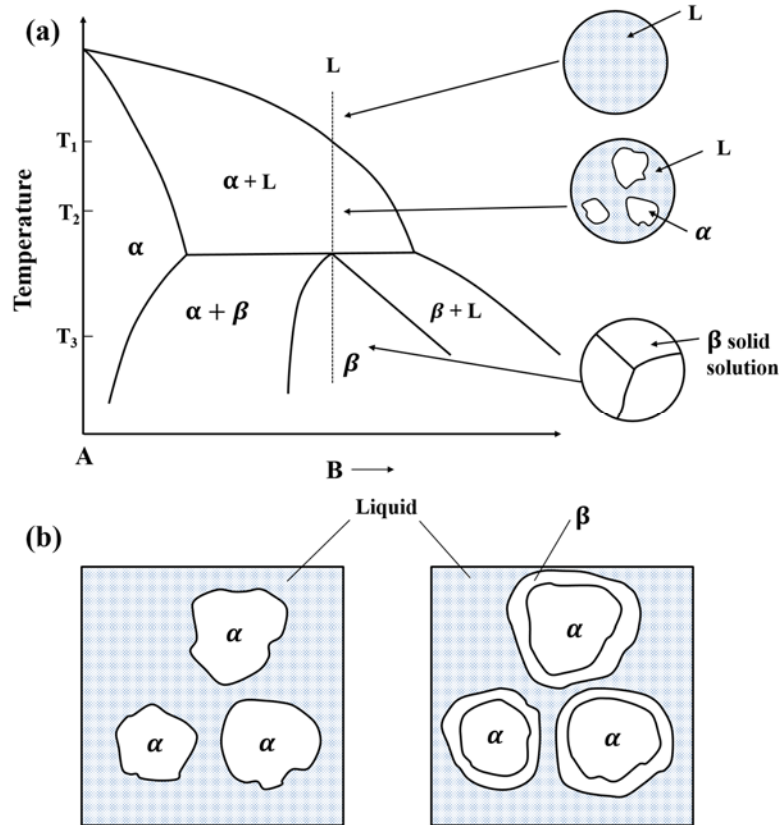


Figure I-16. (a) Schematic of peritectic freezing and (b) diffusion of α atoms through the β crust to reach the liquid.

I-2-6-4-2. Mechanisms of Formation of Peritectic Structures

The formation of peritectic structures can occur by at least three mechanisms:

- **Peritectic reaction**, where all three phases (α , β , and liquid) are in contact with each other. Peritectic reactions can proceed only as long as α and liquid are in contact. The β phase solid nucleates at the α liquid interface and readily forms a layer isolating α from the liquid.
- **Peritectic transformation**, where the liquid and the α phase are isolated by the β phase. The direct peritectic reaction can no longer take place. Further growth of the β phase because of disappearance of the α phase will then occur by solid-state diffusion.
- **Direct precipitation** of β phase from the melt, when there is enough undercooling below the peritectic temperature, T_p . Direct precipitation of β from the melt can occur when a peritectic reaction or peritectic transformation is sluggish.

The terms “peritectic reaction”, “peritectic transformation” and “direct precipitation” are useful for presenting different theoretical stages of peritectic solidification, but in real solidification conditions they are difficult to separate experimentally³³.

I-2-7. Ternary Systems

A **ternary phase diagram** involves three components and represents four dimensions (the three components plus temperature). It can be described as a combination of three binary phase diagrams. As is shown in Figure I-17, a ternary eutectic phase diagram is composed of three binary eutectic phase diagrams.

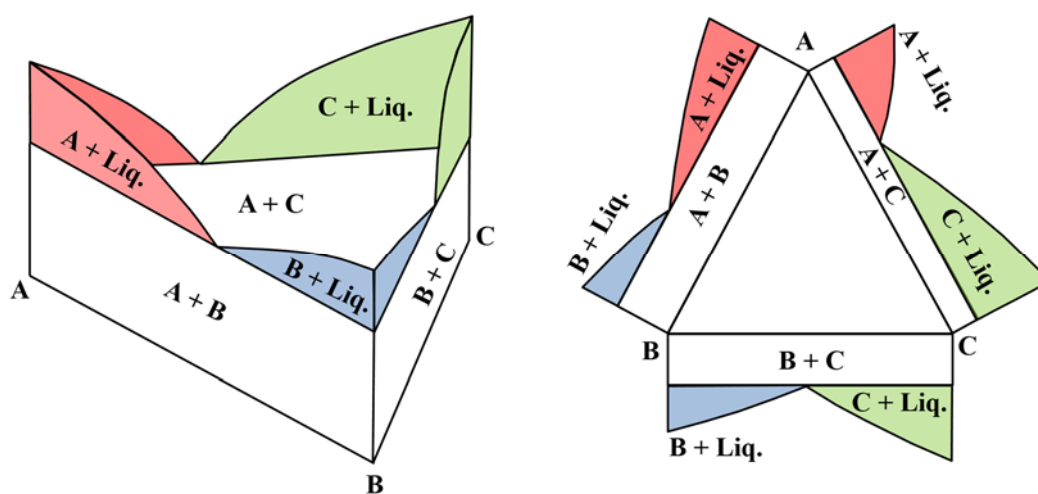


Figure I-17. Schematic ternary eutectic phase diagram and its three binary phase diagrams.

The use of ternary phase diagrams is of great importance in crystallization of molecular compounds. For example, the ternary phase diagram of two enantiomers and a solvent (or a mixture of solvents) provides important data for a successful enantiomeric resolution by means of crystallization, e.g., preferential crystallization (PC)^{34,35}. The use of ternary phase diagrams also helps to understand the purification efficiency and its limits, e.g., presence of solid solutions (a **solid solution** is a single crystalline phase consisting of a main component and a small amount of another component which can exist/dissolve in the crystal structure of the main component)³⁶. To be more convenient, 2D representations are studied: isothermal sections or isoplethal sections (Figure I-18). An **isopleth** section is the study of a composition of particular interest over a range of temperature.

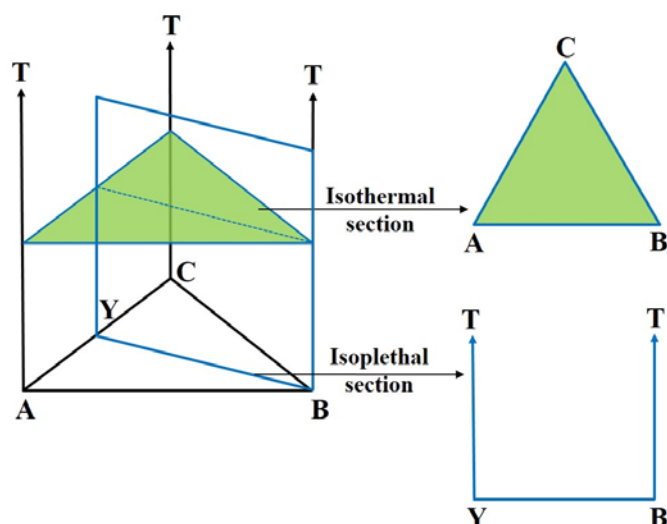


Figure I-18. Isobaric representation of a ternary diagram in 2 dimensions. From this diagram, isothermal section (T remains unchanged) or isoplethal section (composition remains unchanged) can be extracted.

I-3. Solid-state Phase Transitions

The basic knowledge of crystals has been introduced at the beginning of this chapter. The following part will focus on the different forms of the crystals and the transitions between them.

I-3-1. Crystalline Solids

Crystalline solids can exist in the forms of polymorphs, solvates or hydrates. A **polymorph** (Greek: poly = many, morph = form) as defined by McCrone is “a solid crystalline phase of a given compound, resulting from the possibility of at least two different arrangements of the molecules of that compound in the solid-state”³⁷. A common example that shows the changes of polymorphism is chocolate. Cocoa butter is the primary ingredient in chocolate, more than six polymorphs exist, but only one form is ideal as a confection. Improper storage or transport conditions cause it to transform into other polymorphs^{38,39}. Polymorphism is also critical in pharmaceuticals, solid-state pigments and polymer manufacture⁴⁰. **Solvates**, are crystalline solid adducts containing solvent molecules within the crystal structure, in either stoichiometric or nonstoichiometric proportions. If the incorporated solvent is water, a solvate is called a **hydrate**⁴¹. Because different crystalline polymorphs and solvates differ in crystal packing, and/or molecular conformation as well as in lattice energy and entropy, there are usually significant differences in their physical properties, such as density, hardness, tableability, refractive index, melting point, enthalpy of fusion, vapor pressure, solubility, dissolution rate, other thermodynamic and kinetic properties and even color⁴².

A large number of analytical methods are currently used to characterize the crystalline solids. The physical form is characterized by X-ray powder diffraction, infrared and solid-state NMR spectroscopy, differential scanning calorimetry, and microscopy. The valuable piece of information about a crystalline solid, although not always available, is the molecular structure, determined by single-crystal X-ray diffraction⁴³. Besides these classical techniques, a nonlinear optical method — second harmonic generation can be used to monitor the phase transitions involving symmetry changes.

I-3-2. Paths of Forming Crystals

Figure I-19-(a) illustrates 3 ways a liquid behaves. Usually, when a liquid is cooled down slowly or moderately, crystals will be formed through a nucleation-growth process⁴⁴. While by undercooling the liquid rapidly enough, crystallization can be avoided, it will go through a supercooled liquid and form a glass below the glass transition temperature (T_g) (Figure I-19-(b))⁴⁵.

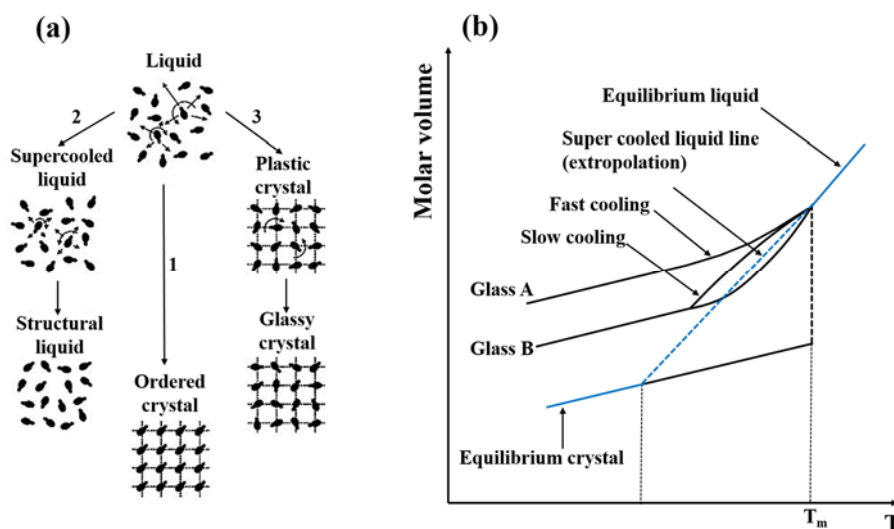


Figure I-19. Schematic representation of the possible transitions of a liquid into an ordered crystal, a structural liquid, or a glassy crystal and (b) schematic typical plots for glass transition. The value of T_g depends on the cooling rate. The higher the cooling rate, the higher the value of T_g .

In a **plastic crystal** (first introduced by Timmermans⁴⁶), which only the orientational degrees of freedom of the molecules show glassy freezing while their centers of mass are completely fixed on a crystalline lattice with strict translational symmetry, thus, it is translationally ordered and orientationally disordered (OD).⁴⁷ When the crystal is cooled rapidly enough to prevent the

transition towards the low-temperature ordered phase, the disordered system is supercooled and ultimately goes into a glassy state.⁴⁸ In this glassy phase the average translational order of the plastic phase is preserved but the orientational disorder is partially frozen. These features have led to the apparently paradoxical term **glassy crystal**⁴⁹.

Attention should be paid to differentiate a “glass” and a “glassy crystal”. A glass is an amorphous solid² that is a non-crystalline solid and lacks the long-range order. So, no reflection peak can be observed from XRD (within the author’s understandings). While a glassy crystal shows essentially all the conventional manifestations of a glass transition at a T_g , and the initial lattice is preserved⁵¹. Therefore, a glassy crystal can exhibit XRD reflections.

I-3-3. Phase Transitions

A **phase transition** is an event which entails a discontinuous (sudden) change of at least one property of a material⁵². Studies of phase transitions in the solid-state play an important role in a number of industrial and commercial applications. The sudden appearance or disappearance of a crystalline form can threaten process development and can lead to serious consequences. In the following part, we mainly focus on the polymorphic transitions.

I-3-3-1. The Classification of Phase Transitions

A thermodynamically stable phase can become unstable relative to another phase by a change of the external conditions (temperature, pressure). This causes a stress that can induce a transition. The transition is **enantiotropic** if it can be reversed by returning to the original conditions. **Monotropic** phase transitions are irreversible, i.e., they start from a phase that is only kinetically stable, but thermodynamically unstable at any condition.

For reversible process (enantiotropic), Ehrenfest (1933) classified phase transitions as first-order and second-order in terms of "continuity" or "discontinuity" from a thermodynamic point of view. In a **first-order phase transition** (Figure I-20-(a)), at least one of the first derivatives of the Gibbs free energy (G) experiences a discontinuous change. Measurement yields a hysteresis curve (Figure I-20-(b)).

² C. A. Queiroz and J. Šesták⁵⁰ tried to differentiate the conceptions “amorphous” and “glass”. Generally, a glass features the phenomenon of glass transition. We can say that, all glasses are amorphous solids, but not all amorphous solids are glasses.

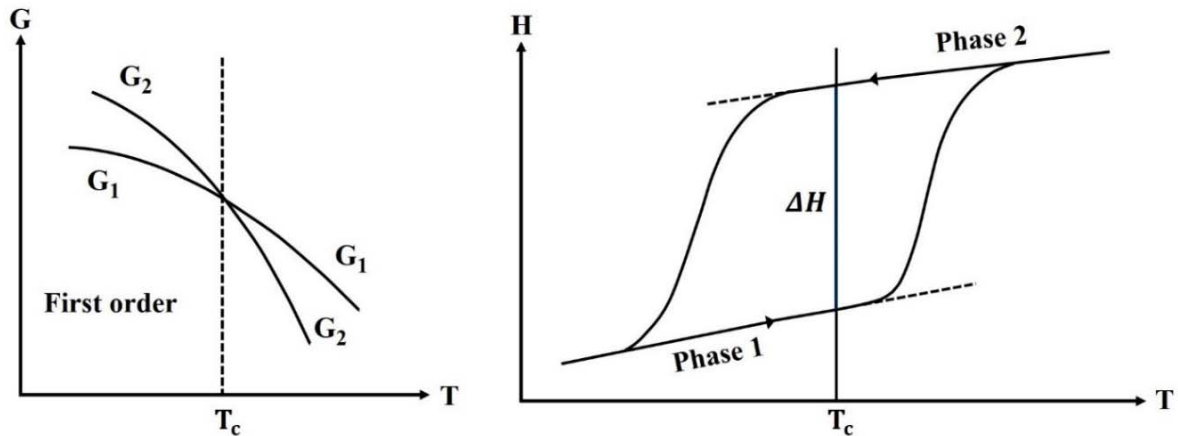


Figure I-20. (a) Temperature dependence of the Gibbs free energies G_1 and G_2 for two phases that are transformed at the temperature T_c of a first-order transition. (b) Hysteresis curve of the heat contents (enthalpy) H of a specimen at an enantiotropic, temperature-dependent first-order phase transition. Arrows mark the direction of temperature change.

For a **second-order phase transition** (Figure I-21), volume and entropy experience a continuous variation, but at least one of the second derivatives of G exhibits a discontinuity. No hysteresis exists. For a phase transition of **n -th order**, a discontinuity appears for the first time at the n -th derivative (however, third and higher order transitions do not really occur)⁵². Concerning the mechanisms, first-order transitions occur by means of full destruction of the initial crystal phase induced by the nucleation and growth of the final crystal phase⁵³. Second-order transitions are often supposed to occur in a concerted manner by a so-called **soft-mode mechanism**. In this type of transition, the two phases are expected to have a high degree of orientational relationship⁵⁴.

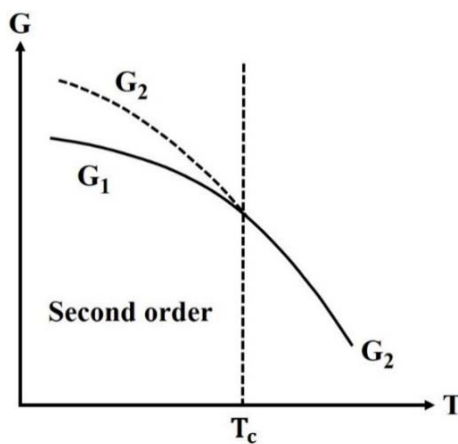


Figure I-21. Temperature dependence of the Gibbs free energies G_1 and G_2 for two phases that are transformed at the temperature T_c of a second-order transition.

However, this classification has been strongly criticized, especially by Mnyukh⁵⁵. To distinguish between first and second order transitions, the reliable indicators are interface, heterophase state, and hysteresis — any of them is sufficient. However, these indicators can be too small to be detected. So, according to Mnyukh, true second-order phase transitions will never be found and the solid-state transitions could only occur through a nucleation and growth mechanism, and the nucleation step would be critically dependent on the presence of suitable defects, such as micro-cavities and other surface irregularities between crystal domains.

Based on changes in the structures, Buerger⁵⁶ proposed to classify the solid-state phase transitions into the following three categories:

- **Reconstructive phase transitions:** chemical bonds are broken and rejoined; the reconstruction involves considerable atomic motions. Such conversions are always first-order transitions.
- **Displacive phase transitions:** atoms experience small shifts.
- **Order-disorder transitions:** different kinds of atoms that statistically occupy the same crystallographic point orbit in a crystal become ordered in different orbits or vice versa. Or molecules that statistically take several orientations become ordered in one orientation.

I-3-3-2. Order-disorder Transitions

Primary characteristic of a crystalline solid is the existence of 3-dimensional periodicity in the arrangement of atoms, i.e., the positional and orientational order. Such a state of crystalline arrangement corresponds to perfect order, which is never realized in materials at any temperature other than 0 K. It is therefore pertinent to speak of the extent of order or disorder in materials. This is best done in terms of order parameters. **Order parameters** are defined in such a way that they are equal to unity in the perfectly ordered state and zero in the completely disordered state. In the case of second-order transitions, the order parameter decreases to zero as the critical temperature T_c is approached. Heat capacity and similar derivative properties increase rapidly. Order-disorder transitions show such behavior, generally referred to as critical phenomena.⁵⁷

I-3-3-3. Landau's Phenomenological Approach

A phenomenological treatment of phase transitions has been given by Landau in 1937⁵⁸. The theory is based on the assumption that the free energy of a system is a continuous function that can be developed in a Taylor series near T_c , depending on the order parameter that is characteristic of degree of order, and noted ξ . It can be magnetization for ferro-paramagnetic transition, the polarization for ferro-paraelectric transition, or the percentage of atoms that are on their right sublattice for an order-disorder transition (will be detailed in chapter IV).

I-3-4. Kinetics of Solid-state Phase Transitions

The notion of kinetics implies phase coexistence, it makes sense only if the mass fraction between the two phases is changing⁵⁹. The only conceivable way of this change is nucleation and propagation of interfaces. Therefore, the investigation of kinetics of phase transitions means recognition of their nucleation-and-growth mechanism. Thermodynamics allows only two mechanisms of crystal phase transitions: (i) by nucleation-and-growth, (ii) by instant change at a critical point⁶⁰. Hereafter, we should make the notions clear that “kinetics” and “thermodynamics” are different but related.

I-3-4-1. The Relationship between Kinetics and Thermodynamics

Thermodynamics tells whether or not a process or a reaction can occur (is there a decrease in free energy), whereas **kinetics** considers how fast a change can occur. As illustrated in Figure I-22, for a process or a reaction to occur, (i) the thermodynamics must be favorable (i.e., $\Delta G = G_2 - G_1 < 0$). The difference between the free energy of the two phases (ΔG) is the **driving force**³². (ii) The kinetics must be fast enough (small E_a , **activation energy**).

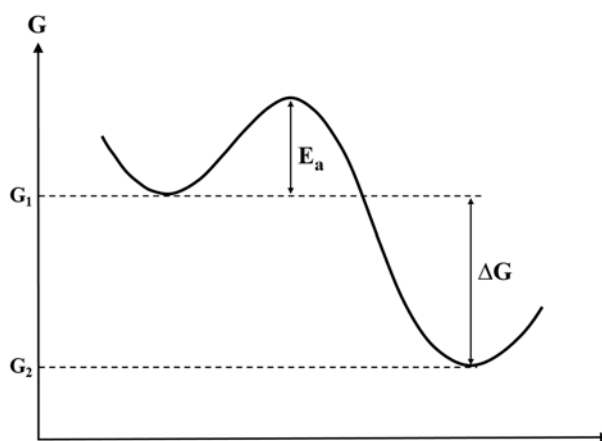


Figure I-22. Schematic representation of the activation energy barrier E_a and the driving force ΔG for two phases.

Some examples show that phase transitions can be thermodynamically favorable but kinetically unfavorable. For example, graphite and diamond are both forms of carbon (Figure I-23), but graphite has a lower free energy at room temperature and pressure. Therefore, diamond is thermodynamically favorable to convert into graphite. However, the transition from diamond to graphite requires a high activation energy. This will never happen within your lifetime — it is always safe on your finger!

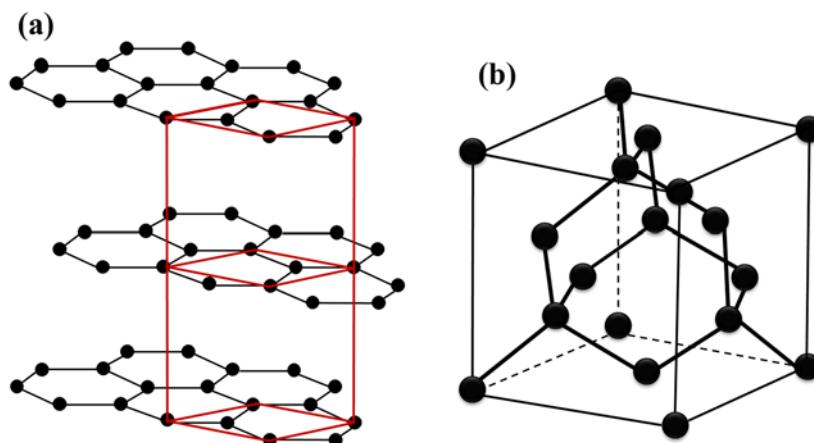


Figure I-23. Two forms of carbon: (a) graphite, thermodynamically favorable at ambient condition; (b) diamond.

I-3-4-2. Crystallization under Isothermal Conditions

Thermoanalytical techniques such as differential thermal analysis (DTA) or differential scanning calorimetry (DSC) have been extensively used to obtain the activation energies and kinetic parameters⁶¹. In isothermal analysis, the converted fraction, x , is determined from the thermal analysis curves recorded versus time. At any time, x is given as $x = \frac{S_t}{S}$ (Figure I-24), where S is the total area of the peak between the time t_i at which the crystallization begins and the time t_f at which the crystallization is completed. S_t is the area between t_i and t .

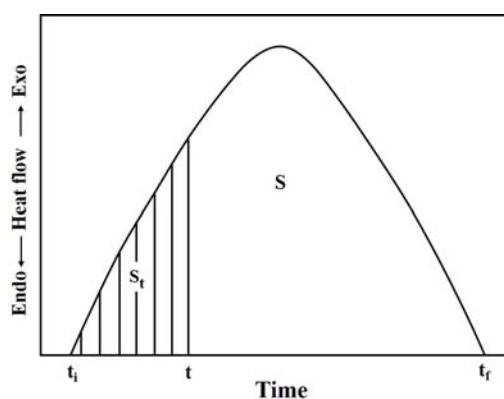


Figure I-24. Computation of the converted fraction x in isothermal method⁶².

Isothermal investigation of crystallization can be described by the Kolmogorov-Johnson-Mehl-Avrami equation as given below⁶³⁻⁶⁵:

$$x = 1 - \exp(-kt^n) \quad (I-3)$$

where k , is the crystallization rate constant and t , is the annealing time. n is the Avrami exponent that is related to the time dependence of the nucleation rate and to the dimensionality of the crystallization. This model is based on the hypothesis that nucleation is homogeneous, nucleation and growth are time-dependent and volume fraction of the recrystallized material is linked to the degree of crystallization.

To get a good fitting of the measuring points in the entire time range, the logarithmic conversion of eq. I-3 is applied:

$$\ln[-\ln(1-x)] = \ln k + n \ln t \quad (I-4)$$

From a linear regression of $\ln[-\ln(1-x)]$ and $\ln t$ (Figure I-25), parameters n and k can be determined as the slope and the intercept of these curves, respectively. It should be noted that this double logarithmic function exaggerates the role of experimental data in the initial stages as well as the role of the stages near the end of the process⁶⁶.

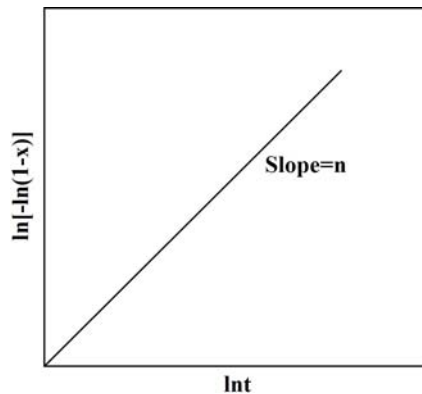


Figure I-25. Plot of $\ln[-\ln(1-x)]$ against $\ln t$ for determining the Avrami parameter, n .

The energetic barrier can be evaluated by Arrhenius equation⁶⁷⁻⁶⁹:

$$k = k_0 e^{\frac{-E_a}{RT}} \quad (I-5)$$

where k is the reaction rate constant; k_0 is the pre-exponential factor; E_a is the activation energy; R is the gas constant. A logarithmic conversion of eq. I-5 is applied:

$$\ln k = \ln k_0 - \frac{1}{RT} E_a \quad (I-6)$$

The activation energy for isothermal temperatures can be calculated from the slopes of the linear fits to the experimental data from a plot of $\ln k$ versus $-1/RT$ (Figure I-26).

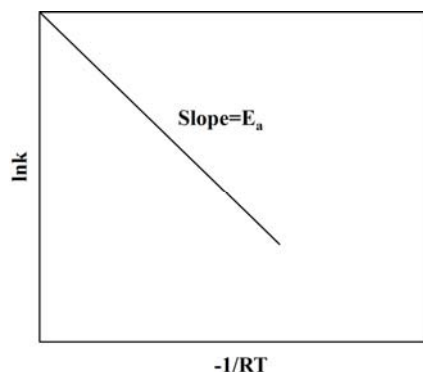


Figure I-26. Plot of $\ln k$ against $-1/RT$ for determining the activation energy, E_a .

I-3-4-3. Crystallization under Non-isothermal Conditions

In the non-isothermal method, crystallization peak temperatures, T_p and the converted fraction, x , are determined from the thermal analysis curves versus temperature at different heating rate β . x , at any temperature T is given as $x = \frac{S_t}{S}$ (Figure I-27), where S is the total area of the exothermic peak between the temperature, T_i , at which the crystallization begins and the temperature, T_f , at which the crystallization is completed. S_t is the partial area of the exothermic peak from T_i up to the temperature T ⁷⁰.

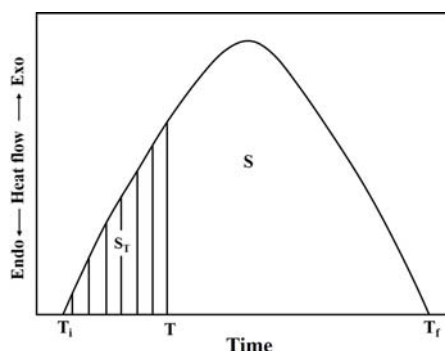


Figure I-27. Computation of the converted fraction x in non-isothermal method.

Based on the Avrami equation, several mathematical functions have been proposed to fit the experimental results and to understand the nucleation and growth process using non-isothermal crystallization thermal data. Table I-5 shows different approaches for the interpretation of the kinetic data obtained from thermal analysis measurements⁷¹. Ozawa and Kissinger plots are the most commonly used equations to calculate non-isothermal kinetic data, such as Avrami constant, n and crystallization activation energy, E_a , respectively^{72,73}.

Table I-5. Different methods for interpretation of non-isothermal kinetic data.

Method	Approach
Ozawa	$\ln[-\ln(1-x)] = -n\ln\beta + \text{const}$
Kissinger modified by Matusita et al.	$\ln\left(\frac{T_p^2}{\beta^n}\right) = \frac{mE_a}{RT_p} + \text{const}$
Ozawa modified by Matusita et al.	$\ln\beta = -1.052\left(\frac{mE_a}{nRT_p}\right) - \left\{\frac{\ln[-\ln(1-x)]}{n}\right\} + \text{const}$
Augis and Bennett	$\ln\left(\frac{\beta}{T_p}\right) = -\frac{E_a}{RT_p} + \ln k_0$
Afify	$\ln\left(\frac{\beta}{T_p^2}\right) = -\left(\frac{m}{n}\right)\left(\frac{E_a}{RT_p}\right) + \text{const}$
	$\ln\beta = -\left(\frac{m}{n}\right)\left(\frac{E_a}{RT_p}\right) + \text{const}$

I-4. Second Harmonic Generation

A nonlinear optical technique — second harmonic generation will be introduced in this part. The origin of the second harmonic, the interactions with matter and the propagation in the solids are discussed.

I-4-1. Linear Optics

Before talking about the nonlinear process, we should first understand what is linear optics. Light is an electromagnetic wave, which consists of electric and magnetic oscillated fields. For most of optics, the optical wave may be characterized by considering its electric field⁷⁴. Based on Maxwell's equations from the electromagnetic theory⁷⁵, the magnetic field is related to the electric field. When an electric field is applied to a dielectric medium (of neutral electric charge), a separation of bound charges is induced as illustrated in Figure I-28.

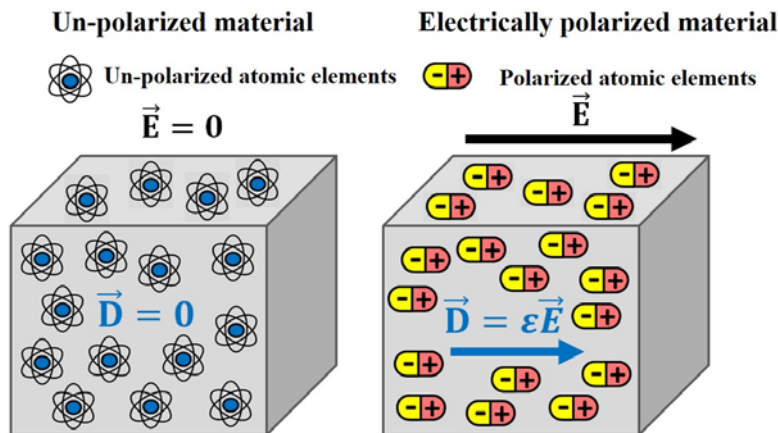


Figure I-28. Illustration of the response of a dielectric medium to an applied electric field. (a) Without field applied, and (b) field applied. Positive and negative charges within individual atoms and molecules try to separate from one another. The electron clouds of atoms will shift in position relative to their nuclei.

Positive charges are pulled in the direction of the field while negative charges are pulled in the opposite direction. This separation of charge results in the induced dipole moments, consequently, the dielectric medium is **polarized**. At low intensities of the applied electric field, the induced polarization (\mathbf{P}) is linearly proportional to the sinusoidal oscillated electric field, and the radiating dipoles produce an outgoing beam at the same frequency⁷⁶. \mathbf{P} is a function of the applied field \mathbf{E} :

$$\mathbf{P} = \varepsilon_0 \chi^{(1)} \mathbf{E} \quad (I-7)$$

Where $\chi^{(1)}$, the linear susceptibility tensor known as the polarizability of the medium, is the Fourier transform of the linear dielectric response tensor. It has nine components. In an isotropic medium, there is only one independent, nonzero component. ε_0 is the vacuum permittivity.

The familiar effects of reflection, refraction, diffraction, absorption, and scattering explain a wide variety of visual experiences common to us, from the focusing of light by a simple lens to the colors seen in a rainbow. This is the realm of what is called **linear optics**.

I-4-2. Nonlinear Optics

I-4-2-1. Nonlinear Optics in Life

In the early 1960s the development of lasers^{77,78} provided light sources of sufficient power to produce nonlinear optical effects in solids. Since then, nonlinear optics not only has developed into a major field of research but also has found important applications as illustrated in Figure I-29. Since lasers generally operate at a fixed wavelength or a narrow range of wavelengths, one important application of nonlinear optics is to shift a laser wavelength to new wavelengths. Thus, providing versatility necessary for many applications. One of the important examples of this type of process is the nonlinear optical process called **Second Harmonic Generation (SHG)**.

Nonlinear Optics in Life

Diversifying lasers and light

1. New colors
2. Control: spatial & frequency
3. Pulsing

Materials interactions

1. Machining
2. Spectroscopy
3. Analysis tools

Information technology

1. Telecom
2. Signal processing
3. Data storage
4. Sensors

Figure I-29. Scheme for organizing nonlinear optical applications⁷⁹.

I-4-2-2. The Origin of Nonlinear Optics

Figure I-30 shows the potential energy of a charge in the material as a function of position r . The sharp increase of the potential at the origin acts as a wall that keeps the charge from reaching the origin. The bottom of the curve represents the equilibrium position r_0 of the charge. When the incident light possesses a moderate energy, the oscillation of each dipole can be viewed as harmonic in the linear domain. At high incident intensities, the oscillations of the induced dipoles may not accurately follow the frequency of the incoming wave and different frequency components are contained in the radiated wave⁷⁶.

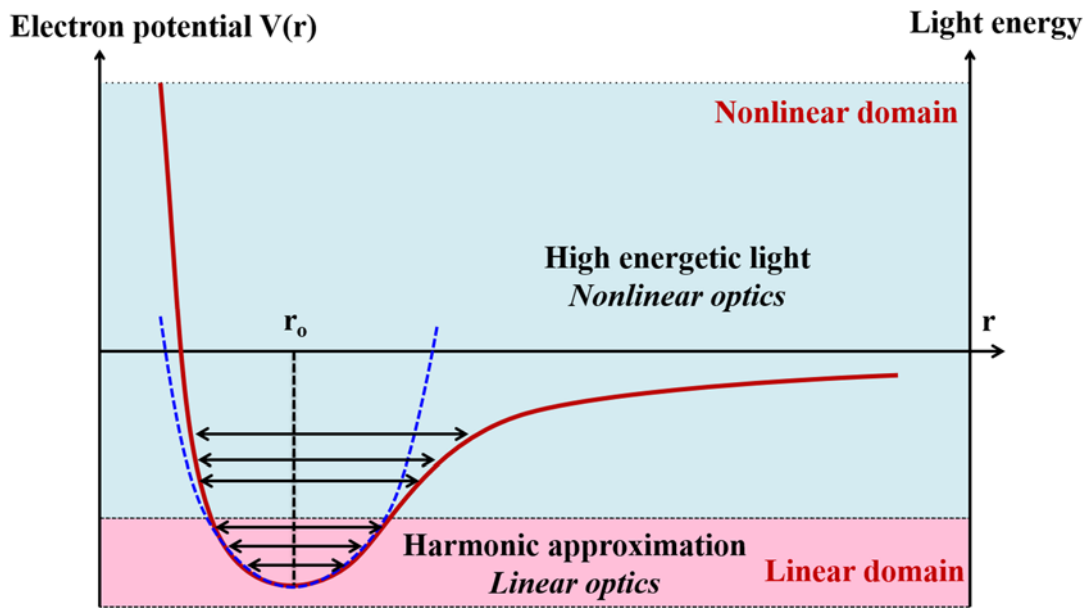


Figure I-30. Electron potential. In linear domain (pink), oscillation of charge can be approximate by harmonic potential (dark blue dash line). For high energetic electric field, the response becomes anharmonic, enter in nonlinear domain (light blue).

When the intensity of the light is sufficiently high (e.g., from a high energy laser), a small additional polarization appears, so that the total polarization can be written as:

$$\mathbf{P} = \mathbf{P}_L + \mathbf{P}_{NL} \quad (I-8)$$

Where \mathbf{P}_L is a linear function of the applied field and \mathbf{P}_{NL} is a nonlinear function of the applied field. Note that the nonlinear polarization serves as a source for the generation of new waves. It can be expressed as a power series expansion in the applied field:

$$\mathbf{P} = \epsilon_0 (\chi^{(1)} E + \chi^{(2)} E \cdot E + \chi^{(3)} E \cdot E \cdot E + \dots) \quad (I-9)$$

$\chi^{(n)}$ corresponds to the linear susceptibility ($n=1$) and the susceptibility tensors of n^{th} order ($n=2, 3, \dots$). The magnitude of the elements of the susceptibility tensor decreases rapidly with

increasing order ($\chi^{(1)} > \chi^{(2)} > \chi^{(3)} > \dots > \chi^{(n)}$) with as a consequence that terms for n higher than 3 can often be neglected. Consequently, $\chi^{(2)}$ and $\chi^{(3)}$ are responsible for most of the nonlinear optical phenomena.

I-4-2-3. Introduction of Second Harmonic Generation

I-4-2-3-1. Types of Quadratic Nonlinear Interactions

In eq. I-9, the third-rank tensor $\chi^{(2)}$ is responsible for optical mixing of three waves traveling in the material, resulting in two main different phenomena: **sum frequency generation (SFG)** or **difference frequency generation (DFG)**, in which two initial beams generate a new beam with the sum or difference of the optical frequencies of the initial beams. Second harmonic generation (SHG) is a special case of SFG as is shown in Figure I-31. The incident laser beams have a frequency of ω and create a new wave at frequency 2ω .

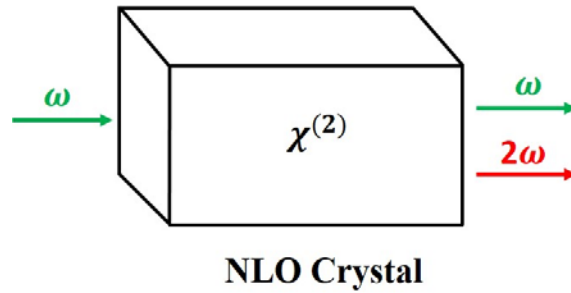


Figure I-31. Schematic illustration of the frequency conversion process in second harmonic generation.

I-4-2-3-2. The Notations of Second-order Nonlinear Susceptibility Tensor

The susceptibility tensors link the polarization vector to the electric field vector, they are composed of $3^{(n+1)}$ components. $\chi_{ijk}^{(2)}$ is a second-order nonlinear susceptibility and is a third-rank tensor ($3 \times 3 \times 3$) composed of 27 components. [i, j, k] corresponds to the crystallographic axes of the crystal [x, y, z]. $\chi_{ijk}^{(2)}$ can be written as:

$$\chi_{ijk}^{(2)} = \begin{bmatrix} \chi_{xxx}^{(2)} & \chi_{xxy}^{(2)} & \chi_{xxz}^{(2)} \\ \chi_{xyx}^{(2)} & \chi_{xyy}^{(2)} & \chi_{xyz}^{(2)} \\ \chi_{xzx}^{(2)} & \chi_{xzy}^{(2)} & \chi_{xzz}^{(2)} \end{bmatrix} \begin{bmatrix} \chi_{yxx}^{(2)} & \chi_{yxy}^{(2)} & \chi_{yxz}^{(2)} \\ \chi_{yyx}^{(2)} & \chi_{yyy}^{(2)} & \chi_{yyz}^{(2)} \\ \chi_{yzx}^{(2)} & \chi_{yzy}^{(2)} & \chi_{yzz}^{(2)} \end{bmatrix} \begin{bmatrix} \chi_{zxx}^{(2)} & \chi_{zxy}^{(2)} & \chi_{zxx}^{(2)} \\ \chi_{zyx}^{(2)} & \chi_{zyy}^{(2)} & \chi_{zyz}^{(2)} \\ \chi_{zxx}^{(2)} & \chi_{zzy}^{(2)} & \chi_{zzz}^{(2)} \end{bmatrix} \quad (I-10)$$

The susceptibility tensor must remain unchanged upon symmetry operations allowed for the medium. This reduces the number of independent and nonzero elements as shown in the following.

At this stage, we shall introduce a common notation used in second-order nonlinear optics. Indeed, the susceptibility $\chi_{ijk}^{(2)}$ is often represented as the so-called **d-coefficient**, where d is a tensor given by:

$$d_{ijk} = \frac{1}{2} \chi_{ijk}^{(2)} \quad (I-11)$$

When tensors are multiplied with vectors, usually the order of the vector multiplication can be changed. In nonlinear optics, it should not matter which of the fundamental fields is the first to be multiplied. This property known as the **intrinsic permutation symmetry** serves to contract the last two subscripts of the d tensor and d_{ijk} is written as d_{il} with

$$\begin{array}{llll} i: x & 1 & jk: xx & 1 \\ & y & yy & 2 \\ & z & zz & 3 \\ & & yz = zy & 4 \\ & & xz = zx & 5 \\ & & xy = yx & 6 \end{array} \quad (I-12)$$

For example, $d_{xyz} = d_{xzy} = d_{14}$ and $d_{zxx} = d_{31}$. The application of this notation is that d -coefficients can be expressed as elements of a 3×6 matrix rather than a $3 \times 3 \times 3$ tensor.

$$d_{il} = \begin{bmatrix} d_{11} & d_{12} & d_{13} & d_{14} & d_{15} & d_{16} \\ d_{21} & d_{22} & d_{23} & d_{24} & d_{25} & d_{26} \\ d_{31} & d_{32} & d_{33} & d_{34} & d_{35} & d_{36} \end{bmatrix} \quad (I-13)$$

Another symmetry property can be used when there is no absorption or dispersion of any of the frequencies. The frequencies can be freely permuted without permuting the corresponding subscripts, and vice versa, and the susceptibility remains unchanged. This is known as **Kleinman symmetry**⁸⁰. If we introduce the Kleinman symmetry condition, not all of the 18 elements of d_{il} are independent ($d_{12} = d_{26}$ and $d_{14} = d_{25}$). Then d_{il} has only 10 independent elements:

$$d_{il} = \begin{bmatrix} \mathbf{d}_{11} & \mathbf{d}_{12} & \mathbf{d}_{13} & \mathbf{d}_{14} & \mathbf{d}_{15} & \mathbf{d}_{16} \\ \mathbf{d}_{16} & \mathbf{d}_{22} & \mathbf{d}_{23} & \mathbf{d}_{24} & \mathbf{d}_{14} & \mathbf{d}_{12} \\ \mathbf{d}_{15} & \mathbf{d}_{24} & \mathbf{d}_{33} & \mathbf{d}_{23} & \mathbf{d}_{13} & \mathbf{d}_{14} \end{bmatrix} \quad (I-14)$$

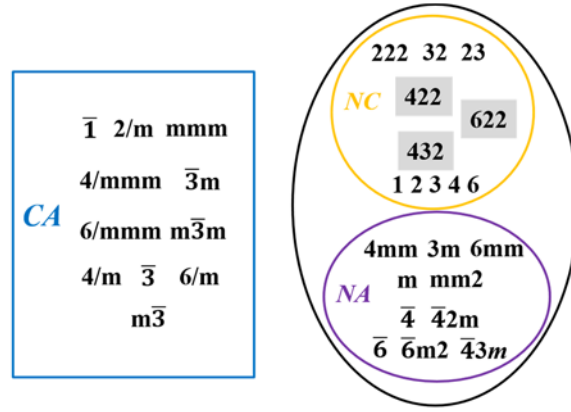
The major consequence of Kleinman symmetry is that it requires all the $\chi^{(2)}$ components in the point groups of 422 and 622 to vanish. Therefore, no SHG signal should be observed for these two point groups. However, there are numerous examples⁸¹⁻⁸³ disapproving this rule since it is quite unusual that no absorption occurs.

Based on the **Neumann's Principle**⁸⁴: *the symmetry elements of any physical property of a crystal must include the symmetry elements of the point group of the crystal.* The physical properties may, and often do, possess more symmetry than the point group. Therefore, other simplifications of the susceptibility tensors can be derived based on specific symmetry properties of material, such as rotation axis and mirror plane symmetries. Except that the susceptibility tensor of the cubic 432 point group has all the components equals to zero whereas it is non-centrosymmetric. The forms of the d -matrix for crystals of several different symmetry classes are given in Appendix II, followed by the form of the matrix when Kleinman symmetry is valid.

To conclude, for the third rank tensor $\chi^{(2)}$, 27 elements are independent. When the contracted notions d is applied, 18 elements are independent. Furthermore, when the Kleinman's symmetry is valid, only 10 elements are independent. Also, any crystalline symmetries of the nonlinear material can reduce this number further.

I-4-2-3-3. Conditions to Generate Second Harmonic Signal

We should note that second harmonic generation can occur only in non-centrosymmetric crystals. That is, in crystals that do not display inversion symmetry. In centrosymmetric material, all elements of even-order susceptibility tensors are identically equal to zero and consequently such materials cannot produce second-order nonlinear optical interactions. Therefore, the SHG process is impossible for liquids, gases, amorphous solids (such as glass), crystals of symmetry class 432. Since 11 of the 32 crystal classes possess inversion symmetry (Figure I-32), this rule is very powerful, as it immediately eliminates all crystals belonging to these classes from consideration for second-order nonlinear effects. While third-order nonlinear optical interactions (i.e., those described by a $\chi^{(3)}$ susceptibility) can occur in both centrosymmetric and non-centrosymmetric media¹².



CA: centrosymmetric achiral point groups (no SHG activity)
NC: noncentrosymmetric chiral point groups (SHG activity)
NA: noncentrosymmetric achiral point groups (SHG activity)
 422, 432, 622: no SHG activity if Kleinman symmetry is applicable

Figure I-32. SHG activity among the 32 crystallographic classes⁸⁵.

I-4-2-3-4. The Conversion Efficiency of SHG

The efficiency of second harmonic conversion is defined as the converted intensity with respect to the incident intensity sent on the material. It is expressed as:

$$\eta(l) = \frac{I_{2\omega}(l)}{I_{\omega}} \quad (I-15)$$

The efficiency of the energy conversion from fundamental to harmonic wave is about 1 part in 10^8 ⁸⁶. Armstrong⁸⁷ assumed that the conversion of the fundamental wave into the second harmonic wave was sufficiently low that the amplitude corresponding to the fundamental wave remains almost unchanged. Under the assumption of no depletion of the incident light beam, this led to the following relation between the incident intensity I_{ω} sent on the medium and the intensity of the second harmonic wave $I_{2\omega}(l)$ after a travelled distance l through the medium:

$$I_{2\omega}(l) = \frac{(\omega I_{\omega} \chi^{(2)})^2 l^2 \sin^2 \left(\frac{l \Delta k}{2} \right)}{2 \epsilon_0 c^3 n_{\omega}^2 n_{2\omega}} \frac{1}{\left(\frac{l \Delta k}{2} \right)^2} = I_{2\omega}^{max} l^2 \text{sinc}^2 \left(\frac{\Delta k l}{2} \right) \quad (I-16)$$

where,

$$I_{2\omega}^{max} = \frac{(\omega I_{\omega} \chi^{(2)})^2}{2 \epsilon_0 c^3 n_{\omega}^2 n_{2\omega}} \quad (I-17)$$

n_{ω} , the refractive index of the material at frequency ω ;

$n_{2\omega}$, the refractive index of the material at frequency 2ω ;

l , the distance travelled through the medium;

c , the speed of light in vacuum;

Δk is the **phase mismatch** expressed as:

$$\Delta k = \left| \overrightarrow{k(2\omega)} - 2\overrightarrow{k(\omega)} \right| = \frac{2\omega}{c} (n_{2\omega} - n_{\omega}) \quad (I-18)$$

If all the generated second harmonic waves add up coherently ($\Delta k = 0$), the SHG intensity increases quadratically with the travelled distance l , the nonlinear medium is called **phase-matchable (PM)** (Figure I-33-(a)). However, due to the dispersion (the velocity of a wave changes with the wavelength), the second harmonic waves and the fundamental waves are not in phase ($\Delta k \neq 0$). The energy cannot only be transferred from the fundamental field towards the second harmonic field, but also from the second harmonic field towards the fundamental field (destructive interference). The nonlinear medium is then called **non-phase-matchable (NPM)** (Figure I-33-(b)).

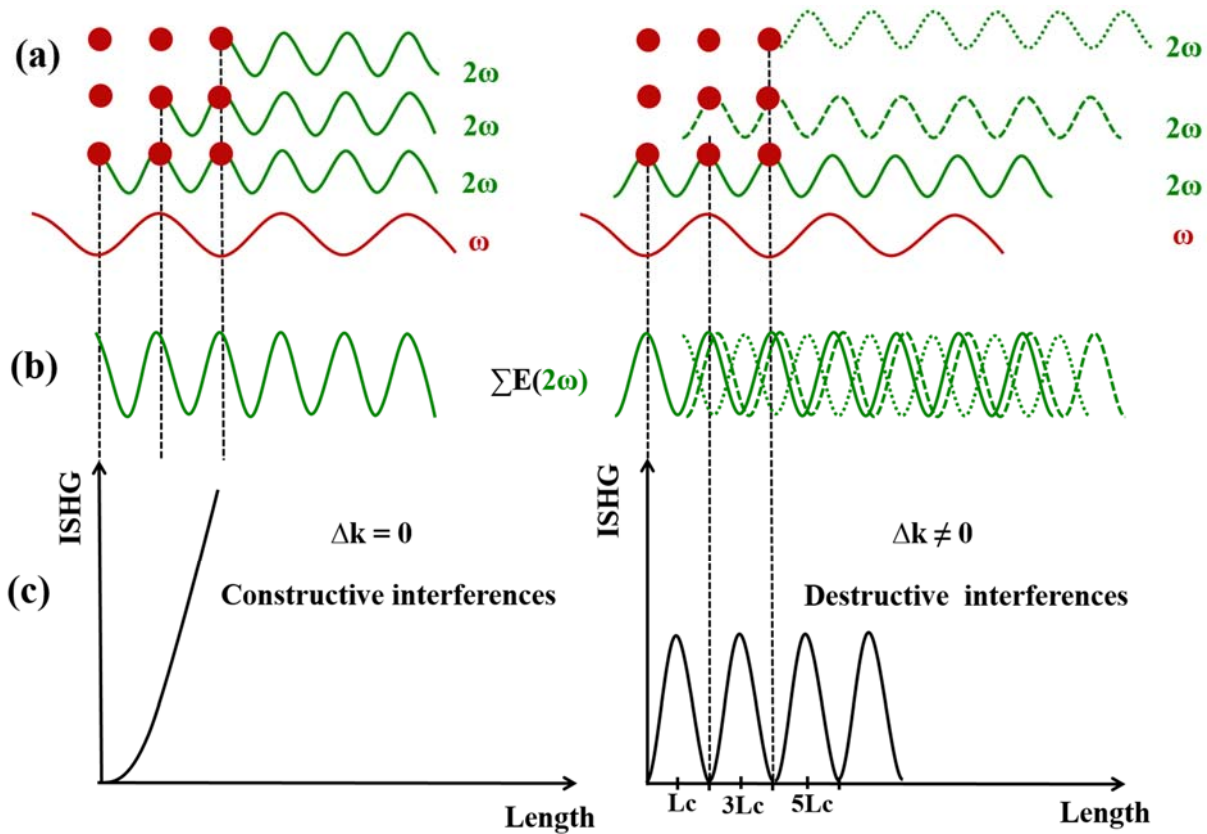


Figure I-33. (a) fundamental wave induced second-harmonic polarization, and second-harmonic waves generated at different positions in a nonlinear material for two different cases. Left: second-harmonic waves travel at the same velocity as the fundamental wave, all are in-phase. Right: different velocities, the usual case, mismatch between the phases of the second-harmonic waves. (b) Consequently, the SHG waves add up coherently (left) or destructively (right). (c) Finally, the SHG intensity grows quadratically with the travelled distance l in the crystal for achieved phase-matching (left) and varies sinusoidally with a maximum every odd coherence length multiples.

The destructive interference induces the SHG intensity to increase and decrease with the traveled distance l in the crystal. The **coherence length** (l_c) is defined as the distance in the crystal for which both waves are in phase. In numerous materials (organic and inorganic), the coherence length has been evaluated to be few μm ⁸⁸. l_c is given by:

$$l_c = \frac{\pi}{|\Delta k|} = \frac{\lambda}{4|n_{2\omega} - n_{\omega}|} \quad (I-19)$$

For efficient energy transfer to occur, the polarized wave and the second-harmonic wave must remain in phase. This will only occur if they have the same phase velocity: $n_{2\omega} = n_{\omega}$.

I-4-2-3-5. How to Enhance the Conversion Efficiency of SHG

The critical factor for achieving efficient second-harmonic generation is minimizing the phase mismatch between the fundamental and second-harmonic light wave. As discussed in I-4-2-3-4, to maximize the conversion efficiency, it is important to match the refractive index of the polarized wave (n_{ω}) and the refractive index of the second-harmonic wave ($n_{2\omega}$). In general, the refractive index of a material exhibits a normal dispersion with frequency (far from any region of absorption). This varies with temperature and with the direction of beam propagation and polarization in the crystal. Controlling these parameters to minimize phase mismatch in nonlinear optics is referred to as “**angle-tuning phase-matching**” and “**temperature-tuning phase-matching**”⁷⁶.

(i) Angle-tuning Phase-matching

This method is based on the “birefringence property” of some materials. In birefringent material, the index of refraction (i.e., the velocity of the electromagnetic waves inside the crystal) depends not only on the wavelength but also on the propagation direction of the incident light and on the direction of polarization of the light relative to the crystal axes. Isotropic crystals exhibit no birefringence. Only anisotropic crystals (uniaxial or biaxial crystals) present birefringence properties (Table I-6).

Table I-6. Crystalline system and dependency of refractive index.

System	Linear optical property	Number of refractive indices
Triclinic, monoclinic, orthorhombic	Biaxial	3
Trigonal, tetragonal, hexagonal	Uniaxial	2
Cubic	Isotropic	1

Angle-tuning phase-matching consists in precisely choosing the angular orientation of the crystal with respect to the propagation direction of the incident light and properly selecting the polarizations of the interacting beams to cancel the phase mismatch between the waves travelling through the crystal. Thus, this can only be accomplished in anisotropic crystals.

In these crystals, for each direction of propagation, there are two refractive indices. As is shown in Figure I-34, **E** polarized perpendicular to the principal plane is called an **ordinary wave**, the refractive index is n_o . **E** polarized in the principal plane is called an **extraordinary wave**, the refractive index is n_e . The difference of these two refractive indices is called **birefringence**:

$$\Delta n = n_o - n_e.$$

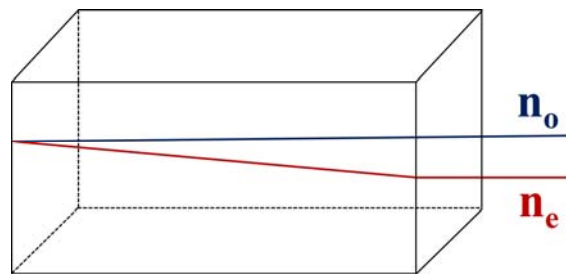


Figure I-34. A fundamental beam entering in a birefringent uniaxial crystal and splits into an ordinary (blue line) and an extraordinary beam (red line).

By orienting the crystals for an appropriate direction, it is possible to obtain the desired index matching ($\Delta k = 0$) as illustrated in Figure I-35. The refractive index of the ordinary wave is always n_o , while the refractive index of the second harmonic wave $n_e(\theta)$ varies between the values of n_o and n_e .

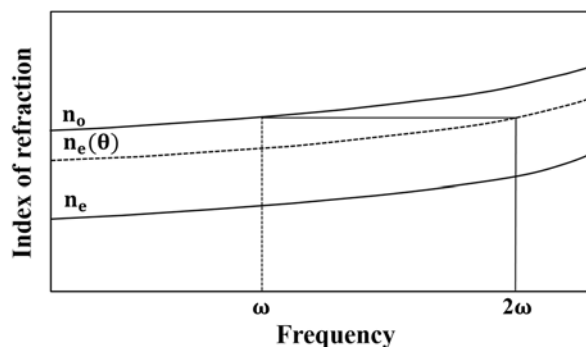


Figure I-35. Matching the refractive index of the incident beam at frequency ω and the generated SHG beam at frequency 2ω .

There are two ways to achieve angle-tuning phase-matching in consideration of the directions of the polarized beams. If the polarizations of two incident beams are parallel to each other, it

is **type I phase-matching** (Figure I-36-(a)). If the polarizations are perpendicular to each other, it is called **type II phase-matching** (Figure I-36-(b)).

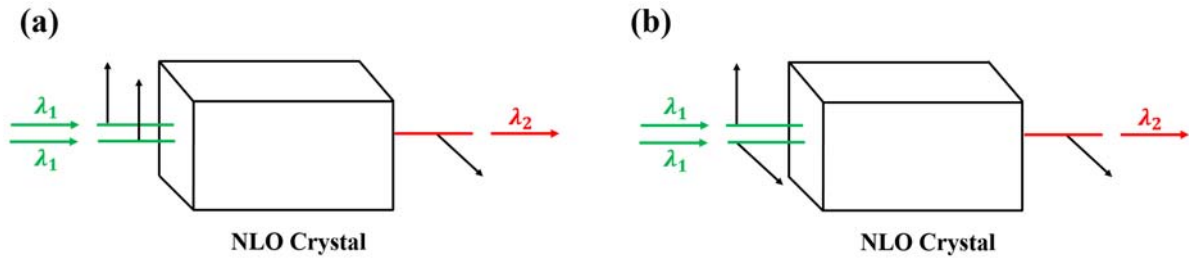


Figure I-36. (a) Type I phase-matching and (b) Type II phase-matching.

(ii) Temperature-tuning Phase-matching

The refractive index changes versus temperature. Figure I-37 shows the temperature effects of the extraordinary refractive index of quartz⁸⁹. Therefore, it is possible to achieve phase-matching conditions by tuning the temperature. This technique is often used in optical devices^{90,91}.

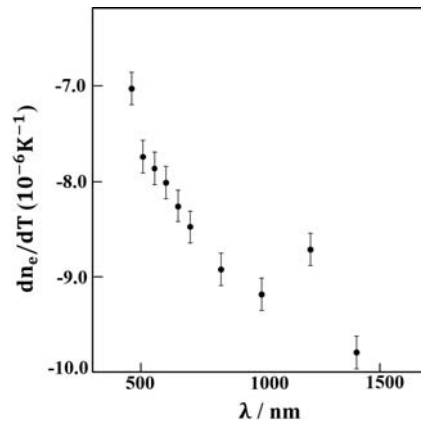


Figure I-37. Dependence of the average thermal coefficient of extraordinary refractive index of crystal quartz dn_e/dT on wavelength λ ⁸⁹.

(iii) Quasi-phase-matching

The angle-tuning phase-matching and temperature-tuning phase-matching belong to **perfect phase-matching** ($\Delta k = 0$). In non-phase-matchable crystals, another way to achieve phase-matching is a periodic modulation of the refractive index in the direction of propagation. This approach does not allow a perfect phase-matching between the fundamental and harmonic waves ($\Delta k \neq 0$). Nevertheless, it can be entirely constructive throughout the interaction length of the material and is termed **quasi-phase-matching (QPM)**^{87,92}. Figure I-38 shows cases of phase-matching, non-phase-matching and quasi-phase-matching, respectively.

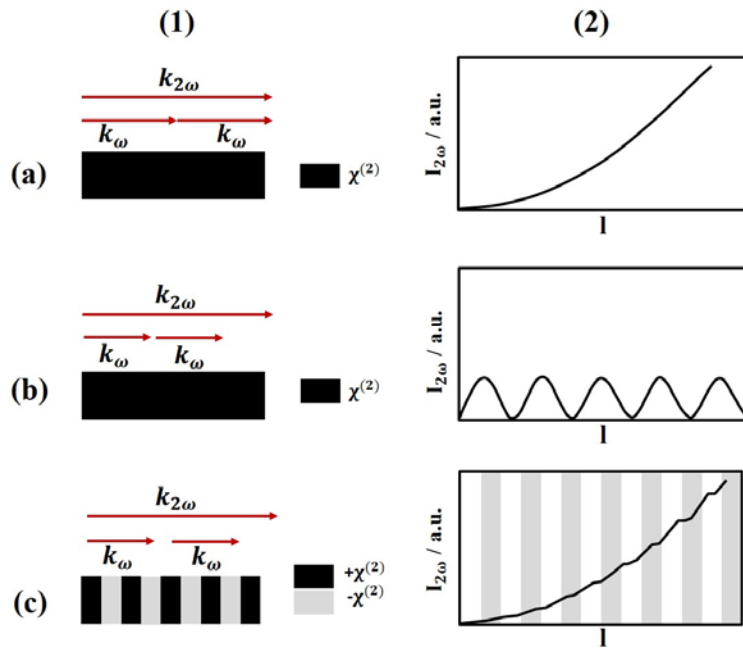


Figure I-38. Nonlinearity along the crystal and k -vector scheme and evolution of the second harmonic intensity along the crystal of (a) phase-matching (b) non-phase-matching, and (c) (1D periodic) quasi-phase-matching⁹³.

The most commonly used technique to create quasi-phase-matching crystals is **periodic poling**⁹⁴, which consists of a sequence of nonlinear segments of opposite optical domain direction. This is vividly illustrated by the way of rabbits breed (Figure I-39).

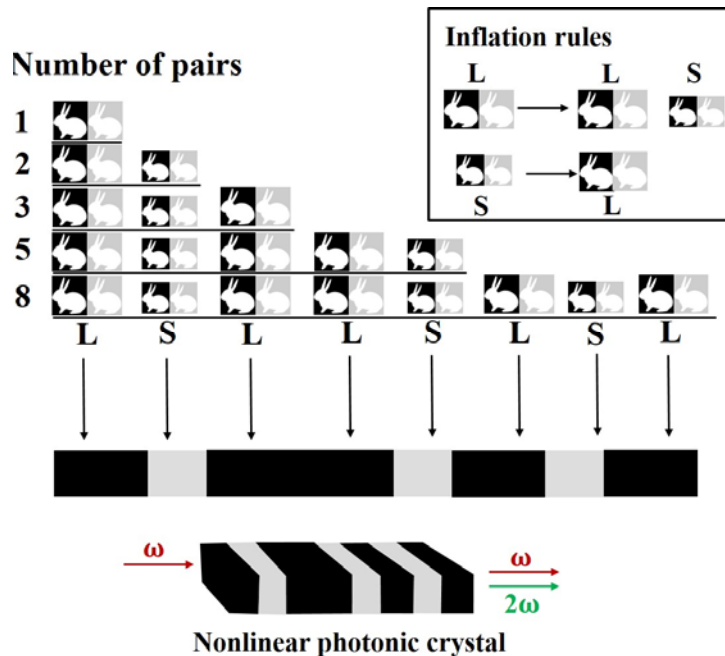


Figure I-39. The way that rabbits breed (studied by Fibonacci in 1202) can be compared to the quasi-periodic sequence. The mature pair can generate a new junior pair, whereas a junior pair become mature pair. In each cycle, they follow the inflation rule shown in the inset. The sequence of mature and junior pairs can be converted into a quasi-periodic nonlinear photonic crystal by replacing these pairs with long (L) and short (S) sections of modulated nonlinearity⁹³.

As can be seen in Figure I-40, the average growth rate of the QPM harmonic wave is lower than that of a phase matched wave in the same medium. As the QPM process does not rely on birefringence, it is even possible to operate in isotropic media.

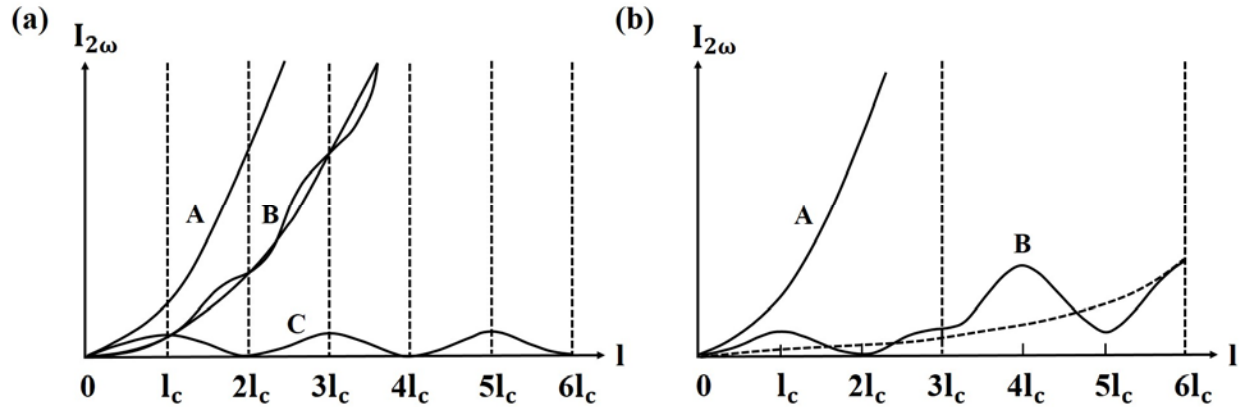


Figure I-40. Effect of phase-matching on the growth of second harmonic intensity with distance traveled in a nonlinear crystal. (a) A: perfect phase-matching; B: first-order QPM by flipping the sign of the spontaneous polarization every coherence length; C: non-phase-matching. (b) A: perfect phase-matching; B: third-order QPM by flipping the polarization every three coherence lengths⁹⁵.

I-5. Powder Second Harmonic Generation

I-5-1. Introduction of Powder SHG

SHG measurements (i.e., measurements of the intensity generated by a sample at the second harmonic wavelength) are commonly performed on single crystals. However, single crystals of reasonably size and/or optical and dielectric quality are difficult to obtain, since in most cases a substantial and costly materials growth program must be undertaken for each individual material. Kurtz & Perry⁸⁸ have described in detail a simple and quick experimental technique to measure the second harmonic response of crystalline powders (which are readily available in most cases). This is the “powder second harmonic generation” (Powder SHG) used in this thesis. We should also note that despite the benefits of using Kurtz & Perry technique, it is not totally equivalent to single crystal SHG measurements. Indeed, some information is only available from SC-SHG, i.e., second-order nonlinear optical coefficients d_{ijk} and the coherence length l_c .^{96,97}

I-5-2. The Behaviors of Materials for Powder SHG

SHG intensity generated by a given crystal depends on numerous parameters (i.e., molecular nature, quality of the long-range order, crystallinity, crystal structures, size and orientation of

the crystal). The evolution of the SHG intensity versus the length travelled by the electromagnetic waves inside the crystal can exhibit two different behaviors, leading to classify materials as phase-matchable or non-phase-matchable. Powder samples are constituted of numerous small randomly oriented crystals, with as a consequence that the second-harmonic fields generated by different particles are uncorrelated. Therefore, the total second-harmonic intensity generated by the powder sample is just the sum of the contributions from each individual particle.^{88,98} On this basis, Kurtz and Perry reviewed the concept of phase-matchability in the case of crystalline powder (Figure I-41).

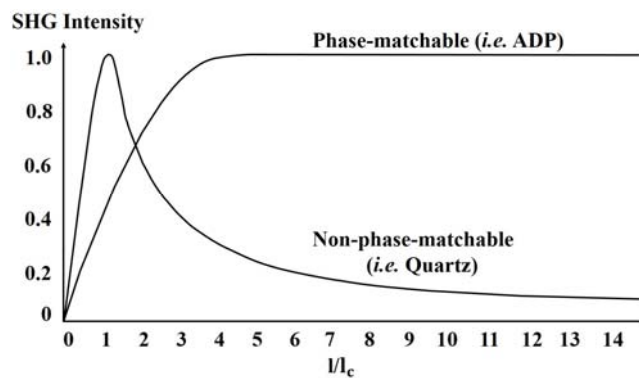


Figure I-41. Schematic representation of different particle-size dependences for phase-matchable and non-phase-matchable materials.

For a powder sample constitutes of phase-matchable crystals, the size of the particles has to be considered. When the particle size r is smaller than the coherence length l_c ($r < l_c$), the SHG signal increases quadratically with particle size r . When the particle size is larger than the coherence length l_c ($r > l_c$), the SHG intensity reaches maximum intensity independent of particle size r . Note that a particle size $r > 100 \mu\text{m}$ generally meets the requirement that $r > l_c$. While for a powder sample constitutes of non-phase-matchable crystals, when the particle size r is smaller than the coherence length l_c , the SHG intensity increases quadratically with r . It reaches a maximum SHG value when $r > l_c$ and then decreases for large particle size ($r > l_c$).

Therefore, when measuring the SHG intensity in a powder sample, the size distribution of the particles should be limited to a certain range in order to obtain a constant intensity. In phase-matchable material, a particle size of $100 \mu\text{m}$ generally greater than the average coherence

length, so the SHG intensity is independent of particle size. While for a non-phase-matchable material, the variation of the SHG signal is more difficult to control.

I-5-3. Description of the Experimental Devices: Powder SHG and Powder TR-SHG

I-5-3-1. Powder SHG Set-up

Figure I-42-(a) shows the experimental set-up used for the SHG measurements along this thesis. An Nd:YAG Q-switched laser (Quantel) operating at 1064 nm is used to deliver up to 330 mJ pulses of 5 ns duration with a repetition rate of 10 Hz. An energy adjustment device made up of two polarizers (P) and a half-wave plate ($\lambda/2$) allows the incident energy to be varied from 30-330 mJ per pulse. A RG1000 filter is placed after the energy adjustment device to remove light from the laser flash lamps. The powder sample put in a small vial is irradiated with the laser beam. The signal generated by the sample (diffuse green light, 532 nm) is collected into an optical fiber (core diameter of 500 μm) and directed onto the entrance slit of a spectrometer (Ocean Optics: spectral range 490-590 nm, resolution of 0.1 nm). This set-up can also be used to measure the crystalline samples in solution, as shown in Figure I-42-(b). Note that because each particle diffuses the emitted SHG light in all directions, only the fraction of the light emitted in the acceptance cone of the optical fiber is collected.

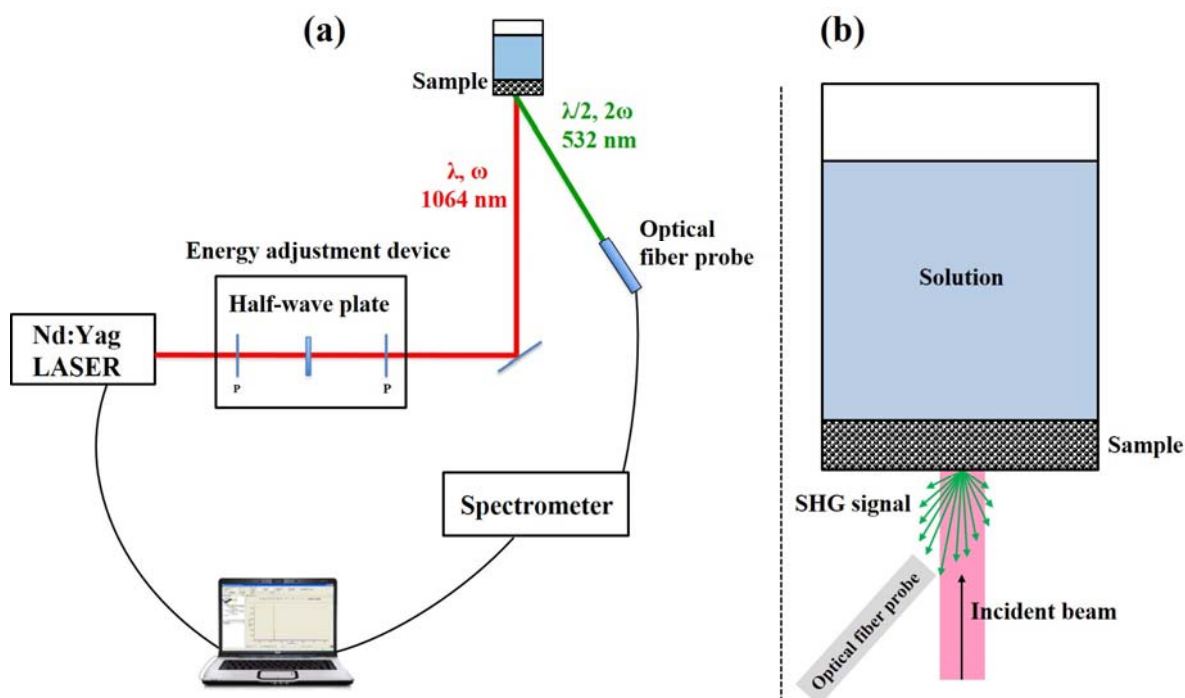


Figure I-42. (a) Schematic powder SHG set-up, and (b) SHG signals emitted from a suspension.

I-5-3-2. Powder TR-SHG Set-up

A heating/cooling stage (Linkam[®] THMS 600) can be coupled to the SHG set-up in order to record the evolution of the SHG signal versus temperature. The temperature can vary from -190°C to 600°C, liquid nitrogen is used as coolant. This set-up is called **temperature-resolved second harmonic generation (TR-SHG)** (Figure I-43). A continuous nitrogen flow can be sent on the heating/cooling stage to limit oxidation processes or to avoid vapor deposition on the window of the Linkam. For cooling experiments, it is necessary to purge air from the stage chamber with dry nitrogen. This prevents the water present in the air from condensing and freezing on the sample. The ice formed on the sample may induce reflections or diffusions of the SHG signal. The purging methods and evaluation of the efficiency can be found in Appendix III.

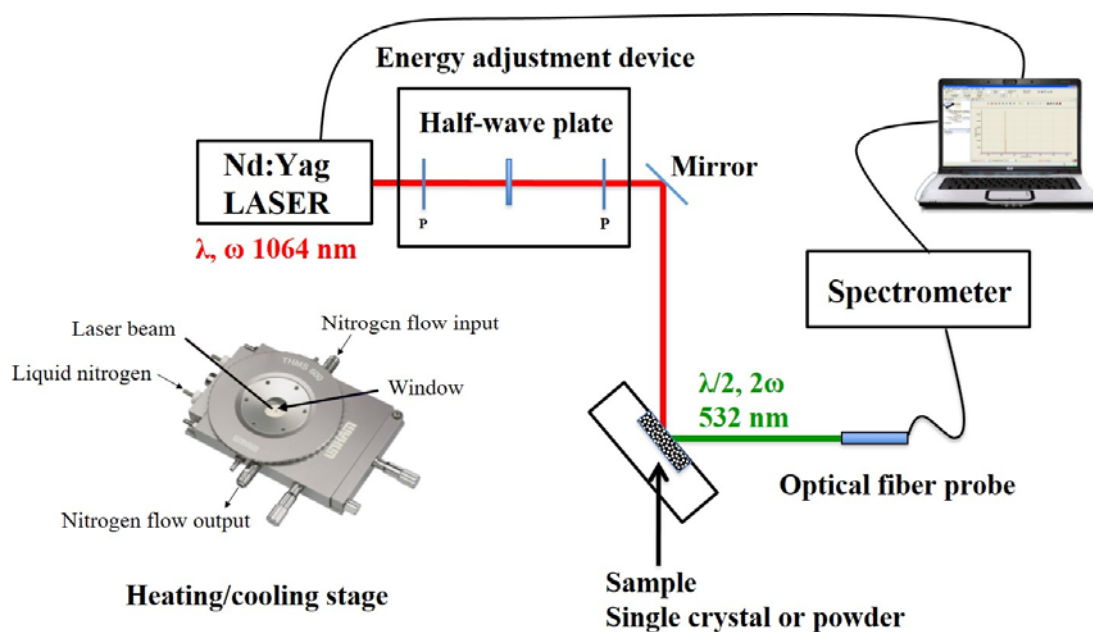


Figure I-43. Schematic experimental powder TR-SHG set-up.

Note that the temperature accuracy of the Linkam at low temperatures was checked. The melting points of tetrahydrofuran ($\text{C}_4\text{H}_8\text{O}$, in HPLC grade) were observed under cold-stage microscope. Different heating/cooling rates were used (0.5 K/min, 1 K/min, 2 K/min, 4 K/min and 5 K/min) and compared with DSC results. As is shown in Figure I-44, at 1 K/min heating rate, the onset temperature of melting in DSC is 165K and the peak temperature is 167K, while observations under microscope shows part of the crystals melted at 166K and all the crystals in

the scope of the observation melted at 167K. So, the temperature difference between cold-stage microscope and DSC was estimated to be lower than 1K.

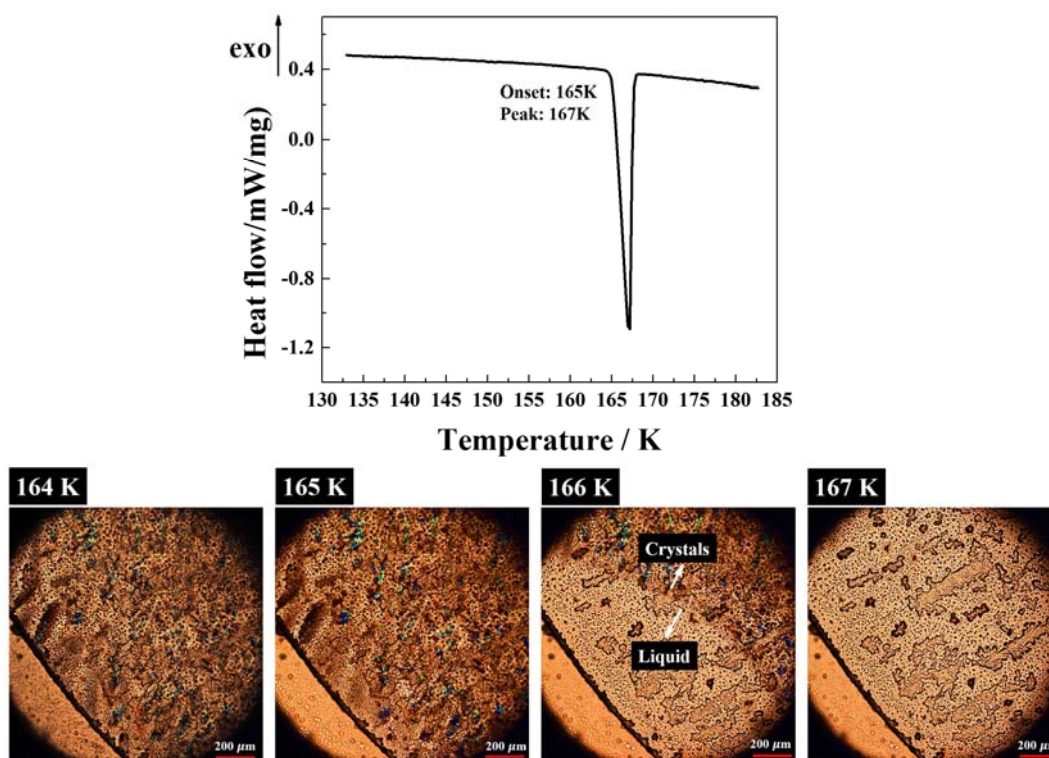


Figure I-44. Comparison of DSC measurement and observations of tetrahydrofuran under microscope at 1 K/min heating rate.

I-5-4. The Applications of Powder SHG and Powder TR-SHG

I-5-4-1. Supplementary Tool to Assign Space Group

Many papers deal with miss assigned space groups^{99–104}. Errors are divided into three categories: (i) incorrect Laue group; (ii) omission of a center of symmetry; (iii) omission of a center of symmetry coupled with a failure to recognize systematic absences. The most common revisions are $P1 \rightarrow P\bar{1}$, $P\bar{1} \rightarrow P2_1/c$ and $Cc \rightarrow C2/c$. A recent survey of approximately 100 000 entries in CSD (from May 2010 to February 2013) has uncovered 156 crystal structures that were apparently described in inappropriate space groups. For circa 50% of these revisions, the change in space group included the addition of a center of symmetry¹⁰⁵. SHG is proved to be a powerful tool to detect the absence of a center of symmetry and it is used to resolve space group ambiguities since the work of Dougherty and Kurtz⁹⁸.

One example encountered in the SMS laboratory demonstrates the usefulness of SHG in resolving the space group ambiguities: the determination of the space group of DMU·H₂O. The crystal structure of DMU·H₂O could be solved in the space group of *C2/c* or in an orthorhombic *Iba2* crystal lattice with a slightly higher reliability factor (R_{wp}). The unit cell parameters of the two are very similar and the crystal packings are essentially the same (see Table I-7). However, SHG measurements clearly indicated that the crystal structure of DMU·H₂O had to be centrosymmetric since no SHG signal was detected. Therefore, the centrosymmetric *C2/c* crystal structure was thus kept and the non-centrosymmetric *Iba2* crystal structure was discarded.

Table I-7. Crystallographic data determined for DMU·H₂O: C2/c and Iba2 solutions.

Form	DMU·H ₂ O	
Temperature (K)	253	253
Crystal system	Monoclinic	Orthorhombic
Space group	<i>C2/c</i>	<i>Iba2</i>
R_{wp}	0.048	0.058
a (Å)	19.1479 (8)	13.6230 (5)
b (Å)	13.9557 (5)	13.4920 (5)
c (Å)	13.4926 (4)	13.9571 (6)
β (°)	134.644 (2)	90
Z	16	16
Z'	2	2
Volume (Å ³)	2565 (1)	2565 (1)
Density (g/cm ³)	1.099 (1)	1.099 (1)

Attention should be paid that the absence of SHG signal is surely a good indicator in favor of a centrosymmetric structure. However, the case that the SHG signal is too low to be detected can never be totally excluded. In the opposite, the generation of a SHG signal is a proof of the non-centrosymmetric nature of the sample if the sample has been purified (without non-centrosymmetric impurities).

I-5-4-2. Spotting Conglomerates

Racemic mixture is a mixture that contain both enantiomers in equal proportion. Racemic mixture can crystallize in 3 different forms:^{106,107}

- **Racemic compound** (formerly called **racemate**): is a stoichiometric defined compound with specific physical properties and crystal structure, which contains both enantiomers in equimolar proportions. It corresponds to 90 to 95% of racemic mixtures. The most popular space groups are $P2_1/c$, $C2/c$, $Pbca$ and $P\bar{1}$ (ca. 95%). Around 4.5-5% crystallizes in the space groups of $Pna2_1$, $Pca2_1$, Cc and Pc ¹⁰⁸. Only in rare occasions (0.02%), racemic compounds crystallize in chiral space groups (mainly $P2_12_12_1$ and $P2_1$)¹⁰⁹.
- **Conglomerate**: is a mechanical mixture of enantiopure crystals in equal proportion and it represents only 5 to 10% of the racemic mixtures. As crystals are constituted of a single enantiomer, only chiral space groups are permitted. The most represented are $P2_12_12_1$, $P2_1$, $C2$ and $P1$ ¹¹⁰.
- **Solid solution**: the obtain crystals are constituted of an equal number of molecules of each enantiomer, but the arrangement is random. It represents less than 1% of the racemic mixture. The three crystal types are permitted, but no data is available about the predominant space groups.

These possibilities for the crystallization of racemic mixtures are summarized in Table I-8. The illustrations of racemic compounds, conglomerates and solid solutions are summarized in Figure I-45.

Table I-8. Formation of crystalline structures from racemic mixtures.

		Achiral structure		Chiral structure
		CA centrosymmetric achiral	NA non-centrosymmetric achiral	NC non-centrosymmetric chiral
Racemic compound	Structure	Permitted	Permitted	Permitted
	Proportion	~95%	4.5-5%	0.02%
	Predominant space groups	$P2_1/c$, $C2/c$, $Pbca$ and $P\bar{1}$	$Pna2_1$, $Pca2_1$, Cc and Pc	$P2_12_12_1$ and $P2_1$
Conglomerate	Structure	Forbidden	Forbidden	Permitted
	Proportion	0%	0%	100%
	Predominant space groups			$P2_12_12_1$, $P2_1$, $C2$ and $P1$
Solid solution <1%	Structure	Permitted	Permitted	Permitted

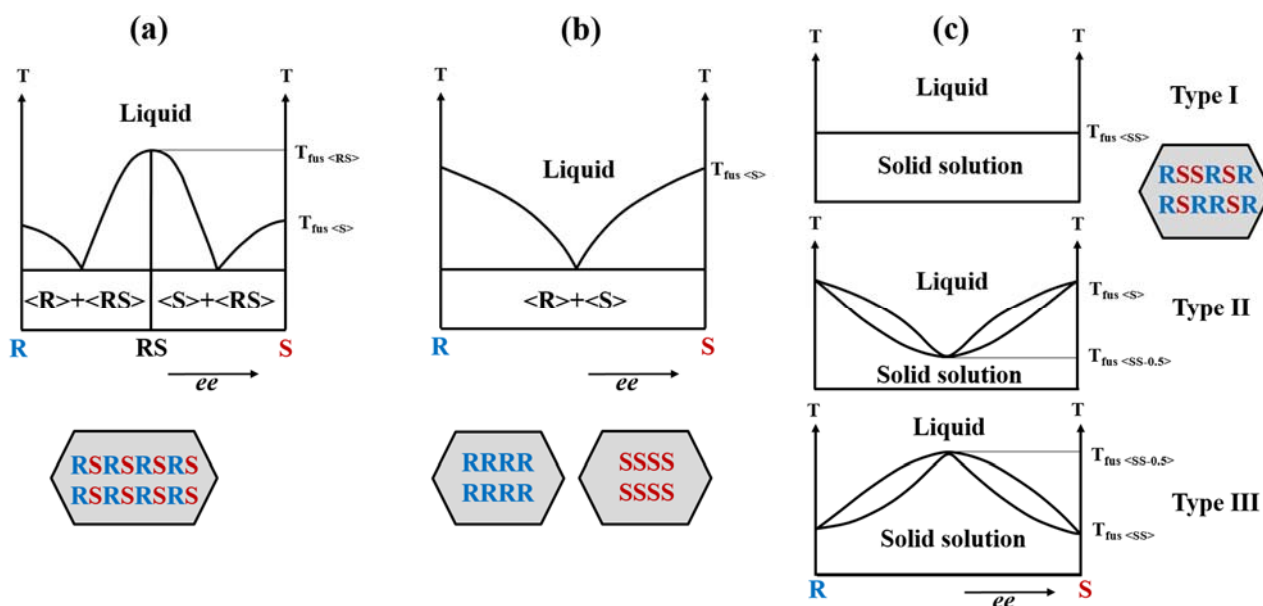


Figure I-45. Typical binary phase diagrams between *R* and *S* enantiomers for (a) racemic compounds, (b) conglomerates, and (c) solid solutions.

The demand for pure enantiomers in the pharmaceutical industry is increasing. **Preferential crystallization (PC)**^{107,111} is a useful technique to obtain pure enantiomers. But it needs as an essential condition that the racemic mixture crystallizes as a conglomerate. Therefore, the detection of conglomerates is required and SHG can be of great help.

The detection of conglomerates by SHG is detailed in the paper of Galland et al⁸⁵. The procedure for the detection of conglomerates by SHG is summarized in Figure I-46. Figure I-46-(a) refers to the case of an observable SHG signal. This can lead to 2 possibilities: (1) The sample is constituted of non-centrosymmetric crystals or (2) the generated signal is false. For the possibility 1, the sample can be conglomerate, which crystallizes in a chiral non-centrosymmetric space group. Alternatively, the sample is a racemic compound, which crystallizes in the non-centrosymmetric space group (around 5% of the known racemic compounds). Supplementary techniques must be used to confirm the nature of the sample. For the possibility 2, due to optical phenomena such as two-photon fluorescence (TPF) or other photoluminescent processes, a signal with a broader spectral bandwidth can be generated. A base line correction allows the distinction between real signal and spurious signal (Figure I-47)¹¹².

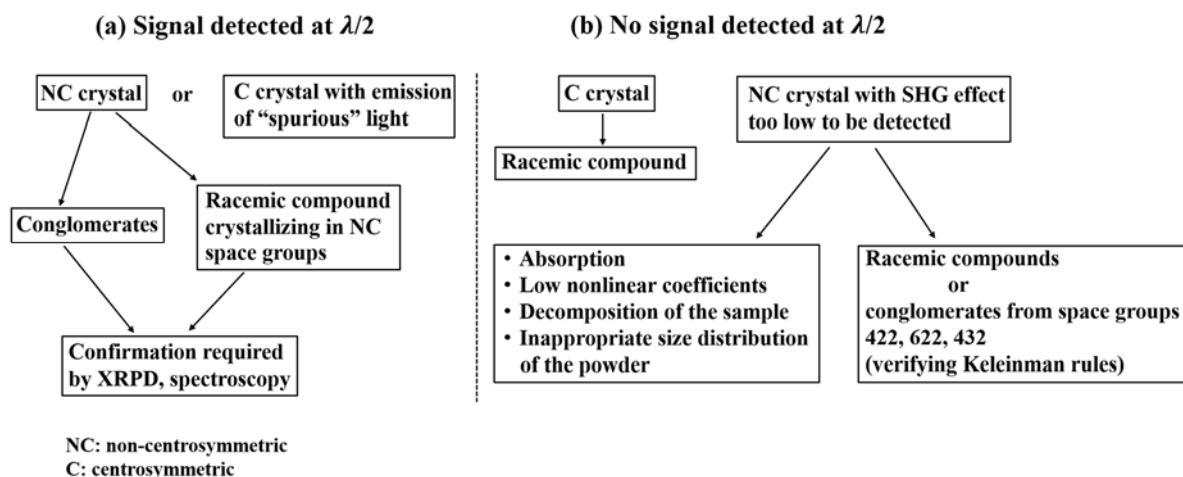


Figure I-46. Detection of conglomerate by using prescreening SHG test: decision diagram.

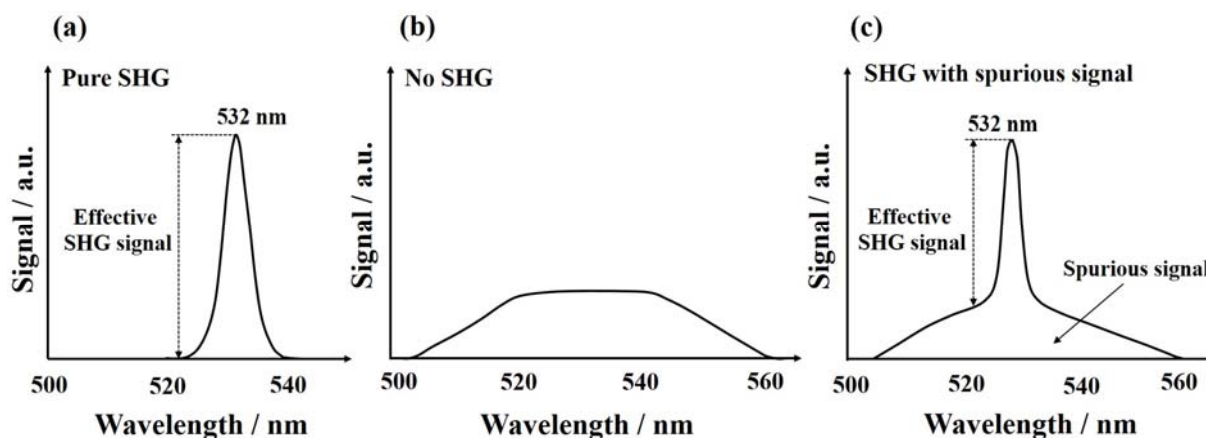


Figure I-47. Representation of (a) A pure SHG signal, (b) No SHG signal, and (c) Removal of false positive responses.

Figure I-46-(b) concerns the case with no SHG signal observed. It corresponds to two possibilities: (i) the sample is centrosymmetric or (ii) the sample is non-centrosymmetric but the generated SHG signal is too weak to be detected by the set-up. For the possibility 1, it is sure that the sample is a racemic compound. For the possibility 2, the weak SHG signal may be due to the properties of the sample: low nonlinear coefficients, random orientations of the crystals, absorption of the 1064 nm or 532 nm light or an inappropriate crystal size distribution especially for a non-phase-matchable material. The last critical situation is that chiral crystals related to point groups 422, 622, and 432 are SHG inactive if Kleinman permutation rules⁸⁰ and if Neumann's Principle⁸⁴ are applicable.

The above detailed procedures are not only used to detect conglomerates but also can be generalized to detect non-centrosymmetric crystals and to solve space group ambiguities.

I-5-4-3. Characterization of Sample Purity

I-5-4-3-1. Chemical Purity

Taking the chemical purity detection of 3,5-dinitrobenzoic acid (DNBA) as an example. DNBA crystallizes in the centrosymmetric space group $C2/c$ at room temperature¹¹³. However, the commercial powder exhibits a small but significant SHG signal (around 1-5% of the reference signal of quartz). By checking with ion chromatography, the presence of an impurity, 3-nitrobenzoic acid (3-NBA), was found at less than 0.5 wt%¹¹⁴. 3-NBA exhibits two stable centrosymmetric polymorphs^{115,116} and a new metastable non-centrosymmetric polymorph. The SHG signal observed in the commercial powder of DNBA is due to the presence of a small amount of metastable 3-NBA impurity.

I-5-4-3-2. Structural Purity

Besides the chemical purity, the **structural purity** is a concept that needs to be clarified. In the paper of Coquerel¹¹⁷, he defined the structural purity: *a solid is “structurally pure” when it exhibits the same 3D molecular arrangement for every particle*. Take the example of 3-hydroxybenzoic acid (3-HBA). 3-HBA has two monotropically related polymorphic forms: the stable form (3-HBA_{ST}) is centrosymmetric (space group $P2_1/c$) and the metastable form (3-HBA_{MET}) is non-centrosymmetric (space group $Pna2_1$). The commercial 3-HBA is not structurally pure but contains a detectable amount of 3-HBA_{MET}. Therefore, a SHG signal was obtained on the commercial 3-HBA and the detection threshold is 2 ppm, whereas XRPD and DSC shows a detection threshold of 1 and 17 wt%, respectively^{118,119}.

I-5-4-4. Detection of Solid-solid Phase Transitions

The disappearance of SHG signal or change in its intensity versus temperature can be used to study structural phase transformations, from non-centrosymmetry to non-centrosymmetry, from non-centrosymmetry to centrosymmetry or the reverse. Examples of polymorphic transitions (monotropically or enantiotropically related solid phases) and order-disorder transitions are summarized in Table I-9.

Table I-9. Examples of solid-solid phase transitions studied by TR-SHG.

	Molecule	References
First-order transition	NH ₄ Cl ³	Bartis 1971 ¹²⁰ ; Herbstein 2006 ¹²¹ ; Monk 2008 ¹²²
	NH ₄ Cl _(1-x) Br _x (for x=0.11)	Hirsch and Stühmer 1976 ¹²³
	2,3-dichloroquinizarin	Hall et al. 1988 ¹²⁴
	HMX	Henson et al. 1999 ¹²⁵ ; Saw et al. 2001 ¹²⁶
	TATB	Son et al. 1999 ¹²⁷ ; Saw et al. 2001 ¹²⁶
	BaTi ₂ O ₅	Masuno et al. 2011 ¹²⁸
	SrTiO ₃	Betzler 1980 ¹²⁹
	Squaric acid	Betzler and Bäuerle 1979 ¹³⁰
	Ba ₂ NaNb ₅ O ₁₅	Schneck et al. 1977 ¹³¹
	Colemanite	Dougherty and Kurtz 1976 ⁹⁸
	Ca ₉ Fe(PO ₄) ₇	Lazoryak et al. 2004 ¹³²
	α-(H ₃ N(CH ₂) ₂ -S	
	S(CH ₂) ₂ NH ₃ BIl ₅	Bi et al. 2008 ¹³³
	[C(NH ₂) ₃] ₄ Cl ₂ SO ₄	Bragiel et al. 2007 ¹³⁴
	[(H ₂ cys)PbI ₆]·2H ₃ O	Louvain et al. 2008 ¹³⁵
	KNbO ₃	Gopalan and Raj 1996 ¹³⁶
	Na _{0.5} Bi _{0.5} TiO ₃	Jones and Thomas 2002 ¹³⁷
	TiNbWO ₆ & RbNbWO ₆	Sleight et al. 1978 ¹³⁸
	LiRbSO ₄ & LiRbSO ₄	Kim et al. 1996 ¹³⁹ ; Henson et al. 1999 ¹²⁵ ; Saw et al. 2001 ¹²⁶
	KNO ₃	Son et al. 1999 ¹²⁷ ; Saw et al. 2001 ¹²⁶ ; Kidyarov et al. 2013 ¹⁴⁰
Order-disorder transition	BaTiO ₃	Vogt 1974 ¹⁴¹ ; Dougherty and Kurtz 1976 ⁹⁸ ; Fox et al. 1990 ¹⁴² ; Masuno et al. 2011 ¹²⁸ ; Kovalevskii et al. 2012 ¹⁴³
	NaNO ₂	Vogt et al. 1970 ¹⁴⁴ ; Iio and Yanagi 1973 ¹⁴⁵ ; Betzler 1980 ¹²⁹ ; Fleury and Lyons 1981 ¹⁴⁶
	Quartz	Dolino 1975 ¹⁴⁷ ; Betzler and Bäuerle 1979 ¹³⁰
	LiTaO ₃ & LiNbO ₃	Miller 1966 ¹⁴⁸ , Bergman 1976 ¹⁴⁹
	PbHPO ₄	Dougherty and Kurtz 1976 ⁹⁸ ; Keens and Happ 2000 ¹⁵⁰
	Triglycine sulphate (Hdabco ⁺)(CF ₃ COO ⁻)	Lazoryak et al. 2004 ¹³² ; Xiong 2013 ¹⁵¹
Conformation change	Collagen	Theodossiou et al. 2002 ¹⁵³

³ See (Herbstein 2006) for clarification between first and second-order phase transition

References

- (1) Tilley, R. J. D. *Crystals and Crystal Structures*; John Wiley & Sons, Ltd, **2006**.
- (2) Mullin, J. W. *The Crystalline State*. In *Crystallization (Fourth Edition)*; Butterworth-Heinemann: Oxford, **2001**; pp 1-31.
- (3) Shafranovskii, I. I. 14.10. Kepler's Crystallographic Ideas and His Tract "The Six-Cornered Snowflake." *Vistas Astron.* **1975**, *18*, 861–876.
- (4) Lax, M. *Symmetry Principles in Solid State and Molecular Physics*; Courier Corporation, **1974**.
- (5) Hammond, C. *The Basics of Crystallography and Diffraction*; OUP Oxford, **2009**.
- (6) Bravais, A. *Études Cristallographiques*; Gauthier-Villars, **1866**.
- (7) Cockcroft, J. K.; Driessen, H.; Moss, D.; Tickle, I. Course Material Master Index <http://pd.chem.ucl.ac.uk/pdnn/pdindex.htm#symm4> (accessed Aug 22, 2016).
- (8) *International Tables for Crystallography: Space-Group Symmetry (Fifth Edition)*; Hahn, T., Ed.; The International Union of Crystallography: Chester, England, **2002**; Vol. A.
- (9) Okamoto, H.; Schlesinger, M. E.; Mueller, E. M. *ASM Handbook: Alloy Phase Diagrams*; ASM International: United States, **2016**; Vol. 3.
- (10) Mighell, A. D.; Ondik, H. M. Crystal Data Space Group Tables. *J. Phys. Chem. Ref. Data* **1977**, *6*, 675–829.
- (11) Urusov, V. S.; Nadezhina, T. N. Frequency Distribution and Selection of Space Groups in Inorganic Crystal Chemistry. *Journal Struct. Chem.* **2009**, *50*, S22–S37.
- (12) Boyd, R. W. *Nonlinear Optics (Third Edition)*; Academic Press, **2008**.
- (13) Dunitz, J. D. *X-Ray Analysis and the Structure of Organic Molecules*; Verlag Helvetica Chimica Acta: Zürich, **1995**.
- (14) Herbstein, F. H.; Marsh, R. E. Changes in Space and Laue Groups of Some Published Crystal Structures. *Acta Crystallogr. B* **1982**, *38* (4), 1051–1055.
- (15) Marsh, R. E.; Bernal, I. More Space-Group Changes. *Acta Crystallogr. B* **1995**, *51* (3), 300–307.
- (16) Marsh, R. E.; Herbstein, F. H. Some Additional Changes in Space Groups of Published Crystal Structures. *Acta Crystallogr. B* **1983**, *39* (2), 280–287.
- (17) Baur, W. H.; Kassner, D. The Perils of Cc: Comparing the Frequencies of Falsely Assigned Space Groups with Their General Population. *Acta Crystallogr. B* **1992**, *48* (4), 356–369.
- (18) Marsh, R. E. Some Thoughts on Choosing the Correct Space Group. *Acta Crystallogr. B* **1995**, *51* (6), 897–907.
- (19) Ashby, M. *Teach Yourself Phase Diagrams and Phase Transformations (Fifth Edition)*; Cambridge, **2009**.
- (20) Campbell, F. C. *Phase Diagrams: Understanding the Basics*; ASM International, **2012**.
- (21) Ricci, J. E. *The Phase Rule and Heterogeneous Equilibrium*; Dover publications: New York University, **1951**.
- (22) McHale, A. E. *The Phase Rule and Heterogeneous Equilibria*. In *Phase Diagrams and Ceramic Processes*; Springer Netherlands, **1998**.
- (23) Tisza, L. The Thermodynamics of Phase Equilibrium. *Ann. Phys.* **1961**, *13* (1), 1–92.
- (24) Gibbs, J. W. On the Equilibrium of Heterogeneous Substances. *Am. J. Sci.* **1878**, *s3-16* (96), 441–458.
- (25) Brazhkin, V. V. Metastable Phases and "Metastable" Phase Diagrams. *J. Phys. Condens. Matter* **2006**, *18* (42), 9643.
- (26) Mnyukh, Y. V.; Panfilova, N. A.; Petropavlov, N. N.; Uchvatova, N. S. Polymorphic Transitions in

- Molecular crystals—III. *J. Phys. Chem. Solids* **1975**, *36* (3), 127–144.
- (27) Legendre, B. Polymorphism and Solvates. Application to Pharmaceutical Compounds. *J. Phys. IV* **2001**, *11* (PR10), Pr10-1-Pr10-19.
- (28) Baricco, M.; Palumbo, M.; Baldissin, D.; Bosco, E.; Battezzati, L. Metastable Phases and Phase Diagrams. *Metall. Ital.* **2004**, 1–8.
- (29) Schwarz, R. B.; Nash, P.; Turnbull, D. The Use of Thermodynamic Models in the Prediction of the Glass-Forming Range of Binary Alloys. *J Mater Res* **1987**, *2* (4), 456–460.
- (30) Zhao, J.-C. *Methods for Phase Diagram Determination*; Elsevier Science Ltd: Oxford, **2007**.
- (31) William D., C.; David G., R. *Fundamentals of Materials Science and Engineering: An Integrated Approach (Fifth Edition)*; John Wiley & Sons, Inc.: United States, **2001**.
- (32) Jackson, K. A. *Kinetic Processes: Crystal Growth, Diffusion, and Phase Transitions in Materials*; John Wiley & Sons, **2010**.
- (33) Kerr, H. W.; Kurz, W. Solidification of Peritectic Alloys. *Int. Mater. Rev.* **1996**, *41* (4), 129–164.
- (34) Coquerel, G. Preferential Crystallization. *Top. Curr. Chem.* **2007**, *269*, 1–51.
- (35) Levilain, G.; Coquerel, G. Pitfalls and Rewards of Preferential Crystallization. *CrystEngComm* **2010**, *12* (7), 1983–1992.
- (36) Burel, A.; Brugman, S. J. T.; Mignot, M.; Cartigny, Y.; Tisse, S.; Couvrat, N.; Peulon-Agasse, V.; Cardinael, P.; Coquerel, G. Phenanthrene Purification: Comparison of Zone Melting and Co-Crystallization. *Chem. Eng. Technol.* **2016**, *39* (7), 1317–1325.
- (37) Joel, B. *Introduction and Historical Background*. In *Polymorphism in Molecular Crystals*; Oxford University Press: New York, **2002**; pp 1–27.
- (38) Talbot, G. *Chocolate Temper*. In *Industrial Chocolate Manufacture and Use*; Beckett, S. T., Ed.; Springer US, **1994**; pp 156–166.
- (39) Garti, N.; Widlak, N. R. *Cocoa Butter and Related Compounds*; Elsevier, **2015**.
- (40) Mangin, D.; Puel, F.; Veesler, S. Polymorphism in Processes of Crystallization in Solution: A Practical Review. *Org. Process Res. Dev.* **2009**, *13* (6), 1241–1253.
- (41) Vippagunta, S. R.; Brittain, H. G.; Grant, D. J. W. Crystalline Solids. *Charact. Solid State* **2001**, *48* (1), 3–26.
- (42) Brittain, H. G. *Polymorphism in Pharmaceutical Solids (Second Edition)*; CRC Press, **2016**.
- (43) Byrn, S. R.; Pfeiffer, R. R.; Stephenson, G.; Grant, D. J. W.; Gleason, W. B. Solid-State Pharmaceutical Chemistry. *Chem. Mater.* **1994**, *6* (8), 1148–1158.
- (44) Mullin, J. W. *Crystallization*; Butterworth-Heinemann, **2001**.
- (45) Descamps, M. *Disordered Pharmaceutical Materials*; John Wiley & Sons, **2016**.
- (46) Timmermans, J. Plastic Crystals: A Historical Review. *J. Phys. Chem. Solids* **1961**, *18* (1), 1–8.
- (47) Brand, R.; Lunkenheimer P.; Loidl A. Relaxation Dynamics in Plastic Crystals. *J. Chem. Phys.* **2002**, *116* (23), 10386–10401.
- (48) Foulon, M.; Amoureux, J. P.; Sauvajol, J. L.; Cavrot, J. P.; Muller, M. Different Aspects of an Interesting Glassy Crystal: 1-Cyanoadamantane. *J. Phys. C Solid State Phys.* **1984**, *17* (24), 4213.
- (49) Adachi, K., Suga, H., Seki, S.; Phase Changes in Crystalline and Glassy-Crystalline Cyclohexanol. *Bull. Chem. Soc. Jpn.* **1968**, *41* (5), 1073–1087.
- (50) Queiroz, C. A.; Šesták, J. Aspects of the Non-Crystalline State. *Phys. Chem. Glas. - Eur. J. Glass Sci. And Technology Part B* **2010**, *51* (3), 165–172.
- (51) Adib, M. E.; Descamps, M.; Chanh, N. B. X-Ray Kinetic Study of Glassy Crystal Formation in

- Adamantane Derivatives: TTT Curves and Crystal Size Effect. *Phase Transit.* **1989**, *14* (1–4), 85–96.
- (52) Müller, U. *Symmetry Relationships between Crystal Structures: Applications of Crystallographic Group Theory in Crystal Chemistry*; OUP Oxford, **2013**.
- (53) Brandel, C.; Cartigny, Y.; Couvrat, N.; Eusébio, M. E. S.; Canotilho, J.; Petit, S.; Coquerel, G. Mechanisms of Reversible Phase Transitions in Molecular Crystals: Case of Ciclopirox. *Chem. Mater.* **2015**, *27* (18), 6360–6373.
- (54) Dunitz, J. D. Phase Transitions in Molecular Crystals from a Chemical Viewpoint. *Pure Appl. Chem.* **1991**, *63* (2).
- (55) Mnyukh, Y. Second-Order Phase Transitions, L. Landau and His Successors. *ArXiv11021085 Phys.* **2011**.
- (56) Buerger, M. J. *Phase Transformations in Solids*; Wiley: New York, **1951**.
- (57) Rao, C. N. R.; Rao, K. J. *Phase Transitions in Solids: An Approach to the Study of the Chemistry and Physics of Solids*; McGraw-Hill, **1978**.
- (58) Landau, L. D. *Collected Papers of L.D. Landau*; Gordon & Breach: New York usw., 1967.
- (59) Mnyukh, Y. V. Polymorphic Transitions in Crystals: Nucleation. *J. Cryst. Growth* **1976**, *32* (3), 371–377.
- (60) Mnyukh, Y. Mechanism and Kinetics of Phase Transitions and Other Reactions in Solids. *ArXiv E-Prints* **2011**, *1110*, arXiv:1110.1654.
- (61) Yinnon, H.; Uhlmann, D. R. Applications of Thermoanalytical Techniques to the Study of Crystallization Kinetics in Glass-Forming Liquids, Part I: Theory. *J. Non-Cryst. Solids* **1983**, *54* (3), 253–275.
- (62) Prasad, N. S.; Varma, K. B. R. Crystallization Kinetics of the LiBO₂–Nb₂O₅ Glass Using Differential Thermal Analysis. *J. Am. Ceram. Soc.* **2005**, *88* (2), 357–361.
- (63) Avrami, M. Kinetics of Phase Change. I General Theory. *J. Chem. Phys.* **1939**, *7* (12), 1103–1112.
- (64) Avrami, M. Kinetics of Phase Change. II Transformation–Time Relations for Random Distribution of Nuclei. *J. Chem. Phys.* **1940**, *8* (2), 212–224.
- (65) Avrami, M. Granulation, Phase Change, and Microstructure Kinetics of Phase Change. III. *J. Chem. Phys.* **1941**, *9* (2), 177–184.
- (66) Avramov, I.; Avramova, K.; Rüssel, C. New Method to Analyze Data on Overall Crystallization Kinetics. *J. Cryst. Growth* **2005**, *285* (3), 394–399.
- (67) Bamford, C. H.; Tipper, C. F. H. *Reactions in the Solid State*; Elsevier: Amsterdam, **1980**; Vol. 22.
- (68) Connors, K. A. *Chemical Kinetics: The Study of Reaction Rates in Solution*; VCH Publishers, Inc: New York, **1990**.
- (69) Grunwald, E. *Thermodynamics of Molecular Species*; John Wiley: New York, **1997**.
- (70) Ray, C. S.; Huang, W.; Day, D. E. Crystallization Kinetics of a Lithia–Silica Glass: Effect of Sample Characteristics and Thermal Analysis Measurement Techniques. *J. Am. Ceram. Soc.* **1991**, *74* (1), 60–66.
- (71) Celikbilek, M.; Erin, A.; Ayd, S. *Crystallization Kinetics of Amorphous Materials*. In *Advances in Crystallization Processes*; Mastai, Y., Ed.; InTech, **2012**.
- (72) Ozawa, T. Kinetics of Non-Isothermal Crystallization. *Polymer* **1971**, *12* (3), 150–158.
- (73) Kissinger, H. E. Variation of Peak Temperature with Heating Rate in Differential Thermal Analysis. *J. Res. Natl. Bur. Stand.* **1956**, *57* (4), 217–221.
- (74) Sutherland, R. L. *Handbook of Nonlinear Optics (Second Edition)*; Marcel Dekker, Inc.: New York,

2003.

- (75) Born, M.; Wolf, E. *Principles of Optics: Electromagnetic Theory of Propagation, Interference and Diffraction of Light (Seventh Edition)*; Cambridge University Press, **1999**.
- (76) Powell, R. C. *Symmetry, Group Theory, and the Physical Properties of Crystals*; Lecture Notes in Physics; Springer New York: New York, **2010**; Vol. 824.
- (77) Maiman, T. H. Optical and Microwave-Optical Experiments in Ruby. *Phys. Rev. Lett.* **1960**, *4* (11), 564–566.
- (78) Franken, P. A.; Hill, A. E.; Peters, C. W.; Weinreich, G. Generation of Optical Harmonics. *Phys. Rev. Lett.* **1961**, *7* (4), 118–119.
- (79) Garmire, E. Nonlinear Optics in Daily Life. *Opt. Express* **2013**, *21* (25), 30532.
- (80) Kleinman, D. A. Theory of Second Harmonic Generation of Light. *Phys Rev* **1962**, *128* (4), 1761–1775.
- (81) Singh, S.; Bonner, W. A.; Van Uitert, L. G. Violation of Kleinman's Symmetry Condition in Paratellurite. *Phys. Lett. A* **1972**, *38* (6), 407–408.
- (82) Dailey, C. A.; Burke, B. J.; Simpson, G. J. The General Failure of Kleinman Symmetry in Practical Nonlinear Optical Applications. *Chem. Phys. Lett.* **2004**, *390* (1–3), 8–13.
- (83) Zhao, H.-J.; Zhang, Y.-F.; Chen, L. Strong Kleinman-Forbidden Second Harmonic Generation in Chiral Sulfide: $\text{La}_4\text{InSbS}_9$. *J. Am. Chem. Soc.* **2012**, *134* (4), 1993–1995.
- (84) Nye, J. F. *Physical Properties of Crystals: Their Representation by Tensors and Matrices*; Clarendon Press, **1985**.
- (85) Galland, A.; Dupray, V.; Berton, B.; Morin-Grognet, S.; Sanselme, M.; Atmani, H.; Coquerel, G. Spotting Conglomerates by Second Harmonic Generation. *Cryst. Growth Des.* **2009**, *9* (6), 2713–2718.
- (86) New, G. *Introduction to Nonlinear Optics*; Cambridge University Press, **2011**.
- (87) Armstrong, J. A.; Bloembergen, N.; Ducuing, J.; Pershan, P. S. Interactions between Light Waves in a Nonlinear Dielectric. *Phys. Rev.* **1962**, *127* (6), 1918–1939.
- (88) Kurtz, S. K.; Perry, T. T. A Powder Technique for the Evaluation of Nonlinear Optical Materials. *J. Appl. Phys.* **1968**, *39* (8), 3798–3813.
- (89) Toyoda, T.; Yabe, M. The Temperature Dependence of the Refractive Indices of Fused Silica and Crystal Quartz. *J. Phys. Appl. Phys.* **1983**, *16* (5), L97–L100.
- (90) Regelskis, K.; Želudevičius, J.; Gavrilin, N.; Račiukaitis, G. Efficient Second-Harmonic Generation of a Broadband Radiation by Control of the Temperature Distribution along a Nonlinear Crystal. *Opt. Express* **2012**, *20* (27), 28544.
- (91) Umemura, N.; Miyata, K.; Kato, K.; Yoshimura, M.; Mori, Y.; Sasaki, T. Temperature Phase-Matching Properties for Harmonic Generation in $\text{GdCa}_4\text{O}(\text{BO}_3)_3$ and $\text{Gd}(x)\text{Y}(1-x)\text{Ca}_4\text{O}(\text{BO}_3)_3$. *Appl. Opt.* **2006**, *45* (16), 3859–3863.
- (92) Fejer, M. M.; Magel, G. A.; Jundt, D. H.; Byer, R. L. Quasi-Phase-Matched Second Harmonic Generation: Tuning and Tolerances. *IEEE J. Quantum Electron.* **1992**, *28* (11), 2631–2654.
- (93) Arie, A.; Voloch, N. Periodic, Quasi-Periodic, and Random Quadratic Nonlinear Photonic Crystals. *Laser Photonics Rev.* **2010**, *4* (3), 355–373.
- (94) Houe, M.; Townsend, P. D. An Introduction to Methods of Periodic Poling for Second-Harmonic Generation. *J. Phys. Appl. Phys.* **1995**, *28* (9), 1747–1763.
- (95) Hum, D. S.; Fejer, M. M. Quasi-Phase-Matching. *Recent Adv. Cryst. Opt.* **2007**, *8* (2), 180–198.

- (96) Aramburu, I.; Ortega, J.; Folcia, C. L.; Etxebarria, J. Second Harmonic Generation by Micropowders: A Revision of the Kurtz–Perry Method and Its Practical Application. *Appl. Phys. B* **2014**, *116* (1), 211–233.
- (97) Aramburu, I.; Ortega, J.; Folcia, C. L.; Etxebarria, J. Second-Harmonic Generation in Dry Powders: A Simple Experimental Method to Determine Nonlinear Efficiencies under Strong Light Scattering. *Appl. Phys. Lett.* **2014**, *104* (7), 071107.
- (98) Dougherty, J. P.; Kurtz, S. K. A Second Harmonic Analyzer for the Detection of Non-Centrosymmetry. *J Appl Cryst* **1976**, *9*, 145–158.
- (99) Marsh, R. E.; Kapon, M.; Hu, S.; Herbstein, F. H. Some 60 New Space-Group Corrections. *Acta Crystallogr. B* **2002**, *58* (1), 62–77.
- (100) Clemente, D. A. A Study of the 8466 Structures Reported in Inorganica Chimica Acta: 52 Space Group Changes and Their Chemical Consequences. *Inorganica Chim. Acta* **2005**, *358* (6), 1725–1748.
- (101) Clemente, D. A. 26 Space Group Changes and 6 Crystallographic Puzzles Found in Tetrahedron Journals. *Tetrahedron* **2003**, *59* (42), 8445–8455.
- (102) Clemente, D. A.; Marzotto, A. 22 Space-Group Changes. *Acta Crystallogr. B* **2003**, *59* (1), 43–50.
- (103) Loiacono, G. M.; Kostecy, G.; White, J. S. Resolution of Space Group Ambiguities in Minerals. *Am. Mineral.* **1982**, *67* (7–8), 846–847.
- (104) Clemente, D. A.; Marzotto, A. 30 space-group corrections: two examples of false polymorphism and one of incorrect interpretation of the fine details of an IR spectrum. *Acta Cryst.* **2004**, B60, 287–292.
- (105) Henling, L. M.; Marsh, R. E. Some More Space-Group Corrections. *Acta Cryst.* **2014**, C70, 834–836.
- (106) Coquerel, G. Review on the Heterogeneous Equilibria between Condensed Phases in Binary Systems of Enantiomers. *Enantiomer* **2000**, *5* (5), 481–498.
- (107) Jacques, J.; Collet, A.; Wilen, S. H. *Enantiomers, Racemates, and Resolutions*; Krieger Pub. Co., **1994**.
- (108) Dalhus, B.; Görbitz, C. H. Non-centrosymmetric racemates: space-group frequencies and conformational similarities between crystallographically independent molecules. *Acta Crystallogr. B* **2000**, *56*, 715–719.
- (109) Flack, H. D. Chiral and Achiral Crystal Structures. *Helv. Chim. Acta* **2003**, *86* (4), 905–921.
- (110) Belsky, V. K.; Zorkii, P. M. Distribution of Organic Homomolecular Crystals by Chiral Types and Structural Classes. *Acta Crystallogr. Sect. A* **1977**, *33* (6), 1004–1006.
- (111) Coquerel, G. *Preferential Crystallization*. In *Novel Optical Resolution Technologies*; Sakai, K., Hirayama, N., Tamura, R., Eds.; Topics in Current Chemistry; Springer Berlin Heidelberg, **2006**; pp 1–51.
- (112) Strachan, C. J.; Rades, T.; Lee, C. J. Determination of the Optical Second Harmonic Response of Pharmaceutical Solid–Solid Mixtures. *Opt. Lasers Eng.* **2005**, *43* (2), 209–220.
- (113) Prince, P.; Fronczek, F. R.; Gandour, R. D. Two Polymorphs of 3,5-Dinitrobenzoic Acid. *Acta Crystallogr. C* **1991**, *47* (4), 895–898.
- (114) Simon, F.; Clevers, S.; Gbabode, G.; Couvrat, N.; Agasse-Peulon, V.; Sanselme, M.; Dupray, V.; Coquerel, G. Enhanced Second Harmonic Generation from an Organic Self-Assembled Eutectic Binary Mixture: A Case Study with 3-Nitrobenzoic and 3,5-Dinitrobenzoic Acids. *Cryst. Growth Des.* **2015**, *15* (2), 946–960.
- (115) Dhaneshwar, N. N.; Tavale, S. S.; Pant, L. M. The Crystal Structure of M-Nitrobenzoic Acid. *Acta Crystallogr. B* **1974**, *30* (3), 583–587.
- (116) Dhaneshwar, N. N.; Kulkarni, A. G.; Tavale, S. S.; Pant, L. M. The Crystal Structure of a Second

- Modification of M-Nitrobenzoic Acid. *Acta Crystallogr. B* **1975**, *31* (7), 1978–1980.
- (117) Coquerel, G. The “structural Purity” of Molecular solids—An Elusive Concept? *Chem. Eng. Process. Process Intensif.* **2006**, *45* (10), 857–862.
- (118) Clevers, S.; Simon, F.; Sanselme, M.; Dupray, V.; Coquerel, G. Monotropic Transition Mechanism of M-Hydroxybenzoic Acid Investigated by Temperature-Resolved Second Harmonic Generation. *Cryst. Growth Des.* **2013**, *13* (8), 3697–3704.
- (119) Clevers, S.; Simon, F.; Dupray, V.; Coquerel, G. Temperature Resolved Second Harmonic Generation to Probe the Structural Purity of M-Hydroxybenzoic Acid. *J. Therm. Anal. Calorim.* **2013**, *112* (1), 271–277.
- (120) Bartis, F. J. Second Harmonic Generation and the Ordering Reaction in NH₄Cl. *Phys. Status Solidi B* **1971**, *43* (2), 665–668.
- (121) Herbstein, F. H. On the Mechanism of Some First-Order Enantiotropic Solid-State Phase Transitions: From Simon through Ubbelohde to Mnyukh. *Acta Crystallogr. Sect. B* **2006**, *62* (3), 341–383.
- (122) Monk, P. M. S. *Physical Chemistry: Understanding Our Chemical World*; John Wiley and Sons, **2008**.
- (123) Hirsch, R.; Stühmer, G. A Simple Technique to Measure Optical SHG in Powder Samples by Means of Electronic Integration. *Phys. Status Solidi A* **1976**, *37* (1), 105–108.
- (124) Hall, R. C.; Paul, I. C.; Curtin, D. Y. Structures and Interconversion of Polymorphs of 2,3-Dichloroquinizarin. Use of Second Harmonic Generation to Follow the Change of a Centrosymmetric to a Polar Structure. *J. Am. Chem. Soc.* **1988**, *110* (9), 2848–2854.
- (125) Henson, B. F.; Asay, B. W.; Sander, R. K.; Son, S. F.; Robinson, J. M.; Dickson, P. M. Dynamic Measurement of the HMX β - δ Phase Transition by Second Harmonic Generation. *Phys. Rev. Lett.* **1999**, *82* (6), 1213–1216.
- (126) Saw, C. K.; Zaugg, J. M.; Farber, D. L.; Weeks, B. L.; Aracne, C. M. Using Simultaneous Time - Resolved SHG and XRD Diagnostics to Examine Phase Transitions of HMX and TATB. *AIP Conf. Proc.* **2002**, *620* (1), 856–859.
- (127) Son, S. F.; Asay, B. W.; Henson, B. F.; Sander, R. K.; Ali, A. N.; Zielinski, P. M.; Phillips, D. S.; Schwarz, R. B.; Skidmore, C. B. Dynamic Observation of a Thermally Activated Structure Change in 1,3,5-Triamino-2,4,6-Trinitrobenzene (TATB) by Second Harmonic Generation. *J. Phys. Chem. B* **1999**, *103* (26), 5434–5440.
- (128) Masuno, A.; Kikuchi, Y.; Inoue, H.; Yu, J.; Arai, Y. Giant Second Harmonic Generation from Metastable BaTi₂O₅. *Appl. Phys. Express* **2011**, *4* (4), 042601.
- (129) Betzler, K. Second Harmonic Generation near the Phase Transition of SrTiO₃. *Ferroelectrics* **1980**, *26* (1), 819–822.
- (130) Betzler, K.; Bäuerle, D. Second Harmonic Generation in Squaric Acid. *Phys. Lett. A* **1979**, *70* (2), 153–154.
- (131) Schneck, J.; Primot, J.; Von der Mühl, R.; Ravez, J. New Phase Transition with Increasing Symmetry on Cooling in Barium Sodium Niobate. *Solid State Commun.* **1977**, *21* (1), 57–60.
- (132) Lazoryak, B. I.; Morozov, V. A.; Belik, A. A.; Stefanovich, S. Y.; Grebenev, V. V.; Leonidov, I. A.; Mitberg, E. B.; Davydov, S. A.; Lebedev, O. I.; Van Tendeloo, G. Ferroelectric Phase Transition in the Whitlockite-Type Ca₉Fe(PO₄)₇; Crystal Structure of the Paraelectric Phase at 923 K. *Solid State Sci.* **2004**, *6* (2), 185–195.
- (133) Bi, W.; Louvain, N.; Mercier, N.; Luc, J.; Rau, I.; Kajzar, F.; Sahraoui, B. A Switchable NLO Organic-Inorganic Compound Based on Conformationally Chiral Disulfide Molecules and Bi(III)I₅

- Iodobismuthate Networks. *Adv. Mater.* **2008**, *20* (5), 1013–1017.
- (134) Bragiel, P.; Piasecki, M.; Kityk, I. Optical and Thermal Tools for the Phase Transitions Detection in the Guanidine Compounds. *J. Phys. Conf. Ser.* **2007**, *79* (1), 012044.
- (135) Louvain, N.; Mercier, N.; Luc, J.; Sahraoui, B. Example of Disulfide Conformational Change in the Solid State: Preparation, Optical Properties, and X-Ray Studies of a Cystamine-Based Iodoplombate Hybrid. *Eur. J. Inorg. Chem.* **2008**, *2008* (23), 3592–3596.
- (136) Domain Structure and Phase Transitions in Epitaxial KNbO_3 Thin Films Studied by in Situ Second Harmonic Generation Measurements. *Appl. Phys. Lett.* **1996**, *68* (10), 1323–1325.
- (137) Jones, G. O.; Thomas, P. A. Investigation of the Structure and Phase Transitions in the Novel A-Site Substituted Distorted Perovskite Compound $\text{Na}_{0.5}\text{Bi}_{0.5}\text{TiO}_3$. *Acta Crystallogr. B* **2002**, *58* (Pt 2), 168–178.
- (138) Sleight, A. W.; Zumsteg, F. C.; Barkley, J. R.; Gulley, J. E. Acentricity and Phase Transitions for Some AM_2X_6 Compounds. *Mater. Res. Bull.* **1978**, *13* (11), 1247–1250.
- (139) Kim, J. H.; Kim, M.; Kim, S.-B.; Hahn, J. H. Temperature-Dependent Second Harmonic Generation in 6LiRbSO_4 and 7LiRbSO_4 . *Solid State Commun.* **1996**, *98* (3), 241–244.
- (140) Kidyarov, B. I.; Kovalevskii, V. I.; Malinovsky, V. K.; Pugachev, A. M.; Rozhkov, A. F. Generation of the Second Harmonic of Laser Radiation in Powders of Pure and Doped Potassium Nitrate in the Temperature Interval of 25–160°C. *Optoelectron. Instrum. Data Process.* **2013**, *49* (3), 293–297.
- (141) Vogt, H. Study of Structural Phase Transitions by Techniques of Nonlinear Optics. *Appl. Phys.* **1974**, *5* (2), 85–96.
- (142) Fox, G. R.; Yamamoto, J. K.; Miller, D. V.; Cross, L. E.; Kurtz, S. K. Thermal Hysteresis of Optical Second Harmonic in Paraelectric BaTiO_3 . *Mater. Lett.* **1990**, *9* (7), 284–288.
- (143) Kovalevskii, V. I.; Malinovskii, V. K.; Pugachev, A. M.; Raevskii, I. P.; Raevskaya, S. I.; Rudych, P. D.; Surovtsev, N. V. Second Harmonic Generation in the Paraelectric Phase in Powders and Ceramics of BaTiO_3 . *Phys. Solid State* **2012**, *54* (5), 920–923.
- (144) Vogt, H.; Happ, H.; Häfele, H. G. Optical Second Harmonic Generation in Sodium Nitrite. *Phys. Status Solidi A* **1970**, *1* (3), 439–450.
- (145) Nonlinear Optical Property of Sodium Nitrite. II. Temperature Dependence of Second Harmonic Generation. *J. Phys. Soc. Jpn.* **1973**, *35* (5), 1465–1471.
- (146) Fleury, P. A.; Lyons, K. Optical Studies of Structural Phase Transitions. In *Structural Phase Transitions I*; Müller, P. D. K. A., Thomas, P. D. H., Eds.; Topics in Current Physics; Springer Berlin Heidelberg, **1981**; pp 9–92.
- (147) Bachheimer, J. P.; Dolino, G. Measurement of the Order Parameter of α -Quartz by Second-Harmonic Generation of Light. *Phys. Rev. B* **1975**, *11* (8), 3195–3205.
- (148) Miller, R. C.; Savage, A. Temperature Dependence of the Optical Properties of Ferroelectric LiNbO_3 and LiTaO_3 . *Appl. Phys. Lett.* **1966**, *9* (4), 169–171.
- (149) Bergman, J. G. Molecular Mechanics of the Ferroelectric to Paraelectric Phase Transition in Lithium Tantalate via Optical Second Harmonic Generation. *J. Am. Chem. Soc.* **1976**, *98* (4), 1054–1055.
- (150) Keens, A.; Happ, H. A Study of the Ferroelectric Phase Transition in PbHPO_4 by Optical Second-Harmonic Generation. *J. Phys. C Solid State Phys.* **1988**, *21* (8), 1661.
- (151) Xiong, R.-G. The Temperature-Dependent Domains, SHG Effect and Piezoelectric Coefficient of TGS. *Chin. Chem. Lett.* **2013**, *24* (8), 681–684.
- (152) Sun, Z.; Luo, J.; Zhang, S.; Ji, C.; Zhou, L.; Li, S.; Deng, F.; Hong, M. Solid-State Reversible

Quadratic Nonlinear Optical Molecular Switch with an Exceptionally Large Contrast. *Adv. Mater.* **2013**, *25* (30), 4159–4163.

- (153) Theodossiou, T.; Rapti, G. S.; Hovhannisyan, V.; Georgiou, E.; Politopoulos, K.; Yova, D. Thermally Induced Irreversible Conformational Changes in Collagen Probed by Optical Second Harmonic Generation and Laser-Induced Fluorescence. *Lasers Med. Sci.* **2002**, *17* (1), 34–41.

Chapter II

Phase Diagram Investigations by TR-SHG

This chapter describes the use of TR-SHG to investigate phase diagrams. In part II-1, TR-SHG is used to explore the binary eutectic system formed by urea and water and to determine precisely the eutectic composition. In part II-2, the metastable eutectic phase diagram between dimethylurea and water is explored. In part II-3, phase diagram between non-phase-matchable hexamethylenetetramine and water is studied.

II-1. Stable Eutectic Phase Diagram Investigations — Urea/Water System

II-1-1. Introduction

A stable binary eutectic mixture is a mixture of two components that has the lowest melting temperature¹⁻⁴. A common example of eutectic mixture is the sodium chloride (NaCl)/water binary system, which has its eutectic temperature (T_E) at -21.1°C and a eutectic composition (X_E) of 23.3 wt% (in salt). NaCl is used as de-icing salt to lower the freezing point of water on roads⁵. The case of deep eutectic solvents (DES), i.e., ionic liquids, can also be mentioned as it has found wide applications in chemistry. For example, the mixture of ammonium salts (such as choline) with urea has been shown to produce eutectics that are liquid at ambient temperature and present uncommon solvent properties^{6,7}. Eutectic mixtures are also commonly used in the pharmaceutical industry to study the compatibility between active pharmaceutical ingredients (API) and excipients during the pre-formulation stage⁸. Therefore, determination of the eutectic parameters (T_E and X_E) is of interest in many fields of the chemical industry.

A widely used technique in eutectic determination is differential scanning calorimetry (DSC). The eutectic temperature is determined as the onset temperature of the first thermal event whereas the liquidus temperature is determined as the peak temperature of the last thermal event on heating^{9,10} (Figure II-1-(a)). From a DSC thermogram, it is easy to extract both the eutectic and liquidus temperatures for compositions far away from the eutectic composition. However, for compositions close to the eutectic composition, the liquidus and eutectic temperatures are too close to be distinguished¹¹ (Figure II-1-(b)).

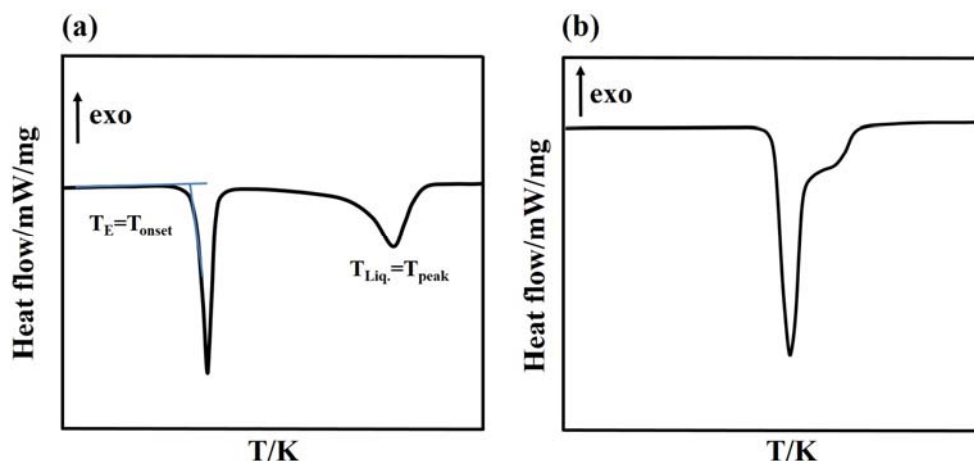


Figure II-1. A schematic DSC curve shows (a) the determination of eutectic temperature (T_E) and liquidus temperature (T_L), (b) the overlap of eutectic and liquidus peaks.

In these cases, it is difficult to precisely determine the eutectic composition. A valuable method is to draw a Tammann graph by plotting the variation of the eutectic invariant enthalpy versus the composition^{12,13}. The eutectic composition is given as the intercept of the straight lines in the Tamman graph (Figure II-2). However, when the eutectic phase diagram covers a very narrow temperature range, it is difficult to extract any enthalpy value even by using a smaller scanning rate¹⁴ or a deconvolution treatment (PeakFit software)¹⁵. Thus, it is necessary to search for alternative experimental methods to solve this problem. In this matter, nonlinear optical second harmonic generation (SHG) deserves attention.

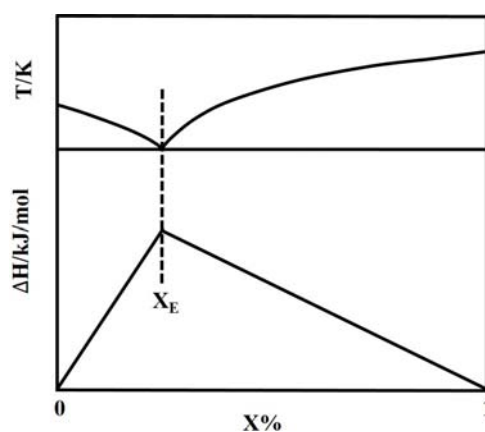


Figure II-2. A schematic illustration of a Tamman graph plotting to determine the eutectic composition (X_E).

Following the recent applications of SHG (illustrated in Chapter I), by tracking the phase transformations of non-centrosymmetric crystals along the heating process, it was logical to envisage using TR-SHG to plot the eutectic phase diagram and precisely assess the eutectic composition of binary eutectic mixtures. Of course, this requires as an essential feature that at

least one of the two components of a binary system crystallizes in a non-centrosymmetric space group.

In the following, the principle of the proposed method is described. Then, the potential of the technique is evaluated through the experimental study of the binary system formed by urea and water. This system is indeed of particular interest for the chemical industry as it is used to reduce the concentration of nitrogen oxides (NO_x) in exhaust emissions from vehicle engines. Marketed under the trade names: DEF (diesel exhaust fluid), Ad-Blue, or AUS 32, this commercial aqueous solution of urea has a concentration of 32.5 wt% urea and a freezing point of -11°C ^{16,17}.

II-1-2. Principle of Eutectic Phase Diagram Determinations by TR-SHG

The SHG intensity generated by a given sample depends on numerous parameters (the molecular nature of the sample, the crystal structure, the size and orientation of the crystallite, etc.)¹⁸⁻²⁰, but a simplified view of the SHG process can lead to the notion that the SHG signal generated by the sample is roughly proportional to the fraction of the crystalline non-centrosymmetric phase. With this assumption, it is possible to speculate on the schematic evolution of the SHG signal for a binary mixture between A (centrosymmetric phase) and B (non-centrosymmetric phase) during the heating process (the route 1→2→3 in the related phase diagram) (see Figure II-3 and Figure II-4).

Figure II-3 relates to the case of a mixture in the hypoeutectic composition domain (fraction of B lower than the eutectic composition).

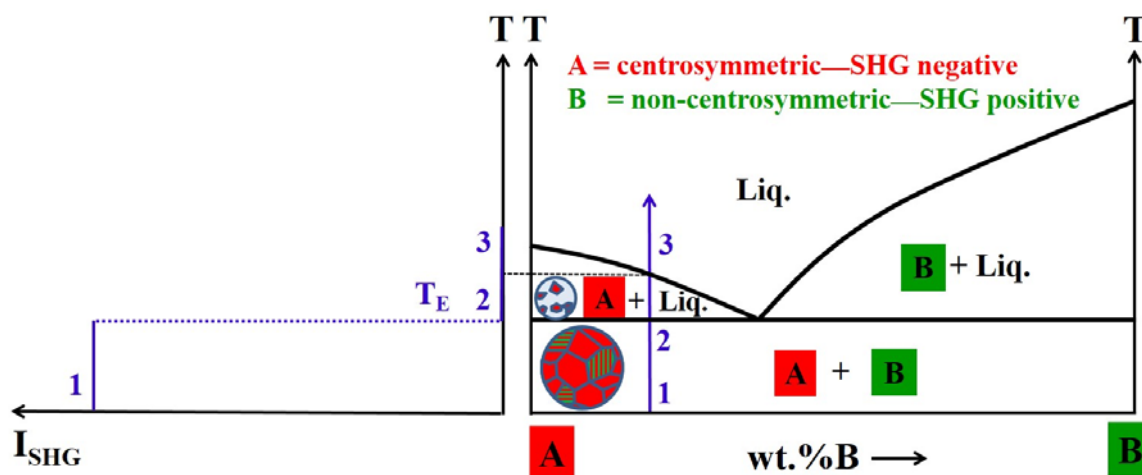


Figure II-3. Basic scheme of the SHG signal evolution for hypoeutectic compositions.

For hypoeutectic compositions, from point 1 to point 2, the SHG signal is supposed to be stable as no change in the solid phase is expected. At point 2 (eutectic temperature, T_E), a sharp decrease of the SHG signal should occur (as the microstructured crystals A+B disappear) and lead rapidly to a zero SHG signal. Indeed, above point 2, the system is only composed of centrosymmetric phases (crystals of A) and/or liquid.

Figure II-4 corresponds to the case of a mixture in the hypereutectic composition domain (fraction of B higher than the eutectic composition).

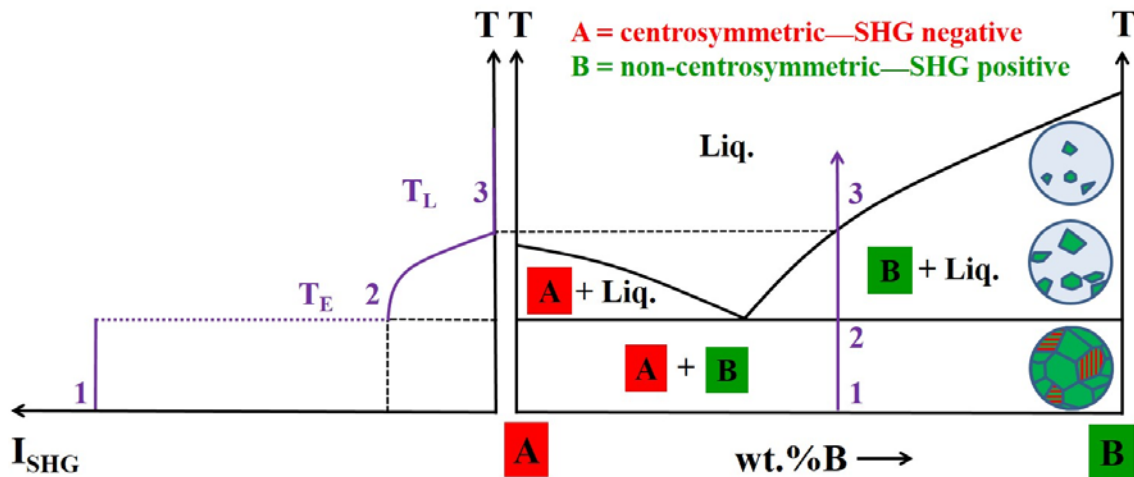


Figure II-4. Basic scheme of the SHG signal evolution for hypereutectic compositions.

For hypereutectic compositions, from point 1 to point 2, the SHG signal should remain stable (similarly to the hypoeutectic case). At point 2, a sharp decrease of the SHG signal should occur at the eutectic temperature (T_E) due to the melting of the SHG-active phase (crystals of B) and the microstructured crystals A+B. From point 2 to point 3, a progressive decrease of the SHG signal should be observed, due to the progressive melting of the SHG-active phase (crystals of B). Finally, at point 3, the SHG signal should totally vanish, meaning that there is no more non-centrosymmetric crystal and that the liquidus temperature (T_L) is reached.

Based on these schematic evolutions of the SHG signal versus the temperature, it is clear that, hypereutectic compositions, both the eutectic and the liquidus temperature could be detected by TR-SHG, while for hypoeutectic compositions only the eutectic temperature could be observed (Figure II-5). Due to the sensitivity of this technique, even for compositions close to the eutectic composition, it should be possible to differentiate whether the liquidus is present or

not. Thus, the eutectic composition can be determined precisely by refining the compositions around the eutectic composition.

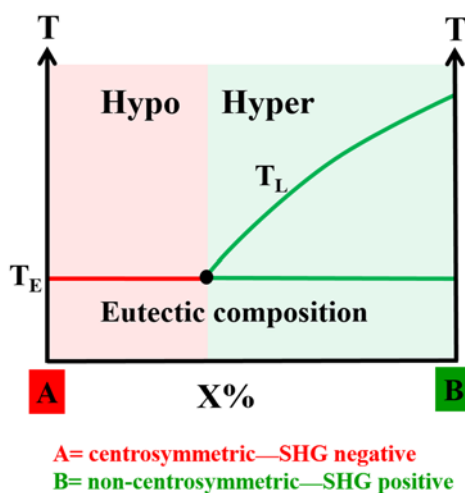


Figure II-5. A schematic view of a binary eutectic phase diagram plotted by TR-SHG.

In the binary eutectic system between urea and water, under normal atmospheric conditions and at the equilibrium, water crystallizes in a centrosymmetric hexagonal space group, $P6_3/mmc$ ^{21,22}, which is SHG inactive. Urea (Figure II-6) crystallizes in a non-centrosymmetric tetragonal space group, $P\bar{4}2_1m$ ²³, which is SHG active.

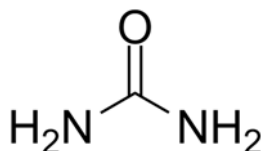


Figure II-6. Molecular structure of urea.

For solid urea: (i) no polymorphism has been reported so far (i.e., no metastable eutectic is foreseen); (ii) it has a high SHG efficiency and it is a phase-matchable material; (iii) it is stable under laser irradiation and its SHG intensity remains constant upon heating in the solid-state^{24,25}. These features make this system simple and suitable for TR-SHG measurements.

II-1-3. Experimental Details

II-1-3-1. Preparation of the Samples

Urea powder was purchased from Acros Organics (CAS registry number: 57-13-6) with a chemical purity higher than 99.5%, it was recrystallized from deionized water before use. Samples of the desired mass fraction were prepared by mixing at ambient temperature the requested amount of urea powder in deionized water (i.e., for a 30 wt% mixture, 3 g of

recrystallized urea powder and 7 g of deionized water). The mixture was then stirred for 5 h to ensure that the urea was fully dissolved. All the samples were prepared with a maximum deviation of 0.05 wt%.

II-1-3-2. TR-SHG Experimental Procedures

20 mg of a pre-prepared urea/water solution of the desired composition placed in an amorphous silicon dioxide crucible, which was covered with a glass slide to make sure that the sample is flat and homogeneously dispersed in the crucible. Each sample was cooled from room temperature to -30°C at 10 K/min and maintained at -30°C for 5 min. The sample was then heated from -30°C to room temperature at 1K/min or 0.5 K/min. For each TR-SHG plot, the SHG data were normalized using the maximum SHG value recorded during heating.

Several compositions of the urea/water mixtures were analyzed. As examples, the results obtained for one hypoeutectic composition (30 wt%, mass fraction of urea) and one hypereutectic composition (35 wt%) are reported hereafter.

II-1-4. Measurements of Hypoeutectic Compositions between Urea and Water by TR-SHG

The experimental results obtained for the composition of 30 wt% urea/water mixture are shown in Figure II-7. The TR-SHG curve (Figure II-7-(a)) fits well with the expected signal evolution for a hypoeutectic composition (Figure II-3). A high SHG signal is detected at low temperature (-30°C) and a plateau is observed from -30°C to -12°C . In region I, ice crystals and microstructured crystals (composed of ice and urea) coexist, but only the urea fraction is responsible for the observed SHG signal. The plateau is followed by a drastic decrease of the SHG signal at -12°C , which totally vanishes at -10°C . Region II corresponds to the melt of the microstructured crystals, and once all urea parts melt, no SHG signal is produced by either ice or liquid.

The onset temperature of the eutectic peak determined from the DSC analysis (Figure II-7-(b)) is -12°C . These calorimetric results are in accordance with the temperature obtained by TR-SHG, confirming that the decrease of the SHG signal can be associated to the eutectic transformation at T_E . The cold-stage microscopy observations (Figure II-8-(a)) show the typical

dendritic microstructure of ice and urea crystals. Upon heating, disappearance of the crystals was observed starting from the temperature of -12°C (Figure II-8(b)).

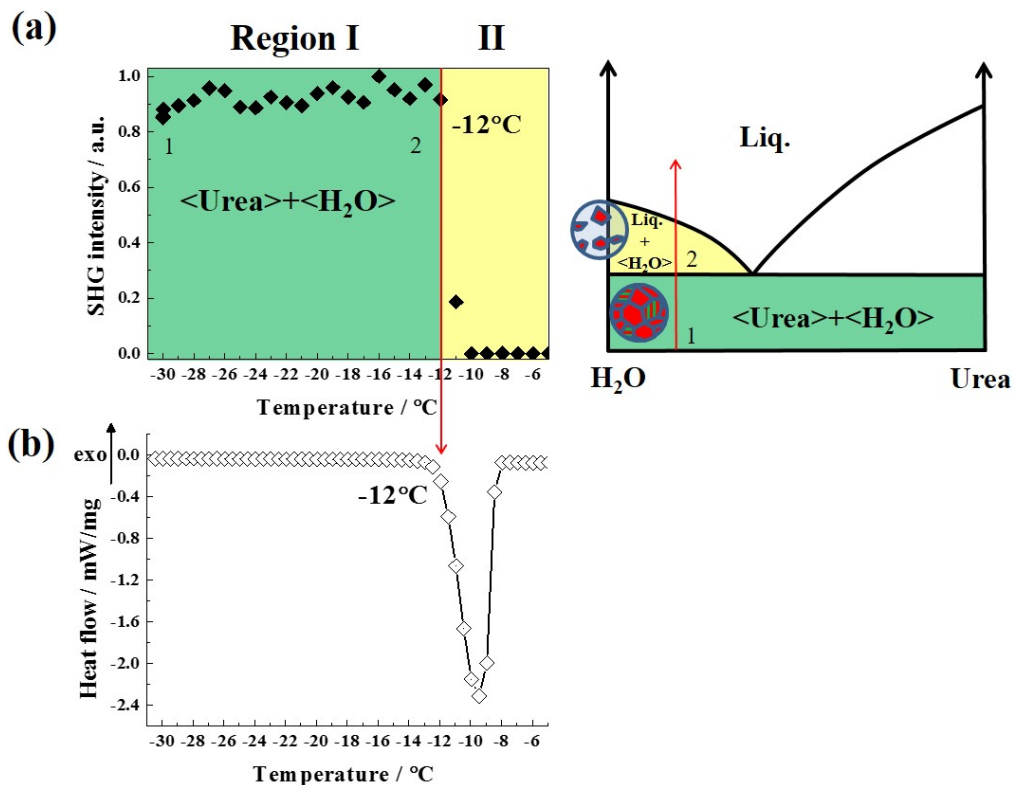


Figure II-7. Comparison between (a) TR-SHG and (b) DSC analysis for the composition of 30 wt% urea/water (1 K/min heating rate).

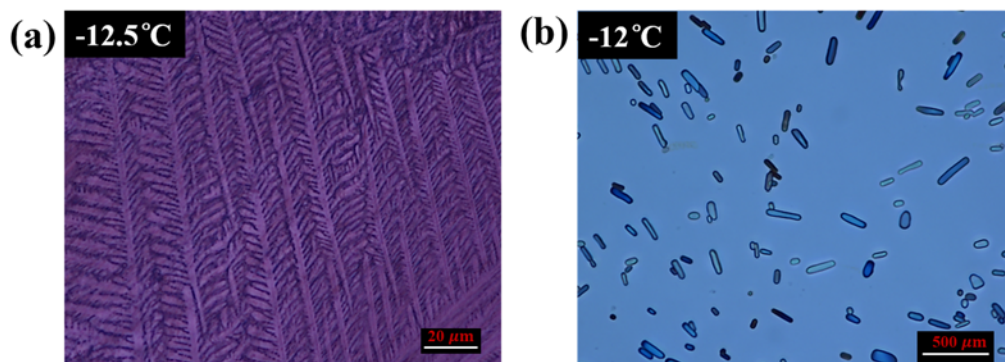


Figure II-8. Microscopy observations of composition of 30 wt% urea/water mixture (a) at -12.5°C , the dendritic eutectic microstructure and (b) at -12°C .

Based on the schematic evolution (Figure II-3), the SHG signal should vanish at the eutectic point (-12°C). However, a 2°C delay of the completion of melting was observed. Increasing the measurement rate to one measurement every 15 s instead of one every minute did not lead to a reduction of this delay. The small thermal gradient due to the heating element and the sample thickness generates a certain thermal inhomogeneity in the sample. Consequently, the whole

sample does not melt at exactly the same time. Thus, the existence of this 2°C delay is not surprising. Nevertheless, it can be mentioned that annealing a sample of hypoeutectic composition at a temperature slightly above -12°C leads to a decrease of the SHG signal with time, whereas for the same sample annealed at a temperature slightly below -12°C, the SHG signal remains stable. So, choosing the temperature at which the SHG signal starts to decrease as eutectic temperature is reasonable (onset temperature).

II-1-5. Measurements of Hypereutectic Compositions between Urea and Water by TR-SHG

The experimental result obtained for 35 wt% urea/water mixture is shown in Figure II-9.

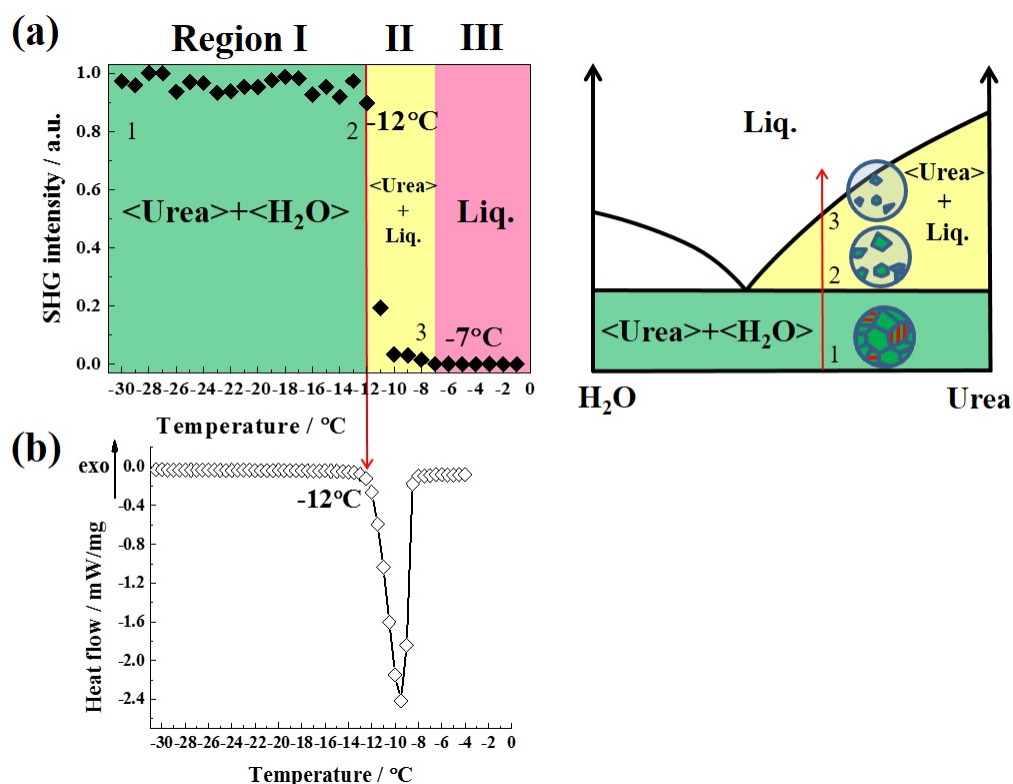


Figure II-9. Comparison between (a) TR-SHG and (b) DSC analysis for the composition of 35 wt% urea/water (1 K/min heating rate).

The TR-SHG curve (Figure II-9-(a)) fits well with the expected signal evolution for a hypereutectic composition (Figure II-4). Between -30°C and -12°C, the TR-SHG signal remains stable. In this region I, pure urea crystals and microstructured crystals of ice and urea coexist. They are both responsible for the TR-SHG signal observed. At -12°C (eutectic temperature), the signal decreases sharply, corresponding to the disappearance (melting) of the microstructured crystals. Then, in region II, the SHG signal decreases progressively (due to the

progressive melting of the urea crystals) and totally vanishes at -7°C . The latter temperature thus corresponds to the liquidus temperature (no more urea crystals exists). In region III, only a single liquid phase exists, no SHG signal is observed.

The onset of the eutectic peak is -12°C from the DSC results (Figure II-9-(b)). This is in agreement with the eutectic temperature determined by TR-SHG. Note that the liquidus temperature (measured by TR-SHG at -7°C), cannot be determined from the DSC curve since the two endothermic peaks overlap.

II-1-6. Plot of the Eutectic Phase Diagram between Urea and Water by TR-SHG

By performing TR-SHG measurements for several different compositions (10 wt%, 20 wt%, 30 wt%, 35 wt%, 40 wt%, 45 wt%, 50 wt% and 60 wt% mass fraction of urea), we constructed the phase diagram of urea/water (Figure II-10).

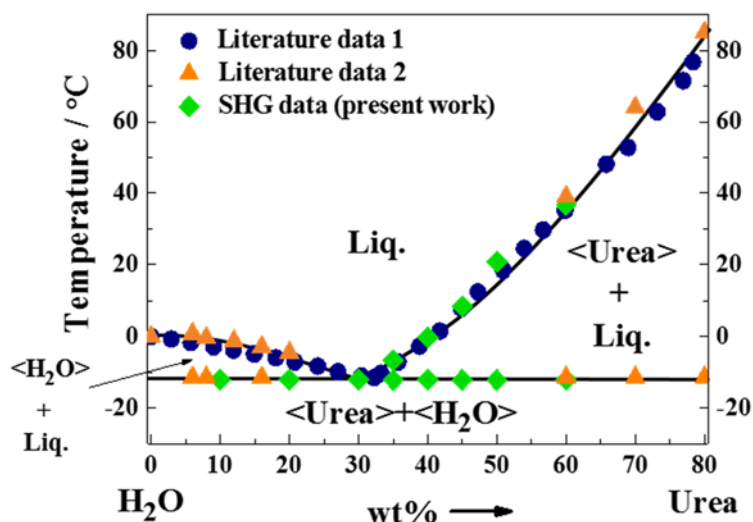


Figure II-10. Binary eutectic phase diagram between urea and water.

Values obtained from TR-SHG fit well with the literature data^{15,26}. At this stage, it is important however to mention:

- The liquidus in the hypoeutectic compositions cannot be obtained by TR-SHG (see Figure II-5). So, only part of the phase diagram can be plotted.
- For compositions higher than 60 wt%, liquidus cannot be determined by TR-SHG. Indeed, the opened crucible used for the experiments does not avoid the solution to evaporate (the liquid-vapor equilibrium is reached at these temperatures) and the concentration during the measurements deviates strongly from the initial composition.

II-1-7. Precise Determination of the Eutectic Composition between Urea and Water by TR-SHG

We described how we constructed the phase diagram of urea/water from TR-SHG data. In the following, we explain how TR-SHG can be used to precisely determine the eutectic composition of this system. For 35 wt% urea/water composition (Figure II-9-(a)), both the eutectic and liquidus temperatures are observable on the TR-SHG curve. This means that this composition is in the hypereutectic composition domain. By contrast, for the 30 wt% composition (Figure II-7-(a)), only the eutectic temperature is observable in the TR-SHG curve, which corresponds to a typical hypoeutectic composition behavior. Therefore, the eutectic composition is comprised in the interval of 30 wt% to 35 wt%.

To precisely determine the eutectic composition, additional TR-SHG measurements were performed for compositions between 30 wt% and 35 wt%. SHG signals were recorded with steps of 0.1°C at a heating rate of 0.5 K/min in the temperature range of -12.5°C to -10°C to precisely differentiate the solidus and liquidus temperatures. Figure II-11 shows the result for 32.8 wt% urea/water mixture and 32.9 wt% in Figure II-12.

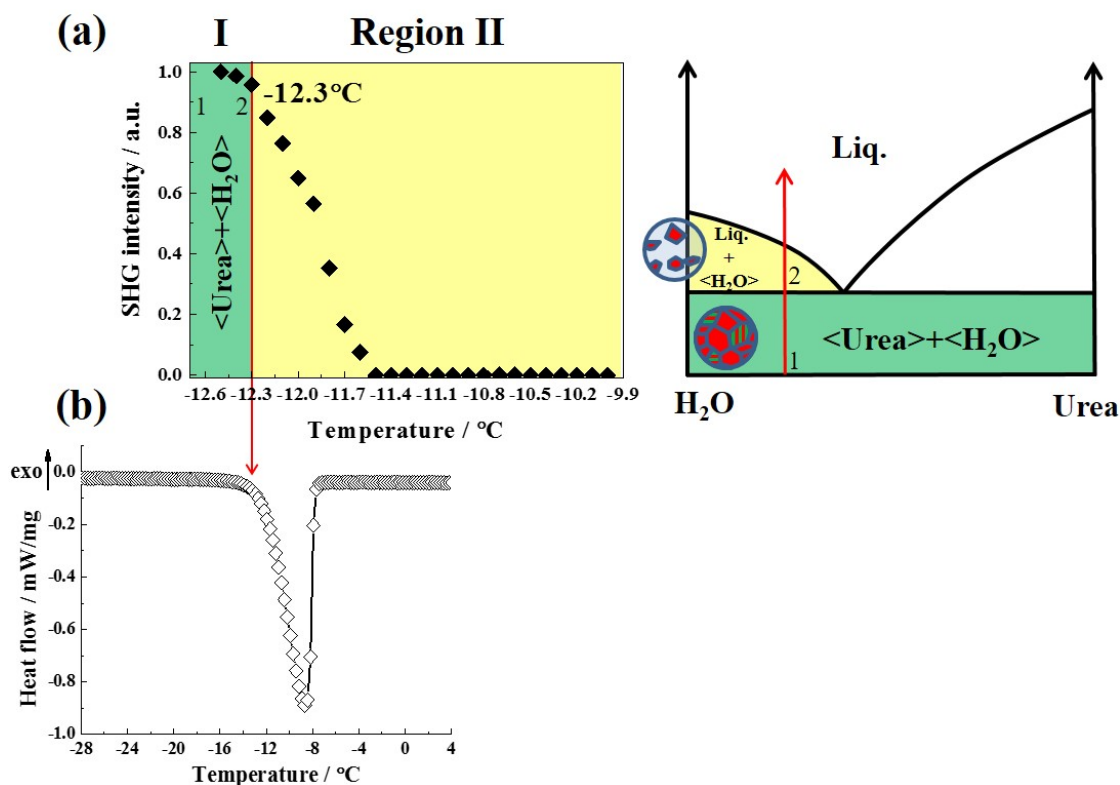


Figure II-11. Comparison between (a) TR-SHG and (b) DSC analysis for the composition of 32.8 wt% urea/water (0.5 K/min heating rate). No liquidus is observed.

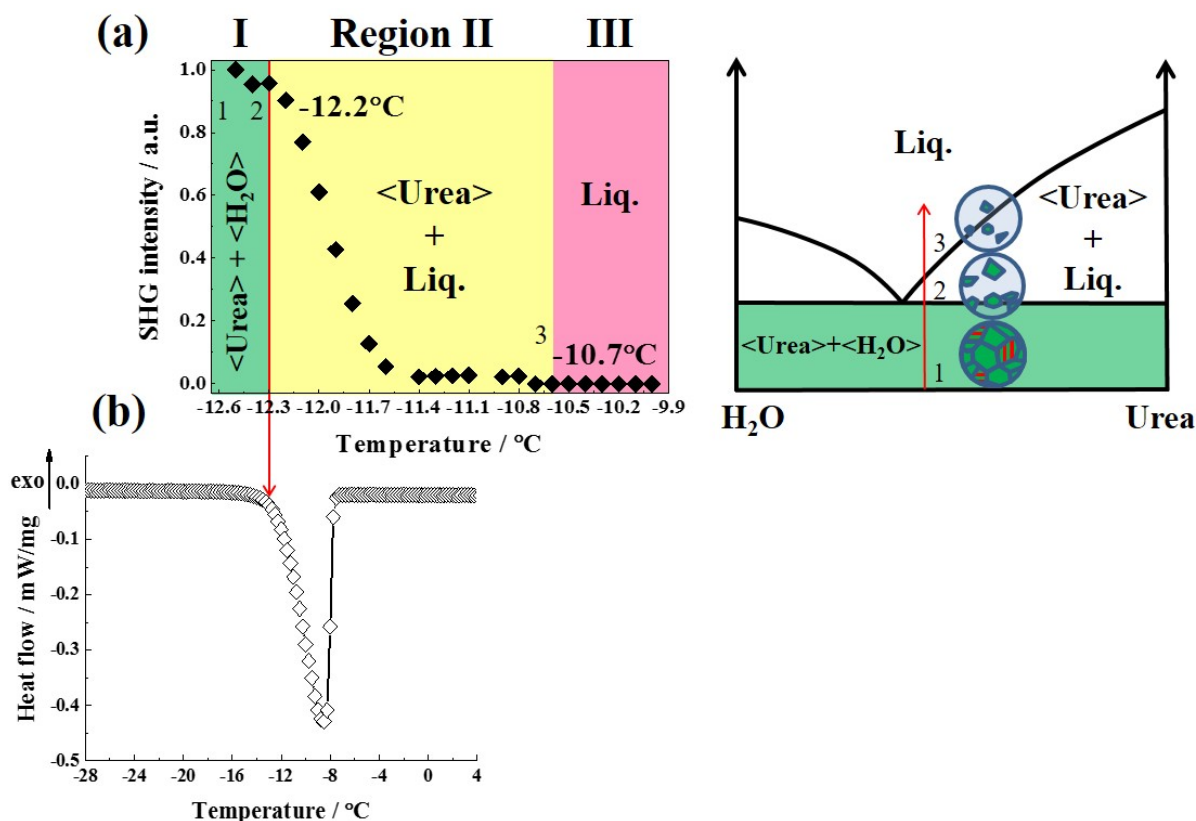


Figure II-12. Comparison between (a) TR-SHG and (b) DSC analysis for the composition of 32.9 wt% urea/water (0.5 K/min heating rate).

Two prominent results are given above. For 32.8 wt%, no liquidus was observed for the composition, while for the composition of 32.9 wt%, TR-SHG gives a liquidus temperature of -10.7°C . Consequently, a eutectic composition between 32.8 wt% and 32.9% was confined by TR-SHG. Besides, we must mention here that the pre-prepared solutions used for experimental measurements have a maximum deviation of 0.05 wt%.

II-1-8. Discussions

A eutectic composition between 32.8 wt% and 32.9 wt% was determined by a direct differentiation between hypoeutectic compositions and hypereutectic compositions. i.e., by differentiating liquidus and solidus. The solidus is obtained when the eutectic reaction starts, I_{SHG} begins to decrease. The liquidus in the hypereutectic compositions are determined by following the dissolution of urea crystals. When urea crystals are totally dissolved, $I_{\text{SHG}}=0$, the liquidus is reached. Since urea crystal possess a high nonlinear optical susceptibility¹⁸ and generates a high second harmonic signal, TR-SHG has a high precision to detect the liquidus and to differentiate hypoeutectic compositions and hypereutectic compositions. Therefore, the

method used to determine the eutectic composition is precise and reliable.

The value (32.8 wt% to 32.9 wt%) obtained by TR-SHG is compared with literature data (summarized in Table II-1).

Table II-1. A summary of eutectic composition and eutectic temperature of urea/water system.

	$X_E/\text{wt}\%$	$T_E/^\circ\text{C}$	Method
Our work	32.9	-12	TR-SHG
Ad-blue	32.5	-11	Unknown
M. Egal et al. ¹⁵	29.4	-11.4	Extrapolation through the deconvolution of the DSC peaks with Peakfit software
I. Durickovic et al. ²⁷	32.26	-16.98	Modeling the characteristic peaks of the liquid, the mixture and the solid phases by Raman spectra recorded

It is slightly different from the eutectic composition of commercial Ad-Blue: 32.5 wt%. Despite an extensive literature review, the origin of the chosen composition of commercial product was not found. However, a few articles can be found in the literature about the urea/water binary system. Babkina and Kuznetsov²⁷ observed that the liquidus peaks of the urea/water system can only be distinguished in the DSC curves if the urea concentration is low, shown in Table II-2.

Table II-2. Liquidus and solidus values of urea/water system by DSC.

Composition/wt% in urea	Solidus/ $^\circ\text{C}$	Liquidus/ $^\circ\text{C}$
2.94	-12.0	-3.2
7.28	-12.1	-5.1
14.40	-11.8	-5.5
20.07	-12.0	-
31.47	-11.8	-
43.26	-12.2	-
44.86	-12.0	-
46.85	-12.0	-

Up to 14.40 wt%, liquidus value cannot be obtained by DSC. We confirmed it by performing DSC measurements (Figure II-13). At the concentration of 10 wt% in urea, liquidus and solidus can be separated, but at 20 wt% the liquidus and solidus begin to merge. Concentration higher than 30 wt%, liquidus and solidus totally merged, no liquidus data can be obtained by DSC.

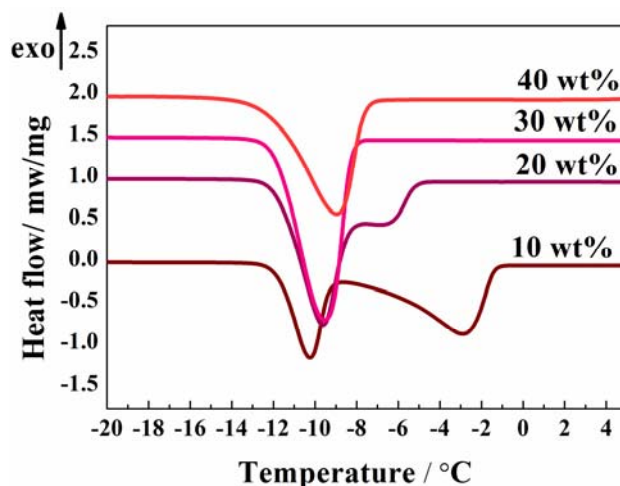


Figure II-13. DSC curves for different compositions of urea/water (wt% in urea).

A eutectic temperature of -11.4°C and a eutectic composition of 29.4 wt% were calculated via extrapolation through deconvolution of the DSC peaks with Peakfit software¹⁵. Durickovic et al.²⁸ reported a eutectic composition of 32.26 wt% and a eutectic temperature of -16.98°C , obtained by modeling the characteristic peaks of the liquid, the mixture, and the solid phases by Raman spectra recorded at various compositions. Concerning the liquidus temperatures determined by TR-SHG (measurable only in the domain rich in urea), a good correlation is observed with previously reported results based on other methods²⁷. As none of the above reported works is based on a clear differentiation between the liquidus and solidus temperatures, the contribution of the present TR-SHG method cannot be neglected.

II-1-9. Conclusion and Perspectives

A new method based on the TR-SHG process was proposed for precise determination of the eutectic composition in binary eutectic systems. The principle was exemplified through the case of the urea/water system, and the eutectic composition was found to be confined between 32.8 wt% and 32.9 wt% in urea for this system. It is worth mentioning that the liquidus temperature of the centrosymmetric phase cannot be determined by TR-SHG, which permits to precisely differentiate hypoeutectic compositions from hypereutectic compositions. This technique reveals its usefulness as a rapid and sensitive tool for the precise determination of eutectic compositions for binary eutectic systems involving one centrosymmetric and one non-centrosymmetric compound.

Note that a careful adjustment of the urea content in Ad-Blue close to the eutectic composition will slightly lower the freezing point. An impact on the crystallization kinetics (slowing down of the crystallization in winter use) might also be envisaged, but further studies are required to confirm this hypothesis. The application of the TR-SHG method could also be envisaged on a ternary system formed by urea, water, and an extra component that would further lower the freezing point. More generally, it could be of interest to evaluate the potential of TR-SHG for the characterization of binary eutectic systems involving two non-centrosymmetric compounds or a non-phase-matchable material (to see if the optical behavior is equivalent to that of the phase-matchable urea).

An odd order harmonic technique could be used, i.e., third-order harmonic (THG), in which the centrosymmetric structures can generate signals. So that the whole phase diagrams of a non-centrosymmetric/centrosymmetric system could be obtained, as is illustrated in Figure II-14.

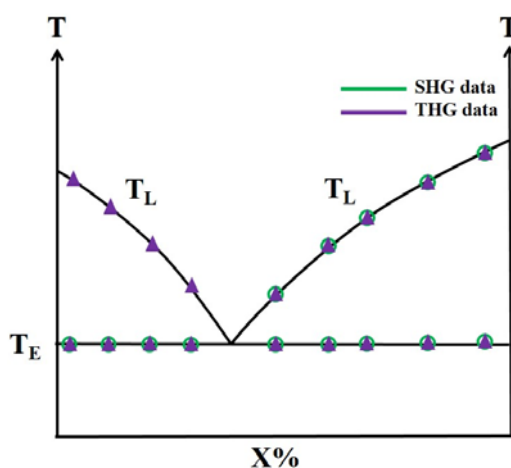


Figure II-14. Schematic drawing of a phase diagram involving one non-centrosymmetric phase that can be constructed by SHG and THG.

II-2. Metastable Eutectic Phase Diagram Investigations — 1,3-Dimethylurea (DMU)/Water System

II-2-1. Introduction

1,3-dimethylurea (DMU) (Figure II-15) is a urea derivative. It is used to block the irreversible solid-solid transition of the metastable forms of pyrazinamide to the stable form at room temperature²⁹ and also as an intermediate in organic synthesis, such as the synthesis of caffeine, chemicals, textile aids and herbicides. It exists as two enantiotropically related polymorphic forms:

- Form I^{30,31} is stable at high temperature and crystallizes in the centrosymmetric *Fdd2* space group.
- Form II^{30,32} is stable at low temperature and crystallizes in the non-centrosymmetric *P2₁2₁2* space group.

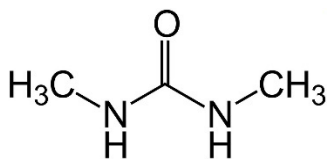


Figure II-15. Molecular structure of DMU.

The interaction of DMU with water gives a rather complex phase diagram, as shown in Figure II-16³³. The presence of hundreds of ppm water decreases the transition temperature (form II → form I) from 58°C down to 25°C. A metatectic invariant between solid solution form II (ss II) and solid solution form I (ss I) ($\langle \text{ss II} \rangle + \text{saturated solution} \leftrightarrow \langle \text{ss I} \rangle$) was detected by temperature-resolved XRPD at 25°C. A $\text{DMU} \cdot \text{H}_2\text{O}$ with a non-congruent fusion at 8°C ($\langle \text{DMU} \cdot \text{H}_2\text{O} \rangle \leftrightarrow \langle \text{ss II} \rangle + \text{saturated solution}$) was revealed by DSC and its crystal structure was resolved in a centrosymmetric *C2/c* space group by XRPD (the crystallographic data of $\text{DMU} \cdot \text{H}_2\text{O}$ and anhydrous DMU are summarized in Table II-3). A metastable eutectic invariant ($\langle \text{ss II} \rangle + \langle \text{water} \rangle \leftrightarrow \text{saturated solution}$, determined by refractometry) and a stable eutectic invariant ($\langle \text{DMU} \cdot \text{H}_2\text{O} \rangle + \langle \text{water} \rangle \leftrightarrow \text{saturated solution}$, determined by DSC) also exist. However, due to the experimental restrictions, the values (liquidus and solidus) close to the eutectic composition cannot be obtained by refractometry and the DSC thermograms shows

merges of all the thermal peaks. Even though it is possible to complete this phase diagram by extrapolation of the liquidus and solidus (colored curves in Figure II-16), the dispersion of the existing hypoeutectic liquidus values (red curve in Figure II-16) will give an inaccurate eutectic composition and a deviation of the liquidus. Therefore, another way should be found to obtain precisely the data close to the eutectic composition.

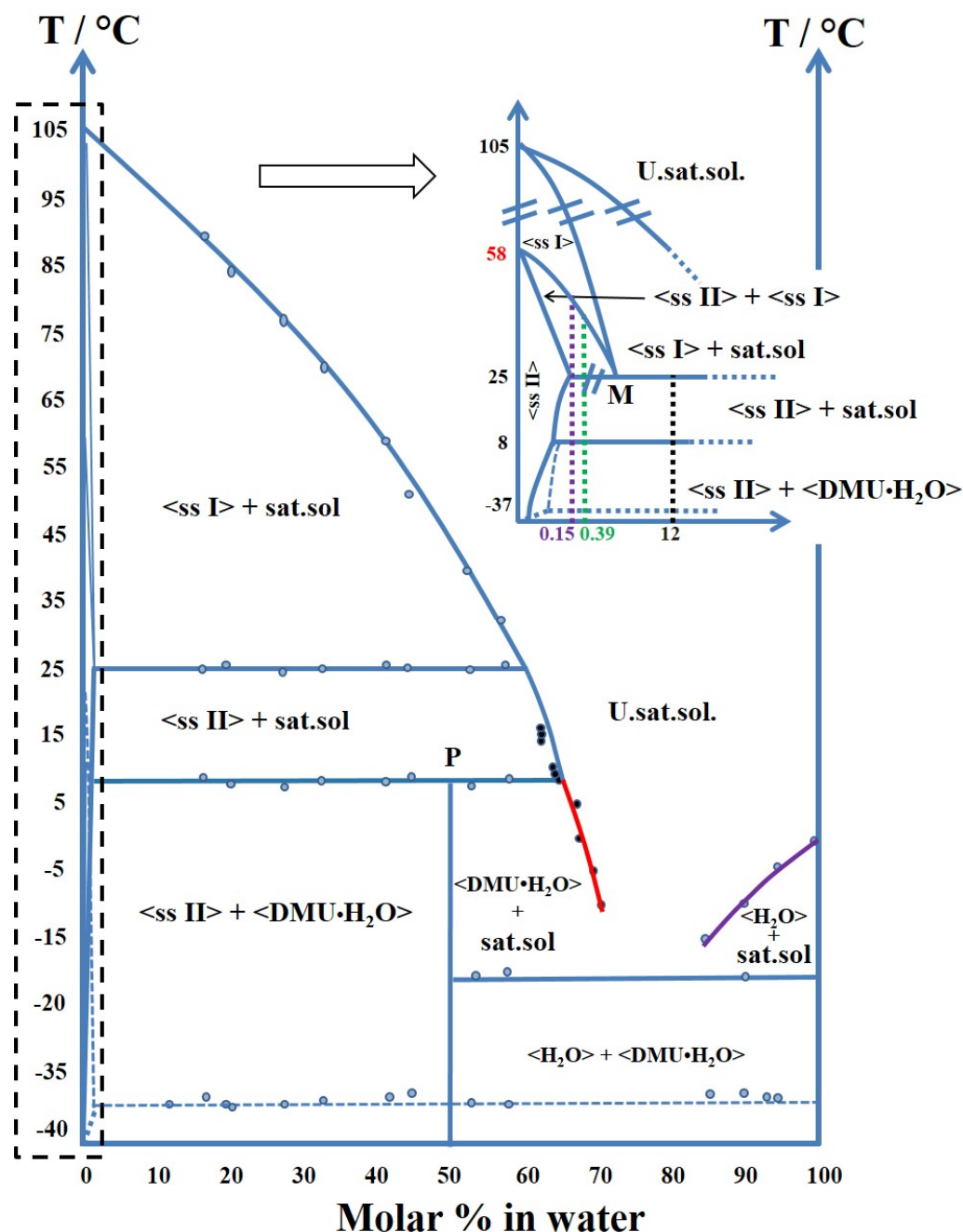


Figure II-16. Phase diagram between DMU and water. (*U.sat.sol* represents under saturated solution, *sat.sol* represents saturated solution. These two abbreviations will be used in the following.)

Table II-3. Crystallographic data of anhydrous DMU and DMU·H₂O.

Form	DMU·H ₂ O	DMU form I	DMU form II
Temperature (K)	253	180	100
Crystal system	Monoclinic	Orthorhombic	Orthorhombic
Space group	C2/c	Fdd2	P2 ₁ 2 ₁ 2
a (Å)	19.1479 (8)	11.3837 (2)	10.8522 (6)
b (Å)	13.9557 (5)	19.6293 (4)	4.9102 (3)
c (Å)	13.4926 (4)	4.5608 (1)	4.5766 (3)
β (°)	134.644 (2)	90	90
Z	16	8	2
Z'	2	0.5	0.5
Volume (Å ³)	2565 (1)	1019 (1)	244 (1)
Density (g/cm ³)	1.099 (1)	1.149 (1)	1.200 (1)

Nucleation and/or growth of DMU·H₂O was/were observed to be slow. Often, the stable equilibrium between DMU·H₂O and water is more difficult to reach than the metastable equilibrium between ss II and water. Therefore, the possible pathway to get access to the liquidus and solidus close to the eutectic composition is to plot the metastable equilibrium between ss II and water, especially to precise the metastable eutectic composition. Then, by extrapolation of this metastable eutectic phase diagram, a more accurate stable phase diagram can be obtained (illustrated in Figure II-17).

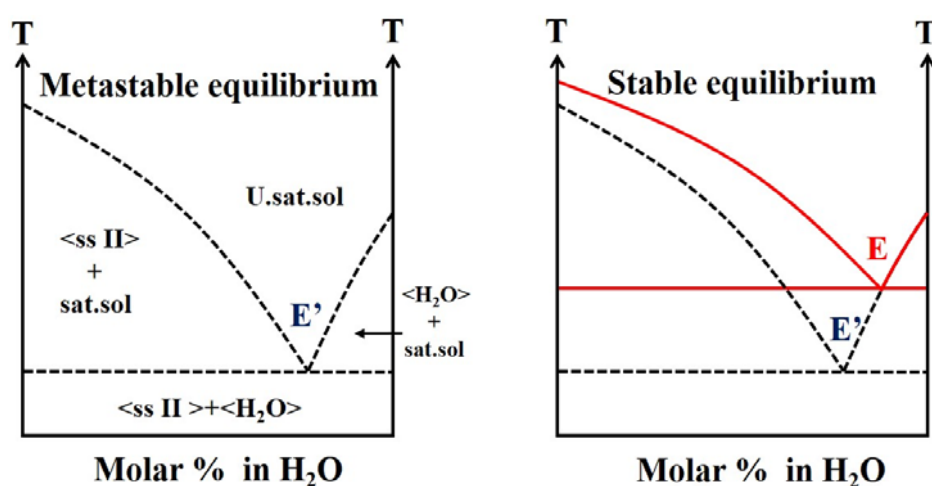


Figure II-17. Illustration of the determination of stable eutectic equilibrium by extrapolation of metastable equilibrium. N.B.: the composition of the solid solution <ss II> is close to the pure composition.

In this work, we report for the first time the use of TR-SHG to plot the metastable eutectic phase diagram between DMU (or more precisely ss II) and water and to accurately determine the metastable eutectic composition.

II-2-2. Preparation of the Samples

1,3-dimethylurea powder was purchased from Merck Schuchardt OHG in Germany (CAS registry number: 96-31-1) with a chemical purity of ca. 99.9% and kept in a desiccator with P_2O_5 at ambient temperature before usage.

Samples of the desired molar fraction were prepared by mixing the requested amount of DMU powder in deionized water at ambient temperature (i.e., for a 70% molar mixture, 6.7692 g of DMU powder and 3.2308 g of deionized water). The mixture was then stirred for 5 h to ensure the full dissolution of the solute. All the samples were prepared with a maximum deviation of 0.1% in molar fraction of water. Of the pre-prepared solutions, 20 mg were used for each TR-SHG experiments.

II-2-3. Establishment of an Experimental Protocol to Study the Metastable Equilibrium between SS II and Water

As previously mentioned, the aim of this study is to precisely determine the metastable eutectic composition for the system formed by ss II and water. To this purpose, it is necessary to select adequate experimental conditions:

- A cooling protocol that allows to reach the metastable state between ss II and water.
- A heating protocol to perform the TR-SHG experiments that minimizes the conversion of ss II towards the stable monohydrate.

The sample holder and the heating/cooling stage used for TR-SHG experiment can also be coupled to a microscope (cold-stage microscope). Thus, the heating/cooling protocols can be chosen and validated by cold-stage microscopy observations. Figure II-18 shows the microscopy observations for a composition of 70 mol% DMU/water mixture. The sample was first cooled down to -50°C at 10 K/min and annealed at this temperature during 60 min to fully crystallize ss II (it should be noted that it also takes time to crystallize ss II). The observations under a microscope were performed during heating at 5 K/min. Small crystals (several micrometers) are clearly visible but their shape is not well defined probably due to the high cooling rate used (10 K/min) to avoid the crystallization of the monohydrate. However, only one crystal shape (i.e., one crystalline form) was observed upon heating up to -21°C which

confirms that the chosen cooling rate allows the ss II form to be solely crystallized.

However, at the end of the melting process of ss II (-20°C , close to the liquidus temperature), a new crystalline form appears at the expense of the former crystals and continues to grow. This new form is $\text{DMU}\cdot\text{H}_2\text{O}$. Several higher heating rates were tried to totally avoid the appearance of $\text{DMU}\cdot\text{H}_2\text{O}$, but the monohydrate appeared no matter how fast the heating is. It appeared when the temperature is close to the liquidus temperature. Moreover, for TR-SHG, a fast heating will lead to less SHG data recorded. 5 K/min is a reasonable heating rate to avoid the fast appearance of $\text{DMU}\cdot\text{H}_2\text{O}$ and to have enough SHG data. It should be noticed that the metastable state between ss I and water cannot be reached by using the above experimental conditions, which has been confirmed by XRPD that only ss II crystallizes.

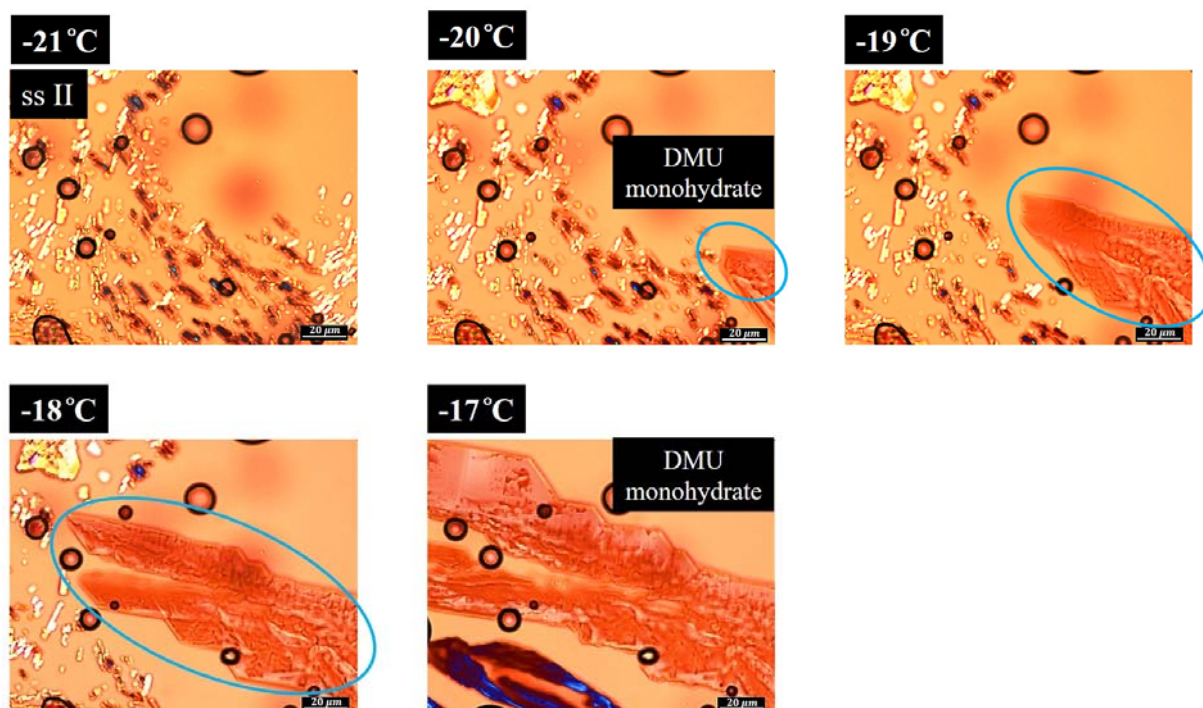


Figure II-18. Microscopy observations for a composition of 70 mol% DMU/water mixture at 5K/min.

Therefore, the protocol for TR-SHG measurements was determined (Figure II-19). The metastable state between ss II and water was reached by cooling the mixture from room temperature (RT) to -50°C at 10 K/min and annealing at this temperature for 60 min. Then, the sample was heated at 5 K/min to minimize the transition from metastable state to the stable state. However, under this condition, the co-existence of the metastable state and the stable state was still observed at the end of the melting.

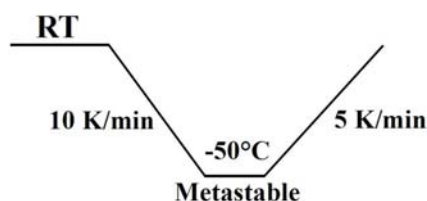


Figure II-19. Protocol to reach the metastable state between ss II and water.

II-2-4. TR-SHG Analysis in the Metastable SS II/Water System

II-2-4-1. SHG Response in the SS II/Water System

DMU (form II) is known to crystallize in a non-centrosymmetric orthorhombic space group $P2_12_12$. It is likely that the analyzed sample at ambient temperature was actually the ss II form (Figure II-16). This confirms that ss II is SHG active (it is not surprising since ss II is likely to keep the same crystal structure as “pure” DMU form II). Water crystallizes in a centrosymmetric hexagonal space group $P6_3/mmc$, which is SHG negative^{21,22}.

Different compositions of DMU/water mixtures were cooled to -50°C at 10 K/min to reach the metastable state and annealed for 60 min to fully crystallize the sample and then heated at 5 K/min and analyzed by TR-SHG. As examples, the results obtained for one hypoeutectic composition (60 mol%, molar fraction in water) and one hypereutectic composition (80 mol%, molar fraction in water) are detailed.

II-2-4-2. Measurements of Hypoeutectic Compositions between SS II and Water by TR-SHG

Figure II-20 shows the TR-SHG results obtained for a DMU/water mixture of composition 60 mol% in water. Each region in Figure II-20-(a) is correlated with the schematic phase diagram (Figure II-20-(b)) labelled with the same color.

In region I, between -50°C and -37.5°C , SHG signal remains relatively stable with a slight deviation due to the stability of the laser beam. ss II crystals and micro-structured crystals containing crystalline ss II and ice coexist and are both responsible for the observed SHG signal. In region II, at -37.5°C , SHG intensity begins to decrease, which corresponds to the decrease of the crystalline non-centrosymmetric fraction in the system, i.e., the beginning of the melting of micro-structured crystals between ss II and ice. Therefore, -37.5°C corresponds to the

eutectic temperature (T_E). The significant decrease occurs from -37.5°C to -30°C , which might be due to the thermal inhomogeneity in the sample. Remind that due to the rather high heating rate (5 K/min) necessary to limit the conversion towards the monohydrate, various area of the sample probably not reach the same temperature simultaneously. From -30°C to 23.8°C , after a small increase that will be discussed later in this chapter, the SHG signal decreases progressively. This decrease is due to the gradual dissolution of the ss II crystals. The signal totally vanishes at 23.8°C , which corresponds to the liquidus temperature. In region III, only liquid phase exists, so no SHG signal is observed.

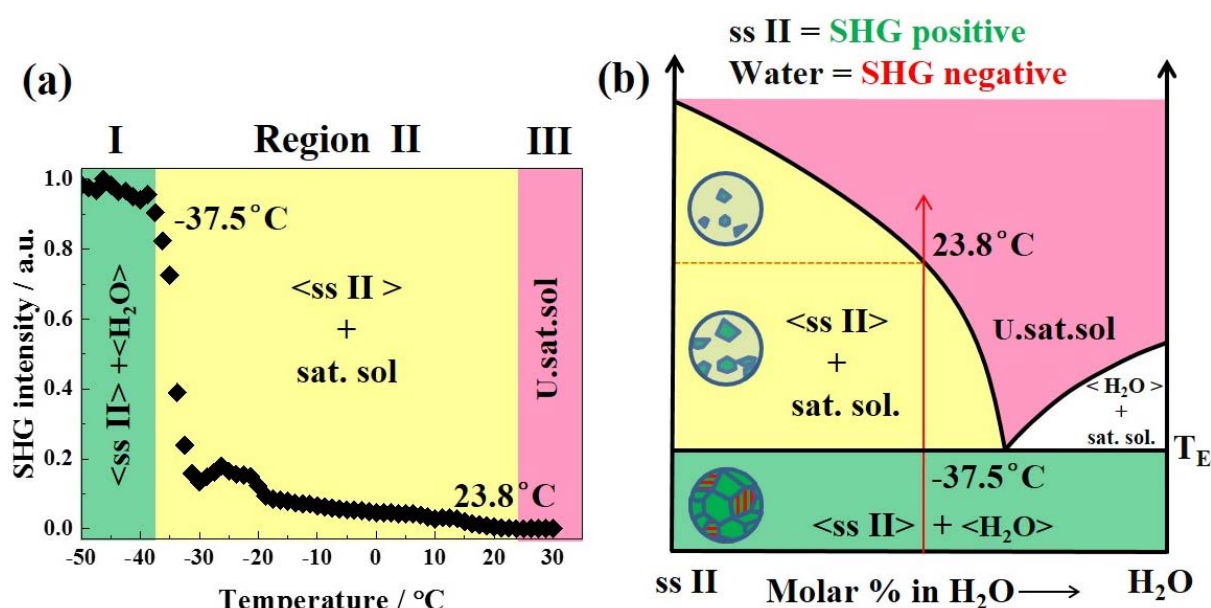


Figure II-20. (a) TR-SHG result for the composition of 60 mol% mixture (molar fraction in water) and (b) schematic DMU/water metastable eutectic phase diagram.

II-2-4-3. Measurements of Hypereutectic Compositions between SS II and Water by TR-SHG

The TR-SHG result for the mixture of composition 80 mol% (molar fraction in water) is shown in Figure II-21. In region I, a high SHG signal is detected and a plateau is observed from -50°C to -37.5°C . Since this hypereutectic mixture is rich in water, ice and micro-structured crystals (between ss II and ice) coexist below the eutectic temperature. Only the micro-structured crystals are responsible for the SHG signal. In region II, a decrease of the SHG signal occurs at -37.5°C , which represents the eutectic temperature. The signal decreases in the temperature range from -37.5°C to -32.5°C , which is the range of the eutectic reaction within dynamic

condition. When all the micro-structured crystals melt, no SHG signal is generated by either ice or liquid. Therefore, the liquidus temperature cannot be observed for this composition.

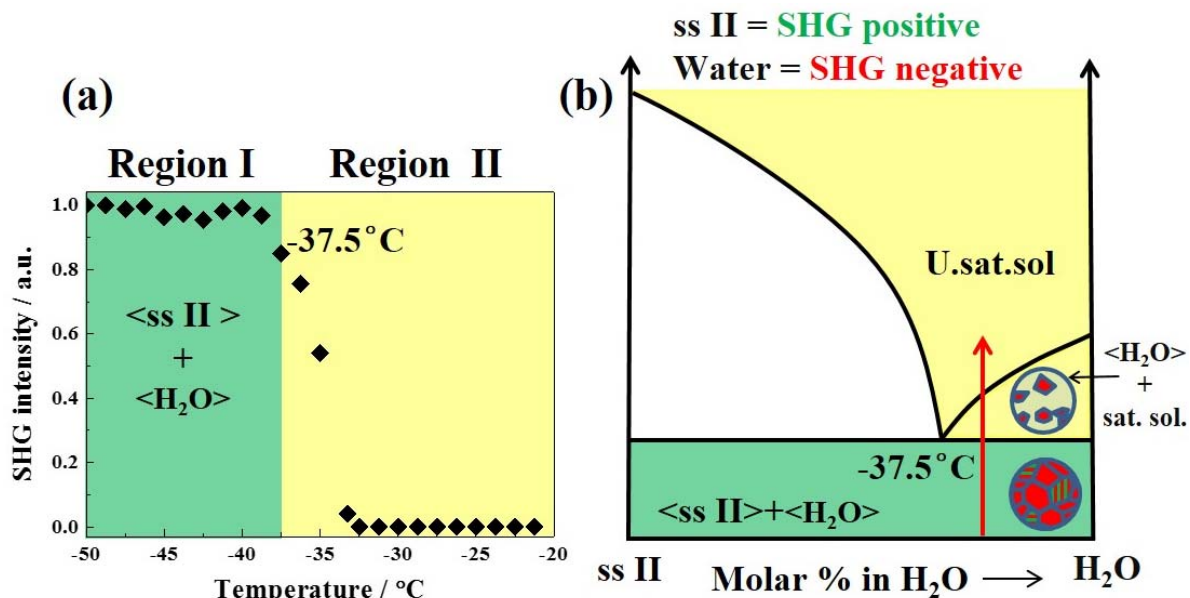


Figure II-21. (a) TR-SHG result for the composition of 80% mixture (molar fraction in water) and (b) schematic DMU/water metastable eutectic phase diagram.

II-2-5. Plot of the Metastable Eutectic Phase Diagram between SS II and Water by TR-SHG

The metastable eutectic phase diagram between ss II and water can be constructed by performing measurements for several compositions (60 mol%, 62 mol%, 65 mol%, 68 mol%, 70 mol%, 71 mol%, 75 mol%, 80 mol%, 90 mol% and 95 mol%, molar fraction in water). Results are shown in Figure II-22. We recall that for this phase diagram, the liquidus in the hypereutectic compositions cannot be obtained by TR-SHG.

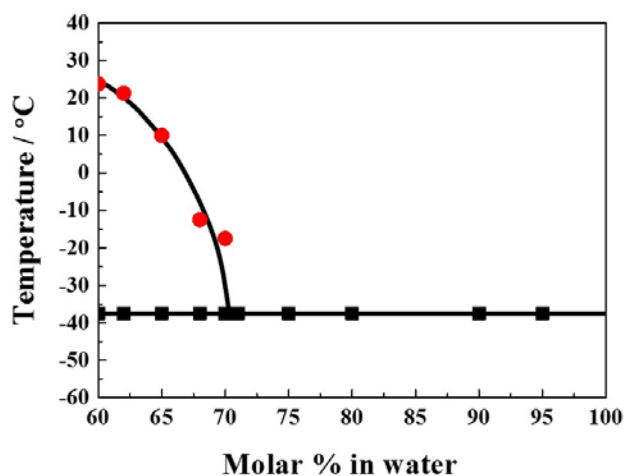


Figure II-22. Metastable eutectic phase diagram between ss II and water.

II-2-6. Precise Determination of the Metastable Eutectic Composition between SS II and Water by TR-SHG

The metastable eutectic phase diagram between ss II and water has been constructed. The following step requires to precise the metastable eutectic composition. To this purpose, two methods were used, as illustrated below.

II-2-6-1. Method 1: Differentiate the Liquidus and Solidus of Compositions Close to the Eutectic Composition

For the 70 mol% DMU/water mixture (Figure II-23-(a)), both the eutectic (-37.5°C) and liquidus (-17.5°C) temperatures can be observed in the TR-SHG curve. This composition is in the hypoeutectic composition domain. By contrast, for 70.5 mol% mixture (Figure II-23-(b)), only the eutectic temperature (-37.5°C) is observable in the TR-SHG curve, which corresponds to a hypereutectic composition. Therefore, the metastable eutectic composition is comprised in the interval of 70% to 70.5%.

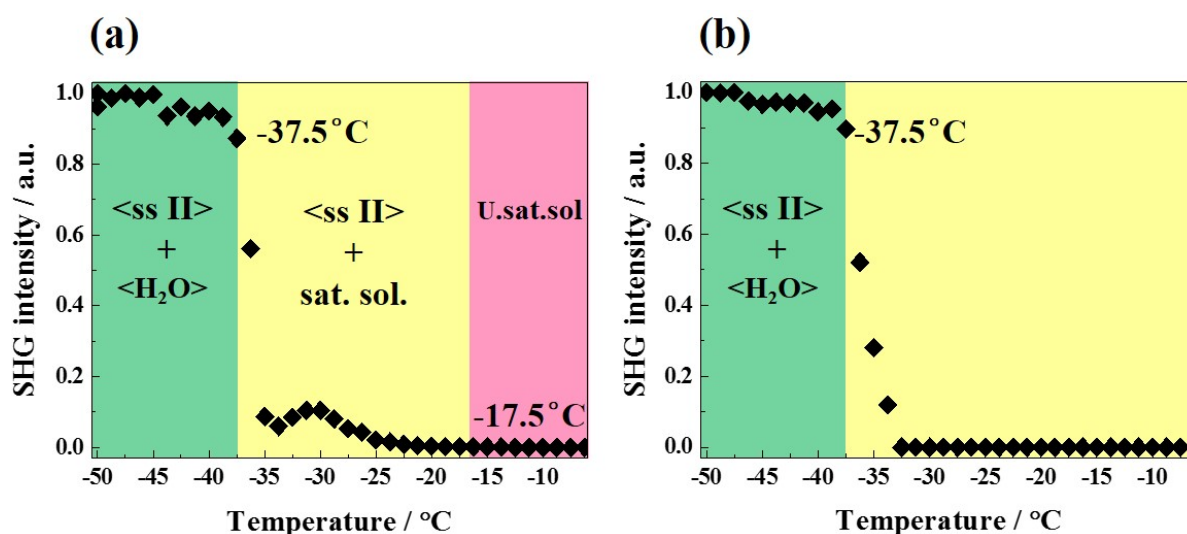


Figure II-23. TR-SHG results for the composition of (a) 70% and (b) 70.5% DMU/water mixtures.

More precise determination of the eutectic composition is difficult in this case. The above SHG measurements were performed every 15 s at a heating rate of 5 K/min, so every 1.25°C per SHG measurement. One way to precise the eutectic composition is using a slower heating rate to accurately differentiate the solidus and the liquidus. However, since the system is in the metastable state, lowering the heating rate would raise the risk of reaching the stable state. Another way is to confine the compositions to 70.1 mol%, 70.2 mol%, 70.3 mol% and 70.4

mol%. But due to the heating rate 5 K/min used, the differences between these compositions cannot be distinguished.

II-2-6-2. Method 2: Enhanced SHG Signal due to the Eutectic Microstructure

For powder SHG measurements, the SHG signal has been reported to increase linearly with the fraction of non-centrosymmetric crystals in the mixture (if the crystal size distribution is not too large). In a eutectic system, due to the impact of the eutectic microstructure, the SHG signal might not evolve linearly. The eutectic microstructure will whether enhance or reduce the SHG signal. Simon et al.³⁴ reported that powders from near-eutectic compositions can exhibit SHG signal up to 20 times higher than that of the powder containing pure non-centrosymmetric phase. This is due to the formation of a suitable eutectic microstructure that enables quasi-phase-matching (QPM, in Chapter 1). This behavior can be used for the determination of the eutectic composition as described in the following.

Figure II-24 shows a binary system composed of A and B components. A is supposed to crystallize in a non-centrosymmetric space group and B in a centrosymmetric space group. At exactly the eutectic composition (position 1), the system is composed of 100% of eutectic microstructured grains, which generate a SHG intensity referred to as I . At a hypoeutectic composition (position 2), at a temperature below the eutectic temperature, the solid sample is composed of pure A crystals and the eutectic microstructured grains. Both are responsible for the generation of SHG signal. Suppose pure A crystals generate a SHG intensity referred to as a and the eutectic microstructured grains generate a SHG intensity referred to as I_{hypo} . So, the total SHG intensity of this hypoeutectic composition is $a + I_{hypo}$. At a hypereutectic composition (position 3), the solid phase at low temperature is composed of pure B crystals and eutectic microstructured grains. Only the eutectic microstructured grains generate a SHG intensity of I_{hyper} (centrosymmetric B crystals cannot generate SHG).

Due to the formation of a suitable eutectic microstructure that enables quasi-phase-matching (QPM), the generated SHG signal is much higher than the intensity generated by the pure non-centrosymmetric material³⁴. In the case of the above mentioned hypoeutectic composition, pure A crystals bring an extra but small contribution to the overall SHG signal, i.e., $I_{hypo} \gg a$. So, the

total SHG signal generated in this hypoeutectic composition can be approximate to only I_{hypo} (summarized in Table II-4).

Table II-4. Sum-up of the phases to generate SHG signal and the corresponding SHG intensity in a binary system composed of A (non-centrosymmetric) and B (centrosymmetric).

Composition	Solid phases at -50°C	Phases generate SHG signal	I_{SHG}	Approximated I_{SHG}
Hypo-	<A>+<microstructure>	<A> +<microstructure>	$a+I_{hypo}$	I_{hypo}
Eutectic	<microstructure>	<microstructure>	I	I
Hyper-	+<microstructure>	<microstructure>	I_{hyper}	I_{hyper}

According to the lever rule, the proportion of microstructured grains increases linearly towards the eutectic composition E' (where the sample constitutes 100% of eutectic grains). Therefore, for hypoeutectic compositions, SHG signal evolves linearly with the proportion of microstructured grains. For hypereutectic compositions, the decrease in SHG signal versus composition could be understood by a decrease of the fraction of eutectic grains. Consequently, the maximum SHG intensity can be reached at the eutectic composition. The constructed graph (Figure II-24) by TR-SHG is similar to a Tammann graph, so called “**SHG Tammann graph**”.

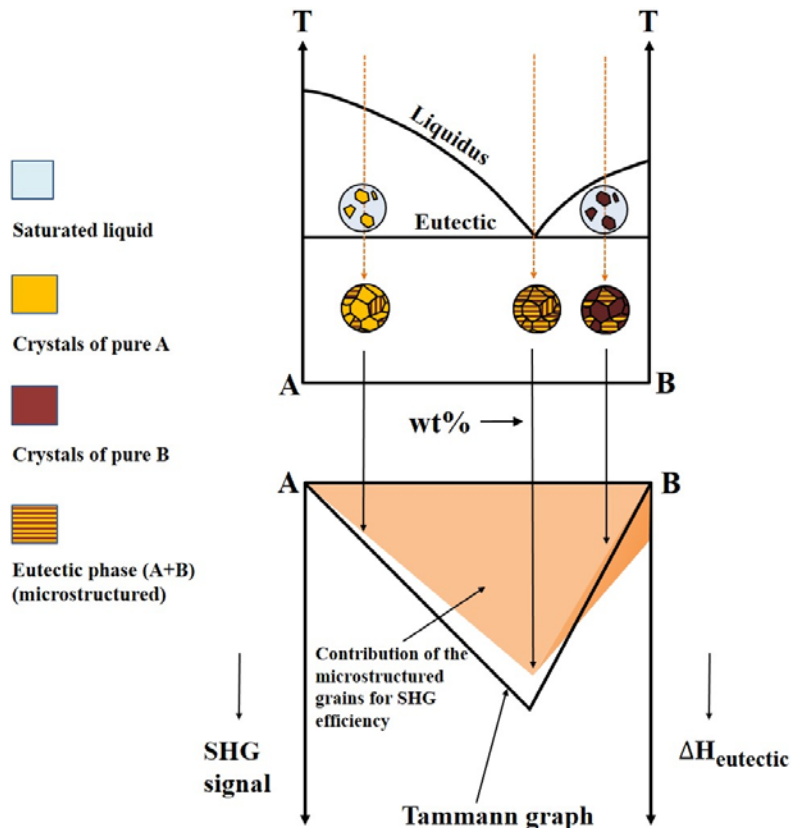


Figure II-24. Schematic rationalization of SHG signals in a eutectic phase diagram. ⟨A⟩ grains (yellow) correspond to a non-centrosymmetric material (SHG positive), and ⟨B⟩ grains (red wine) correspond to a centrosymmetric material (SHG negative).

In the following this method is applied to the DMU/water system. SHG intensity of samples of near-eutectic compositions in DMU/water system were measured by TR-SHG. 150 mg of pre-prepared mixtures at the desired composition were put in an amorphous quartz crucible with a 15 mm *15 mm cover slide on the top to have a flat surface and to maintain the same sample thickness. The sample was cooled down to -50°C at 10 K/min and kept at this temperature. SHG measurements were performed during this annealing at -50°C every minute (the procedures of measurements are summarized in (Figure II-25-(a)). The evolution of SHG intensity for a composition of 90 mol% DMU/water mixture along the annealing at -50°C is shown in Figure II-25-(b). SHG signal increases with time and around 45 min, the signal keeps stable. It means that the mixture has fully crystallized into ss II and no conversion towards the monohydrate occurs during the annealing process (otherwise, the appearance of the monohydrate would have decreased the SHG signal). The intensity generated by the crystallized 90 mol% mixture was taken as the average value of the plateau.

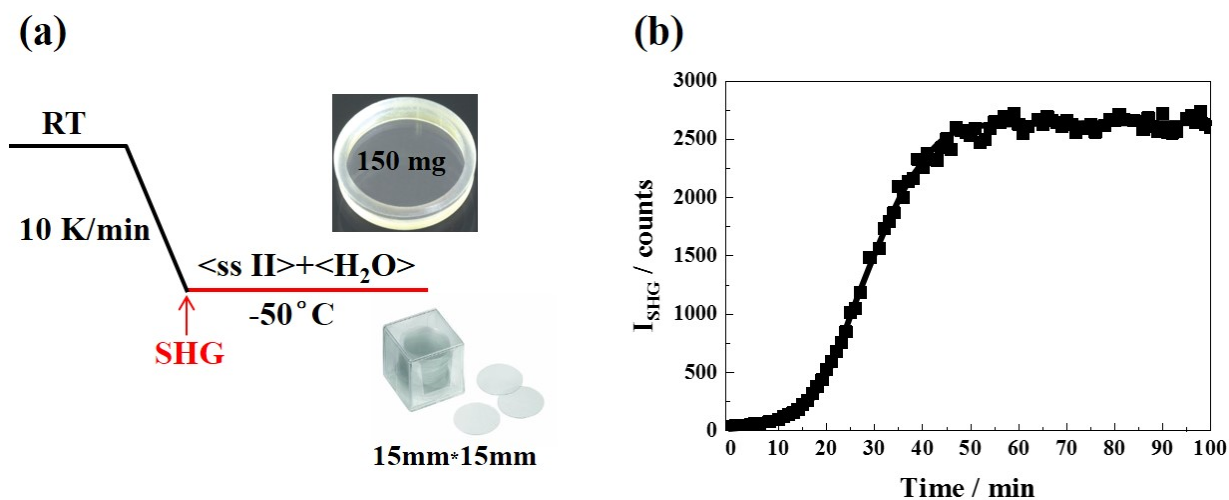


Figure II-25. (a) Conditions to measure the SHG intensity of near-eutectic compositions, (b) the evolution of SHG intensity for a composition of 90 mol% DMU/water mixture annealing at -50°C .

SHG intensity generated by samples of composition of 60 mol%, 65 mol% and 68 mol% DMU/water in the hypoeutectic domain and 75 mol%, 80 mol% and 90 mol% DMU/water in hypereutectic domain were measured the same way. Experimental values are reported on Figure II-26. The intercept of hypoeutectic compositions and hypereutectic compositions is the eutectic composition, which is $69.8\% \pm 1.0\%$.

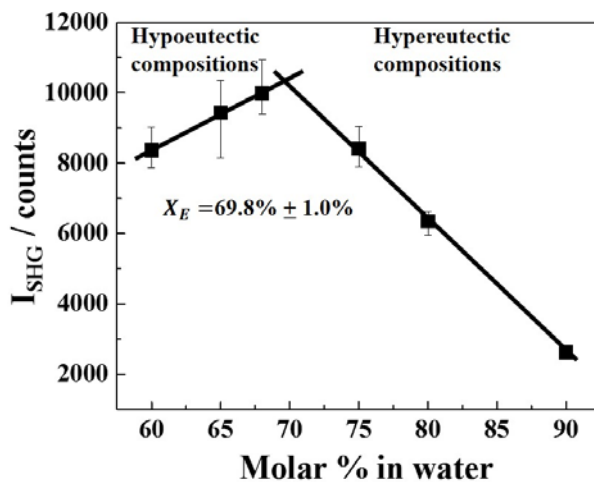


Figure II-26. The determination of eutectic composition of DMU/water system by the intercept of hypo- and hyper-eutectic compositions.

Attention should be paid that in this system, SHG Tammann graph is applicable only in the near-eutectic compositions. Compositions with high DMU concentrations (far from the eutectic composition), the portion of eutectic microstructures is low. Both the ss II crystals and the microstructures are responsible for the SHG intensity. The impact of the enhanced SHG intensity by eutectic microstructures will be small compared to the SHG intensity generated by the ss II crystals.

Thus, for these compositions (high and low DMU concentration), the evolution of the SHG intensity versus composition is no more related to the eutectic character of the system and cannot be used for the determination of the eutectic composition.

II-2-7. Discussions

II-2-7-1. Discussions about the Methods to Precise the Metastable Eutectic Composition

The above two methods to determine the metastable eutectic composition of DMU/water system are in agreements. A composition between 70% and 70.5% was obtained by using method 1, while $69.8\% \pm 1.0\%$ was obtained by method 2. The accuracy of method 1 was discussed in the previous urea/water system in II-1. Here we only focus on the discussion of method 2. In Figure II-26, it is shown that the deviation of the SHG intensity is high, especially in the hypoeutectic compositions. This induces a deviation of 1.0% for eutectic composition. We assume that the crystal size distribution and morphology of each type of grain (<A>, and <eutectic microstructure>) are equivalent, the overall SHG signal is the sum of the

contributions of each type of grain. This might be oversimplified. Indeed, eutectic solidification is strongly governed by kinetic parameters³⁴. However, this method can remain of interest as it provides another way to determine the metastable eutectic composition that without any risk of conversion of ss II towards the stable DMU·H₂O.

II-2-7-2. Discussions about the TR-SHG Curve in the Hypoeutectic Compositions

It can be noticed that in the SHG curves obtained for hypoeutectic compositions, the evolution of SHG signal between the solidus and liquidus temperature is not monotone as observed for the system of urea/water. Indeed, a slight increase is observed before the signal begins again to decrease toward the null value corresponding to the liquidus temperature (as shown in Figure II-27).

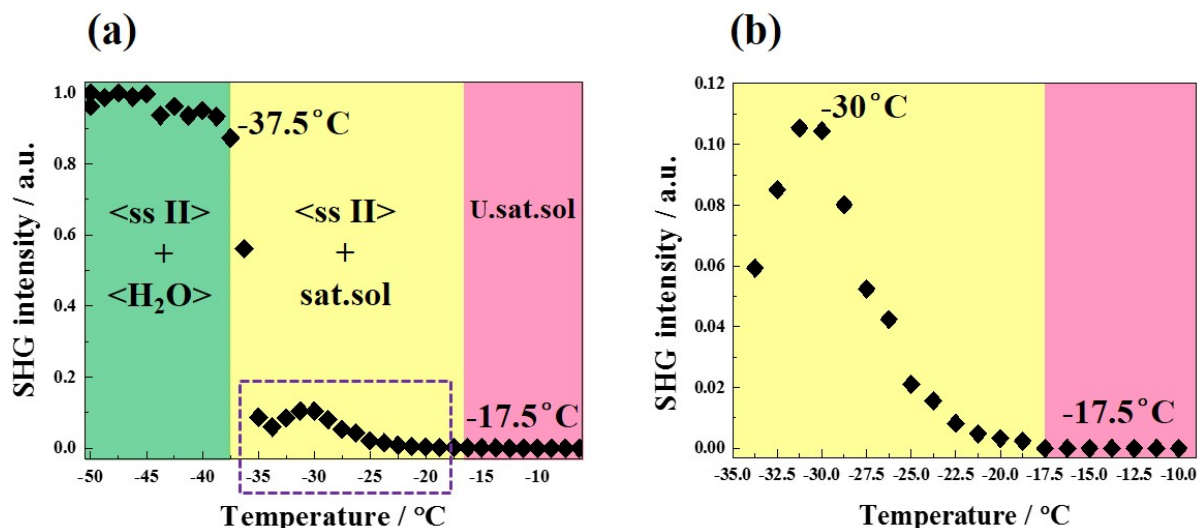


Figure II-27. (a) TR-SHG curve for the composition of 70% DMU/water mixture, (b) a zoom of the peak between solidus and liquidus (purple rectangle).

To understand this behavior, microscopy observations were performed in the temperature range of -35°C to -17.5°C and the size distribution of the crystals at -30°C and -19°C were compared (Figure II-28). The average crystal size at -30°C is 5.19 μm , while the average crystal size at -19°C is 7.86 μm . It is obvious that during heating, the number of crystals decreases while the size of the crystals increases due to the Ostwald ripening phenomenon. Small crystals dissolve and deposit on bigger crystals. Crystals at temperatures below -30°C cannot be clearly observed and measured. But it can be deduced that below -30°C, the number of crystals is higher while the size is smaller compared to crystals at -30°C and -19°C.

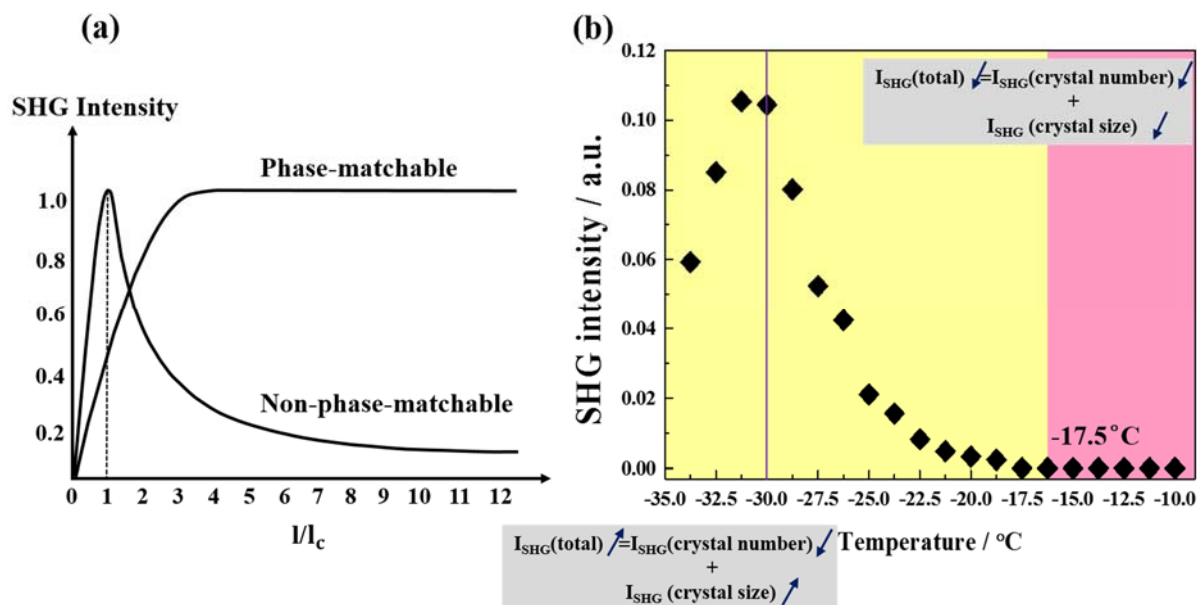


Figure II-29. (a) Evolution of the SHG intensity with the size of the crystals for phase-matchable and non-phase-matchable materials. (b) Interpretation of the changes of SHG intensity. From -35°C to -30°C , the increase of I_{SHG} is due to the growing of the crystal size ($l < l_c$); from -30°C to -17.5°C , the decrease of I_{SHG} is due to the decrease of the number of crystals and the increase of the crystal size ($l > l_c$).

II-2-7-3. Discussions about the Liquidus in the SS II/Water Metastable Eutectic Phase Diagram

The accuracy of the determination of the liquidus is questionable because a metastable state is involved in this case. Microscopy observations (Figure II-18) show that the monohydrate appears at the end of the melting process at the expense of the remaining ss II crystals, which means that the metastable equilibrium and the stable equilibrium co-exist. Since the SHG signal is generated only by ss II, the decrease of the SHG signal is not only due to the melting of ss II crystals, but also due to the transformation to the centrosymmetric monohydrate (no SHG signal generated). However, the appearance of the monohydrate has only been observed at the end of the melting process, only a small deviation of the value of the metastable liquidus temperature measured by TR-SHG is expected.

This can be confirmed by the comparison of liquidus obtained from refractometry. As is shown in Figure II-30, the metastable liquidus obtained from TR-SHG (red spots) are lower than the values from refractometry (black spots), which could be due to the conversion of the ss II to $\text{DMU}\cdot\text{H}_2\text{O}$ at the end of the melting process.

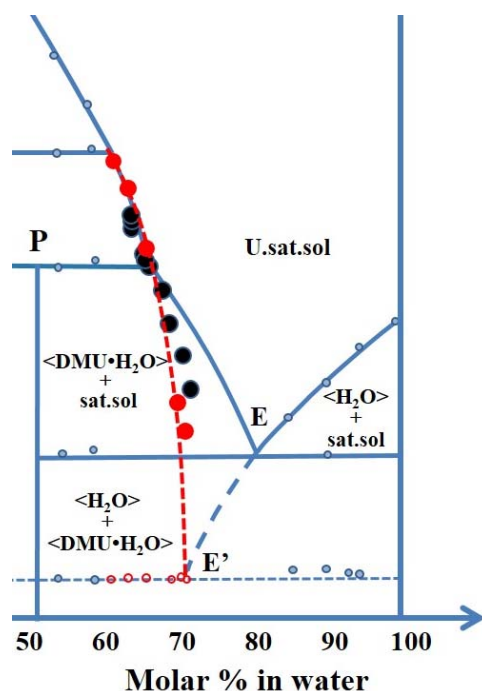


Figure II-30. A comparison of metastable liquidus obtained from TR-SHG (red spots) and from refractometry (black spots).

II-2-8. Conclusion

The metastable phase diagram of DMU/water was constructed by TR-SHG and the metastable eutectic composition was determined (70%-70.5%). By extrapolation, the stable eutectic equilibrium was completed. Consequently, the entire phase diagram of DMU/water has been completed. In total 5 invariants exist in this phase diagram, summarized in Table II-5.

Table II-5. Characteristics of the different invariants in the phase diagram of DMU/water.

$T_{\text{invariant}}/^{\circ}\text{C}$	Equilibrium	Technique	Equilibrium
25	Stable metatectic	<i>In-situ</i> X-ray	<ss II> + saturated solution \leftrightarrow <ss I> (<<1%)
8	Stable peritectic	DSC	<DMU·H ₂ O> \leftrightarrow <ss II> + saturated solution (\approx 65%)
-20	Stable eutectic	DSC	<DMU·H ₂ O> + <water> \leftrightarrow saturated solution (\approx 80%)
-37	Metastable eutectic	TR-SHG/ Refractometry	<ss II> + <water> \leftrightarrow saturated solution (between 70% and 70.5%)

In this case, by microscopy observations, we confirmed that no recalescence appeared, because the crystallization of DMU·H₂O is rather slow. But for the general application of this method, attention should be paid to the possible recalescence phenomenon involved in a peritectic transition with metastable or stable equilibria. For instance, sodium sulfate decahydrate, also known as Glauber's salt, has three important features: (i) a high subcooling ($>15^{\circ}\text{C}$) of its

anhydrous form when no nucleating agent is added, (ii) incongruent melting, and (iii) the presence of a metastable heptahydrate. The phase diagram between anhydrous sodium sulfate and water is shown in Figure II-31. When a mixture of anhydrous sodium sulfate and its saturated solution is put at a temperature lower than 32.4°C (peritectic temperature), one can see a sudden increase of the temperature measured by a thermocouple immersed in the sample. The appearance of this phenomenon — recalescence: a spontaneous return to 32.4°C due to a fast crystallization of the dehydrate — prevents a real isothermal return to the equilibrium.

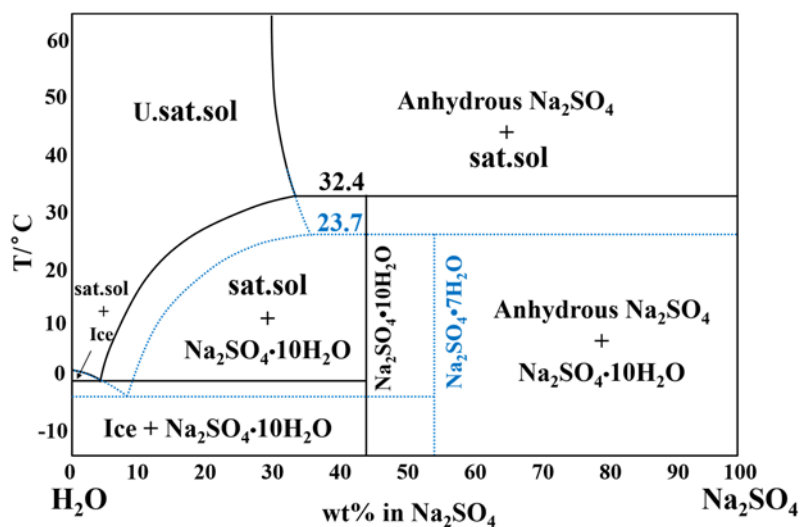


Figure II-31. Phase diagram between sodium sulfate (Na_2SO_4) and water, in which exist a stable equilibrium involving sodium sulfate decahydrate ($\text{Na}_2\text{SO}_4 \cdot 10\text{H}_2\text{O}$) and a metastable equilibrium involving sodium sulfate heptahydrate ($\text{Na}_2\text{SO}_4 \cdot 7\text{H}_2\text{O}$).

II-3. Investigations of Hexamethylenetetramine (HMT)/Water System by TR-SHG

II-3-1. Introduction

Hexamethylenetetramine (HMT, $(\text{CH}_2)_6\text{N}_4$, Figure II-32) has a cage-like structure, which is similar to the structure of adamantane. It is used for the growth of ZnO nanorods and in cyclotrimethylenetrinitramine (RDX) production³⁵⁻³⁸. HMT is one of the exceptional compounds that exhibits nonlinear optical properties³⁹ and crystallizes in the cubic system ($I\bar{4}3m$). Kurtz and Perry¹⁸ classified it as a non-phase-matchable material and its nonlinear coefficients are greater than crystalline quartz.

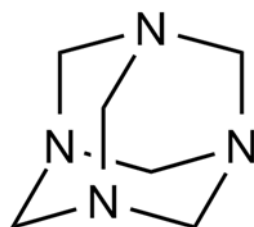


Figure II-32. Molecular structure of hexamethylenetetramine (HMT).

HMT is highly soluble in water and its solubility decreases with increasing temperature⁴⁰ (retrograde solubility). A hexahydrate $(\text{CH}_2)_6\text{N}_4 \cdot 6\text{H}_2\text{O}$ was highlighted and the crystal structure was solved in the $R3m$ space group (Table II-6).

Table II-6. Crystallographic data of HMT and HMT hexahydrate.

Form	HMT	HMT hexahydrate
Temperature (K)	283-303	253
Crystal system	Cubic	Trigonal
Space group	$I\bar{4}3m$	$R3m$
a (Å)	7.028 (2)	11.620
b (Å)	7.028 (2)	11.620
c (Å)	7.028 (2)	8.670
α (°)	90	90
β (°)	90	90
γ (°)	90	90
Z	2	3
Z'	0.04	0.17
Volume (Å ³)	347.132	1013.82
Density (g/cm ³)	1.341	1.22

The dissolution temperature of this hydrate is controversial. Some reported this temperature to be 13.5°C or 15.0°C. Aladko et al.⁴¹ reported two temperatures: 12.9°C and 14.1°C. They mentioned that the most probable explanation of the two observed temperatures was a change in the solubility evolution with temperature. This change may be caused by temperature-induced drastic changes of hydration of HMT molecules in liquid phase.⁴¹ The phase diagram between HMT and water was also proposed (shown in Figure II-33).

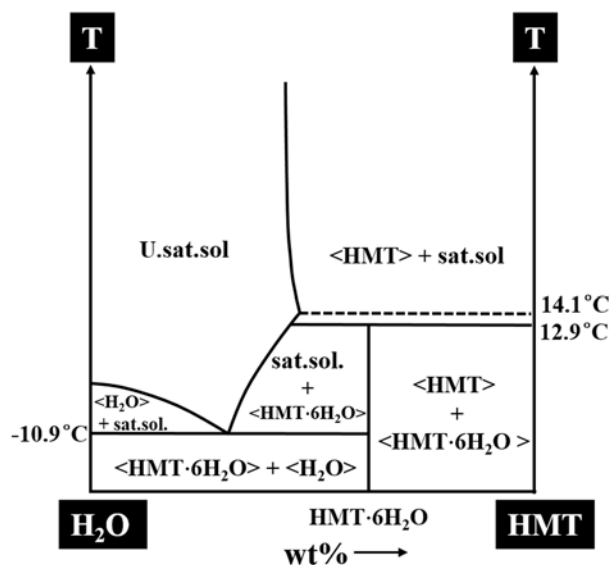


Figure II-33. Phase diagram of the binary HMT/water system proposed by Aladko et al.⁴¹.

The above phase diagram obviously shows that there is a phase transition in HMT at 14.1°C. However, HMT is well known to have only one phase at ambient pressure. Therefore, the above proposed phase diagram might be wrong. A further reinvestigation of HMT/water phase diagram is highly necessary.

In this phase diagram, (i) HMT is a non-phase-matchable material, the behavior between HMT and water might be different from urea/water system, in which urea is phase-matchable. (ii) The phenomena correspond to the two temperatures (12.9°C and 14.1°C) might be differentiated by TR-SHG. Moreover, HMT has a high nonlinear conversion efficiency, it is suitable for TR-SHG measurements.

II-3-2. Study of the Eutectic Phase Diagram in HMT/Water System by TR-SHG

In part II-1 and II-2, stable eutectic phase diagram of urea/water system and metastable eutectic phase diagram of DMU/water system have already been fully investigated. In this system, we

mainly focus on the impact of non-phase-matchable materials on the SHG signal.

II-3-2-1. Measurements of Hypoeutectic Compositions between $\text{HMT}\cdot 6\text{H}_2\text{O}$ and Water by TR-SHG

TR-SHG results for a HMT/water mixture of composition of 30% (mass fraction in HMT) is shown in Figure II-34 (heating rate 1K/min).

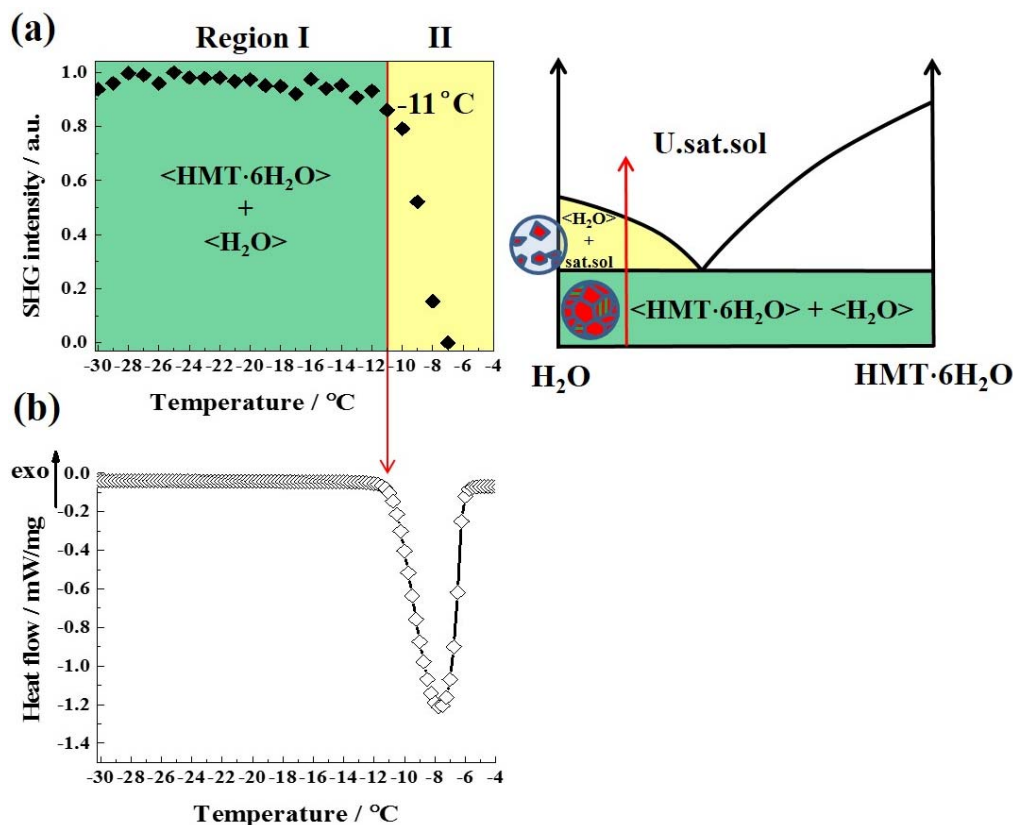


Figure II-34. Comparison between (a) TR-SHG and (b) DSC analysis for the composition of 30 wt% HMT/water mixture (1 K/min heating rate).

In region I, a high SHG signal is detected and a plateau is observed from -30°C to -10°C . This hypoeutectic mixture is rich in water, so ice and microstructured crystals (between $\text{HMT}\cdot 6\text{H}_2\text{O}$ and ice) coexist below the eutectic temperature. Only the microstructured crystals are responsible for the SHG signal (as we speculated). In region II, a decrease of the SHG signal occurs at -11°C , which corresponds to the eutectic temperature. The signal decreases in the temperature range of -11°C to -7°C , which might be due to the thermal inhomogeneous in the sample. No SHG signal is generated by either ice or liquid, so the liquidus temperature cannot be observed for this composition. The eutectic temperature was confirmed by DSC, but the liquidus temperature cannot be obtained by either TR-SHG or DSC.

II-3-2-2. Measurements of Hypereutectic Compositions between $\text{HMT}\cdot 6\text{H}_2\text{O}$ and Water by TR-SHG

Figure II-35 shows the TR-SHG result obtained for 46 wt% HMT/water mixture (mass fraction in HMT).

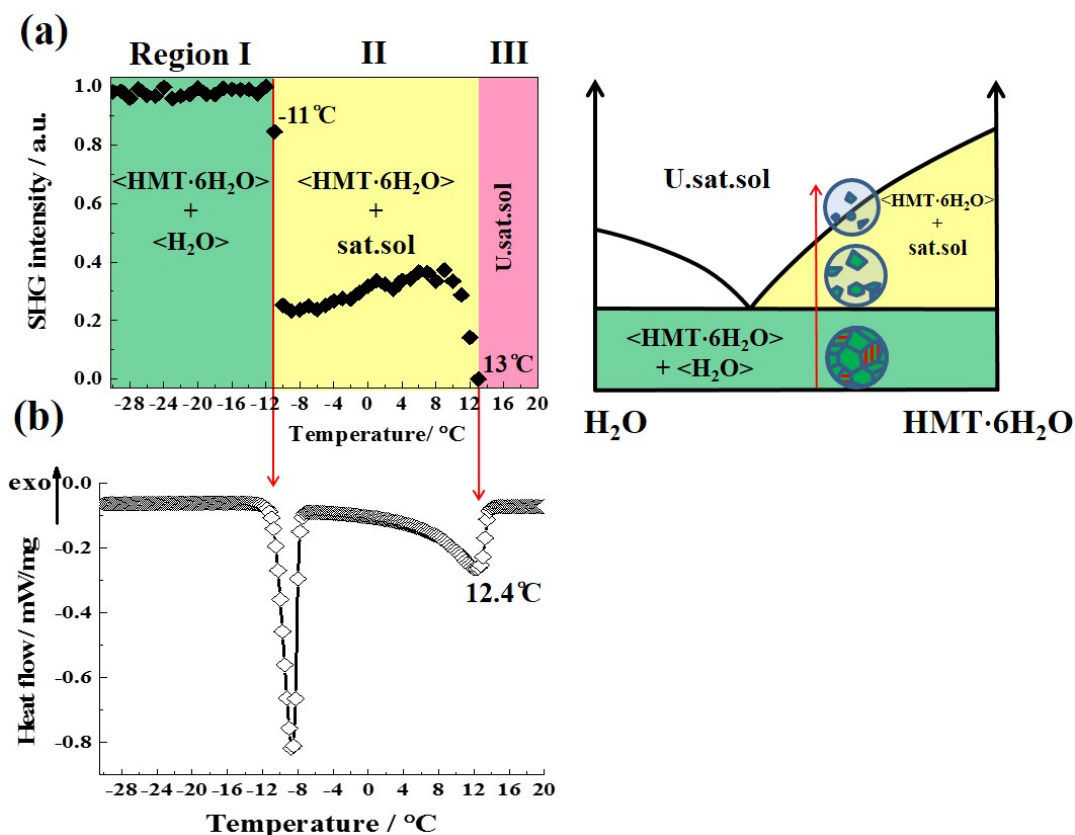


Figure II-35. Comparison between (a) TR-SHG and (b) DSC analysis for the composition of 46 wt% HMT/water mixture (1 K/min heating rate).

In region I, between -30°C and -10°C , SHG signal remains relatively stable. $\text{HMT}\cdot 6\text{H}_2\text{O}$ crystals and microstructured crystals (between $\text{HMT}\cdot 6\text{H}_2\text{O}$ crystals and ice) coexist. They are both responsible for the observed SHG signal. In region II, at -11°C , SHG intensity begins to decrease, which corresponds to the decrease of the crystalline non-centrosymmetric fraction in the system, i.e., the beginning of the melting of micro-structured crystals. Therefore, -11°C corresponds to the eutectic temperature (T_E). From -11°C to 13°C , the SHG signal slightly increases and then decreases again to totally vanish at 13°C , which corresponds to the liquidus temperature. This phenomenon is similar to the behavior observed in the DMU/water system, in which ss II crystals are supposed to be non-phase-matchable. As it is well known that HMT

is a non-phase-matchable material¹⁸, it is highly possible that $\text{HMT}\cdot 6\text{H}_2\text{O}$ is also a non-phase-matchable material. Therefore, we might make the conclusion that for non-phase-matchable materials, due to the Ostwald ripening effect in the melting process, the SHG signal does not decrease directly with temperature but will exhibit an increase followed by a decrease. In region III, only liquid phase exists, no SHG signal is observed. The eutectic temperature and the liquidus temperature determined by TR-SHG are in accordance with the temperature obtained from DSC.

II-3-2-3. Plot of the Eutectic Phase Diagram between $\text{HMT}\cdot 6\text{H}_2\text{O}$ and Water by TR-SHG

The eutectic composition was refined with the method described in part II-1 for urea/water system and II-2 for DMU/water system. The value was determined to be 30.2 wt% - 30.3 wt%. Noted that the samples were prepared with a maximum deviation of 0.05 wt%. Phase diagram between $\text{HMT}\cdot 6\text{H}_2\text{O}$ and water was constructed by measuring several different compositions by TR-SHG and was compared with DSC and literature data²⁶.

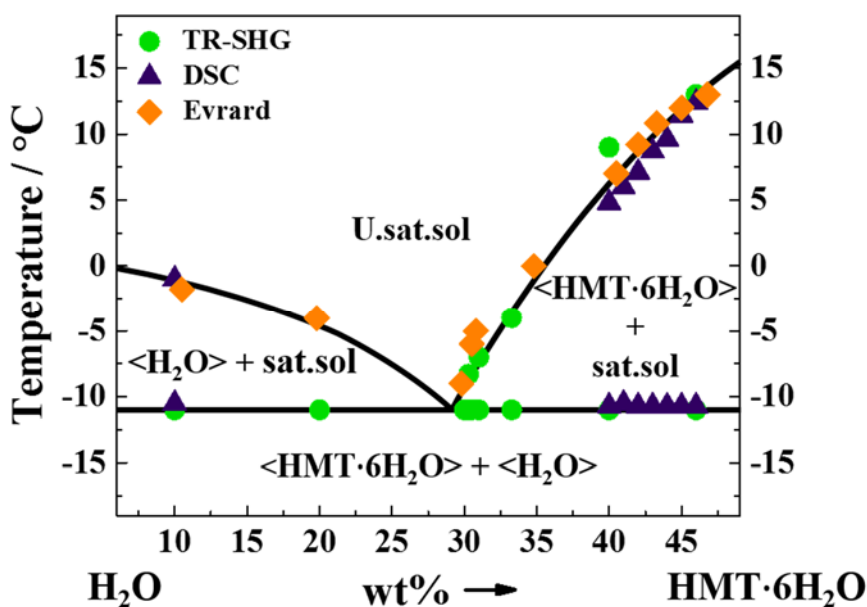


Figure II-36. Binary eutectic phase diagram between $\text{HMT}\cdot 6\text{H}_2\text{O}$ and water.

As can be seen in Figure II-36, the data obtained from TR-SHG (red dots), DSC (blue triangles) and literature (green diamonds) are consistent. In the vicinity of the eutectic composition, DSC cannot provide the liquidus data due to a merge of the peaks (Figure II-37), in contrary, TR-SHG facilitates the determination (in hypereutectic compositions). These two methods can be combined and thus will enlarge the application of both TR-SHG and DSC.

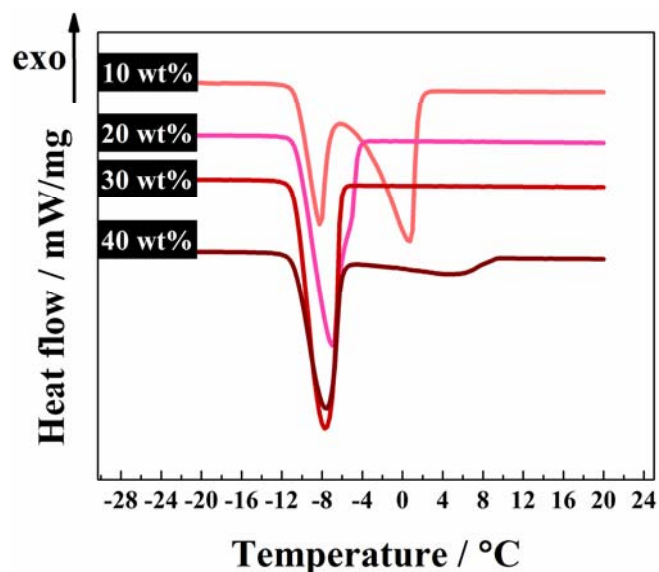


Figure II-37. DSC curves show the merging of eutectic peaks and liquidus peaks for the composition of 20 wt% to 40 wt% HMT/water mixture.

II-3-3. Study of the Peritectic Equilibrium in HMT/Water System by TR-SHG

Figure II-38-(a) shows the TR-SHG result obtained for the composition of 50 wt% HMT/water mixture (mass fraction in HMT).

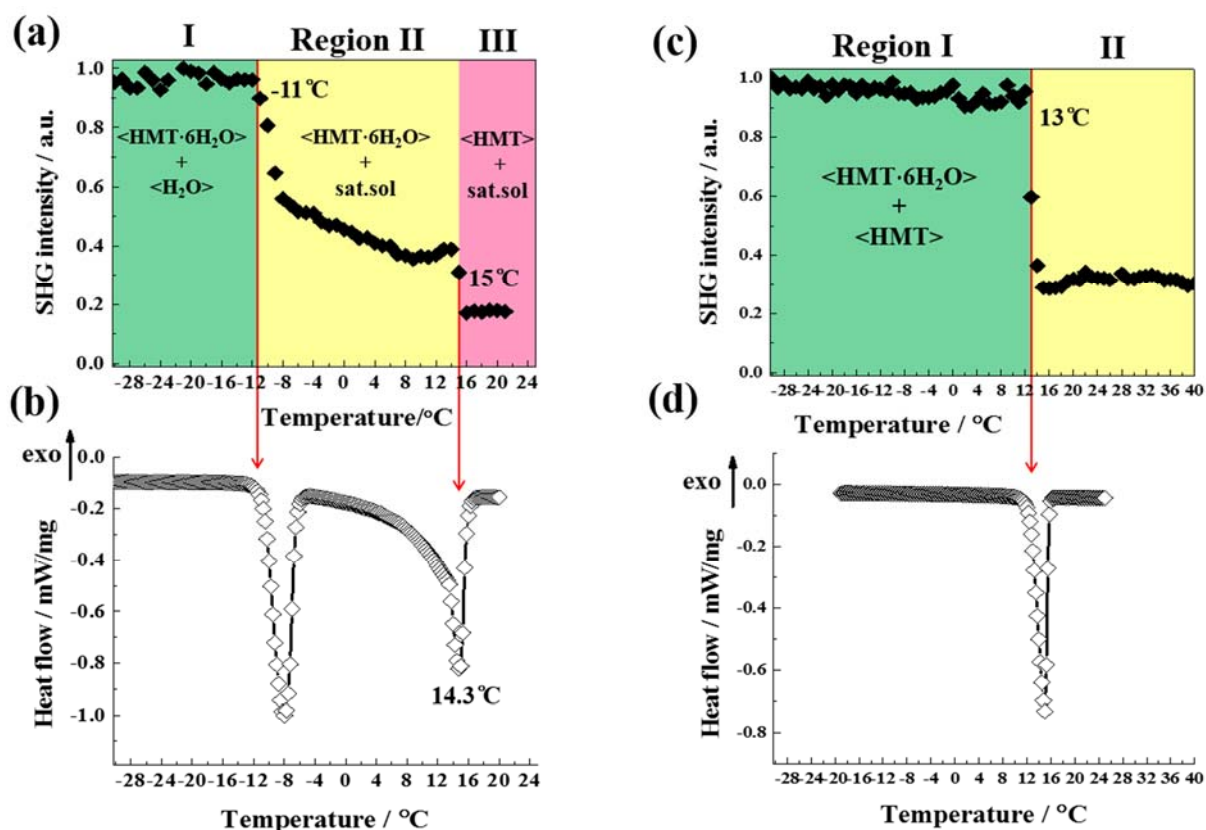


Figure II-38. Comparison between TR-SHG and DSC analysis for the composition of (a)(b) 50 wt% HMT/water mixture (1 K/min heating rate), and (c)(d) 80 wt% HMT/water mixture (1 K/min heating rate).

In region I, between -30°C and -10°C , SHG signal remains relatively stable. $\text{HMT}\cdot 6\text{H}_2\text{O}$ crystals and microstructured crystals (between $\text{HMT}\cdot 6\text{H}_2\text{O}$ crystals and ice) coexist and are both responsible for the observed SHG signal. In region II, SHG intensity begins to decrease at the eutectic temperature -11°C . From -11°C to 14°C , SHG signal decreases progressively due to the gradual dissolution of the $\text{HMT}\cdot 6\text{H}_2\text{O}$ crystals. In region III, at 15°C , the signal decreases drastically, which corresponds to the peritectic temperature. Since the retrograde solubility line is nearly straight (Figure II-33), the amount of HMT crystals remains the same for higher temperature, then the signal keeps stable.

The eutectic temperature determined by TR-SHG is in accordance with the temperature obtained from DSC (Figure II-38-(b)). However, for the peritectic temperature, DSC exhibits two merged peaks. The onset temperature is difficult to determine while the peak temperature is around 14.3°C , which is close to the peritectic temperature (15°C) determined by TR-SHG.

A different SHG behavior was observed for compositions in high HMT concentrations. Figure II-38-(c) shows the TR-SHG result obtained for the 80 wt% HMT/water mixture (mass fraction in HMT). In region I, between -30°C and 12°C , SHG signal remains relatively stable. HMT and $\text{HMT}\cdot 6\text{H}_2\text{O}$ are both responsible for the observed SHG signal. In region II, at 13°C , the signal decreases drastically, which corresponds to the peritectic temperature. Then the signal keeps stable. The peritectic temperature determined by TR-SHG is in accordance with the onset temperature obtained from DSC (Figure II-38-(d)). Moreover, no merged peaks were observed.

II-3-4. Discussions

We noticed that the impact of non-phase-matchability of the material is mainly visible in domains where a liquid phase is present. Due to the Ostwald ripening, size of the non-phase-matchable crystals changes, which influences the intensity of the SHG signal. It is evident that Ostwald ripening occurs easily with the assistance of liquid and therefore, influences the intensity of the SHG signal.

The two temperatures reported by Aladko et al.⁴¹ cannot be differentiated by TR-SHG. The 1.2°C difference is too small. This could be due to the temperature gradients: inside the sample

and between the sample and the heating plate. Besides, the non-phase-matchable property of HMT might influence the SHG behavior. As in Figure II-35-(a), around the peritectic temperature (15°C), the signal increased and then drastically decreased. This enhances the difficulty to determine which temperature exactly corresponds to the peritectic temperature.

In a certain temperature range, we observed by DSC the merge of two peaks close to the peritectic region (Figure II-39-(a)).

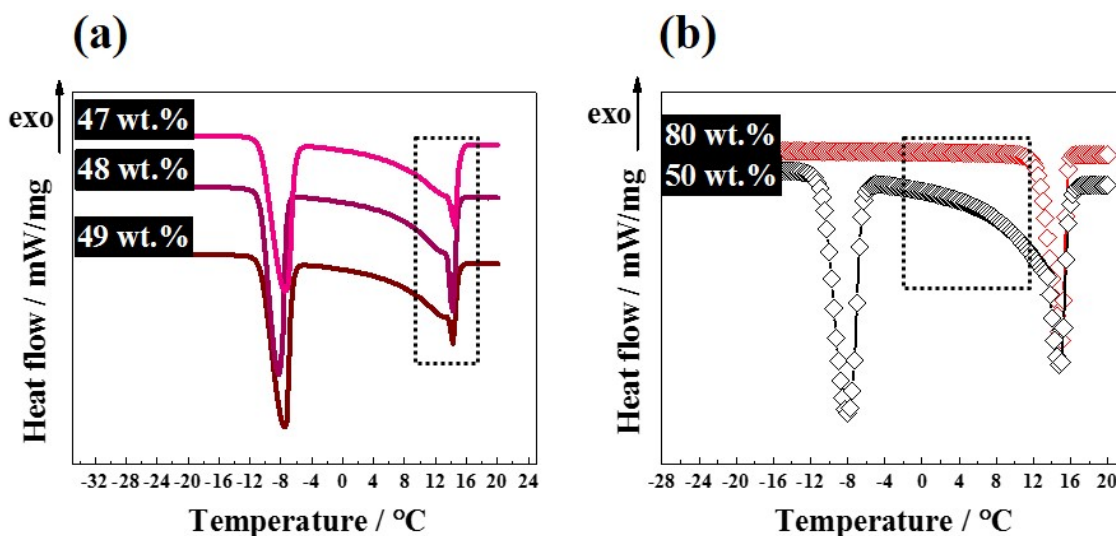


Figure II-39. (a) Observations of two merged peaks in the compositions of 47 wt%, 48 wt% and 49 wt% HMT/water mixtures. (b) Comparison of the DSC curves between 50 wt% and 80 wt% HMT/water mixtures.

Aladko et al.⁴¹ also reported that in many experiments a shoulder at around 14°C was observed for the compositions close to HMTA hexahydrate. Figure II-39-(b) shows the DSC curves obtained for compositions of 50 wt% and 80 wt%. Compared to the 50 wt%, the curve of 80 wt% clearly shows an extra endothermic contribution from -6°C to 10°C . This could be explained by the presence of a new hydrate. This hydrate could experience a peritectic reaction in this temperature range and generate a new endothermic peak merged to the peak corresponding to the dehydration of $\text{HMT}\cdot 6\text{H}_2\text{O}$.

Thus, another hydrate at a composition close to the hexahydrate might be envisaged. The possible phase diagram is shown in Figure II-40. TR-XRD was used to check the possible existence of this “new hydrate”, but no new phase was observed yet.

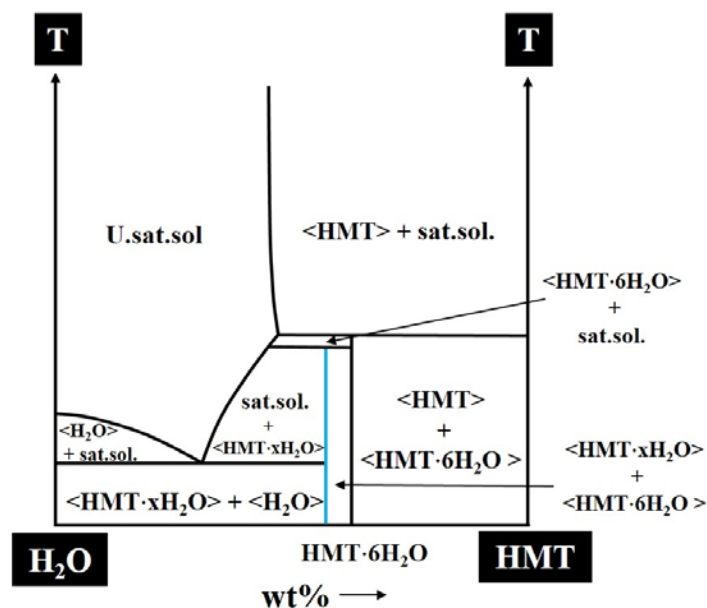


Figure II-40. The possible phase diagram between HMT and water.

II-3-5. Conclusion and Perspectives

The phase diagram between HMT and water was studied by TR-SHG and confirmed by DSC.

- Non-phase-matchable material could exhibit a different TR-SHG behavior in a eutectic phase diagram (or a phase diagram) than the phase-matchable material. Due to the Ostwald ripening, the changes of the crystal size will impact the evolution of the SHG intensity.
- The eutectic composition (between 30.2 wt% and 30.3 wt%) was accurately determined by TR-SHG, which cannot be obtained by DSC due to the merge of eutectic peaks and liquidus peaks in compositions that are close to the eutectic composition.
- A new hydrate might exist close to the hexahydrate and its peritectic temperature is also close to the temperature of hexahydrate. This can be used to explain the merged peaks observed in the DSC experiments and the two temperatures reported by Aladko et al.⁴¹ To further confirm the existence of this hydrate, *in-situ* X-ray analyses ($-\theta/-\theta$) could be helpful.

References

- (1) Ricci, J. E. *The Phase Rule and Heterogeneous Equilibrium*; Dover publications: New York University, **1951**.
- (2) Ashby, M. *Teach Yourself Phase Diagrams and Phase Transformations (Fifth Edition)*; Cambridge, **2009**.
- (3) Hillert, M. *Phase Equilibria, Phase Diagrams and Phase Transformations: Their Thermodynamic Basis (Second Edition)*; Cambridge University Press: New York, **2008**.
- (4) Zemansky, M. W.; Dittman, R. *Heat and Thermodynamics: An Intermediate Textbook*; McGraw-Hill, **1997**.
- (5) Mortimer, R. G. *Physical Chemistry*; Academic Press, **2008**.
- (6) Smith, E. L.; Abbott, A. P.; Ryder, K. S. Deep Eutectic Solvents (DESs) and Their Applications. *Chem. Rev.* **2014**, *114* (21), 11060–11082.
- (7) Abbott, A. P.; Capper, G.; Davies, D. L.; Rasheed, R. K.; Tambyrajah, V. Novel Solvent Properties of Choline Chloride/Urea Mixtures. *Chem. Commun.* **2003**, *1*, 70–71.
- (8) Gala, U.; Pham, H.; Chauhan, H. Pharmaceutical Applications of Eutectic Mixtures. *J. Dev. Drugs* **2013**.
- (9) Rycerz, L. Practical Remarks Concerning Phase Diagrams Determination on the Basis of Differential Scanning Calorimetry Measurements. *J. Therm. Anal. Calorim.* **2013**, *113* (1), 231–238.
- (10) Boettinger, W. J.; Kattner, U. R.; Moon, K.-W.; Perepezko, J. H. *DTA and Heat-Flux DSC Measurements of Alloy Melting and Freezing*. In *Methods for Phase Diagram Determination*; Elsevier BV: Great Britain, **2007**; p 151.
- (11) Ingier-Stocka, E.; Rycerz, L.; Gadzuric, S.; Gaune-Escard, M. Thermal and Conductometric Studies of the CeBr₃-MBr Binary Systems (M = Li, Na). *J. Alloys Compd.* **2008**, *450*.
- (12) Guenet, J.-M. Contributions of Phase Diagrams to the Understanding of Organized Polymer-Solvent Systems. *Thermochim. Acta* **1996**, *284* (1), 67–83.
- (13) Findlay, A. *The Phase Rule and Its Applications*; Green & Co., **1918**.
- (14) Rycerz, L.; Gaune-Escard, M. Phase Diagram of the TbBr₃-RbBr Binary System: Thermodynamic and Transport Properties of the Rb₃TbBr₆ Compound. *Inorg. Chem.* **2007**, *46* (6), 2299–2306.
- (15) Egal, M. Structure and Properties of Cellulose/NaOH Aqueous Solutions, Gels and Regenerated Objects. Ph.D thesis, l'Ecole des Mines de Paris: Paris, **2006**.
- (16) Koebel, M.; Elsener, M.; Kleemann, M. Urea-SCR: A Promising Technique to Reduce NO_x emissions from Automotive Diesel Engines. *Catal. Today* **2000**, *59*, 335–345.
- (17) Choi, B.-C.; Kim, Y. K.; Jung, W.-N.; Lee, C.-H.; Hwang, C.-Y. Experimental Investigation on Melting Characteristics of Frozen Urea–water-Solutions for a Diesel SCR de-NO_x-System. *Appl. Therm. Eng.* **2013**, *50* (1), 1235–1245.
- (18) Kurtz, S. K.; Perry, T. T. A Powder Technique for the Evaluation of Nonlinear Optical Materials. *J. Appl. Phys.* **1968**, *39* (8), 3798–3813.
- (19) Dougherty, J. P.; Kurtz, S. K. A Second Harmonic Analyzer for the Detection of Non-Centrosymmetry. *J. Appl. Cryst.* **1976**, *9*, 145–158.
- (20) Smilowitz, L.; Henson, B. F.; Asay, B. W.; Dickson, P. M. The B- δ Phase Transition in the Energetic Nitramine-Octahydro-1,3,5,7-Tetranitro-1,3,5,7-Tetrazocine: Kinetics. *J. Chem. Phys.* **2002**, *117* (8), 3789–3798.

- (21) Lobban, C.; Finney, J. L.; Kuhs, W. F. The Structure of a New Phase of Ice. *Nature* **1998**, *391*, 268–270.
- (22) Bridgman, P. W. The Pressure–Volume–Temperature Relations of the Liquid, and the Phase Diagram of Heavy Water. *J. Chem. Phys.* **1935**, *3* (10), 597–605.
- (23) Birkedal, H.; Madsen, D.; Mathiesen, R. H.; Knudsen, K.; Weber, H.-P.; Pattison, P.; Schwarzenbach, D. The Charge Density of Urea from Synchrotron Diffraction Data. *Acta Crystallogr. A* **2004**, *60* (5), 371–381.
- (24) Luo, S. J.; Yang, J. T.; Du, W. F.; Laref, A. Mechanism of Linear and Nonlinear Optical Properties of the Urea Crystal Family. *J. Phys. Chem. A* **2011**, *115* (20), 5192–5200.
- (25) Betzler, K.; Hesse, H.; Loose, P. Optical Second Harmonic Generation in Organic Crystals: Urea and Ammonium-Malate. *J. Mol. Struct.* **1978**, *47*, 393–396.
- (26) Timmermans, J. *The Physico-Chemical Constants of Binary Systems in Concentrated Solutions: Systems with Inorganic + Organic or Inorganic Compounds (Excepting Metallic Derivatives)*; Interscience Publishers, **1960**.
- (27) Babkina, T. S.; Kuznetsov, A. V. Phase Equilibria in Binary Subsystems of Urea–Biuret–Water System. *J. Therm. Anal. Calorim.* **2010**, *101* (1), 33–40.
- (28) Durickovic, I.; Thiébaud, L.; Bourson, P.; Kauffmann, T.; Marchetti, M. Spectroscopic Characterization of Urea Aqueous Solutions: Experimental Phase Diagram of the Urea-Water Binary System. *Appl. Spectrosc.* **2013**, *67* (10), 1205–1209.
- (29) Baaklini, G.; Dupray, V.; Coquerel, G. Inhibition of the Spontaneous Polymorphic Transition of Pyrazinamide γ Form at Room Temperature by Co-Spray Drying with 1,3-Dimethylurea. *Int. J. Pharm.* **2015**, *479* (1), 163–170.
- (30) Näther, C.; Döring, C.; Jess, I.; Jones, P. G.; Taouss, C. Thermodynamic and Structural Relationships between the Two Polymorphs of 1,3-Dimethylurea. *Acta Crystallogr. B* **2013**, *69* (Pt 1), 70–76.
- (31) Marsh, R. E. Space Group Cc: An Update. *Acta Crystallogr. B* **2004**, *60* (2), 252–253.
- (32) Martins, D. M. S.; Spanswick, C. K.; Middlemiss, D. S.; Abbas, N.; Pulham, C. R.; Morrison, C. A. A New Polymorph of N, N'-Dimethylurea Characterized by X-Ray Diffraction and First-Principles Lattice Dynamics Calculations. *J. Phys. Chem. A* **2009**, *113* (20), 5998–6003.
- (33) Baaklini, G. The Effects of Spray Drying on the Polymorphism of Pharmaceutical and Organic Compounds. Ph. D thesis, Univeristy of Rouen: France, **2015**.
- (34) Simon, F.; Clevers, S.; Gbabode, G.; Couvrat, N.; Agasse-Peulon, V.; Sanselme, M.; Dupray, V.; Coquerel, G. Enhanced Second Harmonic Generation from an Organic Self-Assembled Eutectic Binary Mixture: A Case Study with 3-Nitrobenzoic and 3,5-Dinitrobenzoic Acids. *Cryst. Growth Des.* **2015**, *15* (2), 946–960.
- (35) Yi, W.-B.; Cai, C. Synthesis of RDX by Nitrolysis of Hexamethylenetetramine in Fluorous Media. *J. Hazard. Mater.* **2008**, *150* (3), 839–842.
- (36) Chen, L.; Huang, F.; Li, S.; Shen, Y.; Xie, A.; Pan, J.; Zhang, Y.; Cai, Y. Biomimetic Synthesis of Aragonite Superstructures Using Hexamethylenetetramine. *J. Solid State Chem.* **2011**, *184* (11), 2825–2833.
- (37) Chen, L.-J.; Chuang, Y.-J. Hydrothermal Synthesis and Characterization of Hexagonal Zinc Oxide Nanorods with a Hexamethylenetetramine (HMTA) Template-Assisted at a Low Temperature. *Mater. Lett.* **2012**, *68*, 460–462.
- (38) Singh, G.; Baranwal, B. P.; Kapoor, I. P. S.; Kumar, D.; Fröhlich, R. Preparation, X-Ray

Crystallography, and Thermal Decomposition of Some Transition Metal Perchlorate Complexes of Hexamethylenetetramine. *J. Phys. Chem. A* **2007**, *111* (50), 12972–12976.

- (39) Babu, B.; Chandrasekaran, J.; Balaprabhakaran, S. Growth and Characterization of Hexamethylenetetramine Crystals Grown from Solution. *Mater. Sci.-Pol.* **2014**, *32* (2), 164–170.
- (40) Walker, J. F. *Formaldehyde*; Reinhold Publ. Corp: New York, **1964**.
- (41) Aladko, L. S.; Komarov, V. Y.; Manakov, A. Y.; Ancharov, A. I. Phase Diagram of the Hexamethylenetetramine: Water System. *J. Incl. Phenom. Macrocycl. Chem.* **2007**, *59* (3–4), 389–391.

Chapter III

Kinetics Studies by TR-SHG

In this chapter, the crystallization kinetics were studied by TR-SHG. In part III-1, the crystallization process of 1,3-dimethylurea monohydrate was investigated. In part III-2, the monotropic phase transition of 2-adamantanone was followed by TR-SHG.

III-1. Investigations of the Crystallization of 1,3-Dimethylurea Monohydrate (DMU·H₂O) by TR-SHG

III-1-1. Introduction

In the pharmaceutical industry, hydrates, solvates and polymorphs are frequently encountered during drug development¹ and at least one thirds of active pharmaceutical ingredients (APIs) crystallizes as hydrates². They commonly have different physical or chemical properties such as solubility, dissolution rate, stability, and bioavailability. Therefore, during processing or storage, control of the solid-state forms is of prior importance to the drug development. Two different but related processes to control the transitions between solid-state forms are thermodynamics and kinetics. Thermodynamics tells whether a process or a reaction can occur (if there is a decrease in the free energy G), whereas kinetics considers how fast a change can occur. For a process or a reaction to occur, (i) the thermodynamics must be favorable (i.e., the driving force $\Delta G < 0$); (ii) The kinetics must be fast enough (small E_a , activation energy)³.

1,3-dimethylurea (DMU) has already been introduced in Chapter II. It exists as solid solutions with ppm amount of water (hereafter ss I and ss II) and a monohydrate with a non-congruent fusion at 8°C⁴. However, the nucleation and/or growth of this hydrated form is/are slow. Therefore, in the DMU-water binary phase diagram⁴, the stable equilibrium between DMU·H₂O and water is often more difficult to reach than the metastable one between ss II and water (See Figure III-1). To further understand this phenomenon, thermodynamics and kinetics in the crystallization of DMU·H₂O have to be investigated.

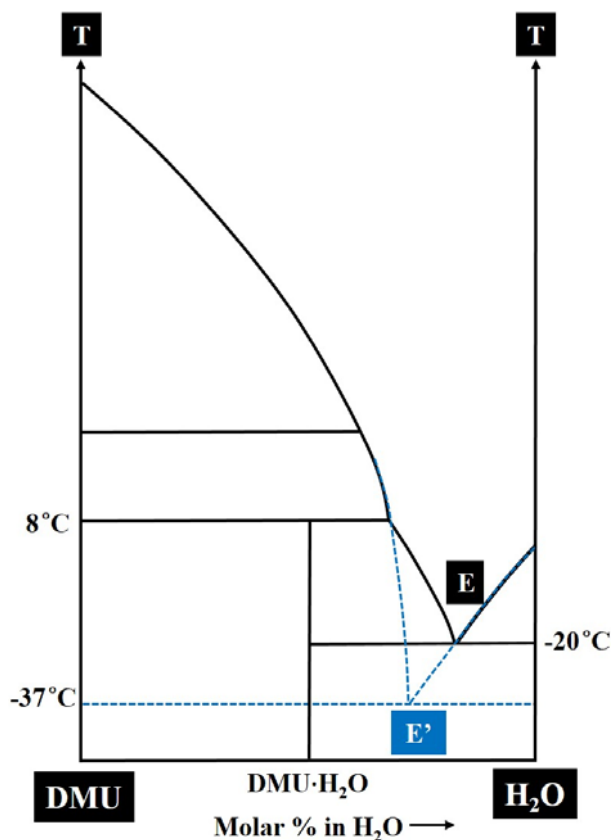


Figure III-1. Schematic illustration of metastable phase diagram between DMU and water, and stable phase diagram between DMU·H₂O and water. Part of the phase diagram close to the DMU part is omitted (the metatectic equilibrium).

From the thermodynamic point of view, a rough estimation of free energies includes intramolecular and intermolecular energetic contributions. Intramolecular contribution represents the variation of bond distances, angles and torsion angles around their equilibrium value (i.e., the conformation). Intermolecular contribution represents Van der Waals and electrostatic interactions. These can be determined from the positions of atoms in the crystal structures.

For the kinetics, thermo-analytical techniques such as differential scanning calorimetry (DSC) has been extensively used to obtain the activation energies and kinetic parameters⁵. However, in the present case, the crystallization process of DMU·H₂O could not be detected by DSC during isothermal and non-isothermal processes. Therefore, an alternative method should be found to solve this problem. In this matter, the nonlinear optical second harmonic generation (SHG) technique could be of great relevance.

In the following, TR-SHG was used to investigate the crystallization process of $\text{DMU}\cdot\text{H}_2\text{O}$ and to determine the corresponding activation energy, and further to understand the sluggish behavior of the formation of $\text{DMU}\cdot\text{H}_2\text{O}$.

III-1-2. Energy Calculations of DMU and $\text{DMU}\cdot\text{H}_2\text{O}$ (Thermodynamics)

In the structure of $\text{DMU}\cdot\text{H}_2\text{O}$, alternate DMU and water molecules are connected by hydrogen bonds and an efficient three-dimensional hydrogen bonding network is built. Neither DMU-DMU nor water-water hydrogen bonds exist (Figure III-2-(a)). Therefore, to build the hetero-molecular hydrogen bonded chains in $\text{DMU}\cdot\text{H}_2\text{O}$, certain amount of energy should be required to destroy the homo-molecular hydrogen bonded chains present in anhydrous DMU form II (Figure III-2-(b)).

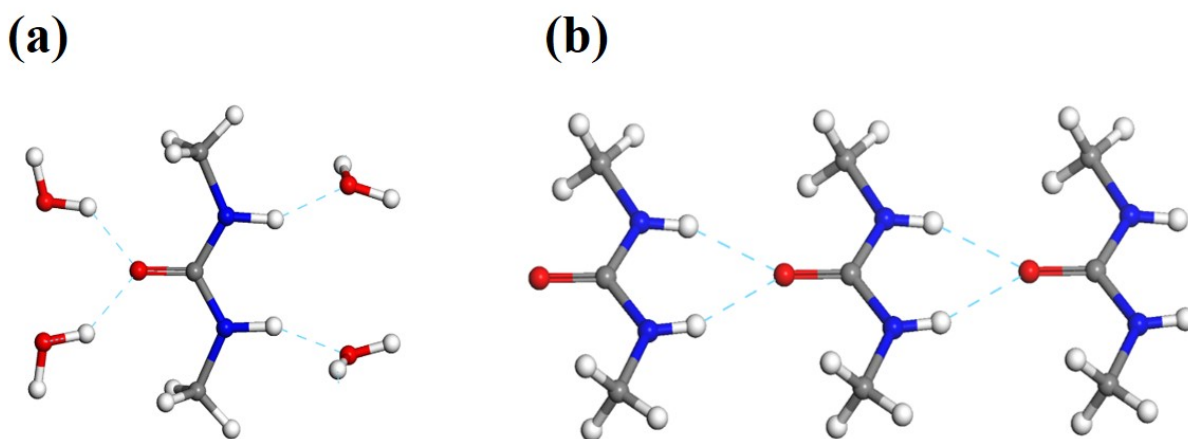


Figure III-2. Portion of a molecular chain of (a) $\text{DMU}\cdot\text{H}_2\text{O}$: DMU and water molecules are connected by hydrogen bonds, and (b) anhydrous DMU form II: DMU and DMU molecules are bonded by homo-molecular hydrogen chains.

Lattice energy calculations are performed using Compass forcefield (included in Material Studio software)⁶ from the crystal structures of DMU form I^{7,8}, DMU form II and DMU monohydrate^{7,9}. Values directly obtained by the calculations are divided by Z (the number of molecules in the unit cell) to obtain the lattice energy per molecule. Temperature and pressure are not explicitly implemented in the energy calculations but the static lattice energy of the different polymorphs can be compared. Results are gathered in Table III-1.

The energetic contributions of intermolecular interactions which are responsible for the cohesion of the crystal structures are also mentioned in Table III-1.

Table III-1. Summary of the results of lattice energy calculations.

Form	DMU·H ₂ O	Anhydrous DMU form I		Anhydrous DMU form II	
Crystal system	Monoclinic	Orthorhombic		Orthorhombic	
Space group	<i>C2/c</i>	<i>Fdd2</i>		<i>P2₁2₁2</i>	
Z	16	8		2	
Reference	Reference	2	3	2	4
Electrostatic contribution (kJ/mol)	-417	-361	-368	-360	-358
Van der Waals contribution (kJ/mol)	-14	-36	-33	-38	-38
Total intermolecular contribution (kJ/mol)	-431	-397	-401	-398	-396

However, because the molecular structures of DMU are very similar among the three solid forms^{7,8}, the energetic contribution of the conformational intramolecular interaction is not relevant for a comparison between the different forms. It is clear that the electrostatic interactions dominate the three solid forms since all these forms essentially rely on hydrogen bond interactions. The electrostatic interactions are more favorable in the case of the DMU·H₂O (-417 kJ/mol) compare to the two anhydrous forms (ca. -360 kJ/mol). This is clearly in agreement with the fact that hydrogen bonds are systematically shorter in the case of DMU·H₂O compared to anhydrous forms.

However, the Van der Waals energy contribution is less favorable for DMU·H₂O (-14 kJ/mol) with a difference of about 20 kJ/mol compared to the anhydrous forms. This is related to the fact that DMU-DMU interactions are reduced in the case of DMU·H₂O due to the presence of water molecules, which systematically surround each DMU molecule. Overall, when both contributions are added (the electrostatic interactions + Van der Waals), the energy of intermolecular interactions of DMU·H₂O (-437 kJ/mol) is still lower than those of anhydrous forms of around 30-35 kJ/mol. Hence, from a thermodynamic point of view, it comes that DMU·H₂O is more stable than the two anhydrous forms (at 0 Pa and 0K). These calculations confirm the established DMU/water phase diagram and the stability of phases at low temperature. Thus, when the conditions are favorable (water content, temperature and pressure), DMU·H₂O should be the solid form present when equilibrium is reached below the peritectic invariant (8°C).

Practically, solid solutions (ss I and ss II) with ppm amount of water (e.g., from moisture in the air) are the phases that exist instead of DMU form I and form II. Solid solutions have the same crystal structure and energy level than the matrix crystal structure. Thus, in the following, the terminology ss II is used instead of DMU form II.

III-1-3. Mechanism of the Crystallization of DMU·H₂O

In order to study the crystallization of DMU·H₂O, a concentration of 60% (molar fraction in water) DMU/water mixture was prepared. According to the phase diagram, the phases in equilibrium (below peritectic invariant 8°C) should be DMU·H₂O and a saturated solution. Nevertheless, upon cooling, a metastable equilibrium can be reached between ss II and saturated solution. Moreover, no phenomenon of recalescence occurs due to the slow formation of DMU·H₂O.

III-1-3-1. Second Harmonic Response of the Crystallization of DMU·H₂O

To understand the second harmonic response of DMU·H₂O, a DMU/water mixture with a concentration of 60 mol% (in water) was:

- Cooled down from room temperature to -50°C at 10 K/min. This procedure leads to the metastable state between ss II and ice to be reached.
- Then heated to 1°C at 10 K/min and annealed at this temperature to wait for the stable equilibrium. Thus, the transition process from ss II to DMU·H₂O (i.e., the crystallization of DMU·H₂O) was monitored by TR-SHG during the isothermal step.

The evolution of the SHG signal during the annealing process is shown in Figure III-3. At the beginning of the annealing, only ss II crystals exist (in the metastable state) and generate the highest SHG signal. Gradually, ss II transforms to DMU·H₂O (centrosymmetric crystal), which leads to a decrease of the SHG signal. After 264 min, the SHG signal completely vanishes, which indicates that the stable state is reached and only DMU·H₂O exists. Furthermore, the null SHG signal confirms that DMU·H₂O is a centrosymmetric crystalline form (confidence higher than 99%¹⁰).

Moreover, in a previous study, temperature-resolved powder X-ray diffraction (TR-XRPD)⁴ confirms that when cooling down the DMU/water mixtures to temperatures below 8°C, ss II

crystallizes first, then the monohydrate crystallizes when the sample is maintained at those temperatures for a long period of time. Observations under a microscope are also in agreement with the SHG and TR-XRPD measurements. At low temperatures, hexagonal-shaped crystals are observed and correspond to ss II crystal. Increasing the temperature, a new form appears at the expense of the former hexagonal form crystals and the propagation of an interface in the bulk of the crystals can be clearly observed. The appearing form corresponds to $\text{DMU}\cdot\text{H}_2\text{O}$.

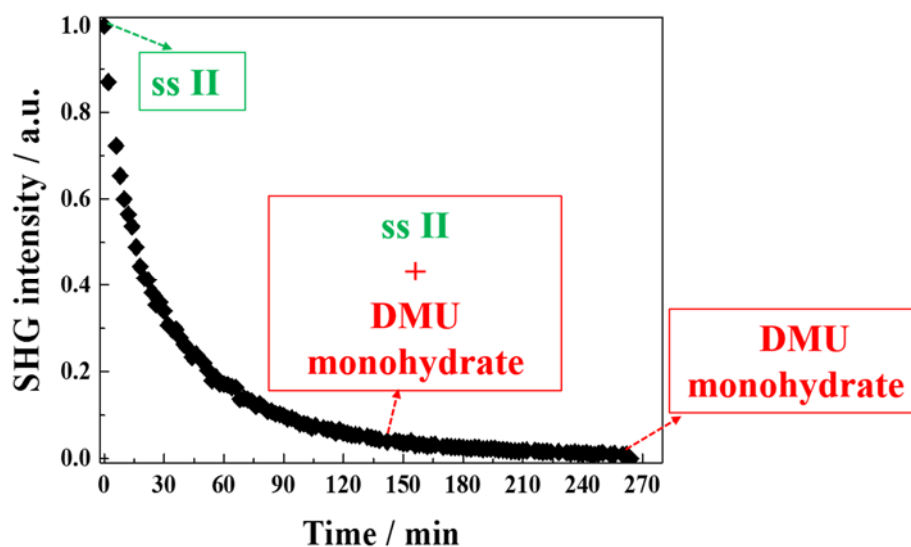


Figure III-3. SHG intensity versus time for a composition of 60% (in molar fraction of water) DMU/water mixture annealing at 1°C . SS II generates a high SHG signal, while $\text{DMU}\cdot\text{H}_2\text{O}$ has no SHG response.

III-1-3-2. Kinetics of the Crystallization of $\text{DMU}\cdot\text{H}_2\text{O}$

SS II generates a high SHG intensity, while $\text{DMU}\cdot\text{H}_2\text{O}$ has no SHG response. Therefore, by tracking the SHG signal of ss II, the kinetics of the transition from ss II to $\text{DMU}\cdot\text{H}_2\text{O}$ (i.e., the crystallization of $\text{DMU}\cdot\text{H}_2\text{O}$) can be followed by TR-SHG.

A concentration of 60% DMU/water mixtures was first cooled down to -50°C , and then heated at 10 K/min to the desired isothermal temperatures, -25°C , -20°C , -10°C and 1°C , respectively. The four different isothermal temperatures are all beyond the metastable eutectic temperature (-37.5°C , between ss II and water) and below the stable peritectic temperature (8°C) (Figure III-4). Therefore, the transition from the metastable ss II to the stable $\text{DMU}\cdot\text{H}_2\text{O}$ can occur with the assistance of a liquid (as the 60% molar composition in water locates in a two-phase domain of saturated solution + DMU).

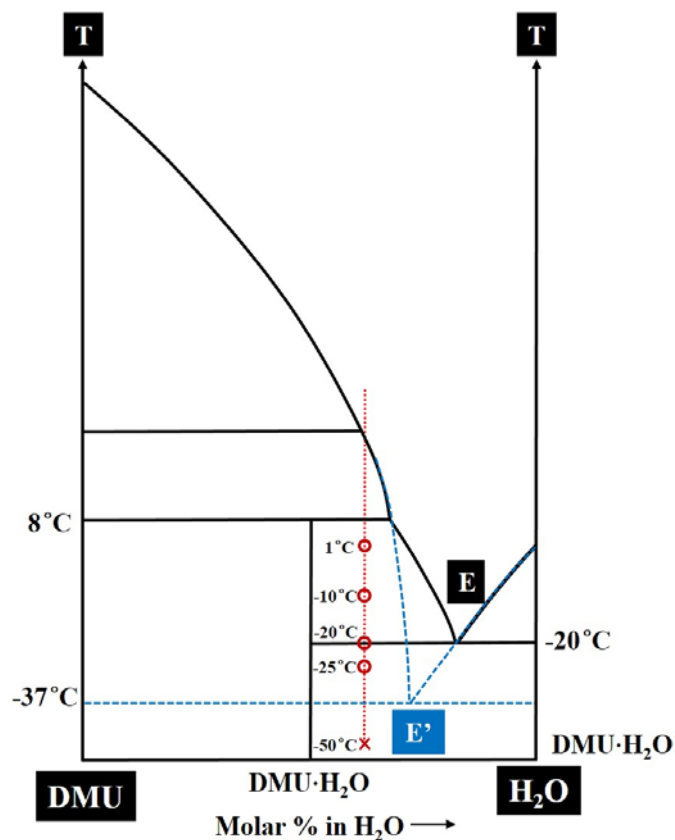


Figure III-4. Illustration of the location of 60 % DMU/water in the phase diagram.

The completion of the transition process is highlighted by the null SHG signal. The evolution of the SHG signal versus time during the isothermal process is shown in Figure III-5.

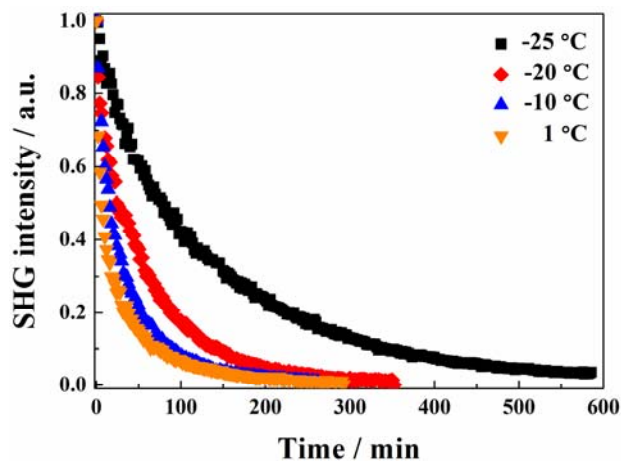


Figure III-5. The SHG signal versus time for the composition of 60% (in molar fraction of water) DMU/water mixture during the isothermal processes at different annealing temperatures.

As can be seen, the transition processes were completed after 264 min, 292 min and 352 min when the sample was annealed at 1°C (pink curve), -10°C (blue curve) and -20°C (red curve), respectively. While after 596 min, the transition process was still not fully completed at -25°C

(black curve). This indicates that temperature is an important factor affecting the crystallization process. The higher the annealing temperature, the faster the process is completed. Especially in this case, at -25°C , which is lower than the stable eutectic temperature (-20°C), all phases are solids in the stable state, the transition process should proceed via molecular diffusion in the solid-state and thus takes comparatively much longer time.

In the work of Kurtz and Perry^{10,11}, it is indicated that the intensity of the SHG signal is proportional to the total number of particles present. Based on this, for all the measurements reported herein, the intensity of the SHG signal is considered to be proportional to the fraction of the crystalline non-centrosymmetric phase in the system.

The crystallized fraction of $\text{DMU}\cdot\text{H}_2\text{O}$ (X) can be defined as follows:

$$X = 1 - \frac{I_{SHG}(t)}{I_{SHG}^0} \quad (III-1)$$

where I_{SHG}^0 is the initial SHG intensity ($t=0$, represents when the isothermal temperatures are reached); $I_{SHG}(t)$ is the SHG intensity measured at time t .

Figure III-6 displays the crystallized fraction of $\text{DMU}\cdot\text{H}_2\text{O}$ versus time. Note that all curves have a characteristic sigmoidal shape. The transition is rapid at the beginning and then slows down approaching the end of the process.

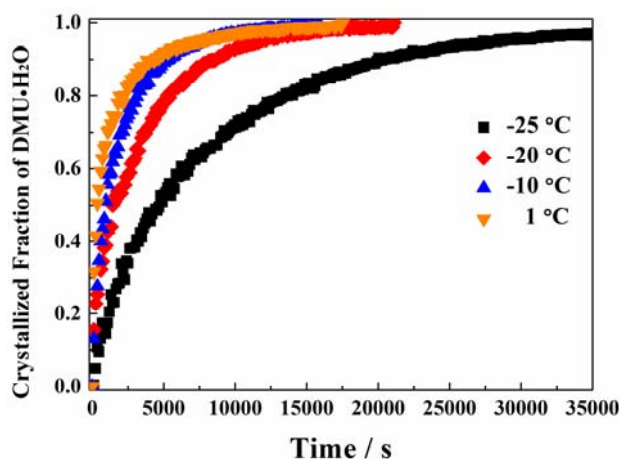


Figure III-6. Plots of crystallized fraction of $\text{DMU}\cdot\text{H}_2\text{O}$ versus time for the 60% (in molar fraction of water) DMU/water mixture during the isothermal processes at different annealing temperatures.

A commonly used model to describe the crystallization kinetics is the Avrami equation¹²⁻¹⁴:

$$X = 1 - \exp(-kt^n) \quad (I-3)$$

where k is the crystallization rate constant and t the annealing time, n is Avrami exponent that is related to the time dependence of nucleation rate and to the dimensionality of the crystallization.

The logarithmic conversion of eq. I-3 leads to:

$$\ln[-\ln(1-x)] = \ln k + n \ln t \quad (I-4)$$

From a linear regression of $\ln[-\ln(1-x)]$ and $\ln t$, parameters n and k can be determined as the slope and the intercept of the straight line obtained, respectively. Figure III-7 shows the Avrami plot based on eq. I-4. The average n value is relatively close to 1, which means that the surface crystallization is the predominant mechanism. It fits well with the microscopy observations in which the DMU·H₂O crystals grow on the surface of the hexagonal shaped ss II crystals.

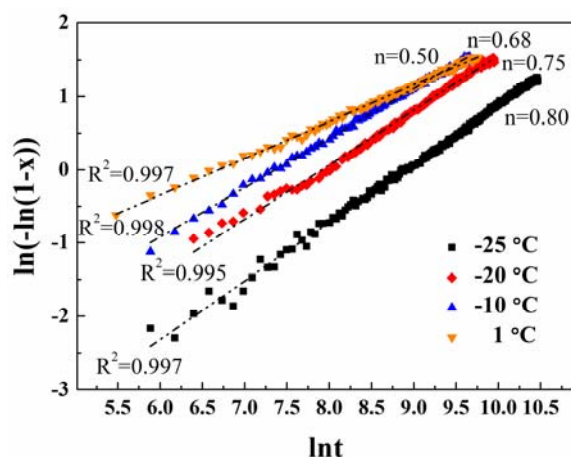


Figure III-7. Plots of $\ln[-\ln(1-x)]$ versus $\ln t$ at the labelled isothermal temperatures for the determination of Avrami parameter n .

III-1-4. Activation Energy Calculation Based on the TR-SHG Measurements

Energetic barrier between ss II and DMU·H₂O can be evaluated by Arrhenius equation¹⁵⁻¹⁷:

$$k = k_0 e^{\frac{-E_a}{RT}} \quad (I-5)$$

where k is the reaction rate constant; k_0 is the pre-exponential factor; E_a is the activation energy; R is the gas constant. A logarithmic conversion of eq. I-5 is applied:

$$\ln k = \ln k_0 - \frac{1}{RT} E_a \quad (I-6)$$

Activation energy for isothermal temperatures can be calculated from the slopes of the linear

fits to the experimental data via a plot of $\ln k$ versus $-1/RT$. Based on the SHG data, E_a of the crystallization of $\text{DMU}\cdot\text{H}_2\text{O}$ is 77 kJ/mol (Figure III-8). This value is in the same order of magnitude than the values reported in the literature for other systems^{18,19}.

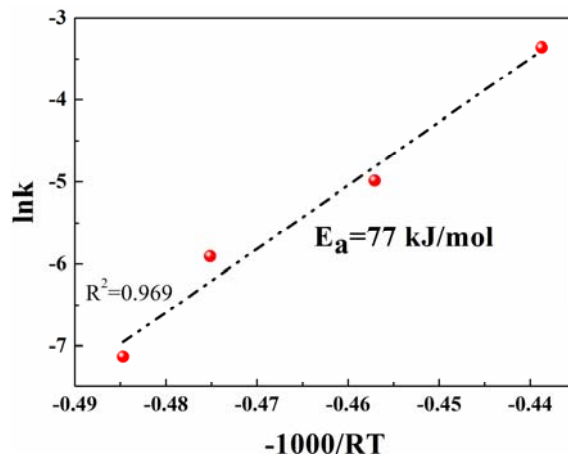


Figure III-8. Plots of $-1000/RT$ versus $\ln k$ for the determination of the activation energy E_a from TR-SHG measurements.

III-1-5. Discussions

The crystallization process of $\text{DMU}\cdot\text{H}_2\text{O}$ is summed up in Figure III-9.

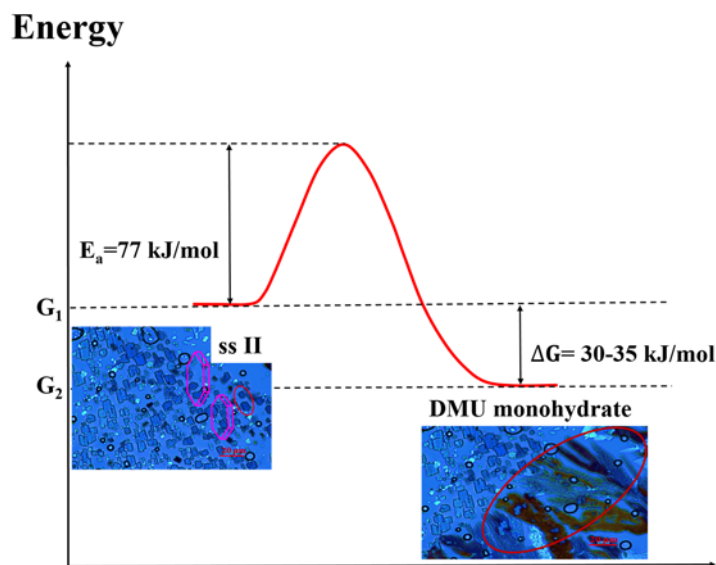


Figure III-9. Gibbs energy variations of the crystallization process of $\text{DMU}\cdot\text{H}_2\text{O}$.

From a thermodynamic point of view, $\text{DMU}\cdot\text{H}_2\text{O}$ has a lower free energy compared to ss II, the driving force is around 30-35 kJ/mol (at 0 Pa, 0K) in the condition that the energetic contributions of the volume change (at 0 Pa, 0K) and the entropy change at the investigated temperature range (-25°C to 1°C) is negligible. Therefore, the formation of $\text{DMU}\cdot\text{H}_2\text{O}$ is thermodynamically favorable.

From a kinetic point of view, the energy barrier (E_a) is 77 kJ/mol, which is a reasonable value but smaller than what was expected taking into account the observed “sluggish” character of the crystallization of DMU·H₂O. The possible explanation is given below.

TR-SHG experiments (Figure III-6) show that the crystallization fraction of DMU·H₂O increases rapidly at the beginning but a certain isothermal time is needed to complete the crystallization process. And this time is much longer than the rapid crystallization at the beginning. i.e., annealing at 1°C, it takes 4440 s to crystallize 90% of the ss II to DMU·H₂O, while 13080 s to crystallize the remaining ss II fraction.

Besides, attention should be paid to the annealing temperature of -25°C. The final equilibrium state of annealing at -25°C is only composed of solids. However, for other annealing temperatures (-20°C, -10°C and 1°C), liquids exist in the final state. Therefore, the crystallization of DMU·H₂O is even more difficult at -25°C. This is shown in Figure III-6 that at -25°C, the SHG curve (black) is away from the curves of -20°C, -10°C and 1°C.

III-1-6. Conclusion

Firstly, static lattice energy calculations were performed, which prove that the crystal arrangement of DMU·H₂O is more favorable than that of anhydrous DMU form I (ss I) and form II (ss II). Then, the crystallization process of DMU·H₂O was monitored by TR-SHG at four different isothermal temperatures: -25°C, -20°C, -10°C and 1°C. Results show that the surface crystallization is the predominant mechanism. Finally, activation energy (77 kJ/mol) of the crystallization process of DMU·H₂O was calculated based on the TR-SHG data. The sluggish behavior of the formation of DMU·H₂O should be understood correctly: the appearance of the monohydrate is easy, but to complete the formation of DMU·H₂O in the whole sample is difficult and takes time.

III-2. Monotropic Phase Transition of 2-Adamantanone Studied by TR-SHG

III-2-1. Introduction

Adamantane ($C_{10}H_{16}$) is formed by a 10-carbon cage made of four cyclohexane rings in chair conformation.²⁰ A set of adamantane derivatives can be obtained, substituting one or two hydrogen atoms by an atom (Cl, Br, O, etc.) or a group of atoms (CN, OH, CH_3 , CH_2OH , NH_2 , etc.) into a tertiary or secondary carbon, given rise to the 1-X- or 2-X-adamantane compounds, respectively.²¹ The 1-X-adamantane derivatives show a rich polymorphic behavior that have been extensively studied²²⁻³⁰ (see chapter IV). While among the few studied 2-X-adamantane derivatives, 2-adamantanone (2-O-adamantane, $C_{10}H_{14}O$, hereinafter 2O-A, Figure III-10) has probably been the mostly investigated compound.^{21,31-34}

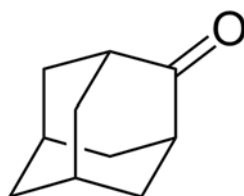


Figure III-10. Molecular structure of 2-adamantanone.

At room temperature, 2O-A exhibits an orientationally disordered (OD) phase and crystallizes in the face-centered cubic structure (space group $Fm\bar{3}m$). On cooling the OD phase, it transforms to an “ordered” low-temperature (LT) phase. However, the phase transition temperature of 2O-A has been argued. Butler et al.³⁵ reported that a large hysteresis in the transition temperature occurs between the first cooling at -102°C and first heating at -68°C , and when the sample is cycled several times through the transition these temperatures shift to -95°C and -52°C . Bazyleva et al.³² reported the transition temperature on heating was determined to be -56.6°C through adiabatic calorimetry. These data are summarized in Table III-2.

Table III-2. Transition temperature of 2O-A reported in the literature.

	Method	T_t on cooling	T_t on heating
		OD→Ordered LT	Order LT→OD
Butler et al. ³⁵	DSC	First cycle -102°C	-68°C
		After cycling -95°C	-52°C
Bazyleva et al. ³²	Adiabatic calorimetry		-56.6°C

Recently, the polymorphic behavior of this compound was thoroughly described in the work of Ph. Negrier et al.²¹ Two low-temperature phases (LT) have been revealed: one stable phase crystallizes in the orthorhombic $Cmc2_1$ ($Z=4$) space group and one metastable phase crystallizes in the monoclinic $P2_1/c$ ($Z=4$) space group. The crystallographic data of stable and metastable LT phases together with HT phase are summarized in Table III-3.

Table III-3. Crystallographic data determined for the stable and metastable LT phases.

	LT phases		HT phase
	Stable	Metastable	
Temperature (K)	190	190	283-303K
Crystal system	Orthorhombic	Monoclinic	Cubic
Space group	$Cmc2_1$	$P2_1/c$	$Fm\bar{3}m$
a (Å)	6.8884 ± 0.0018	6.5920 ± 0.0017	9.524
b (Å)	10.830 ± 0.003	11.118 ± 0.003	9.524
c (Å)	10.658 ± 0.003	12.589 ± 0.003	9.524
α (°)	90	90	90
β (°)	90	118.869 ± 0.011	90
γ (°)	90	90	90
Z	4	4	4
Z'	0.5	1	0.02
V (Å ³)	795.101	807.985	863.889
Density (g/cm ³)	1.255 ± 0.001	1.235 ± 0.001	1.155

The stable LT phase is non-centrosymmetric, thus is SHG positive. While metastable LT phase and HT phase are both centrosymmetric, so SHG negative. Therefore, the phase transitions in 2O-A can be investigated by TR-SHG. In the following, the stable-metastable transition in 2O-A was studied and the activation energy (E_a) was calculated by TR-SHG.

III-2-2. Phase Transitions of 2O-A Studied by TR-SHG

Phase transitions of 2O-A were monitored by TR-SHG, shown in Figure III-11-(a). During cooling (black squares) from 20°C to -170°C, SHG signal appears at -117°C, which corresponds to the formation of the stable LT phase. Metastable LT phase transforms continuously to the stable LT phase, then the signal increases. Finally, the SHG signal remains stable when the system is at equilibrium, only stable LT phase exists. While during heating process (red spots) from -170°C to 20°C, only the stable LT phase transforms back to the HT phase. The transition starts at -80°C and ends at -58°C.

Compare the transition temperature upon cooling and heating, a large hysteresis (59°C) exists. This confirms the difficulty of the conversion from the HT phase to the LT stable phase, which was highlighted by Bazyleva et al.³² Moreover, in TR-SHG (during heating), the end of the transition is at -58°C , close to the temperature (-56.6°C : 216.4K) reported by Bazyleva et al.³² (Figure III-11-(b)).

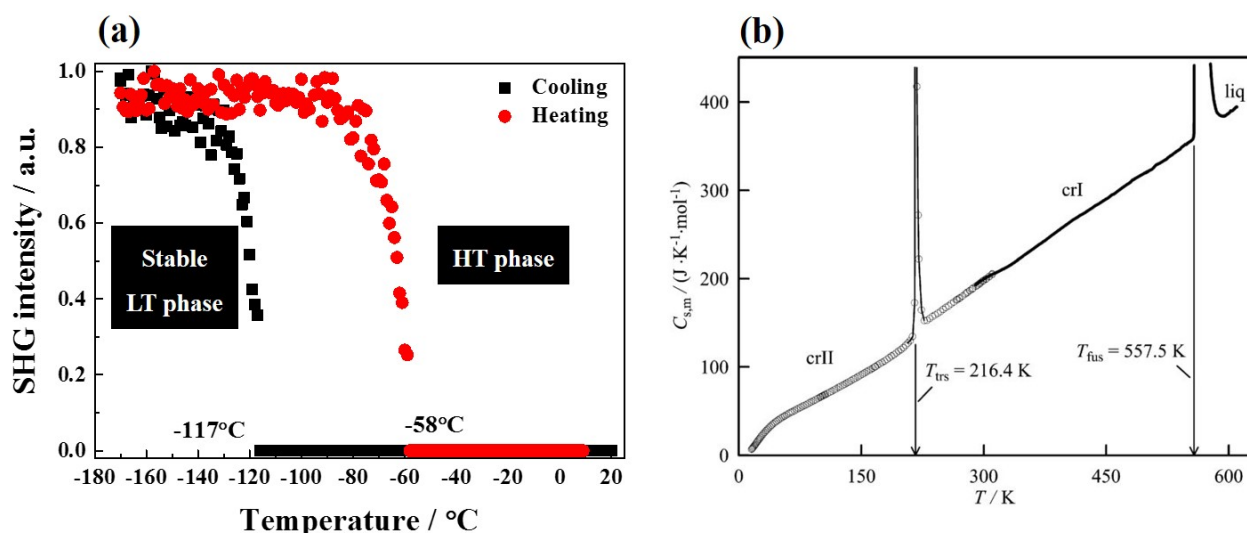


Figure III-11. Phase transitions in 2O-A measured by (a) TR-SHG in the temperature range of -170°C to 20°C at $2\text{K}/\text{min}$ heating/cooling rates, and (b) by adiabatic calorimetry (empty circles) and DSC (solid lines) in the temperature range of 5K (-268°C) to 620K (347°C) at $0.8\text{K}/\text{min}$ heating/cooling rates³².

III-2-3. Path of the Monotropic Transition from HT Phase to the LT Phase

The path of the phase transitions in 2O-A was illustrated in Figure III-12. Upon cooling, the HT phase transforms first to the metastable LT phase, then with high undercooling, the metastable LT phase transforms to the stable LT phase. While during heating, the stable LT phase transforms directly to the HT phase.

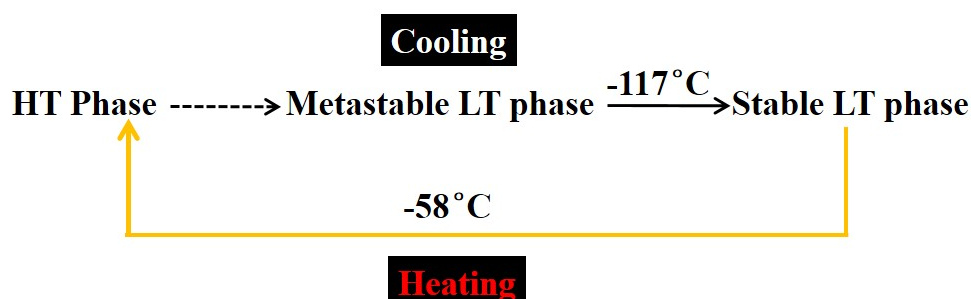


Figure III-12. The path of the phase transitions in 2O-A upon cooling and heating.

III-2-4. Kinetics of the Monotropic Transition from Metastable LT Phase to the Stable LT Phase

Transition from metastable LT phase to stable LT phase was monitored by TR-SHG. First, 2O-A was cooled at 20 K/min to -105°C, -110°C, -115°C and -120°C, respectively to reach the metastable LT phase. Then, during annealing at these temperatures, metastable LT phase transforms to stable LT phase, the SHG signal was followed.

The crystallized fraction of stable LT phase (X) can be defined by

$$X = 1 - \frac{I_{SHG}(t)}{I_{SHG}^0} \quad (III-1)$$

where I_{SHG}^0 is the initial SHG intensity ($t=0$, represents when the isothermal temperatures are reached); $I_{SHG}(t)$ is the SHG intensity measured at time t .

Figure III-13 displays the crystallized fraction of stable LT phase versus time. All curves have a characteristic sigmoidal shape.

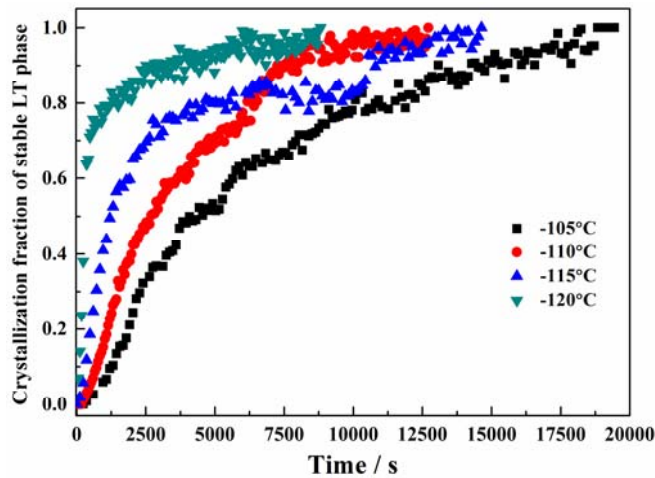


Figure III-13. Plots of crystallized fraction of stable LT phase versus time during the isothermal processes at different annealing temperatures.

A commonly used model to describe the crystallization kinetics is the Avrami equation¹²⁻¹⁴:

$$X = 1 - \exp(-kt^n) \quad (I-3)$$

where k is the crystallization rate constant and t the annealing time, n is Avrami exponent that is related to the time dependence of nucleation rate and to the dimensionality of the crystallization. The logarithmic conversion of eq. I-3 leads to:

$$\ln[-\ln(1-x)] = \ln k + n \ln t \quad (I-4)$$

From a linear regression of $\ln[-\ln(1-x)]$ and $\ln t$, parameters n and k can be determined as the slope and the intercept of the straight line obtained, respectively.

Figure III-14 shows $\ln t$ versus $\ln[-\ln(1-x)]$ based on eq. I-4. The curves show an abrupt change of the slopes (Figure III-14-(a)) and can be divided into two stages. In the first-stage (Figure III-14-(b)), the n value is close to 2. When the nucleation rate is 0 during the thermal analysis experiment (the bulk crystallization with a constant number of nuclei), the growth of the crystals is two-dimensional (disk-like crystallization). If nucleation takes place (bulk crystallization with an increasing number of nuclei), the crystallization is one-dimensional (rod-like or surface crystallization). While in the second-stage (Figure III-14-(c)), n value is close to 1, which means that the surface crystallization is the predominant mechanism.³⁶

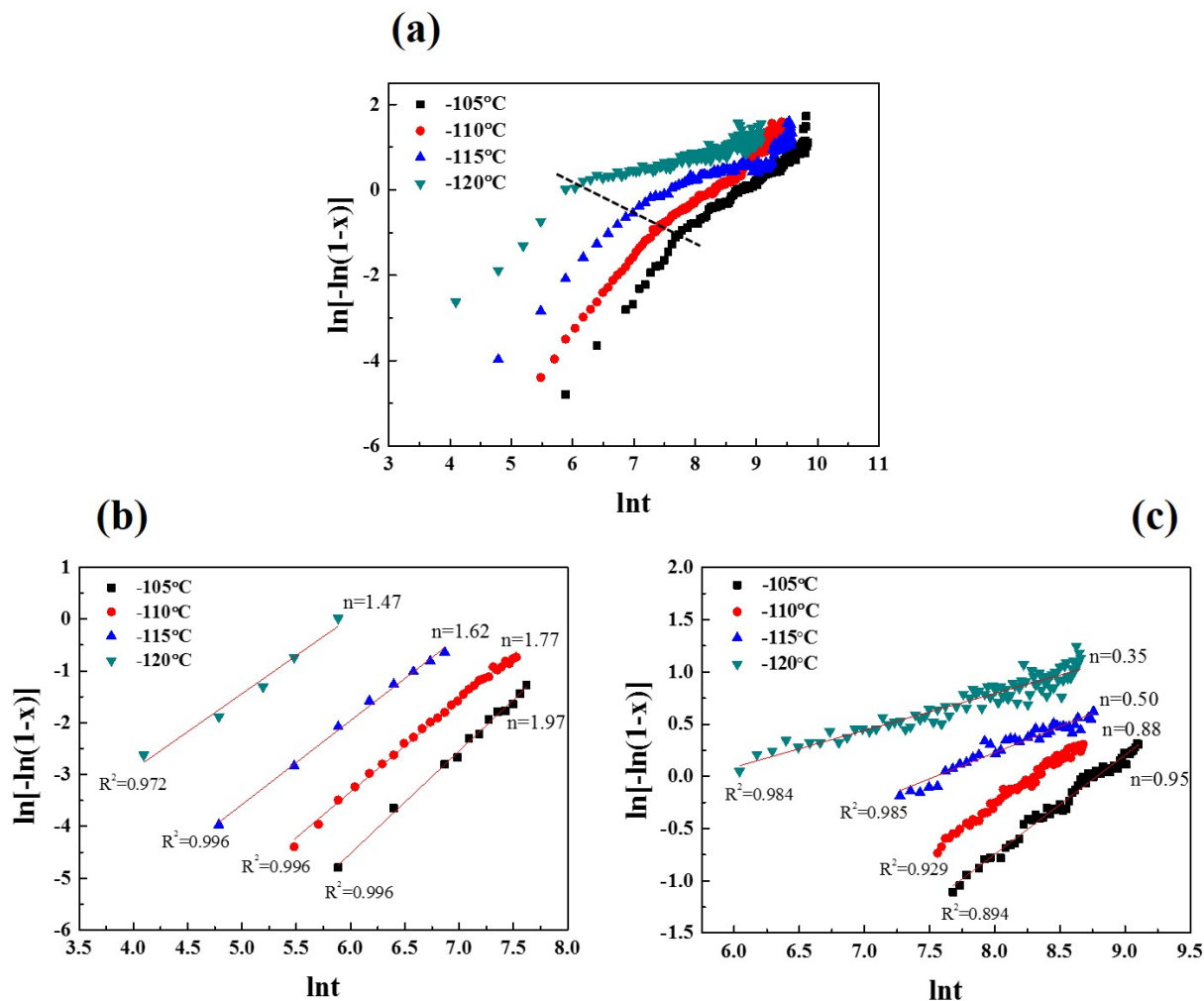


Figure III-14. Plots of $\ln[-\ln(1-x)]$ versus $\ln t$ at the labelled isothermal temperatures for the determination of Avrami parameter n , (a) in the entire time range, (b) in the first-stage, and (c) in the second-stage.

III-2-5. Activation Energy Calculation Based on the TR-SHG Measurements

The energetic barrier between metastable LT phase and stable LT phase can be evaluated by Arrhenius equation¹⁵⁻¹⁷:

$$k = k_0 e^{\frac{-E_a}{RT}} \quad (I-5)$$

where k is the reaction rate constant; k_0 is the pre-exponential factor; E_a is the activation energy; R is the gas constant. A logarithmic conversion of eq. I-5 is applied:

$$\ln k = \ln k_0 - \frac{1}{RT} E_a \quad (I-6)$$

Activation energy for isothermal temperatures can be calculated from the slopes of the linear fits to the experimental data via a plot of $\ln k$ versus $-1/RT$. Based on the SHG data, in the first-stage, E_a of the monotropic transition from metastable LT 2O-A to stable LT 2O-A is -107 kJ/mol (Figure III-15-(a)). In the second-stage, the energy barrier is -97 kJ/mol (Figure III-15-(b)). The activation energies are negative. E_a is sometimes measured as negative if data are fitted to an Arrhenius plot, means that the reaction slows down with increasing temperature. This is in accordance with the transition property of 2O-A: the transition from metastable LT phase to stable LT phase goes through easily with high undercooling. Moreover, the two negative energies are close. Therefore, we can deduce that during the transition process, the energy barriers are similar in the two stages but the mechanisms are different depending on the transition time.

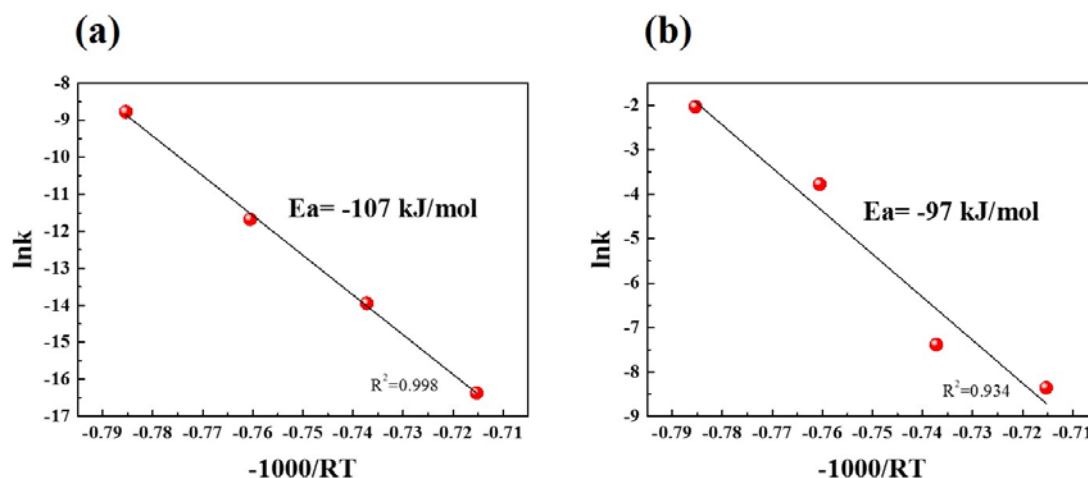


Figure III-15. Plots of $-1000/RT$ versus $\ln k$ for the determination of the activation energy E_a from TR-SHG measurements at different time range, (a) the first-stage, and (b) the second-stage.

III-2-6. Conclusion

Phase transitions of 2O-A was studied by TR-SHG. A two-stage transition mechanism was proposed and the energy barriers were obtained from TR-SHG. In the two stages, the energy barriers are similar but the mechanisms are different. In the first-stage, when the nucleation rate is 0 during the thermal analysis experiment (the bulk crystallization with a constant number of nuclei), the growth of the crystals is two-dimensional (disk-like crystallization). If nucleation takes place (bulk crystallization with an increasing number of nuclei), the crystallization is one-dimensional (rod-like or surface crystallization). While in the second-stage, the surface crystallization is the predominant mechanism. Also, the discrepancies of the transition temperature and transition process were clearly illustrated through TR-SHG results.

References

- (1) Bhardwaj, R. M. Control and Prediction of Solid-State of Pharmaceuticals: Experimental and Computational Approaches. Ph. D thesis, University of Strathclyde: UK, **2016**.
- (2) Brittain, H. G. *Polymorphism in Pharmaceutical Solids (Second Edition)*; CRC Press, **2016**.
- (3) Jackson, K. A. *Kinetic Processes: Crystal Growth, Diffusion, and Phase Transitions in Materials*; John Wiley & Sons, **2010**.
- (4) Baaklini, G. The Effects of Spray Drying on the Polymorphism of Pharmaceutical and Organic Compounds. Ph. D thesis, Univeristy of Rouen: France, **2015**.
- (5) Yinnon, H.; Uhlmann, D. R. Applications of Thermoanalytical Techniques to the Study of Crystallization Kinetics in Glass-Forming Liquids, Part I: Theory. *J. Non-Cryst. Solids* **1983**, *54* (3), 253–275.
- (6) Sun, H. An Ab Initio Force-Field Optimized for Condensed-Phase Applications Overview with Details on Alkane and Benzene Compounds. *J. Phys. Chem. B* **1998**, *102* (38), 7338–7364.
- (7) Näther, C.; Döring, C.; Jess, I.; Jones, P. G.; Taouss, C. Thermodynamic and Structural Relationships between the Two Polymorphs of 1,3-Dimethylurea. *Acta Crystallogr. B* **2013**, *69* (Pt 1), 70–76.
- (8) Marsh, R. E. Space Group Cc: An Update. *Acta Crystallogr. B* **2004**, *60* (2), 252–253.
- (9) Martins, D. M. S.; Spanswick, C. K.; Middlemiss, D. S.; Abbas, N.; Pulham, C. R.; Morrison, C. A. A New Polymorph of N, N'-Dimethylurea Characterized by X-Ray Diffraction and First-Principles Lattice Dynamics Calculations. *J. Phys. Chem. A* **2009**, *113* (20), 5998–6003.
- (10) Kurtz, S. K.; Perry, T. T. A Powder Technique for the Evaluation of Nonlinear Optical Materials. *J. Appl. Phys.* **1968**, *39* (8), 3798–3813.
- (11) Dougherty, J. P.; Kurtz, S. K. A Second Harmonic Analyzer for the Detection of Non-Centrosymmetry. *J. Appl. Cryst.* **1976**, *9*, 145–158.
- (12) Avrami, M. Kinetics of Phase Change. I General Theory. *J. Chem. Phys.* **1939**, *7* (12), 1103–1112.
- (13) Avrami, M. Kinetics of Phase Change. II Transformation-Time Relations for Random Distribution of Nuclei. *J. Chem. Phys.* **1940**, *8* (2), 212–224.
- (14) Avrami, M. Granulation, Phase Change, and Microstructure Kinetics of Phase Change. III. *J. Chem. Phys.* **1941**, *9* (2), 177–184.
- (15) Bamford, C. H.; Tipper, C. F. H. *Reactions in the Solid State*; Elsevier: Amsterdam, **1980**; Vol. 22.
- (16) Connors, K. A. *Chemical Kinetics: The Study of Reaction Rates in Solution*; VCH Publishers, Inc: New York, **1990**.
- (17) Grunwald, E. *Thermodynamics of Molecular Species*; John Wiley: New York, **1997**.
- (18) Thomas, J. J.; Musso, S.; Prestini, I. Kinetics and Activation Energy of Magnesium Oxide Hydration. *J. Am. Ceram. Soc.* **2014**, *97* (1), 275–282.
- (19) Thomas, J. J. A New Approach to Modeling the Nucleation and Growth Kinetics of Tricalcium Silicate Hydration. *J. Am. Ceram. Soc.* **2007**, *90* (10), 3282–3288.
- (20) Negrier, Ph.; Barrio, M.; Tamarit, J. Ll.; Mondieig, D. Polymorphism in 2-X-Adamantane Derivatives (X = Cl, Br). *J. Phys. Chem. B* **2014**, *118* (32), 9595–9603.
- (21) Negrier, P.; Barrio, M.; Romanini, M.; Tamarit, J. L.; Mondieig, D.; Krivchikov, A. I.; Kepinski, L.; Jezowski, A.; Szewczyk, D. Polymorphism of 2-Adamantanone. *Cryst. Growth Des.* **2014**, *14* (5), 2626–2632.
- (22) Clark, T.; Knox, T. M. O.; Mackle, H.; McKervey, M. A. Order-disorder Transitions in Substituted

- Adamantanes. *J. Chem. Soc. Faraday Trans. 1 Phys. Chem. Condens. Phases* **1977**, 73 (0), 1224.
- (23) Foulon, M.; Gors, C. Structure and Steric Hindrance Analyses to Determine the Dynamical Disorder in 1-Iodoadamantane ($C_{10}H_{15}I$). *Acta Crystallogr. B* **1988**, 44 (2), 156–163.
- (24) Foulon, M.; Belgrand, T.; Gors, C.; More, M. Structural Phase Transition in 1-Chloroadamantane ($C_{10}H_{15}Cl$). *Acta Crystallogr. B* **1989**, 45 (4), 404–411.
- (25) Affouard, F.; Guinet, Y.; Denicourt, T.; Descamps, M. Indication for a Change of Dynamics in Plastic Crystal Chloroadamantane: Raman Scattering Experiment and Molecular Dynamics Simulation. *J. Phys. Condens. Matter* **2001**, 13 (33), 7237.
- (26) Amoureux, J. P.; Sauvajol, J. L.; Bee, M. A Symmetry-Adapted-Function Analysis of Plastic Crystals. Application to 1-Cyanoadamantane at Room Temperature. *Acta Crystallogr. A* **1981**, 37 (1), 97–104.
- (27) Amoureux, J. P.; Bee, M.; Sauvajol, J. L. Structure of 1-Fluoroadamantane, $C_{10}H_{15}F$, in Its Plastic Phase. *Acta Crystallogr. B* **1982**, 38 (7), 1984–1989.
- (28) Betz, R.; Klüfers, P.; Mayer, P. 1-Bromo-adamantane. *Acta Crystallogr. Sect. E Struct. Rep. Online* **2009**, 65 (1), o101–o101.
- (29) Virlet, J.; Quiroga, L.; Boucher, B.; Amoureux, J. P.; Castelain, M. Molecular Reorientations of 1-Bromo- and 1-Iodo-Adamantanes 1H N.M.R. Relaxation Study. *Mol. Phys.* **1983**, 48 (6), 1289–1303.
- (30) Bée, M.; Amoureux, J. P. Molecular Reorientations of 1-Chloroadamantane in Its Plastic Solid Phase. *Mol. Phys.* **1983**, 48 (1), 63–79.
- (31) Amoureux, J. P.; Bee, M. A Cubic Harmonic Analysis of the Plastic Crystal Structures of Adamantane, $C_{10}H_{16}$, and Adamantanone, $C_{10}H_{14}O$, at Room Temperature. *Acta Crystallogr. B* **1980**, 36 (11), 2636–2642.
- (32) Bazyleva, A. B.; Blokhin, A. V.; Kabo, G. J.; Kabo, A. G.; Sevrjuk, V. M. Thermodynamic Properties of 2-Adamantanone in the Condensed and Ideal Gaseous States. *Thermochim. Acta* **2006**, 451 (1–2), 65–72.
- (33) Romanini, M.; Negrier, P.; Tamarit, J. L.; Capaccioli, S.; Barrio, M.; Pardo, L. C.; Mondieig, D. Emergence of Glassy-like Dynamics in an Orientationally Ordered Phase. *Phys. Rev. B* **2012**, 85 (13), 134201.
- (34) Harvey, P. D.; Butler, I. S.; Gilson, D. F. R. Raman Study of the Effect of High Pressure on the Order-Disorder Phase Transition in 2-Adamantanone. *J. Phys. Chem.* **1986**, 90 (19), 4546–4549.
- (35) Butler, I. S.; Cole, H. B. R.; Gilson, D. F. R.; Harvey, P. D.; McFarlane, J. D. Differential Scanning Calorimetric Studies of the Phase Transition in Adamantanone. *J. Chem. Soc., Faraday Trans. 2* **1986**, 82 (4), 535–539.
- (36) Celikbilek, M.; Erin, A.; Ayd, S. *Crystallization Kinetics of Amorphous Materials*. In *Advances in Crystallization Processes*; Mastai, Y., Ed.; InTech, **2012**.

Chapter IV

Solid-solid Phase Transitions Investigated by TR-SHG

In this chapter, solid-solid phase transitions of adamantane and its derivatives 1-fluoro-adamantane were studied by TR-SHG. In part IV-1, a new polymorph of 1-fluoro-adamantane is detailed. In part IV-2 the order-disorder nature of adamantane was discussed based on the TR-SHG results.

IV-1. A Newly Discovered Polymorph of 1-Fluoro-adamantane (1-F-A) Investigated by TR-SHG

IV-1-1. Introduction

Diamondoids formed by carbon atoms cages have received a great attention, in particular, for building up organic crystals with large cavities, specific physical and chemical properties¹⁻⁵. The simplest diamondoid, adamantane, and its derivatives exhibit an orientationally disordered (OD) phase (plastic phase) and show rich polymorphic transitions upon temperature or pressure changes⁶⁻¹¹. 1-Fluoro-adamantane (1-F-A hereafter, Figure IV-1) is one of the 1-substituted adamantane and, up to date, two polymorphs have been revealed: one OD phase at high temperature (HT) and a less disordered low temperature (LT) phase.

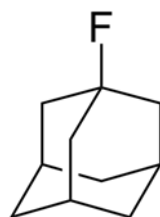


Figure IV-1. Molecular structure of 1-fluoro-adamantane (1-F-A).

The phase transition HT \leftrightarrow LT was first detected by differential scanning calorimetry (DSC) at 222K (upon heating) with an enthalpy of 1.5 kJ/mol.¹² Later, N. T. Kawai et al.¹³ reported the transition occurs at 227K with an enthalpy of 1.7 kJ/mol upon cooling and at 231K with an enthalpy of 1.6 kJ/mol upon heating. The transition displays a hysteresis which indicates a first-order behavior in the Ehrenfest classification.¹⁴ HT phase has been widely studied by thermal analysis¹², X-ray diffraction¹⁵, NMR⁸, single-crystal Raman scattering¹⁶, dielectric analysis¹⁷, and incoherent quasi-elastic neutron scattering¹⁸. The structure of the HT phase was determined as face-centered cubic ($Fm\bar{3}m$) by single-crystal X-ray diffraction¹⁵ and by X-ray powder diffraction (XRPD)¹⁹. However, less was known about the LT phase before the recent publication by Ben Hassine et al.¹⁹, in which reported the resolution of the crystal structure of

LT phase at 100K by XRPD in the tetragonal non-centrosymmetric $P\bar{4}2_1c$ space group ($Z=2$) - CCDC number 1455093¹⁹. The variation of cell parameters and cell volume of 1-F-A was also monitored by temperature-resolved XRPD from 90K to 360K and a sole discontinuity across the HT \leftrightarrow LT transition was observed. Based on these results, it was presumed in the work of Ben Hassine et al.¹⁹ that only two polymorphs exist and, consequently, that the structure of 1-F-A could be resolved in the $P\bar{4}2_1c$ space group from 90K until the phase transition towards the HT phase. As the LT polymorph is still disordered (as assessed by NMR and BDS experiments^{8,19}), 1-F-A is a perfect candidate to go deeper in the study of molecular motions in the solid-state and across polymorphic transition.

In this matter, Temperature-Resolved Second Harmonic Generation (TR-SHG) can be used to gather valuable information. Vogt^{20,21} detailed that the temperature dependence of higher-rank tensors describing second harmonic generation are related to variations of long- and short-range order. Moreover, Dougherty and Kurtz²² mentioned that dynamic disorder possibly couples with local polarization fluctuations can induce modification in the second harmonic signal. These make TR-SHG a useful tool to detect phase transitions and polymorphs for systems involving symmetry changes in crystalline structures and molecular motions in non-centrosymmetric crystalline phases. TR-SHG has already been applied to monitor transitions between monotropically or enantiotropically related solid phases²³⁻²⁶, to track ferroelectric-paraelectric phase transitions^{27,28} and order-disorder phase transitions^{21,29,30} (with as a required condition that at least one non-centrosymmetric crystalline structure is involved).

The HT phase of 1-F-A is centrosymmetric and consequently generates no SHG signal. The LT phase resolved in a non-centrosymmetric space group generates a SHG signal. Thus, the phase transition between the HT phase and the LT phase can be studied by TR-SHG.

Through a careful investigation of phase transitions in 1-F-A (especially at low temperatures) by the synergistic approach of combining TR-SHG and XRPD, not only a new polymorph was ascertained in this work but also the knowledge on the mechanism of ordered-disordered transitions was improved.

IV-1-2. Purification Procedure for 1-F-A

1-Fluoro-adamantane (CAS registry number: 768-92-3) was purchased from ABCR in Germany (98.3% purity, 1.7% impurity of 1-adamantanol). To avoid any influence due to the impurity, 1-F-A was purified prior to the TR-SHG analysis. Crystals used in this work were purified by recrystallization from methanol, detailed steps are as follows: (i) a saturated solution was prepared by dissolving the commercial 1-F-A in methanol (HPLC grade) at 40°C, (ii) the solution was filtrated at this temperature and put at room temperature in a glass vial, (iii) Crystals of 1-F-A were grown from the solution by slow evaporation. The obtained crystals possess an average crystal size of 200 μm . Purity was checked by GC-MS (99.93%) (see Appendix V).

IV-1-3. Characterization of 1-F-A Phase Transitions by DSC and Cold-stage Microscope

One detectable thermal event was observed by DSC between 120K and 300K (Figure IV-2-(a)). Upon cooling, the onset temperature is $226.00 \pm 0.24\text{K}$ with an enthalpy of $1.88 \pm 0.02\text{ kJ/mol}$. Upon heating, a hysteresis is observed, with an onset temperature at $231.00 \pm 0.17\text{K}$ and an enthalpy of $1.81 \pm 0.06\text{ kJ/mol}$. This thermal event obviously corresponds to a first-order phase transition. Moreover, these values are consistent with previously reported data from literature^{12,13,19}.

Cold-stage microscopy observations were performed on single crystals of 1-F-A, which were obtained on the cap of a closed vial by sublimation at 160°C. The crystal was cooled down at 1K/min to 153K, and was heated at 1K/min. The video was recorded during heating from 153K to 243K. At ca. 230K, the transition begins. One can observe the propagation of the transition front and the slight change of the volume, which corresponds to a first-order transition.

IV-1-4. TR-SHG Measurements

It is first necessary to mention that in the present case, the intensity of the measured SHG signal can be generated only by the non-centrosymmetric crystalline LT phase of 1-F-A. Based on S. K. Kurtz and T. T. Perry³¹, SHG intensity can thus be considered proportional to the mass fraction (or molar fraction) of the LT phase. The sample was cooled down from 300K to 100K at 1 K/min and then heated at 1 K/min. The thermal evolution of 1-F-A was monitored by TR-

SHG through tracking the SHG signal generated by the LT phase versus temperature (Figure IV-2-(b)). Apparently, the sample exhibiting a positive SHG signal at 100K, which confirms that the structure is non-centrosymmetric at this low temperature.¹⁹ The highest SHG signal generated by 1-F-A was around 1/5 of quartz SHG signal (a standard material exhibiting relatively low SHG signal with an average crystal size 45 μm).

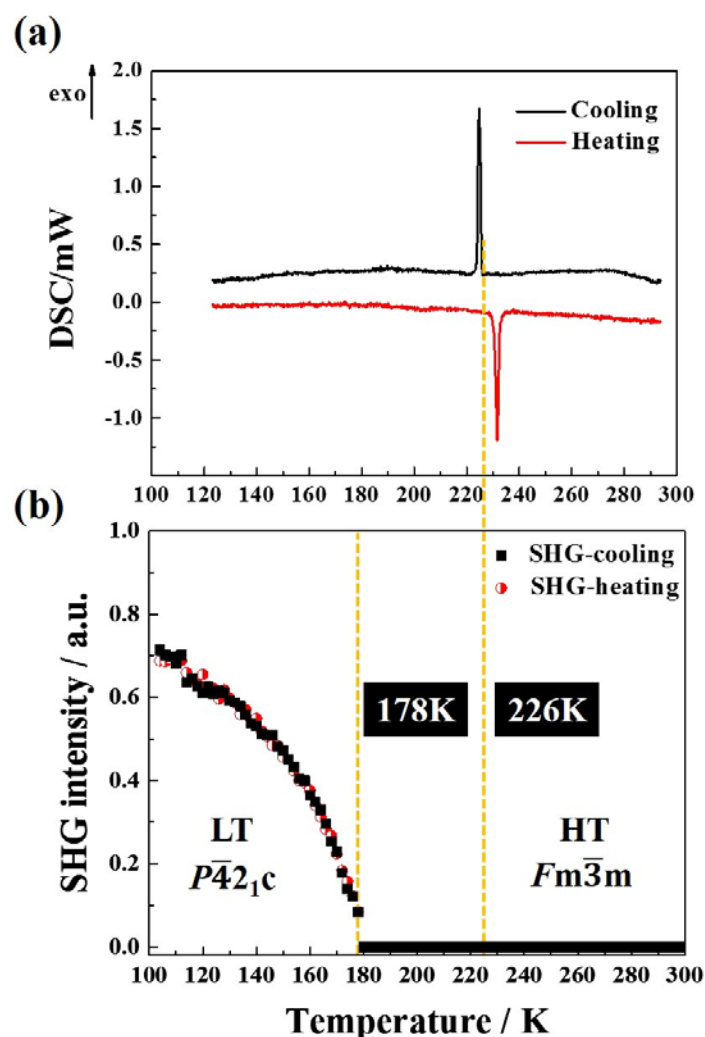


Figure IV-2. (a) DSC measuring curves obtained for the phase transitions of 1-F-A. Black line, upon cooling (1 K/min); red line, upon heating (1 K/min). (b) TR-SHG curves obtained for the phase transition of 1-F-A. Black square, upon cooling (1 K/min); red spot, upon heating (1 K/min).

Surprisingly, the SHG signal was observed to appear only at 178K (upon cooling) while the transition temperature was detected at 226K by DSC (black curve in Figure IV-2-(a)). The temperature difference is 48K. Obviously, this difference is too large to be due to the thermal gradient between the sample and the heating plate. Possible reasons for this phenomenon were investigated. Firstly, we supposed that the SHG signal generated by 1-F-A between 178K and

226K could have fallen under the detection threshold of our apparatus. Even though the detection threshold of our TR-SHG set-up can be considered as good (evaluated at circa 1/100 compared to the SHG intensity of quartz standard- 45 μm), the sample was annealed at 213K, a temperature between 178K and 226K in order to obtain a better crystallization of the sample (i.e., to possibly enhance the SHG signal). After 10 hours, no SHG signal was detected (Figure IV-3), which strongly suggests that no LT phase crystallized in the range of 178K and 226K.

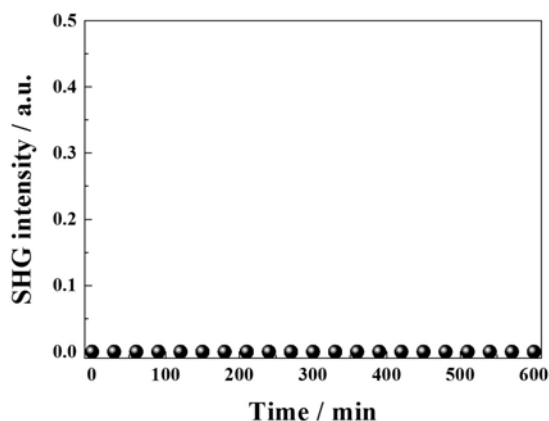


Figure IV-3. TR-SHG curve obtained for 1-F-A by annealing at 213K for 10h. No SHG signal was detected after 10h of annealing. Suggested that no LT phase was crystallized at 213K.

Secondly, it was supposed that the transition kinetics might be low and the thermodynamic equilibrium was not reached in this temperature range. So, the sample was annealed at 167K to possibly reach the thermodynamic equilibrium. Nevertheless, after 10 hours, no variation of the SHG signal was observed, indicating that the maximum amount of LT phase was already reached under the conditions used for the TR-SHG experiments (Figure IV-4).

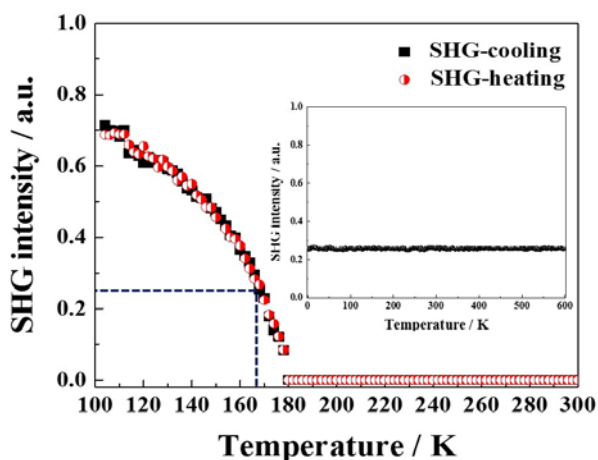


Figure IV-4. TR-SHG curve obtained for 1-F-A by annealing at 167K for 10h (inset). After 10h, no evolution of the SHG signal was observed. Indicates that the maximum amount of LT phase was reached at 167K.

Finally, these results led us to envisage that 1-F-A exhibits an intermediate phase between HT and LT phases in the temperature range of 178K to 226K. In the following, this intermediate phase is referred to as MT (for medium temperature). Since no SHG signal was detected between 178K and 226K, MT phase exhibits probably a centrosymmetric crystalline structure (confidence higher than 99%³⁶).

Another interesting result is that no hysteresis was observed for the SHG signal upon heating and cooling. That is to say, the SHG intensity profile is thus completely reversible (i.e., thermal cycles after cycles or after stopping and resuming the heating/cooling process). Consequently, a second-order transition between $MT \leftrightarrow LT$ can be suspected, complementary with the following observations:

- no detectable enthalpy change detected by DSC around 178K;
- no transition front propagation observed by cold-stage microscopy in the corresponding temperature range;
- no change of the cell volume at the presumed transition temperature (178K) in the work of Ben Hassine et al.¹⁹.

A thorough reinvestigation of the structures resolved from XRPD at various low temperatures confirmed this hypothesis as described in the following.

IV-1-5. Crystal Structure of MT Phase Determined from XRPD

When cooling down from HT phase to LT phase, single crystals break and thus powder diffraction is the only way to determine the structure of the low-temperature phases. Therefore, powder X-ray patterns obtained at 90K and 190K were submitted to a Rietveld refinement³², with the same rigid-body constraints that depicted in the work of Ben Hassine et al.¹⁹. A single overall isotropic displacement parameter and preferred orientation by using the Rietveld-Toraya function were refined. The final refined patterns together with the experimental and refined pattern differences are shown in Figure IV-5. The Rietveld refinement converged for LT phase and MT phase to a final R_{wp} value of 6.60% and 6.32%, respectively. The determined crystallographic data of both phases are summarized in Table IV-1.

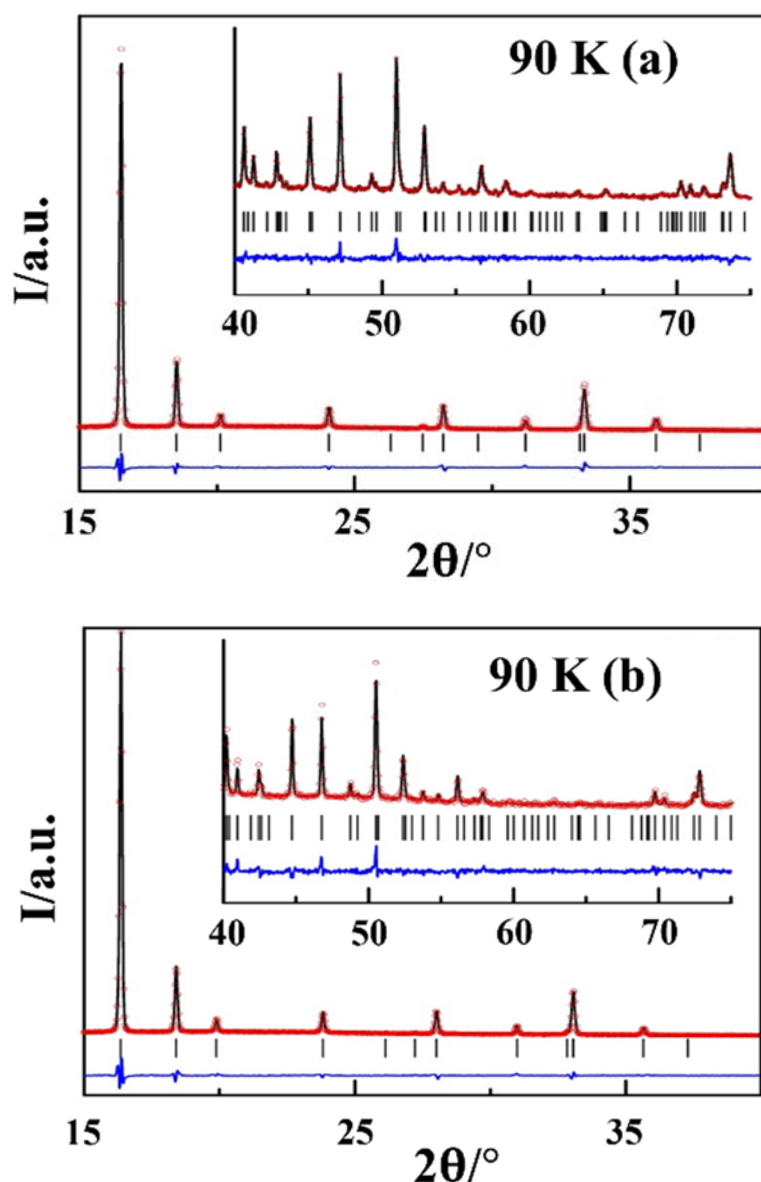


Figure IV-5. Experimental (red circles) and Rietveld refined (black line) diffraction patterns along with the difference profile (blue line) and Bragg reflections (vertical black sticks) of (a) LT phase $P\bar{4}2_1c$ at 90K; (b) MT phase $P4_2/nmc$ at 190K. The insets show the high-angle portion of each pattern (scaled to enhance their visibility).

Table IV-1. Crystallographic data determined for the MT phase and LT phase.

	MT phase	LT phase
Temperature (K)	190	90
Crystal system	Tetragonal	Tetragonal
Space group	$P4_2/nmc$	$P\bar{4}2_1c$
a=b (Å)	6.8145 (5)	6.7696 (4)
c (Å)	8.9232 (9)	8.8211 (9)
Z	2	2
Volume (Å ³)	414.37 (7)	404.25 (6)
Density (g/cm ³)	1.236	1.267

A crystal structure validation by Platon³³ was performed on the two resolved space groups. For the LT crystal structure at 90K, Platon results showed that no space group change is needed. While, if the MT phase is resolved in the space group of LT phase (at 190K), missed or additional symmetry are reported and Platon suggested the space group of $P4_2/nmc$. These results proved that the resolution of the space group in MT and LT phase are robust.

IV-1-6. Mechanism of MT↔LT Phase Transition

The presumed second-order phase transition of MT↔LT can be confirmed and interpreted microscopically by means of analysis of structural changes induced by temperature. The structure of the LT phase is shown in Figure IV-6-(a). The angle (ψ) defined between C-F bond of the four equilibrium positions for the statistical-disordered fluorine atoms (i.e., the molecular dipole direction) with the a (or b) tetragonal axis is ca. 6.8° at 90K. Increasing the temperature such angle continuously decreases and at ca. 180K it vanishes and remains null till the phase transition to the HT phase. Such changes provide two new mirror planes perpendicular to the a and b tetragonal axes. Thus, the non-centrosymmetric space group $P\bar{4}2_1c$ ($Z=2$) transforms to the centrosymmetric space group $P4_2/nmc$ ($Z=2$), giving rise to the so-called MT phase, which represents a subgroup-group transition. In addition, lattice parameters as well as volume as a function of temperature do not show any discontinuity (Figure IV-7). Therefore, the subgroup-group relation and the continuous lattice parameters and volume of LT and MT phases are in agreement with the continuity of the dynamic properties across this second-order phase transition¹⁹.

Figure IV-6-(b) depicts the (001) plane at 190K for MT phase. It is worth noting that the fractional occupancy of 1/4 of the fluorine atoms remains unchanged across the subgroup-group transition (MT↔LT). Therefore, it is probable that the phase transition does not change the type of molecular reorientation and that the dynamics and frequency of molecular motions in the solid-state are not (or slightly) modified at the transition temperature (178K).

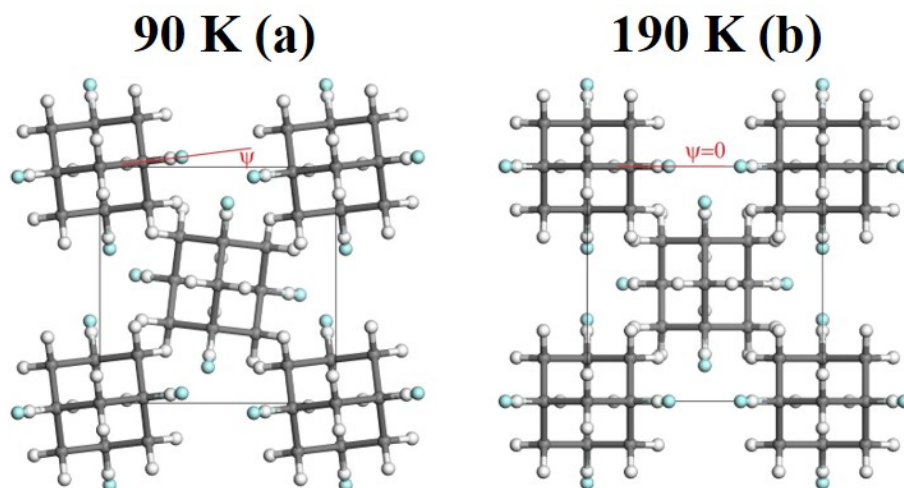


Figure IV-6. Crystal structure of 1-F-A (a) LT phase ($P\bar{4}2_1c$, $Z=2$) at 90K and (b) MT phase ($P4_2/nmc$, $Z=2$) at 190K. The fractional occupancy of 1/4 of the fluorine atoms (blue) remains unchanged across the $MT \leftrightarrow LT$ transition.

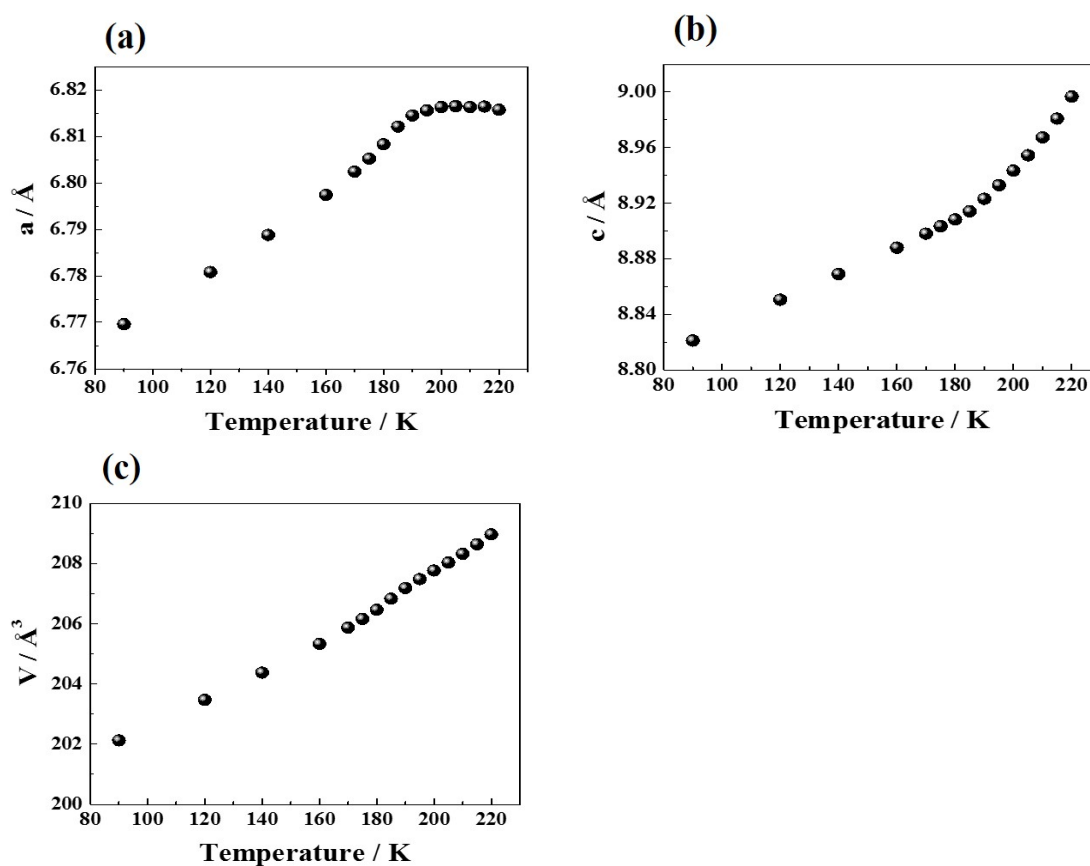


Figure IV-7. Variation of (a) the lattice parameter a and b , (b) the lattice parameter c and (c) the volume of 1-F-A in the temperature range of 90K to 220K. The continuity in the variation of the parameters and the volume as a function of temperature confirms the second-order transition.

To summarize, at 178K (on cooling), a second-order transition from MT to LT phase starts by a tilt of the angle ψ with as a consequence, an immediate change in the crystal structure. Then this angle ψ increases continuously with decreasing temperature but the crystal structure

remains in the LT phase. The above explanations fit well with the TR-SHG results. In Figure IV-2-(b), the SHG signal increases continuously from 178K to 100K. Because second harmonic generation is intrinsically related to the crystal structure and molecular fluctuations³⁴, it suggests that each SHG signal corresponds to a LT form in which 1-F-A molecules are tilted at a certain angle (e.g., $\Psi=6.8^\circ$ at 90K) by thermal agitation.

IV-1-7. Variation of the Order Parameter with Temperature

Order parameter η describes the extent of order or disorder in a material. It is equal to unity in the perfectly ordered state and zero in the completely disordered state³⁵.

TR-SHG was used to track the variation of the order parameter η (according to the Landau theory) versus temperature and to determine the critical exponent β characteristic of this variation.

The temperature dependence of the SHG intensity can be expressed as³⁶:

$$I_{\text{SHG}}(T) \propto (\chi^{(2)}(T))^2 \left[\frac{l^2(T)}{n_1^2(T)n_2(T)} \cdot \frac{\sin^2(\delta(T))}{(\delta(T))^2} \right] \quad (IV-1)$$

where l is the thickness of the crystals, n_1 and n_2 are the indices of refraction for $\lambda_1=1.064 \mu\text{m}$ (fundamental beam) and $\lambda_2=0.532 \mu\text{m}$ (second harmonic beam), respectively. $\chi^{(2)}$ is the nonlinear susceptibility tensor, and $\delta = \frac{\pi l}{2l_c}$ with the coherence length $l_c = \frac{\lambda_1}{4|n_1 - n_2|}$.

The term within brackets in eq. IV-1 is generally responsible for a sinc-square modulation (sinc^2) of the SHG intensity for single crystals. Considering that for powders, the orientations of the crystals are random (averaging over all crystallographic directions) and the particle size (mean value: circa 200 μm in the present study) is likely to exceed the coherence length, this modulation term can be neglected. Thus, in the following we assume that the SHG intensity is proportional to $(\chi^{(2)}(T))^2$. $\chi^{(2)}(T)$ is a third rank tensor with 27 coefficients but the number of independent coefficient can be reduced to 3 in the crystal class $\bar{4}2m$ by symmetry considerations. Moreover, assuming Kleinman conditions³⁷ are valid (no dispersion and absorption), the number of independent coefficient of the susceptibility tensor can be reduced to only one and $\chi^{(2)}(T)$ can be expressed as (in the contracted notation)^{38,39}:

$$\chi^{(2)}(T) = 2 \begin{bmatrix} 0 & 0 & 0 & d_{14} & 0 & 0 \\ 0 & 0 & 0 & 0 & d_{14} & 0 \\ 0 & 0 & 0 & 0 & 0 & d_{14} \end{bmatrix}$$

Taking into account the previous simplifications, $I_{\text{SHG}}(T)$ can be considered proportional to $d_{\text{eff}}^2(T)$, where d_{eff} is the effective coefficient of the nonlinear susceptibility. In the present case, d_{eff} is proportional to d_{14} coefficient (using Voigt's convention)⁴⁰. Moreover, d_{14} has already been shown to be a linear function of the order parameter η ^{30,34} in single crystals. In the present study, measurements are performed on powder samples with random crystallographic orientations but that does not modify the fact that $\chi^{(2)}(T)$ depends only on one coefficient. Therefore, we can assume that the SHG signal variations will be the same in all crystallographic directions. Hence, the square root of the SHG intensity can be taken as an order parameter:

$$\sqrt{I_{\text{SHG}}(T)} \propto d_{\text{eff}}(T) \propto \eta(T) \quad (IV-2)$$

The evolution of the order parameter η with temperature can be described by a simple critical power law derived from Landau theory^{30,41}:

$$\eta = A \left(1 - \frac{T}{T_c}\right)^\beta \quad (IV-3)$$

where, A is a pre-factor, T_c is the transition temperature and β is the critical exponent.

Based on the *eq. IV-2* and *eq. IV-3*, T_c and β values can be extracted from SHG results using:

$$\eta = \sqrt{I_{\text{SHG}}(T)} = A \left(1 - \frac{T}{T_c}\right)^\beta \quad (IV-4)$$

The fitting procedure performed from *eq. IV-4* with A , T_c , and β as free parameters (Figure IV-8) returns upon cooling a A value of 1.064 ± 0.012 , β value of 0.255 ± 0.008 with $T_c = 178.76 \pm 0.32\text{K}$. Upon heating, A value of 1.074 ± 0.011 , β is 0.263 ± 0.008 with $T_c = 179.06 \pm 0.33\text{K}$. The experimental transition temperature (T_c : 178K-180K) is thus consistent with the temperature determined by the fitting.

Order parameter η can also be obtained from XRPD by recording ψ (the angle between the molecular dipole C-F bond and the crystallographic a axis) versus temperature (see Figure IV-8). The XRPD data is fitted to the power-law (*eq. IV-4*), in which A corresponds to $\psi_{(T=0\text{K})}$

and gives rise to $A=1.000\pm 0.043$, $\beta=0.250\pm 0.027$ and $T_c=180.00\pm 0.12\text{K}$. It should be noticed here that the lowest temperature at which the structure was solved is 90K, close to the temperature (92K) at which reorientational motions are characterized by a relaxation time of the order of 100s^{19} . Below such temperature, reorientational motions are frozen, according to the previous dynamic study¹⁹ and thus, the LT phase becomes a low-dimensional glass⁴²⁻⁴⁴. It is obvious that such a LT phase cannot be the stable phase at 0K (the frozen disorder would confer a non-zero entropy) and the true stable phase remains at present elusive. Despite such a thermodynamic evidence, for both TR-SHG and ψ angle data from XRPD, we have assumed a continuous variation with temperature below 90K. Therefore, renormalization was done under the hypothesis that order parameter equals to unity at 0K. Under such assumption, Figure IV-8 clearly shows that both TR-SHG and ψ angle from XRPD describe the second-order transition.

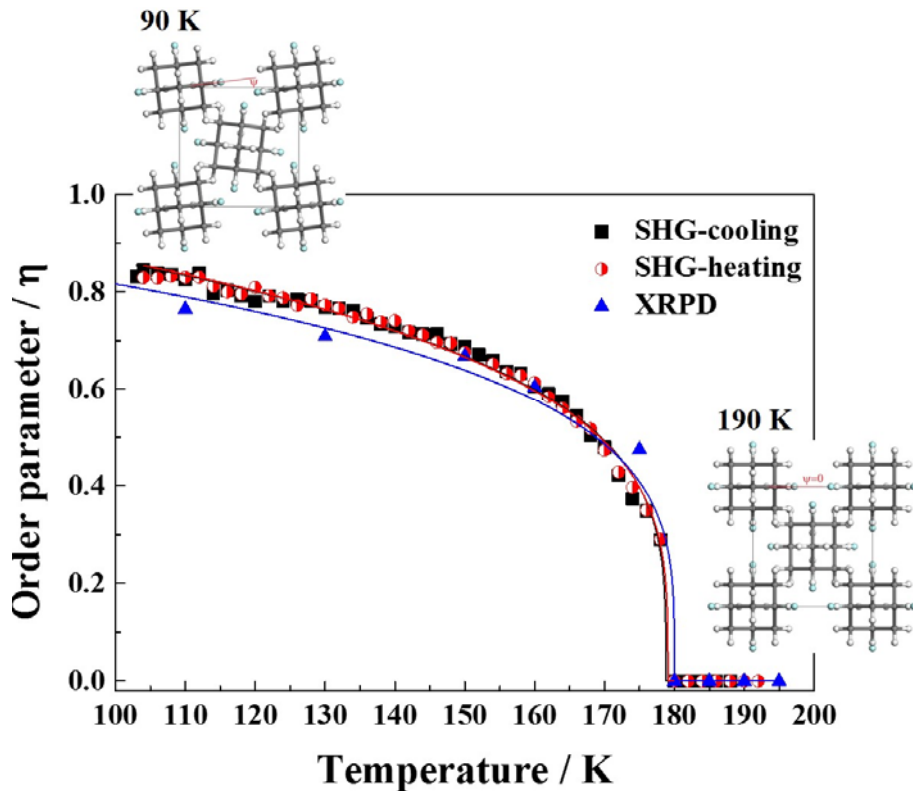


Figure IV-8. Order parameter determined from normalized values of the TR-SHG data and angle ψ between the C-F bond and a (or b) crystallographic axis from XRPD. Black line corresponds to the fit of eq. IV-4 for the TR-SHG data on cooling ($A=1.064\pm 0.012$, β is 0.255 ± 0.008 with $T_c=178.8\pm 0.3\text{K}$). Red line corresponds to the fit on heating ($A=1.074\pm 0.011$, β is 0.263 ± 0.008 with $T_c=179.1\pm 0.3\text{K}$). The blue line corresponds to the fit of XRPD data ($A=1.000\pm 0.043$, β is 0.250 ± 0.027 with $T_c=180.0\pm 0.1\text{K}$).

IV-1-8. Conclusion and Perspectives

Phase transitions of 1-F-A was thoroughly investigated by using TR-SHG and XRPD. The combination of both techniques unveiled a new phase (MT) with a stability domain between 178K and 231K. A second-order transition occurs at 178K between the LT phase ($P\bar{4}2_1c$) and the intermediate temperature phase (MT, $P4_2/nmc$), which arises from a continuous tilt of the molecular dipole around the (001) axis as function of temperature. A first-order transition occurs at 231K between the MT phase and the high temperature cubic phase HT ($Fm\bar{3}m$). Moreover, variation of the order parameter versus temperature for the second-order transition was monitored by TR-SHG and XRPD, results are in good agreement to support the proposed second-order transition mechanism.

In this work, the hint of a second-order phase transition might arouse certain debate as in the literature, for several compounds, second-order transitions finally turned out to be first order transition^{45,46}. For instance, the undetectable thermal signature of these transitions might be interpreted as inconsistent with thermodynamics. In fact, the structure differences between LT and MT phases are very subtle and the phase transition arises from a slight tilt of the 1-F-A molecule. Neither lattice parameters nor volume shows discontinuity at the transition temperature (178K). Consequently, transition between both phases should be difficult even impossible to be detected by usual DSC measurements. Measurement of heat capacity (C_p) at low temperature might give some indications of the MT \leftrightarrow LT transition. So, further study of this second-order transition combining other techniques could be suitable. For example, X-ray absorption near edge structure (XANES) might provide certain information about the change of the local symmetry. Finally, this work underlines that the study of polymorphs and phase transitions should be carried out carefully. The combination of TR-SHG and XRPD seems a suitable tool to monitor subtle symmetry changes when non-centrosymmetric structures are involved.

IV-2. Phase Transitions of Adamantane Investigated by TR-SHG

IV-2-1. Introduction

Adamantane molecule ($C_{10}H_{16}$) consists of six CH groups, which form an octahedron. Four CH groups that stick out from the center of the octahedron and form a tetrahedron (Figure IV-9).⁴⁷ It can be used: (i) for the synthesis of adamantane derivative, (ii) as pharmaceutical intermediates as well as being used as the raw material of light-sensitive material, cosmetic and surfactant intermediates and the epoxy curing agent.⁴⁸ (iii) adamantane is well suitable for sub-ambient calibration. i.e., for calibration of a DSC in the cooling mode because it shows no significant supercooling.⁴⁹⁻⁵³

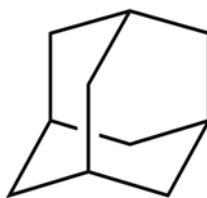


Figure IV-9. Molecular structure of adamantane.

Adamantane undergoes below its melting point ($T_m=541$ K) an order-disorder phase transition at $T_i=208.6$ K. Below 208.6 K, it crystallizes in a tetragonal ordered phase (LT phase) (space group $P\bar{4}2_1c$). At 208.6 K, it transforms to a disordered face centered cubic structure, space group $Fm\bar{3}m$ (HT phase). It was demonstrated that in the cubic phase the adamantane molecules perform 90° rotational jumps around the fourfold symmetry axis of the cubic crystal lattice.⁵⁴⁻⁵⁷ While arrangement of the molecules in the low-temperature phase remains unchanged except for a 9° tilt about the c axis.⁵⁶ Fyfe and Harold-Smith⁵⁴ illustrated that the order-disorder transition in adamantane takes place through a reorientation of the molecules about their two-fold axes. According to the X-ray diffraction measurements, the reorientation angle is either 9° or 81° , depending on which of the two disorder positions the individual adamantane molecule assumes in the disordered phase (depicted in Figure IV-10).

The HT phase of adamantane is centrosymmetric and consequently generates no SHG signal. LT phase is non-centrosymmetric (i.e., generates a SHG signal). Thus, in the following, TR-SHG was applied to study the phase transition of adamantane in order to give some information about the mechanism of the order-disorder transition.

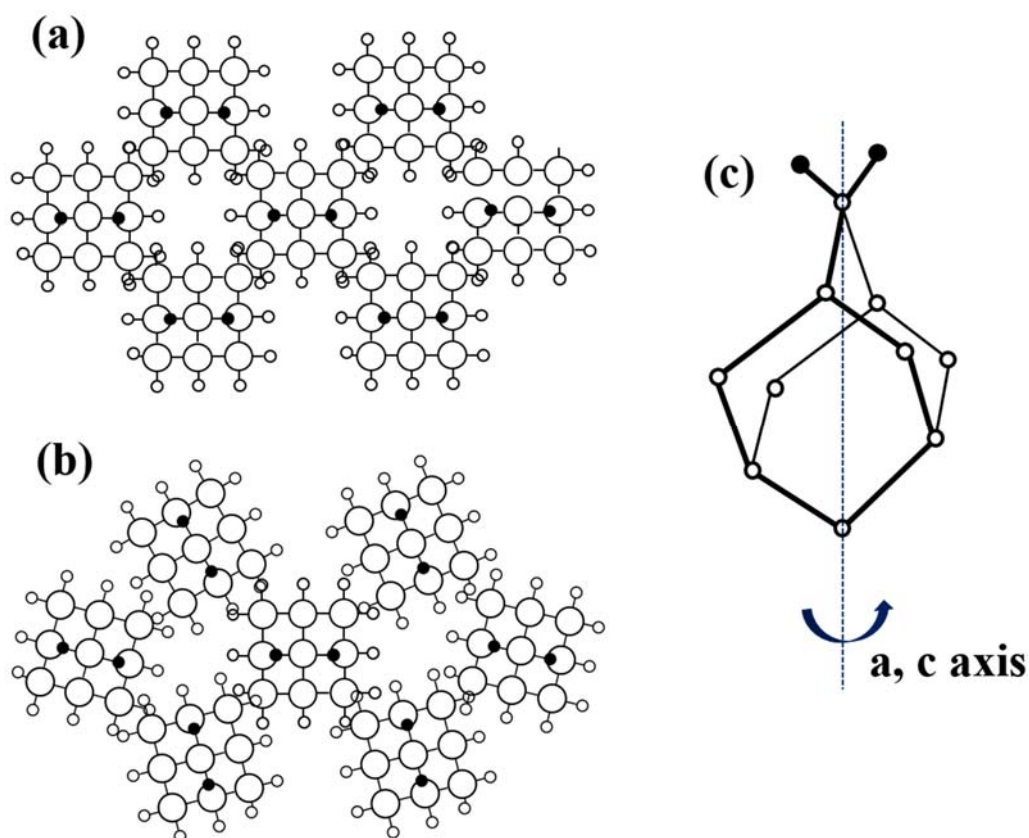


Figure IV-10. Illustration of order-disorder transition in adamantane. (a) HT phase. The random distribution of the molecules between two orientations, which are interchangeable by a 90° rotation about the projection axis is illustrated by the upper methylene hydrogens (dark circles). (b) LT phase. Ordered phase produced by molecular rotations of 9° and 81° . (c) Illustration of the adamantane molecules projected in (a) and (b). All of the hydrogen atoms have been omitted, except the upper pair of methylene hydrogens (dark circles).⁵⁴

IV-2-2. Preparation of the Sample

Adamantane (CAS registry number: 281-23-2) was purchased from Merck in Germany (99.83% purity). Crystals used in this work were purified by recrystallization from acetone. The obtained crystals possess an average crystal size of 200 μm . Purity was checked by GC-MS (99.99%) (same procedure as that used in 1-F-A).

IV-2-3. Characterization of Adamantane Phase Transitions by DSC and XRPD

One detectable thermal event was observed by DSC (Figure IV-11). Upon cooling (black curve), the onset temperature is $207.6 \pm 0.3\text{K}$ with an enthalpy of $3.1 \pm 0.1\text{KJ/mol}$. Upon heating (red curve), a hysteresis is observed, with an onset temperature at $208.5 \pm 0.3\text{K}$ and an enthalpy of $3.1 \pm 0.1\text{KJ/mol}$. These values are in consistency with previously reported data from literature^{47,54-58} and the transition corresponds to a first-order phase transition.

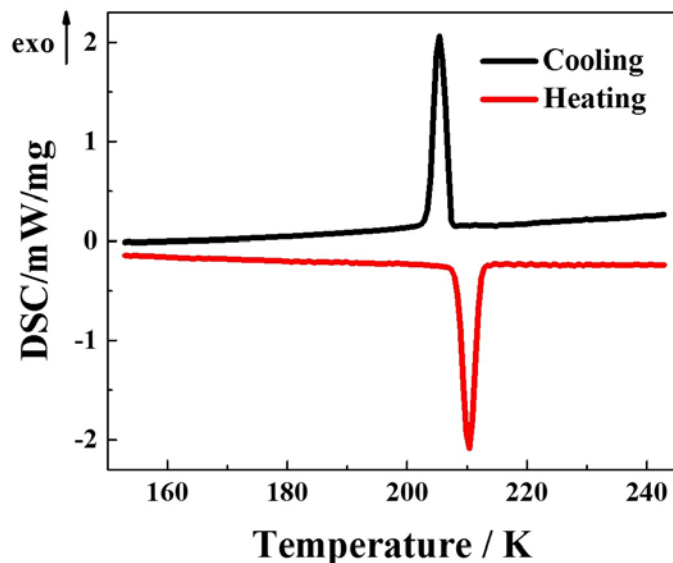


Figure IV-11. DSC measuring curves obtained for the phase transitions of adamantane. Black line, upon cooling; red line, upon heating.

XRPD pattern of the HT phase was collected at ambient temperature and the LT phase was obtained in the CSD database. XRPD patterns of two phases were compared (Figure IV-12).

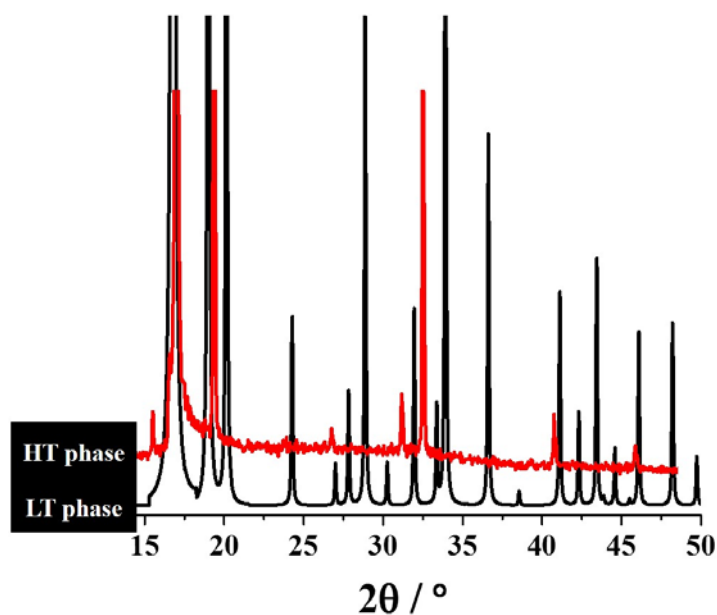


Figure IV-12. Comparison of XRPD patterns between the HT phase ($T=293\text{K}$) and the LT phase ($T=188\text{K}$) of adamantane.

Since the HT phase belongs to the cubic system and is highly disordered, less peaks were observed. The LT phase preserves main peaks of HT phase, two phases are related by a subgroup-group relation. Moreover, peaks in the LT phase shift to higher 2θ at different extent. This is due to different contraction extent in directions of a, b and c.

Cold-stage microscopy observations were also performed on single crystals of adamantane, only the transition at ca. 208 K (the temperature of first-order transition) was observed.

IV-2-4. TR-SHG Measurements of Adamantane Phase Transitions

The phase transition of adamantane was monitored by TR-SHG. The SHG signal is only generated by the non-centrosymmetric LT phase.

IV-2-4-1. Existence of an Intermediate Phase?

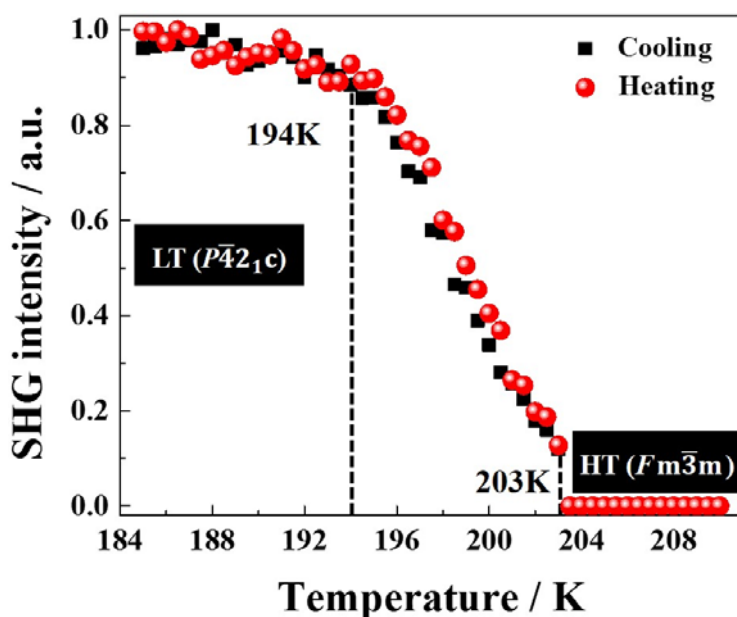


Figure IV-13. TR-SHG curves obtained for the phase transition of adamantane. Black square, upon cooling (0.5 K/min); red spot, upon heating (0.5 K/min). The signal appears at 203K, SHG intensity increases with lowering the temperature down to 194K and then keeps stable.

As is shown in Figure IV-13, SHG signal appears at 203K while the transition temperature was detected at ca. 208K by DSC (Figure IV-11), the temperature difference is 5K. This 5K difference might be due to (1) the inaccurate temperature regulation, or (2) the low detection threshold of the TR-SHG set-up. The precision of the Linkam in low temperatures was previously estimated at 1K, so the possibility 1 is inappropriate. To obtain a better crystallinity of the sample (i.e., to enhance the SHG signal) and to reach the thermodynamic equilibrium, the sample was annealed at 204K, 205K and 206K for 10h, no SHG signal was detected. Annealing at 191K, 197K, 199K, 201K and 203K for 10h, respectively, no variation of the SHG signal was observed, indicating that the maximum amount of LT phase was already reached under the conditions used for TR-SHG experiments.

Moreover, no hysteresis was observed in SHG signal upon heating and cooling. Consequently, if a phase transition could be confirmed, it should be a second-order like transition, while the transition of adamantane is reported to be a first-order like with a hysteresis (also shown in the DSC curves in Figure IV-11).

This presents great similarity to the phenomenon observed in the case of 1-fluoro-adamantane and thus led us to envisage that a centrosymmetric intermediate phase could exist between the HT and the LT phase. Moreover, the space groups of the HT and the LT phase in 1-fluoro-adamantane are the same as in adamantane. Therefore, an intermediate phase (MT) can be envisaged in adamantane. Further study with single crystal XRD or powder XRD is highly necessary to prove the existence of this MT phase.

IV-2-4-2. Transition Mechanism of Adamantane

Suppose only the HT phase and the LT phase exist in adamantane. At 203K, the cubic HT phase transforms to the tetragonal LT phase via a destruction-reconstruction process (first-order transition). This LT phase is not an ordered phase but moves continuously from 203K to 194K. Proves can be found in the work of Amoureux and Foulon⁵⁵, they declaimed that the low-temperature phase of adamantane still presents some slow dynamical disorder. At 194K, the molecules are frozen, thus the LT becomes a glassy crystal.

IV-2-5. Conclusion and Perspectives

Through the investigation of phase transition in adamantane by TR-SHG, an intermediate centrosymmetric phase was envisaged. But further confirmation via single crystal XRD or powder XRD is necessary. Moreover, since the HT phase and the LT phase of adamantane crystallize in the same space groups as in 1-F-A, we could expect a complete solid-solution between adamantane and 1-F-A, shown in Figure IV-14. By changing the concentration of 1-F-A/A mixture, we expect to see the variation of the transition temperatures. The temperature range goes from 48K in pure 1-F-A to 4K in pure A (the shrinkage of the green region).

In light of the present study of adamantane and 1-fluoro-adamantane, a thoroughly reinvestigation of phase transitions in adamantane derivatives could be envisaged.

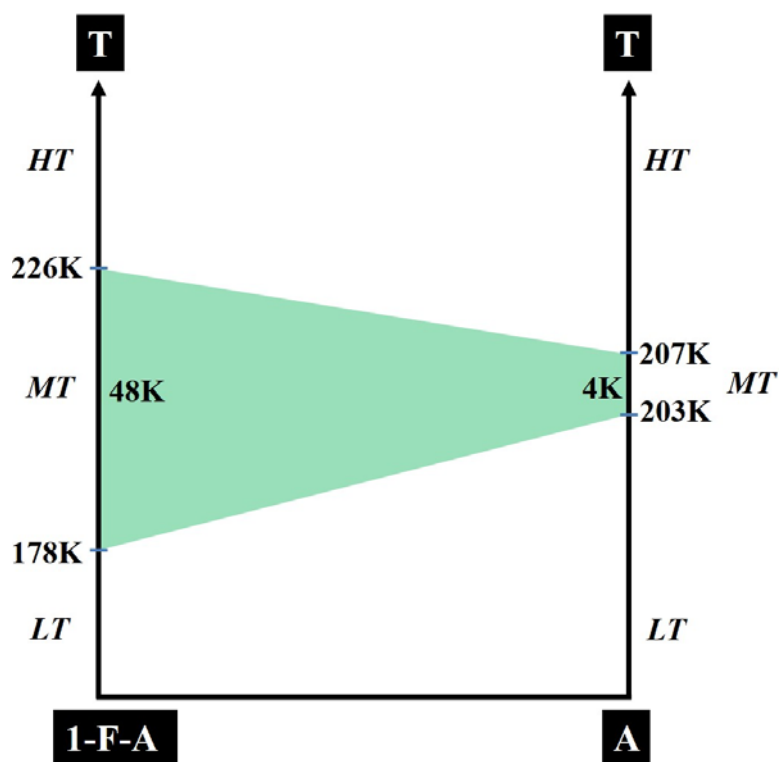


Figure IV-14. Schematic phase diagram between adamantane (A) and 1-fluoro-adamantane (1-F-A).

References

- (1) McIntosh, G. C.; Yoon, M.; Berber, S.; Tománek, D. Diamond Fragments as Building Blocks of Functional Nanostructures. *Phys. Rev. B* **2004**, *70* (4), 045401.
- (2) Dahl, J. E.; Liu, S. G.; Carlson, R. M. K. Isolation and Structure of Higher Diamondoids, Nanometer-Sized Diamond Molecules. *Science* **2003**, *299* (5603), 96–99.
- (3) Yang, W. L.; Fabbri, J. D.; Willey, T. M.; Lee, J. R. I.; Dahl, J. E.; Carlson, R. M. K.; Schreiner, P. R.; Fokin, A. A.; Tkachenko, B. A.; Fokina, N. A.; et al. Monochromatic Electron Photoemission from Diamondoid Monolayers. *Science* **2007**, *316* (5830), 1460–1462.
- (4) Wang, Y.; Kioupakis, E.; Lu, X.; Wegner, D.; Yamachika, R.; Dahl, J. E.; Carlson, R. M. K.; Louie, S. G.; Crommie, M. F. Spatially Resolved Electronic and Vibronic Properties of Single Diamondoid Molecules. *Nat. Mater.* **2008**, *7* (1), 38–42.
- (5) Guo, W.; Galoppini, E.; Gilardi, R.; Rydja, G. I.; Chen, Y.-H. Weak Intermolecular Interactions in the Crystal Structures of Molecules with Tetrahedral Symmetry: Diamondoid Nets and Other Motifs. *Cryst. Growth Des.* **2001**, *1* (3), 231–237.
- (6) Affouard, F.; Guinet, Y.; Denicourt, T.; Descamps, M. Indication for a Change of Dynamics in Plastic Crystal Chloroadamantane: Raman Scattering Experiment and Molecular Dynamics Simulation. *J. Phys. Condens. Matter* **2001**, *13* (33), 7237–7248.
- (7) Bée, M.; Amoureux, J. P. Molecular Reorientations of 1-Chloroadamantane in Its Plastic Solid Phase: Correlation Times from Incoherent Quasielastic Neutron Scattering Study. *Mol. Phys.* **1983**, *48* (1), 63–79.
- (8) Decressain, R.; Amoureux, J. P.; Carpentier, L.; Nagy, J. B. NMR in Molecular Crystals: An Example: Fluoroadamantane C₁₀H₁₅F. *Mol. Phys.* **1991**, *73* (3), 553–569.
- (9) Ben Hassine, B.; Negrier, Ph.; Barrio, M.; Mondieig, D.; Massip, S.; Tamarit, J. Ll. Phase Transition in Hydrogen-Bonded 1-Adamantane-Methanol. *Cryst. Growth Des.* **2015**, *15* (8), 4149–4155.
- (10) Negrier, Ph.; Barrio, M.; Romanini, M.; Tamarit, J. Ll.; Mondieig, D.; Krivchikov, A. I.; Kepinski, L.; Jezowski, A.; Szewczyk, D. Polymorphism of 2-Adamantanone. *Cryst. Growth Des.* **2014**, *14* (5), 2626–2632.
- (11) Negrier, Ph.; Barrio, M.; Tamarit, J. Ll.; Mondieig, D. Polymorphism in 2-X-Adamantane Derivatives (X = Cl, Br). *J. Phys. Chem. B* **2014**, *118* (32), 9595–9603.
- (12) Clark, T.; Knox, T. M. O.; Mackle, H.; McKervey, M. A. Order–disorder Transitions in Substituted Adamantanes. *J. Chem. Soc. Faraday Trans. 1 Phys. Chem. Condens. Phases* **1977**, *73* (0), 1224.
- (13) Kawai, N. T.; Gilson, D. F. R.; Butler, I. S. Phase Transitions in Adamantane Derivatives: 1-Fluoroadamantane. *Can. J. Chem.* **1991**, *69* (11), 1758–1765.
- (14) Jaeger, G. The Ehrenfest Classification of Phase Transitions: Introduction and Evolution. *Arch. Hist. Exact Sci.* **1998**, *53* (1), 51–81.
- (15) Amoureux, J. P.; Bee, M.; Sauvajol, J. L. Structure of 1-Fluoroadamantane, C₁₀H₁₅F, in Its Plastic Phase. *Acta Crystallogr. Sect. B* **1982**, *38* (7), 1984–1989.
- (16) Guinet, Y.; Sauvajol, J. L.; Muller, M. Raman Studies of Orientational Disorder in Crystals. *Mol. Phys.* **1988**, *65* (3), 723–738.
- (17) Amoureux, J. P.; Castelain, M.; Bee, M.; Benadda, M. D.; More, M. Dielectric Properties of 1-Fluoroadamantane C₁₀H₁₅F. *Mol. Phys.* **1985**, *55* (1), 241–251.
- (18) Bée, M.; Amoureux, J. P. Temperature Dependence of the Molecular Reorientation Rates in the Plastic

- Solid Phase of 1-Fluoroadamantane. *Mol. Phys.* **1983**, *50* (4), 585–602.
- (19) Ben Hassine, B.; Negrier, Ph.; Romanini, M.; Barrio, M.; Macovez, R.; Kallel, A.; Mondieig, D.; Tamarit, J. Ll. Structure and Reorientational Dynamics of 1-F-Adamantane. *Phys. Chem. Chem. Phys.* **2016**, *18* (16), 10924–10930.
- (20) Vogt, H. Study of Structural Phase Transitions by Techniques of Nonlinear Optics. *Appl. Phys.* **1974**, *5* (2), 85–96.
- (21) Vogt, H. Study of Disordered Crystals by Optical Second Harmonic Generation. *Phys. Status Solidi B* **1973**, *58* (2), 705–714.
- (22) Dougherty, J. P.; Kurtz, S. K. A Second Harmonic Analyzer for the Detection of Non-Centrosymmetry. *J. Appl. Cryst.* **1976**, *9*, 145–158.
- (23) Clevers, S.; Simon, F.; Sanselme, M.; Dupray, V.; Coquerel, G. Monotropic Transition Mechanism of M-Hydroxybenzoic Acid Investigated by Temperature-Resolved Second Harmonic Generation. *Cryst. Growth Des.* **2013**, *13* (8), 3697–3704.
- (24) Smilowitz, L.; Henson, B. F.; Asay, B. W.; Dickson, P. M. The B- δ Phase Transition in the Energetic Nitramine-Octahydro-1,3,5,7-Tetranitro-1,3,5,7-Tetrazocine: Kinetics. *J. Chem. Phys.* **2002**, *117* (8), 3789–3798.
- (25) Smilowitz, L.; Henson, B. F.; Romero, J. J. Intercomparison of Calorimetry, Raman Spectroscopy, and Second Harmonic Generation Applied to Solid-Solid Phase Transitions. *J. Phys. Chem. A* **2009**, *113* (35), 9650–9657.
- (26) Hall, R. C.; Paul, I. C.; Curtin, D. Y. Structures and Interconversion of Polymorphs of 2,3-Dichloroquinizarin. Use of Second Harmonic Generation to Follow the Change of a Centrosymmetric to a Polar Structure. *J. Am. Chem. Soc.* **1988**, *110* (9), 2848–2854.
- (27) Aktsipetrov, O. A.; Misuryaev, T. V.; Murzina, T. V.; Blinov, L. M.; Fridkin, V. M.; Palto, S. P. Optical Second-Harmonic-Generation Probe of Two-Dimensional Ferroelectricity. *Opt. Lett.* **2000**, *25* (6), 411–413.
- (28) Bergman, J. G. Molecular Mechanics of the Ferroelectric to Paraelectric Phase Transition in Lithium Tantalate via Optical Second Harmonic Generation. *J. Am. Chem. Soc.* **1976**, *98* (4), 1054–1055.
- (29) Clevers, S.; Rougeot, C.; Simon, F.; Sanselme, M.; Dupray, V.; Coquerel, G. Detection of Order-disorder Transition in Organic Solids by Using Temperature Resolved Second Harmonic Generation (TR-SHG). *J. Mol. Struct.* **2014**, *1078*, 61–67.
- (30) Steinbrener, S.; Jahn, I. R. The Order-Disorder Phase Transition in NH₄Cl: A New Investigation by Means of Optical Second Harmonic Generation at Atmospheric Pressure. *J. Phys. C Solid State Phys.* **1978**, *11* (7), 1337–1349.
- (31) Kurtz, S. K.; Perry, T. T. A Powder Technique for the Evaluation of Nonlinear Optical Materials. *J. Appl. Phys.* **1968**, *39* (8), 3798–3813.
- (32) Rietveld, H. M. A Profile Refinement Method for Nuclear and Magnetic Structures. *J. Appl. Crystallogr.* **1969**, *2* (2), 65–71.
- (33) Spek, A. L. Structure Validation in Chemical Crystallography. *Acta Crystallogr. D Biol. Crystallogr.* **2009**, *65* (2), 148–155.
- (34) Chemla, D. S. Nonlinear Optical Properties of Condensed Matter. *Rep. Prog. Phys.* **1980**, *43* (10), 1191.
- (35) Rao, C. N. R.; Rao, K. J. *Phase Transitions in Solids: An Approach to the Study of the Chemistry and Physics of Solids*; McGraw-Hill, **1978**.

- (36) Boyd, G.; Kasper, H.; McFee, J. Linear and Nonlinear Optical Properties of AgGaS₂, CuGaS₂, and CuInS₂, and Theory of the Wedge Technique for the Measurement of Nonlinear Coefficients. *IEEE J. Quantum Electron.* **1971**, *7* (12), 563–573.
- (37) Boyd, R. W. *Nonlinear Optics*. In *Nonlinear Optics (Third Edition)*; Academic Press: Burlington, **2008**; pp 1–67.
- (38) Nye, J. F. *Physical Properties of Crystals: Their Representation by Tensors and Matrices*; Clarendon Press, **1985**.
- (39) Marder, S. R.; Sohn, J. E.; Stucky, G. D. *Materials for Nonlinear Optics: Chemical Perspectives*; American Chemical Society, **1991**.
- (40) Dmitriev, V. G.; Gurzadyan, G. G.; Nikogosyan, D. N.; Lotsch, H. K. V. *Handbook of Nonlinear Optical Crystals*; Springer Series in Optical Sciences: Berlin, Heidelberg, **1999**; Vol. 64.
- (41) Bruins, D. E.; Garland, C. W. Piezoelectricity and Long-range Order in NH₄Cl. *J. Chem. Phys.* **1975**, *63* (10), 4139–4142.
- (42) Romanini, M.; Negrier, Ph.; Tamarit, J. Ll.; Capaccioli, S.; Barrio, M.; Pardo, L. C.; Mondieig, D. Emergence of Glassy-like Dynamics in an Orientationally Ordered Phase. *Phys. Rev. B* **2012**, *85* (13), 134201.
- (43) Pérez, S. C.; Zuriaga, M.; Serra, P.; Wolfenson, A.; Negrier, P.; Tamarit, J. L. Dynamic Characterization of Crystalline and Glass Phases of Deuterated 1,1,2,2 Tetrachloroethane. *J. Chem. Phys.* **2015**, *143* (13), 134502.
- (44) Tripathi, P.; Mitsari, E.; Romanini, M.; Serra, P.; Tamarit, J. L.; Zuriaga, M.; Macovez, R. Orientational Relaxations in Solid (1,1,2,2) Tetrachloroethane. *J. Chem. Phys.* **2016**, *144* (16), 164505.
- (45) Mnyukh, Y. *Fundamentals of Solid-State Phase Transitions, Ferromagnetism and Ferroelectricity*; AuthorHouse, **2001**.
- (46) Mnyukh, Y. Second-Order Phase Transitions, L. Landau and His Successors. *ArXiv11021085 Phys.* **2011**.
- (47) Parliński, K. On the Phase Transition in Adamantane. *Phys. Status Solidi A* **1982**, *74* (1), K37–K40.
- (48) Mansoori, G. A.; Araujo, P. L. B. D.; Araujo, E. S. D. *Diamondoid Molecules: With Applications in Biomedicine, Materials Science, Nanotechnology & Petroleum Science*; World Scientific, **2012**.
- (49) Hakvoort, G.; Hol, C. M.; Ekeren, P. J. van. DSC Calibration During Cooling. A Survey of Possible Compounds. *J. Therm. Anal. Calorim.* **2001**, *64* (1), 367–375.
- (50) Hakvoort, G.; Hol, C. M. DSC Investigation of Some Testing and Calibration Compounds, Particularly During Cooling. *J. Therm. Anal. Calorim.* **1998**, *52* (1), 195–202.
- (51) Hakvoort, G.; Hol, C. M. DSC Calibration During Cooling. *J. Therm. Anal. Calorim.* **1999**, *56* (2), 717–722.
- (52) Hakvoort, G. DSC Calibration below 0°C. *J. Therm. Anal.* **1994**, *41* (6), 1551–1555.
- (53) Van Ekeren, P. J.; Van Genderen, A. C. G.; Van den Berg, G. J. K. Redetermination of the Thermodynamic Properties of the Solid–Solid Transition of Adamantane by Adiabatic Calorimetry to Investigate the Suitability as a Reference Material for Low-Temperature DSC-Calibration. *Thermochim. Acta* **2006**, *446* (1–2), 33–35.
- (54) Fyfe, C. A.; Harold-Smith, D. Potential Energy Calculations of the Rotational Barriers of Molecular Solids. II. The Dynamic Structures of Adamantane and Hexamethylenetetramine in the Solid State and the Nature of the Phase Transition in Adamantane. *Can. J. Chem.* **1976**, *54* (5), 769–782.
- (55) Amoureux, J. P.; Foulon, M. Comparison between Structural Analyses of Plastic and Brittle Crystals.

Acta Crystallogr. B **1987**, *43* (5), 470–479.

- (56) Nordman, C. E.; Schmitkons, D. L. Phase Transition and Crystal Structures of Adamantane. *Acta Crystallogr.* **1965**, *18* (4), 764–767.
- (57) Resing, H. A. NMR Relaxation in Adamantane and Hexamethylenetetramine: Diffusion and Rotation. *Mol. Cryst.* **1969**, *9* (1), 101–132.
- (58) Chang, S.-S.; Westrum, E. F. Heat Capacities and Thermodynamic Properties of Globular Molecules. I. Adamantane and Hexamethylenetetramine 1. *J. Phys. Chem.* **1960**, *64* (10), 1547–1551.

General Conclusion and Perspectives

The main objective of this research work was to develop complementary analytical approaches based on temperature-resolved second harmonic generation (TR-SHG) to address various issues of solid-state characterization and solid-solid transitions.

In chapter I, basic notions in solid-states and nonlinear optics were introduced. Various studies based on the second harmonic generation (SHG) were reviewed.

In chapter II, the usefulness of TR-SHG for the construction of phase diagrams was evaluated. Following an initial work conducted by a former student Dr. Simon Clevers on the system constituted by formic acid and water, the binary phase diagram between urea and water was studied by TR-SHG. A comprehensive approach of the evolution of the SHG signal versus temperature was developed to make the best use of the experimental results. This allowed us to construct the phase diagram and to precisely determine the eutectic composition. The method was further applied to other two systems: 1,3-dimethylurea (DMU)/water and hexamethylenetetramine/water and the impact of the non-phase-matching property of crystals on SHG signal was discussed. These results confirmed the potential of TR-SHG to complement classical techniques, such as DSC, with of course as an essential condition that one of the component should be non-centrosymmetric.

The study of binary phase diagrams by TR-SHG presented in this work is only a first step and potential future work could be envisaged. Other phase equilibria could be studied: ternary phase diagrams between two non-centrosymmetric components and one centrosymmetric component could be constructed by TR-SHG, unary system versus temperature and pressure could be also explored and the combination of DSC, TR-XRPD and TR-SHG would be powerful. An odd order harmonic technique could be used, i.e., third-order harmonic (THG), in which the centrosymmetric structures can generate signals. So that the whole phase diagrams of a non-centrosymmetric/centrosymmetric system could be obtained. Despite the advantages of the TR-SHG shown in the cases studied in this work, challenges are also obvious. First, TR-SHG cannot be an independent technique without combining with other techniques. Second, the SHG signal generated by the non-centrosymmetric components should be high or at least prominent to

discern the variations of the SHG signals. Third, the application of TR-SHG on ternary phase diagrams would encounter more difficulties, the interpretations of the SHG signals would be more complicated than for the binary system.

In chapter III, we focused on the potential of TR-SHG for tracking mechanisms and kinetics of phase transitions through two cases: crystallization of DMU monohydrate and monotropic transition of 2-adamantanone. Activation energies in both cases were calculated based on the TR-SHG results. The sluggish behavior of the formation of DMU monohydrate was explained and a two-step transition mechanism was proposed for the transition in 2-adamantanone. Again, TR-SHG provided another approach to determine kinetic parameters and to evaluate the activation energies involved. In particular, it is shown that for isothermal processes, the determination of activation energies by TR-SHG can be more reliable than by DSC. Therefore, this work could find direct extensions for the study of kinetics of crystallization from amorphous state or crystallization from solution.

In Chapter IV, we reported our investigations on solid-solid phase transitions of 1-fluoro-adamantane and adamantane. An intermediate new phase (MT) of 1-fluoro-adamantane between the high-temperature and the low temperature phases was revealed by TR-SHG and further confirmed by XRPD through resolving its structure. The transition mechanism between MT and LT phases was proposed as a second-order like transition. A new intermediate phase in adamantane was also speculated. The proposition of the second-order transition for 1-fluoro-adamantane might be seen as controversial. Indeed, some researchers (e.g., Dr. Yuri Mnyukh) believe that only first-order transition exists, that all the transitions go through a destruction-reconstruction processes, and that no well-documented example of “pure” second-order transition exists. 1-fluoro-adamantane could thus be considered as an interesting case to go further on that subject by comparing TR-SHG results with results obtained from other techniques, such as solid-state NMR, low-temperature heat capacity measurements and BDS.

Through these two case studies, TR-SHG showed its high sensitivity to subtle symmetry changes and showed its particular relevance when low-temperature measurements are required

as low temperature analyses are often difficult to implement on classical equipment. In addition, a modeling approach could also be coupled to correlate SHG signal to the sample characteristics. The evolution of: the internal disorder, the crystallographic packing (position of atoms in the crystal lattice, molecular conformation) and the coefficient of thermal expansion of the crystalline mesh versus temperature may have effects on the SHG signal. Recently, researchers speculated that the disordered materials might be more efficient candidates for nonlinear optical devices than perfect crystals. So, adamantane and its derivatives might play a role in the domain of nonlinear optics.

Besides the potential of SHG based analysis techniques highlighted in this PhD work, it is important to remain aware that because of the polycrystalline character of the samples used, our investigations were mainly based on a simplified theory of the SHG process. Of course, SHG signals are affected by crystal form, particle size, particle size distribution, degree of crystallinity and even crystal habit but in the powder SHG, most of these parameters are averaged.

The issues developed in this thesis could benefit from a SHG microscopy and imaging approach (see figures below).

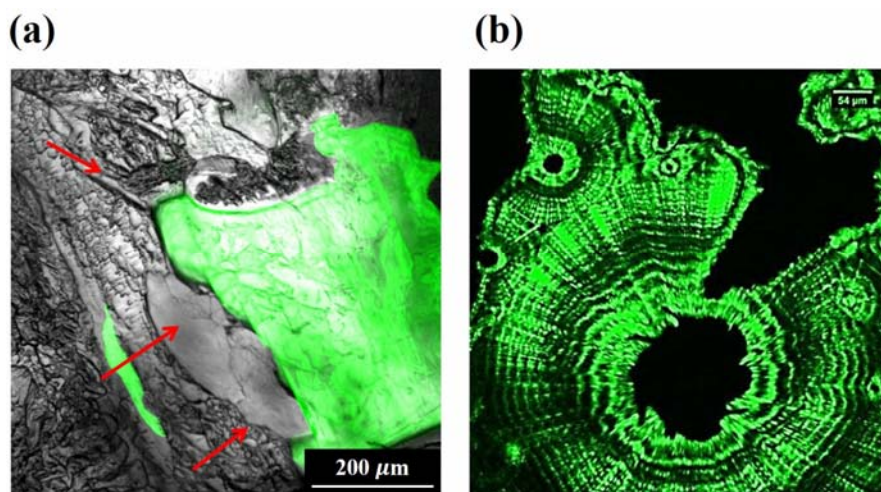


Figure. (a) Image of a single crystal undergoing polymorphic transition, and (b) semi-crystalline polymer crystallizing in a non-centrosymmetric space group.

For example, polarization resolved SHG image could afford to discriminate various sources of SHG signals (which exhibit different susceptibility tensors). Then, the analysis of image

contrast could make possible the visualization of localized structural inhomogeneities. In addition, the high spatial resolution offered by SHG microscopy would allow the characterization of very small crystals (micrometric scale or slightly lower) with a minimum sample preparation. This type of device could also be easily coupled to modules allowing to work at variable temperatures and under controlled atmosphere.

Appendices

Appendix I. Table of 230 Space Groups

All the 230 space groups are shown below. In blue are all the centrosymmetric achiral space groups, in orange are all the non-centrosymmetric chiral space groups and in purple are all the non-centrosymmetric achiral space groups.

Space Groups								
Triclinic								
1	<i>P1</i>							
$\bar{1}$	<i>P$\bar{1}$</i>							
Monoclinic								
2	<i>P2</i>	<i>P2₁</i>	<i>C2</i>					
m	<i>Pm</i>	<i>Pc</i>	<i>Cm</i>	<i>Cc</i>				
2/m	<i>P2/m</i>	<i>P2₁/m</i>	<i>C2/m</i>	<i>P2/c</i>	<i>P2₁/c</i>	<i>C2/c</i>		
Orthorhombic								
222	<i>P222</i>	<i>P222₁</i>	<i>P2₁2₁2</i>	<i>P2₁2₁2₁</i>	<i>C222₁</i>	<i>C222</i>	<i>F222</i>	<i>I222</i>
	<i>I2₁2₁2₁</i>							
mm2	<i>Pmm2</i>	<i>Pmc2₁</i>	<i>Pcc2</i>	<i>Pma2</i>	<i>Pca2₁</i>	<i>Pnc2</i>	<i>Pmn2₁</i>	<i>Pba2</i>
	<i>Pna2₁</i>	<i>Pnn2</i>	<i>Cmm2</i>	<i>Cmc2₁</i>	<i>Ccc2</i>	<i>Amm2</i>	<i>Abm2</i>	<i>Ama2</i>
	<i>Aba2</i>	<i>Fmm2</i>	<i>Fdd2</i>	<i>Imm2</i>	<i>Iba2</i>	<i>Ima2</i>		
mmm	<i>Pmmm</i>	<i>Pnnn</i>	<i>Pccm</i>	<i>Pban</i>	<i>Pmma</i>	<i>Pnna</i>	<i>Pmna</i>	<i>Pcca</i>
	<i>Pbam</i>	<i>Pccn</i>	<i>Pbcm</i>	<i>Pnmm</i>	<i>Pmnm</i>	<i>Pbcn</i>	<i>Pbca</i>	<i>Pnma</i>
	<i>Cmcm</i>	<i>Cmca</i>	<i>Cmmm</i>	<i>Cccm</i>	<i>Cmma</i>	<i>Ccca</i>	<i>Fmmm</i>	<i>Fddd</i>
	<i>Immm</i>	<i>Ibam</i>	<i>Ibca</i>	<i>Imma</i>				

Space Groups								
Tetragonal								
4	<i>P4</i>	<i>P4₁</i>	<i>P4₂</i>	<i>P4₃</i>	<i>I4</i>	<i>I4₁</i>		
$\bar{4}$	<i>P$\bar{4}$</i>	<i>I$\bar{4}$</i>						
4/m	<i>P4/m</i>	<i>P4₂/m</i>	<i>P4/n</i>	<i>P4₂/n</i>	<i>I4/m</i>	<i>I4₁/a</i>		
422	<i>P422</i>	<i>P4₂2₁2</i>	<i>P4₁22</i>	<i>P4₁2₁2</i>	<i>P4₃22</i>	<i>P4₂2₁2</i>	<i>P4₃22</i>	<i>P4₃2₁2</i>
	<i>I422</i>	<i>I4₁22</i>						
4mm	<i>P4mm</i>	<i>P4bm</i>	<i>P4₂cm</i>	<i>P4₂nm</i>	<i>P4cc</i>	<i>P4nc</i>	<i>P4₂mc</i>	<i>P4₂bc</i>
	<i>I4mm</i>	<i>I4cm</i>	<i>I4₁md</i>	<i>I4₁cd</i>				
$\bar{4}2m$	<i>P$\bar{4}$2m</i>	<i>P$\bar{4}$2c</i>	<i>P$\bar{4}$2₁m</i>	<i>P$\bar{4}$2₁c</i>	<i>P$\bar{4}$m2</i>	<i>P$\bar{4}$c2</i>	<i>P$\bar{4}$2b</i>	<i>P$\bar{4}$n2</i>
	<i>I$\bar{4}$m2</i>	<i>I$\bar{4}$c2</i>	<i>I$\bar{4}$2m</i>	<i>I$\bar{4}$2d</i>				
4/mmm	<i>P4/mmm</i>	<i>P4/mcc</i>	<i>P4/nbm</i>	<i>P4/nnc</i>	<i>P4/mbm</i>	<i>P4/mnc</i>	<i>P4/nmm</i>	<i>P4/nnc</i>
	<i>P4₂/mmc</i>	<i>P4₂/mcm</i>	<i>P4₂/nbc</i>	<i>P4₂/nnm</i>	<i>P4₂/mbc</i>	<i>P4₂/mnm</i>	<i>P4₂/nmc</i>	<i>P4₂/ncm</i>
	<i>I4/mmm</i>	<i>I4/mcm</i>	<i>I4₁/amd</i>	<i>I4₁/acd</i>				

Space Groups							
Trigonal							
3	$P3$	$P3_1$	$P3_2$	$R3$			
$\bar{3}$	$P\bar{3}$	$R\bar{3}$					
32	$P312$	$P321$	$P3_112$	$P3_121$	$P3_212$	$P3_221$	$R32$
3m	$P3m1$	$P31m$	$P3c1$	$P31c$	$R3m$	$R3c$	
$\bar{3}m$	$P\bar{3}1m$	$P\bar{3}1c$	$P\bar{3}m1$	$P\bar{3}c1$	$R\bar{3}m$	$R\bar{3}c$	
Hexagonal							
6	$P6$	$P6_1$	$P6_2$	$P6_3$	$P6_4$	$P6_5$	
$\bar{6}$	$P\bar{6}$						
6/m	$P6/m$	$P6_3/m$					
622	$P622$	$P6_122$	$P6_222$	$P6_322$	$P6_422$	$P6_522$	
6mm	$P6mm$	$P6cc$	$P6_3cm$	$P6_3mc$			
$\bar{6}m2$	$P\bar{6}m2$	$P\bar{6}c2$	$P\bar{6}2m$	$P\bar{6}2c$			
6/mmm	$P6/mmm$	$P6/mcc$	$P6_3/mcm$	$P6_3/mmc$			

Space Groups								
Cubic								
23	$P23$	$F23$	$I23$	$P2_13$	$I2_13$			
$m\bar{3}$	$Pm\bar{3}$	$Pn\bar{3}$	$Fm\bar{3}$	$Fd\bar{3}$	$Im\bar{3}$	$Pa\bar{3}$	$Ia\bar{3}$	
432	$P432$	$P4_332$	$F432$	$F4_132$	$I432$	$P4_332$	$P4_132$	$I4_132$
$\bar{4}3m$	$P\bar{4}3m$	$F\bar{4}3m$	$I\bar{4}3m$	$P\bar{4}3n$	$F\bar{4}3c$	$I\bar{4}3d$		
$m\bar{3}m$	$Pm\bar{3}m$	$Pn\bar{3}n$	$Pm\bar{3}n$	$Pn\bar{3}m$	$Fm\bar{3}m$	$Fm\bar{3}c$	$Fd\bar{3}m$	$Fd\bar{3}c$
	$Im\bar{3}m$	$Ia\bar{3}d$						

Appendix II. Form of the d -Matrix for Different Symmetry Classes in General Conditions and Kleinman Symmetry

Symmetry class	General conditions	Kleinman symmetry
<u>Biaxial crystals</u>		
1	$\begin{bmatrix} d_{11} & d_{12} & d_{13} & d_{14} & d_{15} & d_{16} \\ d_{21} & d_{22} & d_{23} & d_{24} & d_{25} & d_{26} \\ d_{31} & d_{32} & d_{33} & d_{34} & d_{35} & d_{36} \end{bmatrix}$	$\begin{bmatrix} d_{11} & d_{12} & d_{13} & d_{14} & d_{15} & d_{16} \\ d_{16} & d_{22} & d_{23} & d_{24} & d_{14} & d_{12} \\ d_{15} & d_{24} & d_{33} & d_{23} & d_{13} & d_{14} \end{bmatrix}$
2	$\begin{bmatrix} 0 & 0 & 0 & d_{14} & 0 & d_{16} \\ d_{21} & d_{22} & d_{23} & 0 & d_{25} & 0 \\ 0 & 0 & 0 & d_{34} & 0 & d_{36} \end{bmatrix}$	$\begin{bmatrix} 0 & 0 & 0 & d_{14} & 0 & d_{16} \\ d_{16} & d_{22} & d_{23} & 0 & d_{14} & 0 \\ 0 & 0 & 0 & d_{23} & 0 & d_{14} \end{bmatrix}$
m	$\begin{bmatrix} d_{11} & d_{12} & d_{13} & 0 & d_{15} & 0 \\ 0 & 0 & 0 & d_{24} & 0 & d_{26} \\ d_{31} & d_{32} & d_{33} & 0 & d_{35} & 0 \end{bmatrix}$	$\begin{bmatrix} d_{11} & d_{12} & d_{13} & 0 & d_{15} & 0 \\ 0 & 0 & 0 & d_{24} & 0 & d_{12} \\ d_{15} & d_{24} & d_{33} & 0 & d_{13} & 0 \end{bmatrix}$

Appendix III. Purging Methods and Evaluation of the Efficiency

Two methods are possible for purging the stage. One uses recycled nitrogen gas produced by the LNP95 from the Dewar (most used in this thesis, Figure A. III-1), the other method uses an inert gas from a gas cylinder to purge the stage. The detailed purging methods can be found in the user guide of THMS 600. The efficiency of the purging process was evaluated through microscopy observations of water condensation on the sample holder:

- With the stage not purged and the gas purge valves opened during the cooling process, ice forms on the sample holder as shown in Figure A. III-2 (at -60°C and -100°C).
- With the stage not purged and the gas purge valves closed, the amount of ice on the sample holder is reduced (Figure A. III-3).
- With the stage purged at ambient temperature and the gas purge valves closed during the cooling process, nearly no ice can be observed (Figure A. III-4).

This last protocol was thus chosen to avoid ice forming when performing low-temperature experiments.

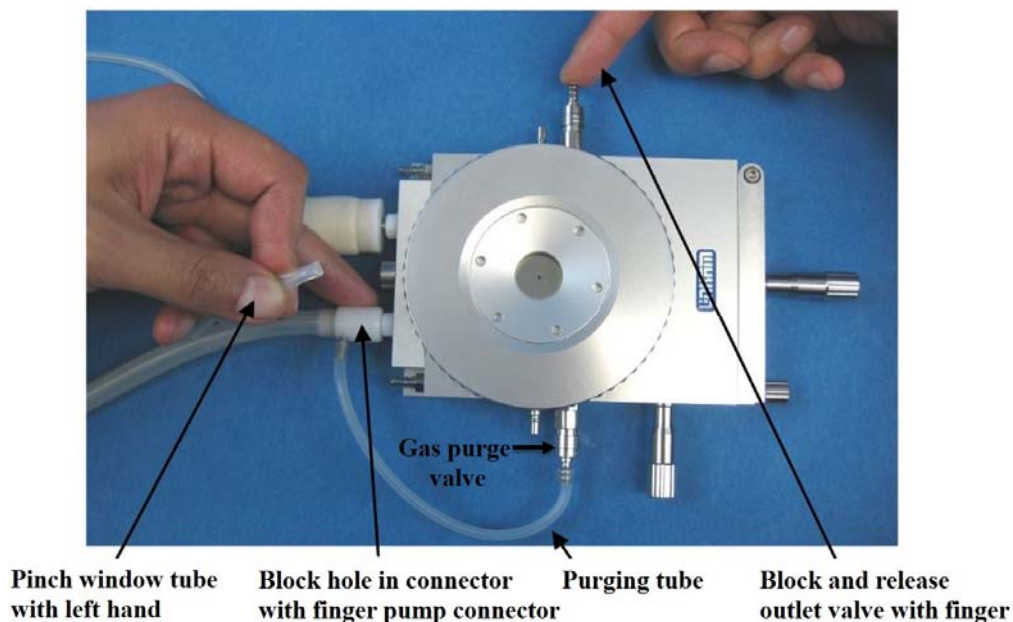


Figure A. III-1. Purging process using recycled nitrogen gas produced by the LNP95 from the Dewar.

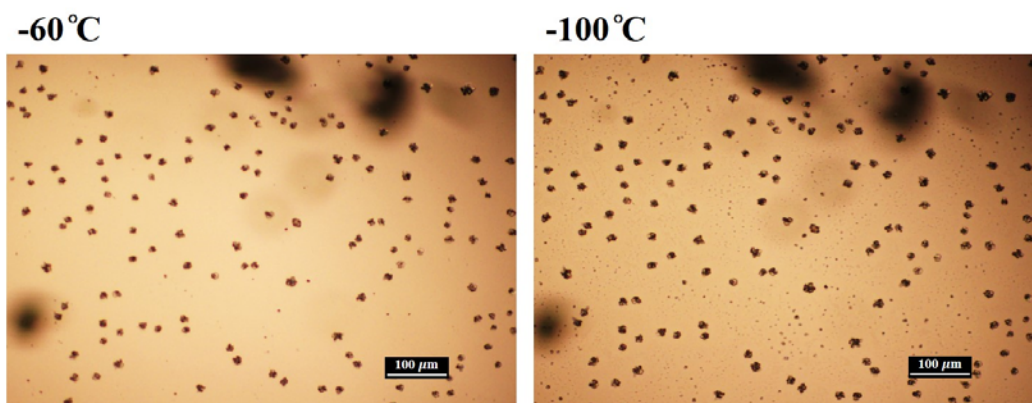


Figure A. III-2. Microscopy observations of water condensation without purging (opened Linkam).

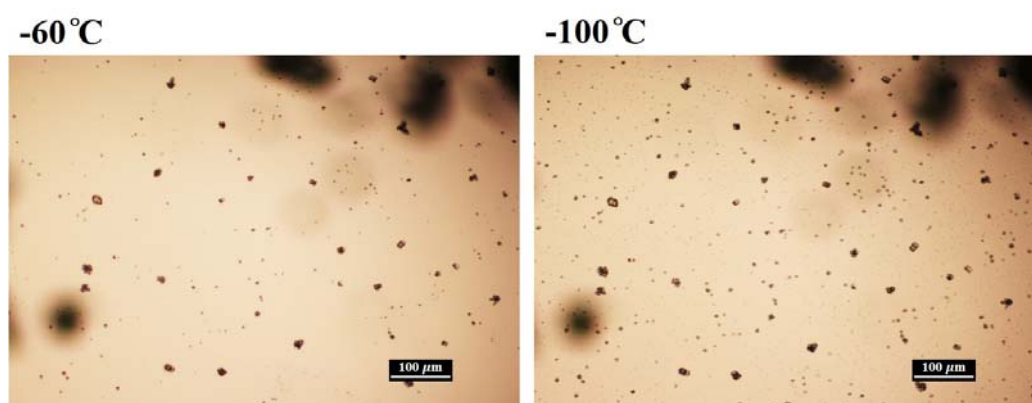


Figure A. III-3. Microscopy observations of water condensation without purging (closed Linkam).

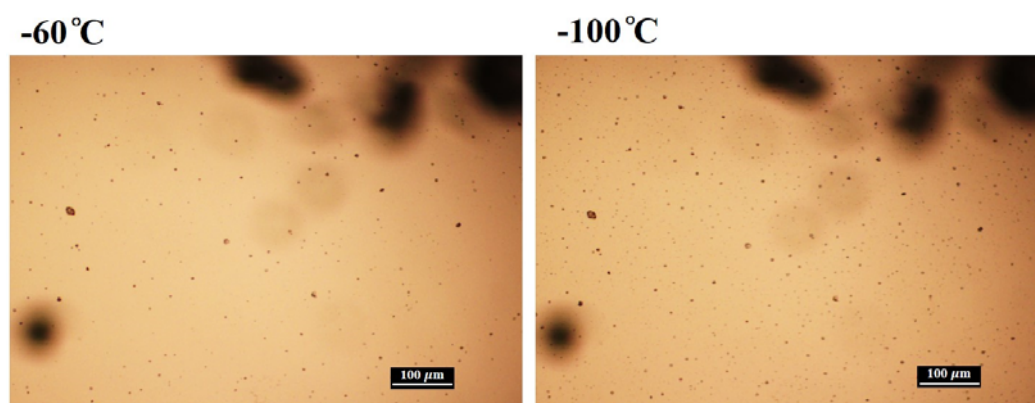


Figure A. III-4. Microscopy observations of water condensation after purging (closed Linkam).

Appendix IV. Reliability of TR-SHG Measurements

Most of the SHG experiments performed along this thesis involved the TR-SHG set-up. This is why it was of utmost importance to assess the reliability of the measurements and to define the accuracy of the technique.

We first analyzed the impact of the fluctuation of the laser energy. Q-Switched lasers are commonly subject to energy fluctuations from one pulse to another. As the SHG intensity evolves as the square of the incident intensity ($I_{2\omega} = I_{\omega}^2$), large fluctuations can indeed induce large variations of the SHG signal.

The energy fluctuations of the incident beams were recorded thanks to a pyrodetector (Ophir Nova). To prevent damages due to the high energy of the beam, the detector was placed behind the first mirror of the set-up that let a small fraction of the energy passing through. Measurements were performed for the laser energy levels 130 mJ/pulse and 250 mJ/pulse) which were the two levels mostly used to analyze our samples. For each energy level, 5 different durations of the laser signal were tested: 3 s, 5 s, 10 s, 30 s, 60 s corresponding respectively to 30, 50, 100, 300 and 600 consecutive laser pulses. Each measurement was repeated 6 times.

Figure A. IV-1 (a) shows the results of the laser stability measurements for the 130 mJ/pulse laser beam. The average pulse energy and its standard deviation is plotted for each signal duration. It decreases with increasing the duration, 3 s measurement has the highest average energy per pulse. In the Q-Switched mode, the laser emission is obtained by preventing light from travelling back and forth in the cavity and by suddenly enabling emission after having stocked a sufficient amount of energy in the amplifying medium. For a longer laser duration, sufficient light waves (photons emitted by the flash lamp) are needed. The standard deviation represents how disperse the laser beam is and the lowest standard error is 10 s measurements. However, in the actual applications, 10 s continuous laser beam may heat the sample or may even damage the sample. A compromise between a higher laser energy (3 s) and a more stable laser beam (10 s) is needed for the use of a 130 mJ/pulse laser beam.

For the 250 mJ/pulse laser beam test (Figure A. IV-1 (b)), the highest laser energy and the lowest standard deviation were achieved for a 3 s measurement. The average energy over 6 measurements is 60.52 $\mu\text{J}/\text{pulse}$ and the standard deviation is 0.15 $\mu\text{J}/\text{pulse}$. A laser duration of 3 s is the optimized experimental condition for this energy.

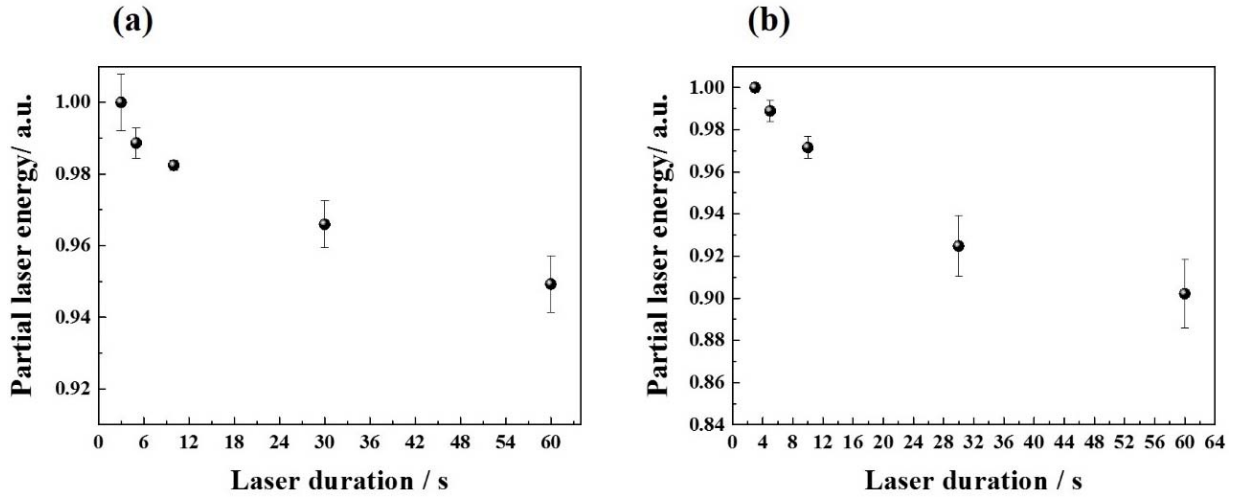


Figure A. IV-1. The stability test of laser beam of (a) 130 mJ/pulse, and (b) 250 mJ/pulse for a duration of 3 s, 5 s, 10 s, 30 s and 60 s.

Therefore, the stability of a duration of 3 s was tested. In Figure A. IV-2, every point represents a 3s measurements. The standard deviation of the 6 measurements is of ca. 1.4%. The intensity of the SHG signal is quadratic to the initial SHG light ($I_{2\omega} = I_{\omega}^2$). So, the uncertainty of the SHG signal is at ca. 3% due to the deviation of the initial laser beam.

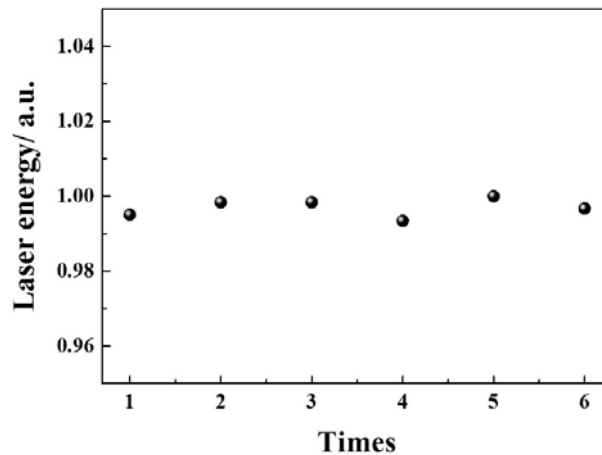


Figure A. IV-2. The stability test of laser beam of 250 mJ/pulse for a duration of 3 s measurements.

Appendix V. Identification and Quantification of the Impurities in 1-Fluoro-adamantane

Identification of impurities in 1-F-A

The impurities in 1-F-A was identified by using GC-MS. A 10,000 ppm 1-F-A solution in acetone was analyzed according to the method detailed below.

A Thermo Scientific Trace GC equipped with a split injector (10 mL/min split flow) and a ITQ-900 mass spectrometer (300 °C transfer line, scan of positive ions from 50 to 250 m/z values) was used for the analysis. Helium was used as carrier gas. A BP-5ms UI column (30 m×0.25 mm×0.25 μ m, 1 mL/min outlet flow) was used for the separation. Temperature was programmed from 50 to 150°C at 5 °C/min. 1 μ L of solution was injected. Data were acquired and processed using Thermo Xcalibur 2.1.0 software. Mass spectra were compared to those of the NIST database (Oct. 2008).

Chromatogram of the sample is presented below (Figure A. V-1).

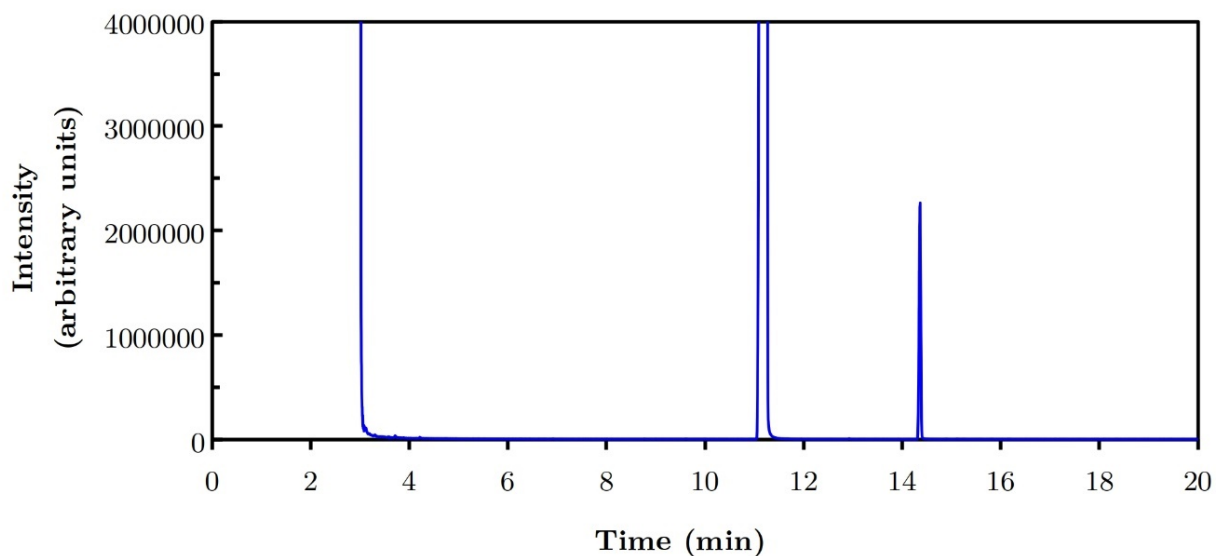


Figure A. V-1. GC-MS chromatogram of the 1-F-A sample.

The large signal at 3 min corresponds to acetone (solvent). The major peak starting at 11.15 min corresponds to 1-F-A (Figure A. V-2). The minor one at 14.35 min corresponds to the impurity, which is further identified as 1-adamantanol (Figure A. V-3).

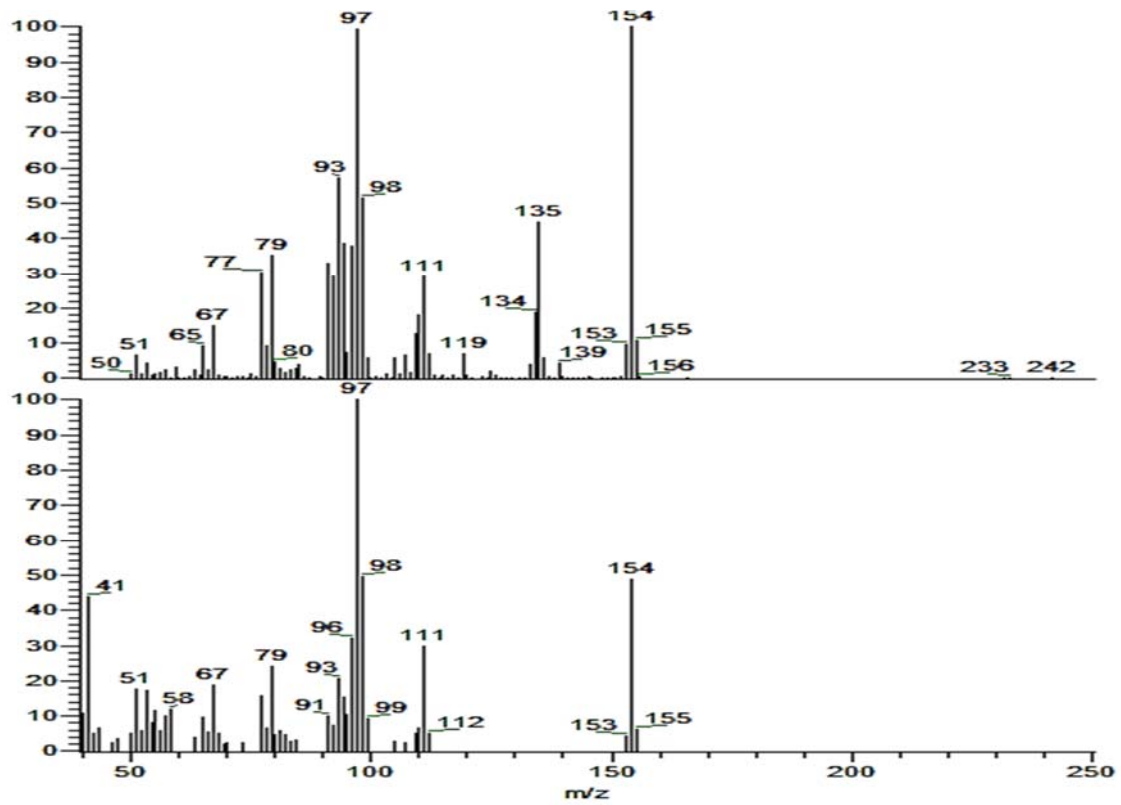


Figure A. V-2. Mass spectra of 1-F-A (top: chromatogram peak at 11.15 min, bottom: reference spectrum from NIST database).

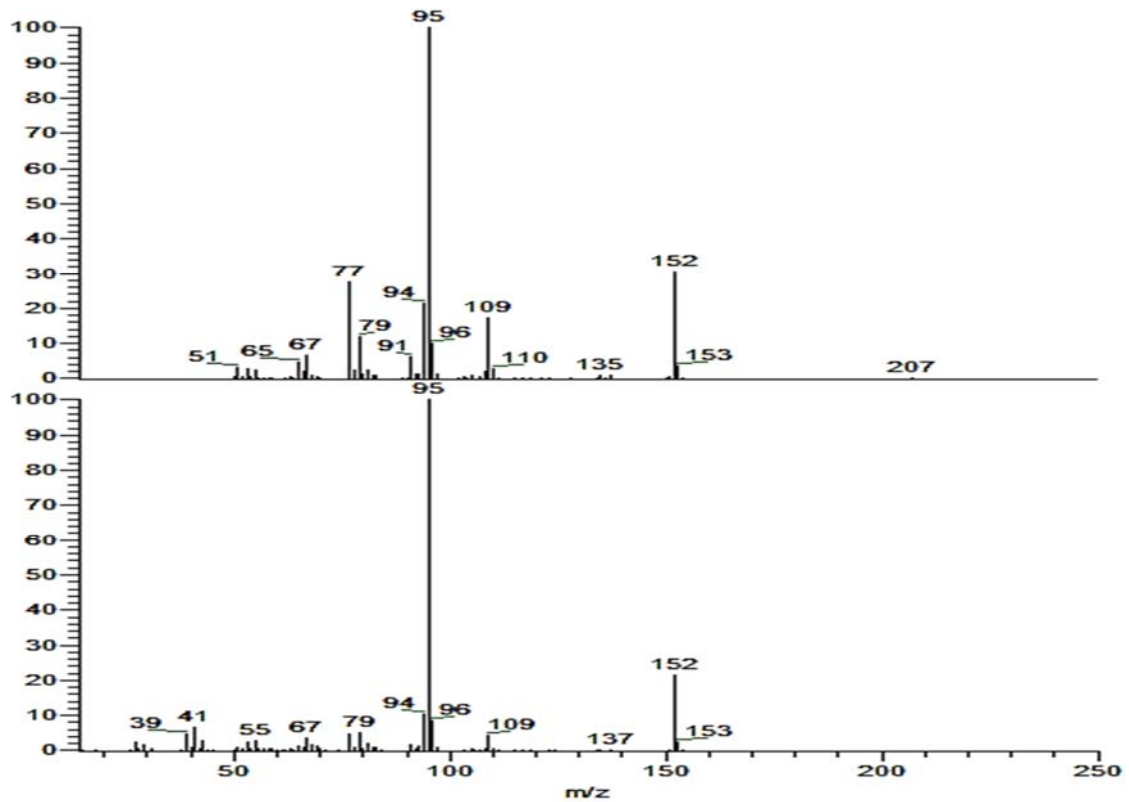


Figure A. V-3. Mass spectra of 1-adamantanol (top: chromatogram peak at 14.35 min, bottom: reference spectrum from NIST database).

Therefore, the only detectable impurity in 1-F-A sample is 1-adamantanol. Next step is to quantify the impurity.

Quantification of the 1-adamantanol impurity in 1-F-A sample

Impurity levels in 1-F-A were monitored by Gas Chromatography (GC) according to the method described below.

Chromatographic conditions: GC measurements were carried out on an Agilent 7890B Series GC equipped with a flame ionization detector (FID) and an auto-sampler (10 μ L syringe). The injector and detector temperatures were set at 300 $^{\circ}$ C. Hydrogen was used as carrier gas. A DB-35ms 30 m \times 0.25 mm \times 0.25 μ m column was used for separations. The inlet split flow was 10 mL/min. The column outlet flow was 1.0 mL/min. Oven temperature was programmed from 50 to 150 $^{\circ}$ C at 5 $^{\circ}$ C/min. The FID was supplied with 30 mL/min hydrogen and 300 mL/min air. The acquisition rate was 200 Hz. For every solution, the injection volume was set at 1 μ L --- this volume was repeatable which allowed quantification by external standard calibration. In these conditions, 1-F-A and 1-adamantanol retention times were 14.80 and 18.50 min, respectively.

FID calibration: The detector was calibrated by injection of 1-adamantanol solutions in acetone ranging from 10 to 100 ppm. Detector response (1-adamantanol peak area) was modeled with respect to concentration by a straight line (Figure A. V-4: slope: 0.659 pA/ppm, intercept: 0.582 pA, $R^2 = 0.998$).

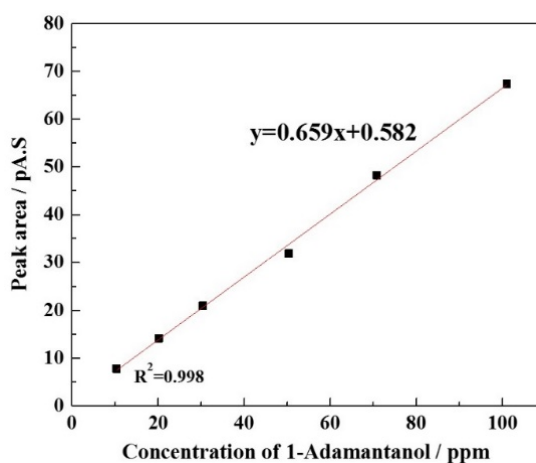


Figure A. V-4. Calibration curve of 1-adamantanol.

1-adamantanol quantification: Sample solutions were prepared by dissolution of 8 mg 1-F-A in 1 g acetone. After analysis by GC, 1-adamantanol concentration in the solution was determined using the calibration curve. The value was divided by the concentration of sample in the analyzed solution to obtain 1-adamantanol level in the sample. After 5 times repeating, the determined average impurity level of 1-adamantanol in 1-F-A sample is 0.07%. So, the purity of the 1-F-A sample is 99.93%.

Appendix VI. Experimental Details

Temperature-Resolved X-Ray Powder Diffraction

Temperature-resolved X-ray powder diffraction data were collected by means of a horizontally mounted INEL cylindrical position-sensitive detector (CPS 120) to pursue a careful structure determination from the HT to LT phases. The detector constituted by 4096 channels was used in Debye-Scherrer geometry. External calibration using the Na₂Ca₂Al₂F₁₄ (NAC) cubic phase mixed with silver behenate was performed by means of cubic spline fittings providing an angular step of 0.029° (2θ) between 4° and 120°. Monochromatic Cu $k_{\alpha 1}$ radiation ($\lambda=1.5406$ Å) was selected with an asymmetric focusing incident-beam curved quartz monochromator. The samples were introduced into 0.5 mm-diameter Lindemann capillaries which were rotated perpendicular to the X-ray beam direction in order to decrease as much as possible the effects of preferred orientations. Temperature was controlled with an accuracy of 0.1K by means of a liquid nitrogen 600 series cryostream cooler from Oxford Cryosystems.

X-Ray Powder Diffraction (XRPD)

XRPD analyses were performed using a D8 diffractometer (Bruker, Germany) equipped with a Lynx Eyes[®] linear detector and a modified goniometer of reverse-geometry (-θ/-θ). The incident X-ray beam consisted of the Cu K_{α} ($\lambda=1.5418$ Å) with a tube voltage and amperage set at 40 kV and 40 mA respectively. XRPD analyses were performed with a step of 0.04° (2θ), and a 12 s per step counting time from 3° to 50° (2θ). Powder samples were placed onto a flat-frosted glass and analyzed at room temperature.

Differential Scanning Calorimetry (DSC)

Thermal analyses were conducted in a DSC 214 Netzsch equipped with an intra-cooler (-70°C). The pre-prepared sample (mass of ca. 10mg with a maximum deviation of 0.05 mg) was placed in a 25 μ L closed aluminum crucible. The atmosphere during the measurements was regulated by nitrogen flux (50mL/min), and heating runs were conducted under conditions similar to those of the TR-SHG measurements in order to compare the results. Data treatment was performed with a Netzsch Proteus V.6.1.

Low-temperature Differential Scanning Calorimetry

Thermal analyses were conducted in a Netzsch 204 F₁ DSC apparatus equipped with liquid nitrogen as the coolant. Both the temperature and the enthalpy changes of the calorimeter were calibrated by using the phase transition of cyclohexane and mercury. Samples were sealed in a 25 μ L aluminum crucible. Thermograms were obtained at a scanning rate of 1 K/min. The atmosphere during the measurements was regulated by a nitrogen flux (40 mL/min). Data treatment was performed with Netzsch-TA Proteus V4.8.4 software.

Cold-stage Microscopy

Microscopy observations were performed under controlled cooling system. Samples (either powder, thin-films or single crystals) were loaded into an amorphous quartz crucible and controlled by a THMS 600 thermal stage setup (Linkam), which allows an accurate control of the sample temperature ($\pm 0.1^\circ\text{C}$). Liquid nitrogen was used as the refrigerant for cooling ramp down to -120°C and the nitrogen flux was regulated via an automatic pump. The setup is coupled with a Nikon Eclipse LV100 microscope (maximum magnification: x1000) connected to a computer for image captures by using a CCD camera.

Crystal Size Distribution

A Mastersizer 2000 was used to determine the particle size of the samples (accuracy better than 1%). By measuring the intensity of light scattered as a laser beam passes through a dispersed particulate sample, the size of the particle was measured. Data are analysed to calculate the size of the particles that generated the scattering patterns. Sample dispersion is controlled by a wet

dispersion unit. This ensures that the particles are delivered to the measurement area of the optical bench at the correct concentration and in a suitable, stable state of dispersion. The solvent used to disperse the powder depends on the solubility properties of the sample.

Curve Fitting

Data were fitted to specific expressions by application of the Levenberg-Marquardt (least-squares method) algorithm using the program Origin 10.